University of Southampton

FACULTY OF ENGINEERING AND THE ENVIRONMENT

NATIONAL CENTRE FOR ADVANCED TRIBOLOGY (NCATS)

DEVELOPING ARTIFICIAL BIOFILMS FOR INVESTIGATING THE EFFECTS OF PHYSICO-MECHANICAL PROPERTIES ON MARINE BIOFILM-ASSOCIATED DRAG

by

ALEXANDRA ANNE SNOWDON

27691268

ORCID ID: 0000-0001-6672-937X

Thesis for the degree of: DOCTOR OF PHILOSOPHY

Submission: 04/2023

Supervisors:

Julian Wharton, nCATS, University of Southampton

Paul Stoodley, nCATS, University of Southampton

Jennifer Longyear, AkzoNobel, Gateshead

Simon Dennington, nCATS, University of Southampton

Bharath Ganapathisubramani, Aeronautical and Astronautical Engineering, University of Southampton

University of Southampton

ABSTRACT

FACULTY OF ENGINEERING AND THE ENVIRONMENT

NATIONAL CENTRE FOR ADVANCED TRIBOLOGY (NCATS)

Thesis for the degree of Doctor of Philosophy

DEVELOPING ARTIFICIAL BIOFILMS FOR INVESTIGATING THE EFFECTS OF PHYSICO-MECHANICAL PROPERTIES ON MARINE BIOFILM-ASSOCIATED DRAG

ALEXANDRA ANNE SNOWDON

Marine biofilms cause a significant increase in drag on ships. From the current literature it is understood that physical and mechanical (physico-mechanical) properties of biofilms influence drag, yet it remains understudied. In part, this is explicable by biofilm heterogeneity and adaptability which complicate efforts to link biofilm properties to frictional drag. As a result, rigid and homogeneous structures are typically used as the benchmark for studying biofilm-associated drag, but as they neglect natural biofilm behaviour, such as viscoelasticity, they could be causing underestimations in drag predictions. To improve drag predictions there is a need to better understand biofilm fluid-structure interactions and the role these play in drag production.

In the current work, it was shown that mesoscopic structural properties: thickness, coverage, and roughness, of marine biofilms interact with viscoelasticity and therefore implicate drag. This relationship was reported using a meso-scale flow cell with an integrated pressure drop system in conjunction with Optical Coherence Tomography (OCT) which enabled deformation behaviour to be captured *in-situ* in real-time whilst simultaneously measuring drag (expressed as a friction coefficient). To build on rigid conventional models, a material sandpaper system with a tailored mechanical profile and surface roughness was proposed. The results showed that, over a Reynolds number range of 1.2×10^4 to 5.2×10^4, an elastomeric sandpaper system caused up to a 52 % higher drag and produced a different drag curve when compared to rigid alternatives of equivalent roughness; differences were attributed to differences in the mechanical response to increasing shear. Similar drag curves were also found for marine biofilms grown at Hartlepool Marina (UK) under hydrodynamic conditions and using OCT it was revealed that viscoelastic behaviour (such as deformation and streamer behaviour) was, in part, responsible for the deviation from rigid drag trends. From the experimental model, and from marine biofilm testing, it was concluded that viscoelasticity plays a critical role in drag production, displays a relationship with structural properties and should not be neglected when estimating biofilm-associated drag by using rigid rough models.

Marine biofilms grow on different surfaces, for example on different coatings, or under varying hydrodynamic conditions which likely alter biofilm physico-mechanics and implicate drag.

Despite this, marine biofilm viscoelasticity has not been previously quantified in the literature. Here, marine biofilms were cultivated across different surfaces in-field and were rheologically characterised using a parallel-plate rheometer. An OCT was utilised to capture biofilm structure and to further investigate links between biofilm structure and mechanics under different conditions.

This Thesis confirmed that marine biofilms are viscoelastic, with a shear modulus ranging from 11 Pa to 7500 Pa depending on growth conditions. For example, biofilms grown under a low flow velocity were softer, thinner, experienced greater structural disruption and produced a 5.7 % higher drag (over a Reynolds number range of 1.2×10^4 to 5.2×10^4) than biofilms grown under a higher flow. In this work it has been emphasised how marine biofilms exhibit dynamic physico-mechanical behaviour when exposed to shear and how elastomeric materials could be better suited for mimicking biofilm-associated drag. The results presented offer insight into the complex and dynamic interactions between biofilm properties and how different surface or growth conditions can alter these relationships. In the long term, this data could be used to improve estimations of biofilm-associated drag and support the development of future marine coatings for targeting drag-producing properties, such as viscoelasticity.

Table of Contents

List of Figures

List of Tables

List of Accompanying Material

- Chapter 5 has already been published in the Ocean Engineering Journal. All data supporting this study is available from University of Southampton Repository at: https://doi.org/10.5258/SOTON/D2287
- Chapter 6 has already been published in the Soft Matter Journal. All data supporting this study will be available from University of Southampton Repository at: https://doi.org/10.5258/SOTON/D2439

List of Presentations

- **Jackson A.** *Physico-mechanical properties of artificial and natural marine biofilms and the associated drag penalty.* Flash presentation at a National Biofilms Innovation Centre (NBIC) meeting (NBIC HQ, Southampton University, UK, 13th – 14th January 2020).
- **Jackson A**, An S-Q, Webb J, Dennington S, Longyear J, Wharton J, Stoodley P. *Elastomeric sandpaper replicas as model systems for studying marine biofilm physico-mechanical properties and hydrodynamic drag penalty.* Poster presentation at the Young Microbiologist Symposium (online conference, Southampton University, UK, 26th – 27th August 2020).
- **Jackson A**, An S-Q, Webb J, Dennington S, Longyear J, Wharton J, Stoodley P. *Using elastomeric materials to model marine biofilm physico-mechanical properties and the associated drag penalty.* Oral presentation at the Biofilms 9 conference (online conference, Karlsruhe Insitut of Technology, Germany, 29th September – 1st October 2020).
- **Snowdon A**, Dennington S, Longyear J, Wharton J, Stoodley P. *An elastomeric model biofilm system for assessing the effect of physico-mechanical properties of marine biofilms on drag.* Oral presentation at the Biofilms 10 conference (HelmHoltz Centre for Environmental Research, Leipzig, Germany, 9th – 11th May 2022).
- **Snowdon A**, Dennington S, Longyear J, Wharton J, Stoodley P. *Using elastomeric sandpaper replicas to model the effect of biofilm physico-mechanical properties on drag.* Oral presentation at the NBIC Summit (Edinburgh University, UK, 14th – 15th June 2022).
- **Snowdon A.** *Marine biofilm physico-mechanical properites and ship drag.* Invited to present a guest lectur at the KTH Royal Institute of Technology in Stockholm, Sweden, for the Fluid and Surfaces Research Department (29th – 30th September 2022).
- **Snowdon A**, An S-Q, Finnie A, Dale M, Dennington S, Longyear J, Wharton J, Stoodley P. *An elastomeric model system for assessing the contribution of physico-mechanical properties of marine biofilms on drag.* Poster presentation at the 2nd GloFouling Partnerships R&D Forum and Exhibition on Biofouling Prevention and Management for Maritime Industries (International Maritime Organisation Headquarters (IMO), London, UK, 11th – 14th October 2022).
- **Snowdon A**, Finnie A, Dennington S, Longyear J, Wharton J, Stoodley P. *Ship hull coatings influence the structure and rheological properties of marine biofilms with implications for drag.* Oral presentation at the American Society for Microbiology (ASM) Biofilms conference (North Carolina, USA, 13th – 17th November 2022).

List of Publications

- **Snowdon, A.** *et al.*, (2022) ‘Elastomeric sandpaper replicas as model systems for investigating elasticity, roughness and associated drag in a marine biofilm flow cell’, *Ocean Engineering*, 266. doi: 10.1016/J.OCEANENG.2022.112739.
  Published online: 8th October 2022
- **Snowdon, A.** *et al.,* (2023) ‘Surface properties influence marine biofilm rheology, with implications for ship drag’, *Soft Matter*, doi: 10.5258/SOTON/D2439.
  Published online: 2nd May 2023

Declaration of Authorship

I, ALEXANDRA ANNE SNOWDON,

declare that this thesis and the work presented in it are my own and has been generated by me as the result of my own original research.

Developing artificial biofilms for investigating the effects of viscoelasticity and roughness on marine biofilm-associated drag

I confirm that:

1. This work was done wholly or mainly while in candidature for a research degree at this University;
2. Where any part of this thesis has previously been submitted for a degree or any other qualification at this University or any other institution, this has been clearly stated;
3. Where I have consulted the published work of others, this is always clearly attributed;
4. Where I have quoted from the work of others, the source is always given. With the exception of such quotations, this thesis is entirely my own work;
5. I have acknowledged all main sources of help;
6. Where the thesis is based on work done by myself jointly with others, I have made clear exactly what was done by others and what I have contributed myself;
7. Parts of this work have been published as:

- Snowdon, A. *et al.,* (2022) ‘Elastomeric sandpaper replicas as model systems for investigating elasticity, roughness and associated drag in a marine biofilm flow cell’, *Ocean Engineering*, 266. DOI: 10.1016/J.OCEANENG.2022.112739.
- Snowdon, A. *et al.,* (2023) 'Surface properties influence marine biofilm rheology, with implications for ship drag, *Soft Matter*, 19. DOI: 10.5258/SOTON/D2439

Signed:

Date:

Acknowledgments

I have a multitude of people I would like to give thanks to, for without them this work would not have happened. My thanks go to:

- my supervisory team for their fantastic support over the past 3 ½ years, despite us being scattered all over the world and for introducing me to the wide world of fluid mechanics, for being patient with me when I was an engineering novice and for helping make my PhD a reality. Specifically, I wish to thank: Prof. Julian Wharton for the time and effort put into my supervision, for providing high level feedback, and for keeping me on track with progressing my engineering knowledge: Prof. Paul Stoodley for being a fountain of knowledge on biofilms, I am very grateful to have learnt from you first-hand and thank you for always being available to offer feedback and have a catch up: Dr Jennifer Longyear for never saying no to a Hartlepool trip - whatever the weather – and for always being available to help and talk things through, you have been an incredible support over my PhD at AkzoNobel: Dr Simon Dennington, for advising me in my journey through materials science and rheometry and for endless discussions on Granville analysis.

- my AkzoNobel team: Marie Dale, who has been an amazing support - thank you for always being up for a chat whether it be work or life and for being my PhD buddy: Graeme Lyall who I have been fortunate to share the lab and many cold Hartlepool trips with and who has always been there to make me laugh along the way: Alison Parry for introducing me to the world of polymer science and for making it an enjoyable experience: Andrea Lloyd for her patience when teaching me how to use a rheometer and helping me navigate the tricky situation of using this equipment to characterise biofilms: Dr Alistair Finnie for providing his expertise on coatings, fouling and drag from the perspective of the shipping industry.

- the National Biofilm Innovation Centre (NBIC), for introducing me to a cohort of other biofilm researchers across multiple industries and for providing access to training events over the years. Specifically, Shi-Qi An, whose help in analysing biofilm images helped progress the publication of my first academic paper.

Finally, I would like to give a special thanks to my husband, Oli, who now knows more about marine biofilms and hydrodynamics than a normal person should and who I couldn't have done this PhD without; thank you for sharing in the highs (having my manuscripts accepted for publication), and for always being supportive during the inevitable lows (biofilms dying after months of growth). A special thank you also goes to my family, I am extremely grateful for your amazing support over the years and for believing in me every step of the way.

Author Contribution Statement

The study presented in Chapter 5 was published in the ‘Ocean Engineering’ Journal (2022) and was part of a collaboration with the NBIC. A. Snowdon designed the experiments under the general supervision of J. Wharton, P. Stoodley, J. Longyear, M. Dale and S. Dennington. M. Dale, J. Longyear, J. Wharton, and P. Stoodley provided feedback on experimental design and handling of data. S. Dennington provided input on the design of materials that could be used for the artificial system. A. Snowdon conducted all laboratory experiments, data handling and statistical analysis of results. SQ. An, of NBIC, constructed the ImageJ code used to analyse Optical Coherence Tomography (OCT) images and trained A. Snowdon in the methods used. A. Finnie gave input on the significance of experimental design and results for the shipping industry on behalf of AkzoNobel. The manuscript was written by A. Snowdon and the final draft was reviewed by all co-authors.

The study presented in Chapter 6 has been accepted for publication in the ‘Soft Matter’ Journal (2023) and is currently in the review process. A. Snowdon designed the experiments under the general supervision of J. Wharton, P. Stoodley, J. Longyear and S. Dennington. All co-authors provided feedback on experimental design and handling of data. A. Snowdon conducted all laboratory experiments, data handling and statistical analysis of results. The manuscript was written by A. Snowdon and the final draft was reviewed by all co-authors.

The study presented in Chapter 7 has been prepared for publication in the ‘Environmental Microbiology’ Journal (-). A. Snowdon designed the experiments under the general supervision of J. Wharton, P. Stoodley, J. Longyear and S. Dennington. All co-authors provided feedback on experimental design and handling of data. A. Snowdon conducted all laboratory experiments, data handling and statistical analysis of results. The manuscript was written by A. Snowdon and the final draft was reviewed by all co-authors.

The study presented in Chapter 8 has been prepared for publication in the ‘Biofouling’ Journal (-). A. Snowdon designed the experiments under the general supervision of J. Wharton, P. Stoodley, J. Longyear and S. Dennington. J. Longyear assisted with maintenance trips to Hartlepool Marina and with running flow cell experiments. All co-authors provided feedback on experimental design and handling of data. A. Snowdon conducted all laboratory experiments, data handling and statistical analysis of results. The manuscript was written by A. Snowdon and the final draft was reviewed by all co-authors.

List of Abbreviations

1D – One Dimensional

2D – Two Dimensional

3D – Three Dimensional

ACP – Anticorrosive Primer

AFM – Atomic Force Microscopy

ANOVA – Analysis of Variance

ASW – Artificial Seawater

CFD - Computational Fluid Dynamics

CLSM – Confocal Laser Scanning Microscopy

DAQ – Data Acquisition

DIC – Digital Image Correlation

EPS – Extracellular Polymeric Substances

eDNA – extracellular DNA

FEPA – Federation of European Producers of Abrasives

FRC – Foul Release Coating

HF – High Flow

LF – Low Flow

LTSEM – Low Temperature Scanning Electron Microscopy

LVR – Linear Viscoelastic Region

MBFC – Marine Biofouling Flow Cell

OCA – Optical Contact Angle

OCT – Optical Coherence Tomography

PDMS – Polydimethylsiloxane

PIV – Particle Image Velocimetry

PTFE – Polytetrafluoroethylene

PVC – Polyvinyl Chloride

PVOH - Polyvinyl alcohol

RSS – Root of the Sum of Squares

SD – Standard Deviation

SEM – Scanning Electron Microscopy

List of Symbols and Units

α – Angle of deformation (^{o})

C_{f} – Fanning Friction coefficient (dimensionless)

C_{f}^{*} – Fanning Friction coefficient (dimensionless) in the MBFC system

$C_{f,I}$ – Instantaneous Fanning Friction coefficient (dimensionless)

C_{m} – Momentum coefficient (dimensionless)

D_{h} – Hydraulic diameter (m)

∂ – Uncertainty of a variable 95 % confidence

E – Young's modulus of Elasticity (Pa)

E_{app} – Apparent Young's modulus of Elasticity (Pa)

E_{IT} – Indentation modulus (Pa)

f – Fanning friction factor (dimensionless)

G – Shear modulus (Pa)

G_{app} – Apparent shear modulus (Pa)

G' – Storage modulus (Pa)

G'' – Loss modulus (Pa)

H – Channel height of flow cell (m)

H_{m} – Marten's hardness (MPa)

k – Loss coefficient (dimensionless)

L – Length between pressure ports (m)

η – Viscosity (Pa s^{-1})

η^{*} – Complex viscosity (Pa s^{-1})

ΔP – Pressure drop (Pa)

ρ – Water density (kg m^{-3})

Re – Reynolds number (dimensionless)

R_a^* – Roughness coefficient (dimensionless)

S_a – Average surface roughness (µm)

S_z – Average peak to trough roughness height (µm)

σ – Shear stress applied for rheometer experiments (Pa)

σ_y – Yield stress (Pa)

τ – Shear stress (Pa)

τ_w – Shear stress acting at the wall (Pa)

u – Average flow velocity (m s^{-1})

v – Poisson's ratio (dimensionless)

v_k – Kinematic viscosity of water (m^2 s^{-1})

ϖ – Angular frequency (rad s^{-1})

w – Channel width of the flow cell (m)

γ – Shear strain (%)

λ – Elastic relaxation time (seconds)

List of Definitions

Physico-mechanical – physical structure and mechanical properties of a material.

Source – the basis of the material *replicas* formed during casting and moulding. Sandpaper of varying roughness grades (P40, P80 and P240) and a smooth PVC panel were used as *sources*.

Sandpaper-P40 – sandpaper (source) of the roughness grade P40 (as per FEPA standards).

Sandpaper-P80 – sandpaper (source) of the roughness grade P80 (as per FEPA standards).

Sandpaper-P240 – sandpaper (source) of the roughness grade P240 (as per FEPA standards).

PVC-smooth – a smooth polyvinyl chloride (PVC) panel, used as a source.

Intermediate – an *intermediate* material was used to form a negative mould of a *source*. Urethane putty and silicone moulding rubber were used.

Urethane-P40 – a urethane putty *intermediate* mould which was cast from sandpaper at a roughness grade of P40 (as per FEPA standards) and used to mould the elastomer P40 *replicas*.

Urethane-P80 – a urethane putty *intermediate* mould which was cast from sandpaper at a roughness grade of P40 (as per FEPA standards) and used to mould the elastomer P80 *replicas*.

Urethane-P240 – a urethane putty *intermediate* mould which was cast from sandpaper at a roughness grade of P240 (as per FEPA standards) and used to mould the elastomer P240 *replicas*.

Silicone-P40 – a silicone moulding rubber *intermediate* mould which was cast from sandpaper at a roughness grade of P40 (as per FEPA standards) and used to mould the filler P40 *replicas*.

Silicone-P80 – a silicone moulding rubber *intermediate* mould which was cast from sandpaper at a roughness grade of P80 (as per FEPA standards) and used to mould the filler P80 *replicas*.

Silicone-P240 – a silicone moulding rubber *intermediate* mould which was cast from sandpaper at a roughness grade of P240 (as per FEPA standards) and used to mould the filler P240 *replicas*.

Silicone-smooth – a silicone moulding rubber *intermediate* mould which was cast from a smooth PVC panel and used to mould the filler smooth *replicas*.

Replica – a material mimic of the source. A *replica* material was poured into the negative *intermediate* mould of the *source*. An elastomer and yacht filler were used as *replica* materials and the *intermediate* material chosen for the mould depended on the *replica* material.

Elastomer-P40 – an elastomer material *replica* of sandpaper at a roughness grade of P40 (as per FEPA standards).

Elastomer-P80 – an elastomer material *replica* of sandpaper at a roughness grade of P80 (as per FEPA standards).

Elastomer-P240 – an elastomer material *replica* of sandpaper at a roughness grade of P240 (as per FEPA standards).

Elastomer-smooth – an elastomer material *replica* of a smooth PVC panel.

Filler-P40 – a filler material *replica* of sandpaper at a roughness grade of P40 (as per FEPA standards).

Filler-P80 – a filler material *replica* of sandpaper at a roughness grade of P80 (as per FEPA standards).

Filler-P240 – a filler material *replica* of sandpaper at a roughness grade of P240 (as per FEPA standards).

Filler-smooth – a filler material *replica* of a smooth PVC panel.

ACP biofilms – biofilms cultivated on circular PVC coupons coated in anti-corrosive primer.

FRC biofilms – biofilms cultivated on circular PVC coupons coated in a foul-release coating.

PVC biofilms – biofilms cultivated on circular PVC coupons.

1 Chapter 1: Introduction

Biofilms are composed of a community of sessile microorganisms embedded within a viscous exudate (the matrix) which is mainly composed of extracellular polymeric substances (EPS) (Flemming and Wingender, 2010; Di Martino, 2018) and water (Berlanga and Guerrero, 2016). It is widely accepted that this thick, biopolymer matrix offers protection to microbial cells from external stressors, such as: environmental (Karimi *et al.*, 2015), medical (e.g. antibiotics) (Fux *et al.*, 2009; Gloag *et al.*, 2021), chemical (e.g. biocides) (Finnie and Williams, 2010) and mechanical (Peterson *et al.*, 2015). Consequent to these tolerant characteristics, biofilms are difficult to prevent, and/or remove, which causes problems across an array of industries, including wastewater treatment, medical and shipping (Charlton *et al.*, 2019).

In the shipping industry, biofouling occurs, which is simply the unwanted colonisation of a submerged surface by living organisms. Marine biofilms are often referred to as slime, or soft fouling, and are comprised of microalgae and bacteria (Salta *et al.*, 2013; Papadatou *et al.*, 2021). When marine biofilms colonise a ship surface, they can significantly increase frictional resistance and can recruit larger fouling organisms (Wahl, 1989), such as macroalgae and calcareous organisms (barnacles and mussels for example), which further increases vessel resistance (Schultz, 2007; Schultz *et al.*, 2015; Demirel *et al.*, 2017). This leads to serious environmental consequences, such as higher fuel consumption and greater greenhouse gas emissions (Schultz and Swain, 2000; Townsin, 2003). In 2021, the International Maritime Organisation published data that revealed that ship emissions were equivalent to 2.89 % total CO_2 emissions in 2018 (IMO, 2021). There are also substantial economic consequences (Eyring *et al.*, 2010; de Carvalho, 2018) as it has been estimated that the presence of biofouling on the hulls of 30 % of the US naval fleet could cost up to $56 million per year (Schultz *et al.*, 2011). Aside from issues related to frictional drag, fouling can also enable the unwanted translocation of invasive species around the world (Hewitt, Gollasch and Minchin, 2009; Sylvester *et al.*, 2011).

There is a large body of research that has investigated harder fouling (calcareous organisms, for example) (Townsin, 2003; Turan *et al.*, 2016; Demirel *et al.*, 2017) where biofilm-associated drag remains poorly understood. In part this is due to biofilms displaying a high level of heterogeneity and morphological adaptability to physical forces which makes them complex to study and may cause variation in efforts to relate biofilm characteristics to drag (Schultz *et al.*, 2015). It has been estimated that biofilms alone can cause up to an 18 % increase in ship powering requirements (Schultz *et al.*, 2011) and as biofilms are critical for surface colonisation (Salta *et al.*, 2013; de

Carvalho, 2018) it is believed that combatting these could limit macro-fouler presence (Baba and Tokunaga, 1980).

With an aim to simplify studies on biofilm-associated drag, experimental and computational models have been adopted which typically use homogenous and/or rigid structures to mimic biofilms (Yusim and Utama, 2017; Hartenberger *et al.*, 2020). Rigid structures, such as sandpaper or embedded sand grains have been utilised as they have displayed roughness length scales comparable to biofilms and have induced drag indicative of a rigid surface under specified experimental conditions (Schultz *et al.*, 2015; Murphy *et al.*, 2018; Hartenberger *et al.*, 2020). Although roughness is significant in influencing drag, it is known that biofilms deform when exposed to hydrodynamic shear (Peterson *et al.*, 2015; Gloag *et al.*, 2020), such as on a ship (Dennington *et al.*, 2015). This behaviour can be referred to as viscoelasticity which means that a material (natural or synthetic) can exhibit an elastic- or viscous-dominated response depending on the length of time shear stress is applied for (Shaw *et al.*, 2004; Gordon *et al.*, 2017). From studies comparing drag associated with rigid structures to compliant ones it is acknowledged that the compliant nature of biofilms plays a role in drag production (Picologlou, Zelver and Characklis, 1980; Stoodley, Lewandowski, Boyle, *et al.*, 1999; Schultz *et al.*, 2015; Hartenberger *et al.*, 2020) although this relationship has not been directly quantified.

Therefore, whilst conventional rigid biofilm substitutes can successfully simulate roughness, they do not account for physico-mechanical properties, such as elastic or viscous behaviour, which possibly leads to the mis-estimation of drag (Picologlou, Zelver and Characklis, 1980; Hartenberger *et al.*, 2020; Snowdon *et al.*, 2022). As a result, a model is required that can encompass both biofilm geometry and viscoelasticity, but to achieve this marine biofilm viscoelasticity must first be characterised. Understanding how physical and mechanical properties of biofilms interact with one another and with fluid flow, and how these interactions influence drag would further research on strategies for managing and preventing biofilm presence on ship hull and could be used to inform the coating industry of more efficient biofilm targets.

2 Chapter 2: Research questions and thesis structure

2.1 Research questions, aims and objectives

The central hypothesis of this work is that viscoelasticity of marine biofilms plays a critical role in associated drag. Therefore, in order to better relate biofilm-associated drag to roughness parameters and physico-mechanical properties, it would be useful to develop a suitable method of testing and a model that can represent all biofilms, not just those that align well with sandpaper data or those that possess specific features (Hartenberger, 2019). Such a method and model would allow more realistic correlations to be made between marine biofilm viscoelasticity, roughness and drag.

This PhD will address questions such as: what role does biofilm viscoelasticity play in increasing drag; is there a relationship between biofilm structure and mechanics and does this implicate drag; and finally, how do different conditions during biofilm growth alter these relationships? With a goal to address these questions, the aims and objectives are laid out as follows:

1) Determine the relative contribution of roughness and elasticity to biofilm-associated drag using a tailored and elastomeric model system

To build on rigid conventional models used to estimate and predict biofilm-associated drag a tailored elastic component was added. Sandpaper of different grit sizes were used as the basis for the model and material replicas with elastomeric and rigid profiles were produced. Replicas were placed in a meso-scale flow cell with an integrated pressure drop system used for measuring drag. In conjunction Optical Coherence Tomography (OCT) was set up to visualise topographical changes which were analysed using Fiji, ImageJ.

2) Determine the physico-mechanics of marine biofilms grown statically on different surfaces

Biofilms were grown statically at the Dove Laboratory (UK) on circular polyvinyl chloride (PVC) coupons (4 cm dia.) coated in three commercial grey paints. A parallel-plate rheometer was used to rheologically characterise marine biofilms and amplitude sweeps, frequency sweeps and creep-recovery tests were performed. OCT and MATLAB scripts were used to assess structural properties before and after rheometer testing.

3) Determine how surface colour affects the physico-mechanics of marine biofilms grown statically

Biofilms were grown statically in Hartlepool Marina (UK) on PVC coupons (4 cm dia.) coated in a commercially available paint in three different colours: red, white, and black. A parallel-plate rheometer was used to rheologically characterise marine biofilms and amplitude sweeps, frequency sweeps and creep-recovery tests were performed. OCT and MATLAB scripts were used to assess structural properties before and after rheometer testing.

4) Determine the effect of hydrodynamics on the physico-mechanical properties of marine biofilms and the overall impact on drag

Marine biofilms were grown in Hartlepool Marina (UK) under two different flow conditions: low flow and high flow. After four-months growth, a clean flow cell complemented with an OCT was used to determine biofilm structure, mechanics and drag simultaneously over a *Re* range of 1.2×10^4 to 5.2×10^4. Fiji, ImageJ was used to analyse two-dimensional (2D) OCT-scans, MATLAB scripts were used to analyse three-dimensional (3D) OCT-scans and C_f was used as a proxy for drag. As biofilms were cultivated under different hydrodynamic conditions the effect of growth on biofilm structure, mechanics and drag was also assessed.

2.2 Thesis structure

This thesis consists of nine chapters. The literature review is provided in Chapter 3 and looks at the current state of knowledge surrounding marine biofilms and the problems in the shipping industry, biofilm viscoelasticity and finally biofilm-associated drag.

Chapters 5 to 8 have been written in paper format where each chapter has an abstract, introduction, methods, results, discussion, and conclusion. As a result, there may be some repetition between chapters where similar methods have been applied. To provide additional information on methodology and equipment design, that would perhaps be in the supplementary information of a paper, Chapter 4 has been added.

In Chapter 5 a repeatable elastomeric model system for estimating biofilm-associated drag which used sandpaper roughness as the basis for the model is introduced. An OCT was set up in conjunction with a flow cell which allowed surface topography and drag to be measured simultaneously. As surface roughness was controlled, confirmed using Blue-Light Interferometry, the relative contribution of roughness and elasticity on drag could be estimated at different Reynolds numbers (*Re*). This work included a collaboration with Shi-Qi An from the National Biofilms Innovation Centre (NBIC) who developed script in Fiji, ImageJ to determine topographical changes of the material sandpaper replicas using OCT-scans. This chapter has already been published in the Ocean Engineering Journal (Snowdon *et al.*, 2022).

To validate the use of the material system proposed in Chapter 5 the mechanical properties of ship-relevant marine biofilms were studied - this has not been previously reported in the open published literature. A parallel-plate rheometer was used to rheologically characterise marine biofilms grown statically in the Dove Laboratory (UK) on different surfaces. In Chapter 6, the effect of different coatings of the same colour (grey) was investigated and in Chapter 7 different colours (red, white, and black) of the same coating were studied. In Chapter 5 it was concluded that roughness and elasticity interact and have a combined effect on drag. Therefore, to determine how structural and mechanical properties of natural marine biofilms are interlinked, an OCT (complemented with MATLAB scripts) was used to quantify biofilm thickness, cover and a roughness coefficient (R_a^*). To give an indicator of biofilm strength OCT was used before and after rheometer testing. As the results could be used to inform the design of future biofilm-associated drag models the implications for ship-drag were also presented.

Chapter 8 compiles the information produced in previous chapters and aims to determine how hydrodynamic conditions affect marine biofilm physico-mechanical properties and demonstrates how this could influence drag. Marine biofilms were cultivated in-field under ‘low flow’ and ‘high flow’ in Hartlepool Marina, (UK). For hydrodynamic testing, a flow cell and OCT were used in conjunction for quantifying biofilm structure, viscoelasticity and drag simultaneously. The data produced in this chapter was also used as verification for the model proposed in Chapter 5.

Chapter 9 provides an overarching discussion by emphasising the key insights from this body of work. Finally, Chapter 10 offers a conclusion, followed by future recommendations and final remarks.

3 Chapter 3: Literature review

3.1 Marine biofilms in the shipping Industry

3.1.1 Marine biofilms

Marine biofilms are a community of sessile bacteria and microalgae that exist within a hydrated, viscoelastic exudate, otherwise known as the matrix (Flemming and Wingender, 2010). The matrix is primarily composed of extracellular polymeric substances (EPS) which are known to protect embedded cells by acting as a barrier against external stressors, whether they be environmental, chemical or mechanical (Gloag *et al.*, 2020; Tuck *et al.*, 2022). Further, the EPS aids in biofilm attachment to surfaces, such as the hull of a ship (Zargiel, Coogan and Swain, 2011; Zargiel and Swain, 2014). In conjunction with the protective nature of the matrix, biofilms are adaptable and display a high level of heterogeneity to external forces. Overall, these properties make biofilms difficult to prevent or remove as not one method can be applied to combat them. As a result, biofilms cause problems across an array of industries, including shipping, wastewater and medical (Flemming and Wingender, 2010).

3.1.2 Problems in the shipping industry

Within the shipping industry, marine biofilms (often referred to as slime) induce serious economic and environmental implications, as their presence on a ship hull leads to an increase in frictional drag (Watanabe, 1969; Townsin, 2003). Even just a thin layer of slime can increase drag significantly (Lewthwaite, Molland and Thomas, 1985; Haslbeck and Bohlander, 1992; Schultz and Swain, 2000; Schultz, 2004). Schultz *et al.,* (2011) estimated a 1 – 18 % increase in shaft power in the presence of biofilms, which is supported by an earlier study by Haslbeck and Bohlander (1992) who recorded an 18 % increase in ship power when biofilms were found on antifouling ship coatings. Although a relationship between biofilm presence and drag is recognised, and has been since 1916 (McEntee, 1916), little is known about how biofilm physico-mechanics interact with fluid flow and thus influence hydrodynamic resistance.

Macro-fouling, for example calcareous organisms and seaweeds, on the other hand, has been well studied (Schultz and Swain, 2000; Leer-Andersen and Larsson, 2003; Townsin, 2003). Barnacles and mussels present more obvious and rigid fouling geometries that can be considered simpler to model (either experimentally or computationally) than compliant micro-fouling, namely biofilms. Demirel *et al.,* (2017) found excellent agreement between drag results obtained for barnacles, 3D-printed barnacles and a Computational Fluid Dynamics (CFD) model when investigating roughness effects of fouling on ship hydrodynamics (Demirel, Turan and Incecik, 2017; Song, Demirel and

Atlar, 2019). For marine biofilms, however, the physical mechanisms acting during hydrodynamic shear complicate efforts to model roughness and drag (Schultz *et al.*, 2015; Hartenberger *et al.*, 2020).

To combat biofouling, whether it be micro- or macro-fouling, coatings are often applied to ship hulls (Finnie and Williams, 2010). Coatings can be classified according to whether they are biocidal (toxic) or non-biocidal (non-toxic). Traditionally, biocidal coatings, that house toxic components, have been applied to ship hulls and work to control the settlement of fouling organisms. Although biocidal coatings have been the most popular choice for ship owners, there is growing concern over the potential negative environmental consequences caused by the release of biocides into the surrounding water. As a result, research into non-biocidal alternatives has increased and foul-release coatings (FRC's) are being applied. Simply, FRC's do not house an active ingredient and instead focus on minimising the adhesion capability of settling organisms by acting as a non-stick elastomeric surface with a low surface energy (Atlar *et al.*, 2003). Even if an organism manages to settle on an FRC surface, the ability for it to strongly bind to a surface is compromised and removal could be facilitated by hydrodynamic shear experienced on the side of a ship.

Although both coating types have demonstrated success, it cannot be expected that a single coating can be highly efficient against all fouling organisms. Biofilms alone are largely heterogeneous and adaptable, and several studies have shown how different biofilm communities thrive when cultivated on different surfaces, whether it is consequence to wetting properties, surface roughness, and chemical composition (Zargiel, Coogan and Swain, 2011; Muthukrishnan *et al.*, 2014; Zargiel and Swain, 2014; Papadatou *et al.*, 2021) or even colour (Dobretsov, Abed and Voolstra, 2013; Gambino *et al.*, 2018). Yet, less is known on how different coated surfaces alter the physical structure or mechanical properties of a marine biofilm, both of which are known to play a role in drag production. To inform future marine coating development there is a need to better understand fluid-structure interactions between biofilms and the surrounding flow, and to better understand how different surfaces implicate this relationship. These studies would aid in designing future marine-coatings by offering insight into more efficient biofilm targets for new prevention and removal technologies.

3.2 Viscoelasticity of biofilms and synthetic materials

The mechanical response observed when a biofilm is exposed to stress is controlled by the physical structure and mechanical properties of the EPS matrix (Wilking *et al.*, 2011; Tierra *et al.*, 2015; Boudarel *et al.*, 2018). Simply, the structure and components of the EPS matrix dictates the biofilm elasticity and the pores (voids) and channels, which allow fluid flow through the biofilm (Stoodley, DeBeer and Lewandowski, 1994), constitute the viscous elements (Lembre, Lorentz and Di, 2012; Majumdar *et al.*, 2017). This view offers explanation for why biofilms are often considered comparable to cross-linked polymeric gels (Kavanagh and Ross-Murphy, 1998; Wilking *et al.*, 2011; Mazza, 2016).

Under normal environmental conditions biofilms are viscoelastic entities (Towler et al., 2003), which means they exhibit a time-dependent response when external stress is applied that has elastic and viscous elements (Klapper et al., 2002; Guélon, Mathias and Stoodley, 2011; Mazza, 2016). Typically, if stress is applied for a short period (up to a few minutes) a biofilm will exhibit an elastic response and will recover to its pre-deformed state once the stress is removed (Körstgens *et al.*, 2001a; Klapper *et al.*, 2002; Mathias and Stoodley, 2009). Yet, if stress is applied for a longer duration a viscous response can be observed where the biofilm will begin to flow as a fluid; once the stress is removed there can be evidence of irreversible deformation as the biofilm recoils but not to its pre-deformed state (Figure 3-1) (Klapper *et al.*, 2002; Fabbri *et al.*, 2016; Mazza, 2016; Gloag *et al.*, 2020). Elements of permanent deformation are characteristic of a viscoelastic fluid and is believed to be due to slippage between the polymer strands within the structure, caused by breakage of hydrogen bonds (Stoodley, Boyle and Lappin-scott, 2000; Prades *et al.*, 2020) (Figure 3-1). This behaviour is also recognised in polymers (Stoodley, Boyle and Lappin-scott, 2000; Vincent, 2012).

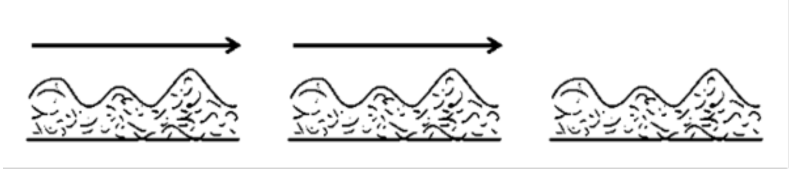

Rigid materials under flow

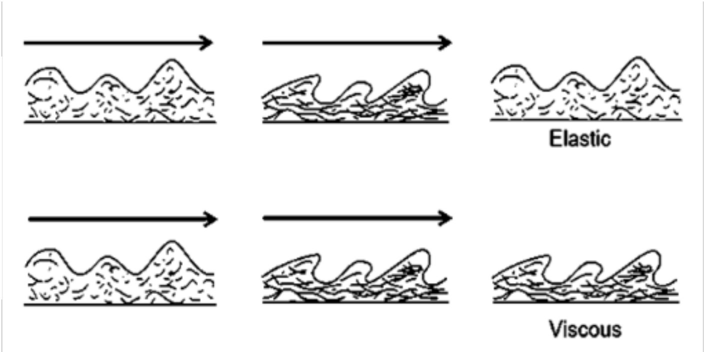

Viscoelastic materials, ex. biofilms, under flow

Figure 3-1. *Schematic showing the mechanical response of rigid and viscoelastic material under flow, adapted from Klapper et al., (2002). The elastic and viscous responses both show deformation under applied stress but exhibit differences once the stress is removed. An elastic material will fully recover, whereas a viscous material will maintain its deformed state.*

The analogy between biofilms and polymer gels is supported by the fact that although biofilms and gels are deformable and display low elastic moduli they can also be strong and withstand imposed stress (Grillet, Wyatt and Gloe, 2012; Sun *et al.*, 2013; Souza-Egipsy *et al.*, 2021). As a result, viscoelasticity has been attributed with increasing the mechanical integrity of biofilms and the protective nature of the EPS (Peterson *et al.*, 2015; Gloag *et al.*, 2020).

3.2.1 Viscoelastic properties

Viscoelastic deformation can be quantified using shear modulus (*G*), and elastic (or Youngs) modulus (*E*), which describe the rigidity and elasticity of a material, natural or synthetic. Both parameters are defined as the ratio of stress to strain but differ in the nature of applied stress: *E* is related to tensile stress and *G* to shear stress (Figure 3-2) (Vincent, 2012).

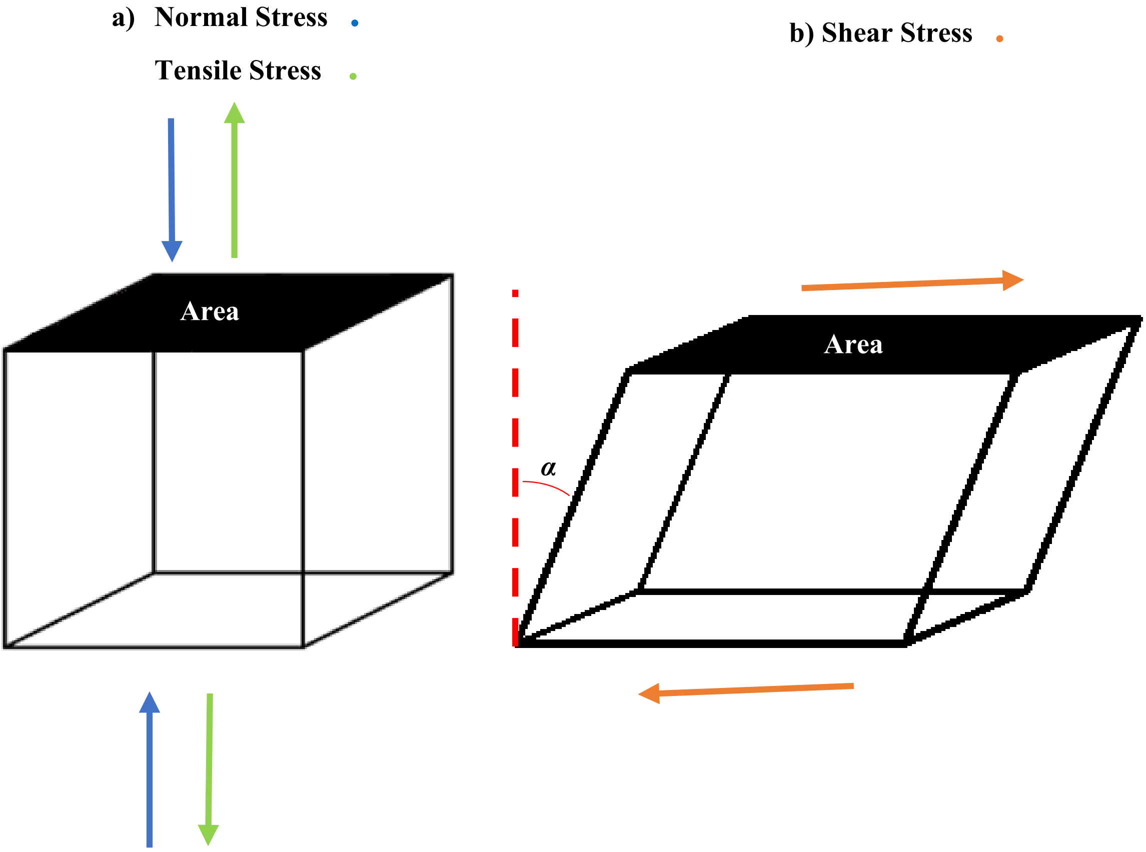

Figure 3-2. *Schematic showing the differences between a) normal (blue) and tensile (green) stress and b) shear (orange) stress. The arrows show the direction of the applied force.*

E, is typically calculated using:

$$E = \frac{\sigma}{\varepsilon} \qquad \textit{Equation 3-1}$$

where ε is strain calculated as the ratio between the change in relative elongation of the material compared to the original material length and σ is the tensile stress applied (Figure 3-2).

Alternatively, G is calculated using:

$$G = \frac{\tau}{\gamma}$$ *Equation 3-2*

where, τ is the shear stress applied and γ is shear strain calculated using $\tan(\alpha)$ where α is the change in the angle of deformation (in radians) (Figure 3-2). By plotting stress-strain curves the slope of the can also be used to provide single estimates of G or E over a strain range. These methods have been successfully applied in biofilm studies (Stoodley, Lewandowski, Boyle, *et al.*, 1999; Laspidou and Aravas, 2007).

For an isotropic material (one that displays homogeneity with respect to physical properties, regardless of the direction of applied stress) a relationship exists between E and G. They can be linked to each other using the Poisson's ratio, ν:

$$E = 2G\,(1 + \nu)$$ *Equation 3-3*

Poisson's ratio describes the relation between transverse and longitudinal strain in the direction of applied stress (Geissler and Hecht, 1981; Greaves *et al.*, 2011). For biofilms, ν is assumed to range between 0.4 and 0.5 (Laspidou and Aravas, 2007; Taherzadeh, Picioreanu and Horn, 2012; Kundukad *et al.*, 2016). A value of 0.4 is often reported for polymeric gels (Geissler and Hecht, 1981), and has been adopted for the majority of biofilm studies (Taherzadeh *et al.*, 2010; Jafari *et al.*, 2018). Although for mature biofilms, a value of 0.5, which is characteristic of materials such as polyvinyl alcohol (PVOH) hydrogels (Park and Hrymak, 2016) or rubber that shows little to no compression under stress (Greaves *et al.*, 2011), can be used instead (Rmaile *et al.*, 2013; Safari *et al.*, 2015; Kundukad *et al.*, 2016; Gloag *et al.*, 2018). Interestingly, biofilms have also been known to exhibit a negative Poisson's ratio (Blauert, 2017) which is a feature of anisotropic materials that display different physical properties depending on the direction of applied stress.

Another property often reported when rheologically characterising viscoelastic materials, such as biofilms, is the elastic relaxation time (λ); the time it takes for a biofilm to transition from an elastic to viscous response when stress is applied (Wilking et al., 2011).

3.2.1.1 Non-linear behaviour of viscoelastic materials

A stress-strain curve characteristic of a viscoelastic material will display a linear regime, referred to as the linear viscoelastic region (LVR), followed by a non-linear regime consequence to the viscous elements of the material leading to irreversible deformation (Vincent, 2012). Further, if mechanical loading and unloading regimes have been applied to a viscoelastic material, the stress-strain curves of each regime will not coincide due to energy dissipation which leads to permanent deformation (Figure 3-3) (Grillet, Wyatt and Gloe, 2012; Vincent, 2012). This behaviour is indicative of hysteresis, which has been observed in hydrogels (Sun *et al.*, 2013; Kamemaru *et al.*, 2018) and biofilms (Stoodley, Lewandowski, Boyle, *et al.*, 1999; Rupp, Fux and Stoodley, 2005; Pavlovsky, Younger and Solomon, 2013; Karimi *et al.*, 2015; Gloag *et al.*, 2020). Hysteresis is a mechanical response to stress and can be defined as a lag in a physical property value, such as *G* or *E*, when a force has been applied (Figure 3-3).

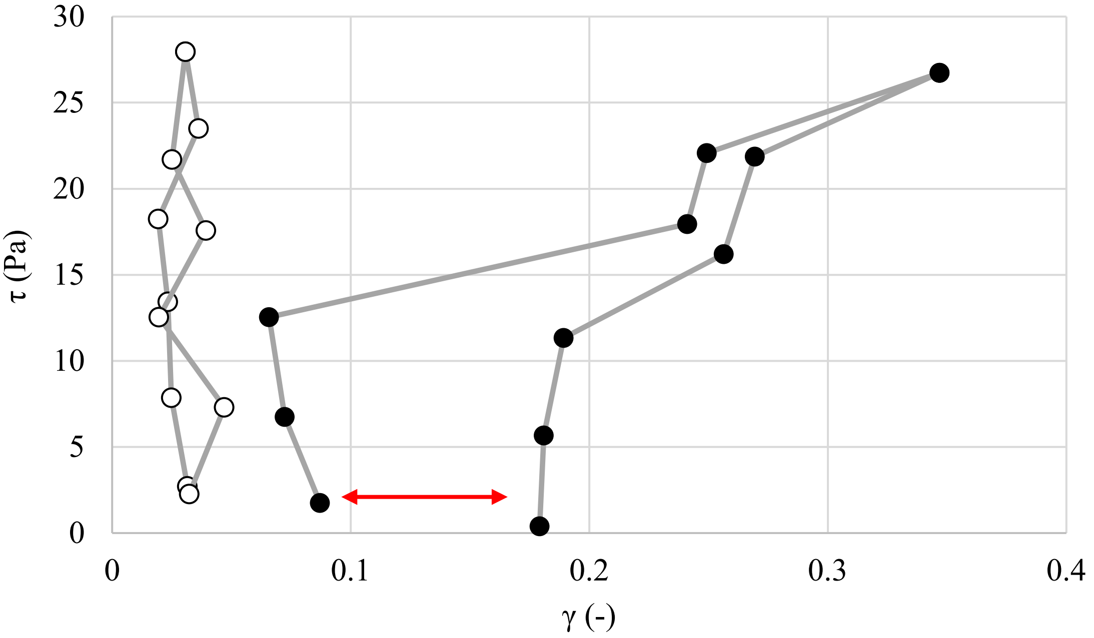

Figure 3-3. *Example stress-strain data for a rigid material (open circles) and an elastomeric material (closed circles). The red arrow is indicative of hysteresis.*

It is worth noting two additional non-linear behaviours that biofilms exhibit: shear thinning and shear thickening (Jana *et al.*, 2020; Souza-Egipsy *et al.*, 2021). Simply, shear thinning occurs when viscosity decreases with increasing shear rate and has been observed in biofilms that are exposed to high shear stress (Prades *et al.*, 2020). Shear thickening is the opposite in that viscosity increases with an increase in shear rate and has also been observed in biofilms (Klapper *et al.*, 2002). Thickening is a rheological behaviour and is typical of colloidal gels (Kunz *et al.*, 2018), where an increase in resistance to deformation has been attributed to increased cohesiveness within a material structure (Vieira *et al.*, 2020).

Souza-Egipsy *et al.*, (2021) used Low Temperature Scanning Electron Microscopy (LTSEM) in conjunction with a rheometer to rheologically characterise biofilms grown in extreme environments. For further rheometer details see Section 3.2.2.1. The authors observed shear thickening in soft biofilms dominated by eukaryotic organisms (Souza-Egipsy *et al.*, 2021) which allowed the biofilm structure to retain mechanical integrity and resist deformation in response to increasing stress (Jana *et al.*, 2020; Vieira *et al.*, 2020). Alternatively, prokaryotic biofilms demonstrated shear thinning behaviour (Souza-Egipsy *et al.*, 2021), which was comparable to a mechanical responses often found for polymeric solutions (Lieleg *et al.*, 2011; Vieira *et al.*, 2020). The results of the study presented by Souza-Egipsy *et al.,* (2021) demonstrates the diversity of rheological properties that biofilms exhibit based on dominated organisms within the community.

3.2.2 Measuring biofilm viscoelasticity using experimental methods

Rheological methods have been deemed invaluable for studying biofilm viscoelasticity (Böl *et al.*, 2013; Charlton *et al.*, 2019; Gloag *et al.*, 2020) and involves implementing microscopic techniques, such as fluorescence microscopy (Cense *et al.*, 2006), and macroscopic techniques, such as creep analysis using a rheometer (Towler *et al.*, 2003; Snowdon *et* al., 2023) or a flow cell (Stoodley, Lewandowski, Boyle, *et al.*, 1999; Blauert, Horn and Wagner, 2015; Picioreanu *et al.*, 2018), and compression measurements (Körstgens *et al.*, 2001b; Kandemir *et al.*, 2018) (Figure 3-4). In the present literature, these methods have determined mechanical differences of biofilms based on species present, growth conditions and testing conditions (Paul *et al.*, 2012). For a recent review on mechanical characterisation of biofilms please refer to Boudarel *et al.*, (2018).

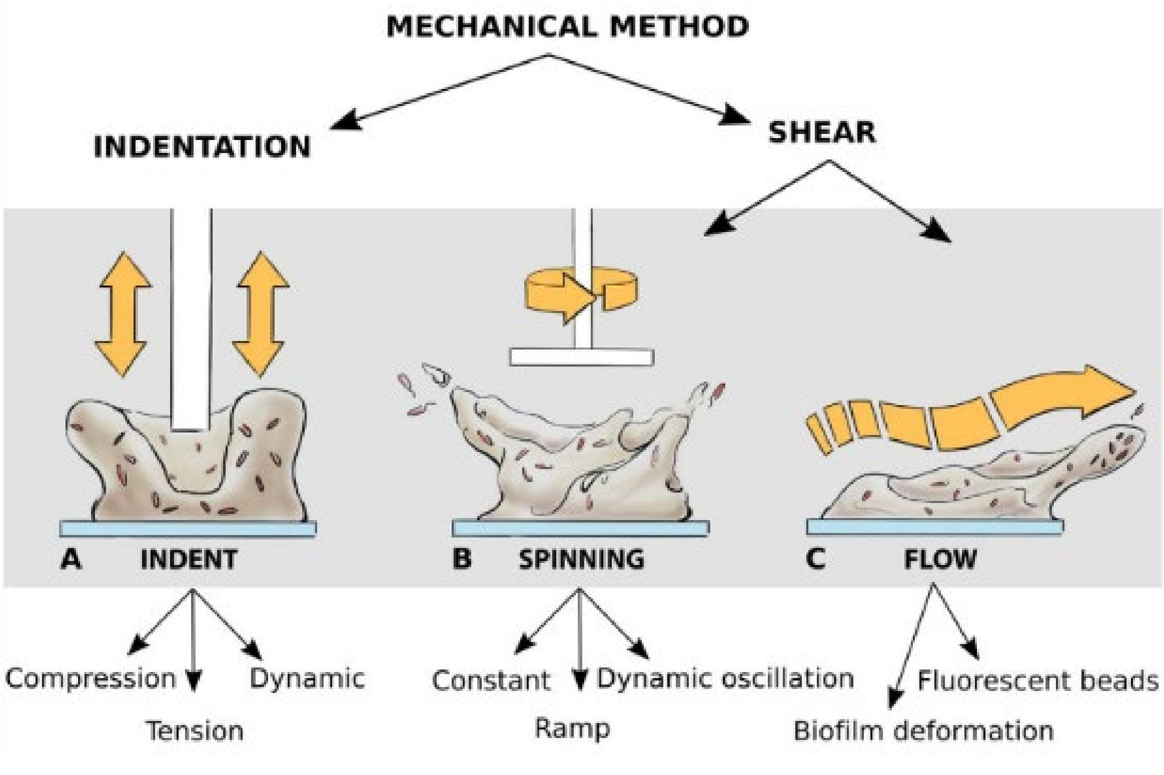

Figure 3-4. *Schematic of different methods used to mechanically characterise biofilms, taken from Gloag et al., (2020). A) Indentation methods use normal force and compression (pushing), tension (pulling) and dynamic (cycles of compression or tension) testing. B) Spinning using shear forces and includes applying a constant stress or strain (creep relaxation test), increasing stress or strain (ramp tests) or dynamic oscillation (frequency, amplitude, stress, or strain sweep). C) Flow methods use shear forces and can be used to measure deformation using imagining techniques, or fluorescent beads.*

Wagner and Horn, (2017) concluded that two main scales were important in biofilm research, the micro-scale for studying single microorganisms and the meso-scale for investigating fluid-structure interactions between a biofilm and surrounding fluid. Mechanical characterisation at the macro-scale, using equipment such as a rheometer, can also be advantageous as it provides average properties for the bulk biofilm (Safari *et al.*, 2015; Boudarel *et al.*, 2018), which can be used as inputs to biofilm models. However, it must be noted that macro-scale methods do not necessarily consider the mechanical heterogeneity that biofilms naturally exhibit (Jafari *et al.*, 2018; Picioreanu *et al.*, 2018; Gloag *et al.*, 2020; Pavissich, Li and Nerenberg, 2021). *E* values reported for individual bacterial cells, using microscopic methods, can be 10 - 1000 times higher than that of an overall biofilm (Barai, Kumar and Mukherjee, 2016; Even *et al.*, 2017) and could explain why biofilm elasticity reported using methods such as indentation and atomic force microscopy (AFM) is orders of magnitudes higher than those taken using meso- or macro-scale techniques (Table 3-1) (Blauert, 2017). Interestingly, the effect of bacterial cell stiffness has also been measured at the meso-scale, where biofilms housing a high concentration of bacterial cells have been found to be stiffer than those with a low concentration, as determined by a high *E* (Barai, Kumar and Mukherjee, 2016). As a result, mechanical data collected for biofilms could also be skewed if microscopic methods are utilised as measurements tend to relate to individual bacterial cells not the overall biofilm. Evidently, different scales are required to study different areas of biofilm research and therefore care must be taken when comparing mechanical data collected using different methods (Figure 3-4 and Table 3-1) (Ochoa *et al.*, 2007; Safari *et al.*, 2015; Azeredo *et al.*, 2017; Boudarel *et al.*, 2018).

Table 3-1. *A sample of biofilm E (Pa) values presented in the current literature using an array of mechanical test methods. For a more extensive overview please refer to Böl et al., 2013.*

	E **(Pa)**	**Method**	**Reference**
***Pseudomonas* aeruginosa**	1 - 85	Flow cell	(Stoodley et al., 2002)
Mixed species biofilm	17 - 40	Flow cell	(Stoodley, Lewandowski, Boyle, *et al.*, 1999)
***Desulfovibrio* sp. EX625** **Pseudomonas aeruginosa**	17-353	Flow cell	(Dunsmore et al., 2002), (Mathias and Stoodley, 2009) as referenced in (Guélon, Mathias and Stoodley, 2011)
Mixed species biofilm	33 - 39	Flow cell	(Blauert, 2017)
Mixed species biofilm	70 - 700	Flow cell and CFD	(Picioreanu et al., 2018)
***Euglena* mutabilis biofilm**	430,000	Rheometer - strain amplitude sweeps	(Souza-Egipsy et al., 2021)
***Pinnularia* sp. biofilm**	110	Rheometer - strain amplitude sweeps	(Souza-Egipsy et al., 2021)
***Chlorella* sp. biofilm**	8	Rheometer - strain amplitude sweeps	(Souza-Egipsy et al., 2021)
***Pseudomonas* aeruginosa**	5,000 – 47,000	Rheometer - uniaxial compression	(Körstgens et al., 2001b)
Mixed species biofilm	6 - 51	Uniaxial compression	(Paramonova et al., 2009)
Single species biofilms	5 – 17	Uniaxial compression	(Paramonova et al., 2009)
***Staphylococcus* epidermidis**	500 - 2200	Micro-cantilever (tensile)	(Aggarwal and Hozalski, 2010)
***Pseudomonas* aeruginosa**	40,000 – 45,000	AFM	(Baniasadi et al., 2015)
***Shewanella* oneidensis MR-1**	33,000 – 38,000	AFM	(Kim, Kwon and Kim, 2017)

3.2.2.1 Rheometer experiments

A rotational rheometer is perhaps the most cited instrument for measuring biofilm mechanical properties under shear (Figure 3-4) (Boudarel *et al.*, 2018) and typically operates at the macro-scale (cm-scale). Characklis (1980) pioneered the use of a rheometer for characterising biofilms and determined a G of 60 Pa for a mixed microbial population. Since then, several studies on biofilms have involved the use of rheometer, in part due to it being a high-throughput method and ease of application (Boudarel *et al.*, 2018). Interestingly, a rheometer can also be employed for studying biofilm-associated drag by using a momentum coefficient (C_m) as a proxy (Dennington *et al.*, 2015, 2021).

Rheometer analysis involves lowering a spinning disk to a biofilm surface and applying shear to determine mechanical properties (Figure 3-4b). Briefly, changes in stress and strain can be measured using different modes of testing; a constant stress can be applied and changes in strain can be measured (creep tests) or the opposite can be used, where strain is constant and stress is measured (relaxation tests); increasing stress or strain can also be applied to the biofilm (ramp tests which produce stress-strain curves) or dynamic oscillation, where there can be oscillating increases in stress, strain, or frequency (frequency sweep, amplitude sweep, stress sweep or strain sweep). An amplitude sweep is a common test applied as it can determine the LVR of a biofilm as well as give a yield stress (σ_y) which is the point at which a biofilm will display non-linear behaviour as it begins to transition to fluid-like behaviour (Charlton *et al.*, 2019). Another popular test is creep-recovery analysis, which involves applying a constant stress and tracking biofilm deformation, then removing the stress and tracking the recovery. Creep-recovery curves can be used to measure an effective shear modulus (G), effective viscosity (η) and elastic relaxation time of biofilms (λ) (Gloag *et al.*, 2018, 2020). The term effective (or apparent) is applied as the estimates describe the biofilm as a whole (Shaw *et al.*, 2004), whereas due to biofilm heterogeneity it is likely that there is spatial variation in G and η that is not being captured.

Studies employing a rheometer have revealed essential results to better understanding biofilm mechanics (Charlton, 2019; Jana *et al.*, 2020) and can be applied in conjunction with other test methods to study structure-function relationships. Souza-Egipsy *et al.*, (2021) studied biofilms taken from highly acidic environments and determined significant differences in the mechanical profiles of biofilms dominated by eukaryotes or prokaryotes. From rheometer tests, the authors concluded that eukaryotic biofilms were softer (indicated by a lower E) which was attributed to the presence of highly motile organisms, such as flagellates and diatoms, as they caused an open and less cohesive microstructure, visualised using LTSEM (Souza-Egipsy *et al.*, 2021). A more open microstructure suggests a higher porosity within the biofilm and therefore it could be expected that a lower E would be exhibited as flow through the structure is promoted (Lembre, Lorentz and Di, 2012). In addition, Shaw *et al.*, (2004) studied the elastic relaxation time of 44 different biofilms using a parallel-plate rheometer. Perhaps unsurprisingly, the material properties of the biofilms were significantly different, yet all behaved as a viscoelastic fluid in response to mechanical stress and displayed an average elastic relaxation time of 18 minutes (1080 seconds) (Shaw *et al.*, 2004). Since then, an elastic relaxation time of around 18 minutes has been frequently reported (Stefano *et al.*, 2009; Pavlovsky, Younger and Solomon, 2013; Souza-Egipsy *et al.*, 2021), although deviations from this general rule do exist. For example, in 2015, Blauert, Horn and Wagner, visualised a mixed species biofilm using OCT and found that after 30 minutes of applying a constant shear stress (of 1.64 Pa) the biofilm still displayed an elastic response.

Despite the success of rheometry in rheologically characterising biofilms it does present some limitations. A spinning disk does not encompass the in-field conditions that a biofilm would be subject to (Karimi *et al.*, 2015). Also, samples are typically transferred from a growth chamber to the rheometer plate which can disrupt biofilm architecture and consequently skew measurements (Böl *et al.*, 2013; Boudarel *et al.*, 2018). Despite this, efforts have been made to keep biofilms intact by developing systems whereby biofilms can be grown within the testing chamber (Towler *et al.*, 2003; Vinogradov *et al.*, 2004; Pavlovsky, Younger and Solomon, 2013).

3.2.2.2 Flow cell experiments

Flow cells can be used to conduct fluid-shear experiments under controlled hydrodynamic conditions (Crusz *et al.*, 2012; Fabbri *et al.*, 2019) (Figure 3-4c). Biofilms are typically grown under controlled conditions within a flow cell and are then exposed to a hydrodynamic testing regime which involves increasing and decreasing shear stress (controlled by flow velocity) (Stoodley *et al.*, 2002; Blauert, Horn and Wagner, 2015; Fabbri *et al.*, 2019). An advantage of culturing and testing biofilms in a single flow cell is that it eliminates disruption to the biofilm structure caused by transportation between growth and test facilities. Further, by installing an optical ‘window’ in a flow cell top-plate imaging equipment can be installed for capturing biofilm behaviour *in-situ* in real-time and without compromising the biofilm structure (Wagner *et al.*, 2010; Fabbri *et al.*, 2018). Viscoelasticity of a biofilm shares complex interactions with a multitude of other biofilm properties, such as porosity (Valladares Linares *et al.*, 2016). By employing a flow cell and imaging methods such interactions can be captured using snapshots and videos (Haisch and Niessner, 2007; Wagner *et al.*, 2010; Depetris *et al.*, 2019).

OCT is becoming increasingly popular for visualising biofilm structure and behaviour, as an alternative to Confocal Laser Scanning Microscopy (CLSM) (Neu and Lawrence, 2015; Wagner and Horn, 2017). Briefly, an OCT uses interferometry and infrared lasers to generate a point reflection signal that penetrates a translucent sample and returns depth-resolved intensity profiles that can be used to produce 1D-, 2D- and 3D- scans (Huang *et al.*, 1991; Haisch and Niessner, 2007; Wagner *et al.*, 2010). For more information on OCT design and methodology see Section 4.2.

OCT is a non-invasive imaging technique that requires no sample preparation, has a quick acquisition time, and can be used to measure biofilm characteristics at the meso-scale (mm scale) (Xi *et al.*, 2006; Wagner *et al.*, 2010). On the other hand, CLSM has been widely applied in micro-scale biofilm studies to characterise biofilm composition, architecture (pores and channels), internal processes such as interactions between matrix constituents (Staudt *et al.*, 2004; Neu *et al.*, 2010; Neu and Lawrence, 2015) and reactions to environmental cues (Stoodley, Boyle, De Beer and Lappin-Scott, 1999). As a result, CLSM fails to capture meso-scale biofilm heterogeneity (Morgenroth and Milferstedt, 2009); although larger images can be tiled together this takes a substantial amount of time due to slow acquisition of single images which also means dynamic behaviour cannot be captured (Peterson *et al.*, 2015). On the other hand, OCT is capable of fast imaging, on the order of seconds for 2D-scans, as demonstrated by studies that have investigated biofilm deformation in real-time using time-lapsed scans (Blauert, Horn and Wagner, 2015; Depetris *et al.*, 2019). As a result, OCT can be utilised for estimating biofilm structural and mechanical properties in real-time (Fabbri *et al.*, 2019; Narciso *et al.*, 2022) and lends itself well to computer modelling (Fortunato *et al.*, 2017; Picioreanu *et al.*, 2018; Li *et al.*, 2019). Real-time observations are made possible by the fact that an OCT is compact, meaning it can be easily installed in conjunction with biofilm culturing rigs and testing equipment, such as flow cells (Figure 3-5) (Fabbri *et al.*, 2018, 2019; Depetris *et al.*, 2019). As an optical imaging technique there are inevitable limitations to OCT related to light reflection and back-scattering (Huang et al., 1991), which can cause artefacts, such as speckling, or shading which consequently alter the image output (Neu and Lawrence, 2015). Vibrations of an OCT monitor could also cause imaging artefacts, especially when used alongside biofilm culturing or testing equipment where flow is involved. Nevertheless, due to the reasons listed above, OCT is being increasingly implemented in place of CLSM for biofilm studies; for a detailed review on these two methods please refer to Wagner and Horn (2017).

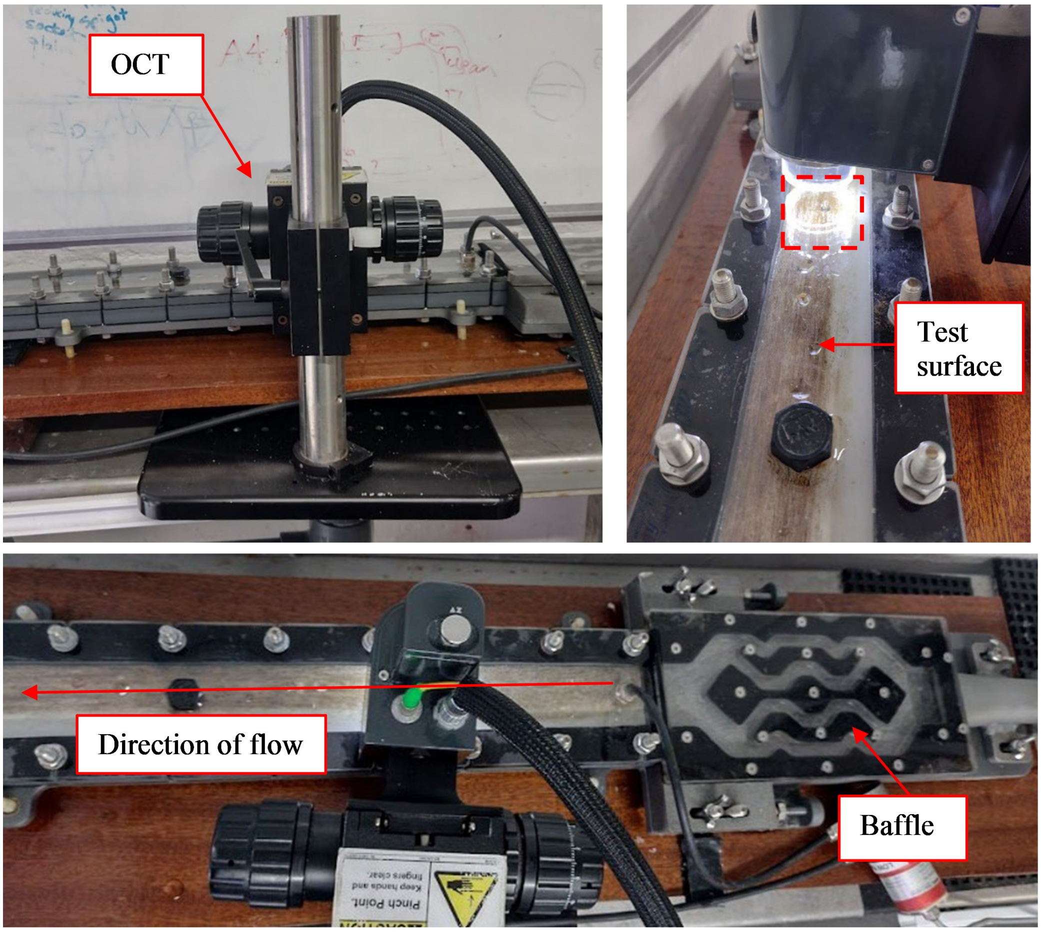

Figure 3-5. *An example of an OCT set up with a meso-scale flow cell for visualising and measuring biofilm deformation in-situ. Red arrows show key components of the set up and the red dashed box provides an indication of a scan area.*

It is important to note that CLSM transformed the way in which biofilm structure was studied in the 1990's as it allowed the three-dimensional structure of fully hydrated biofilms to be visualised for the first time in detail (Norton *et al.*, 1998; Stoodley, Boyle, De Beer and Lappin-Scott, 1999), but CLSM does present some limitations. Although CLSM is classified as a non-destructive technique it does require sample preparation in the form of fluorescent staining and possesses a low penetration depth. This latter point is perhaps the biggest limitation of CLSM and can cause uncertainties in the data collected on biofilm architecture (Neu and Lawrence, 2015). For example, blank space in an image could be a void within the biofilm or it could be indicating the absence of fluorescent signals (Norton *et al.*, 1998); this can also complicate efforts to measure biofilm thickness (Staudt *et al.*, 2004; Wagner *et al.*, 2010). On the contrary, the high penetration depth and fast acquisition time of an OCT scanner is arguably the main advantages over alternative imaging methods (Wagner and Horn, 2017).

3.2.2.3 Quantifying viscoelasticity from images

Stoodley *et al.*, (1999) reported the first *in-situ* E and G measurements for mixed and pure culture biofilms using a flow cell coupled with a high-speed camera and fluorescent particles. The authors estimated an apparent G (G_{app}) of 27 Pa for the mixed species biofilm by capturing photographs of the biofilms under increasing shear stress (τ) and measuring angles of deformation (α) as depicted in Figures 3-2 and 3-6. To estimate τ, the theoretical shear stress of a smooth wall (τ_w) was calculated using:

$$\tau_w = \frac{f \cdot \rho \cdot u^2}{2} \qquad \textit{Equation 3-4}$$

where f is the friction factor, ρ is the density of water and u is the flow velocity. An apparent E (E_{app}) was also estimated using an adaptation of Equation 3-1, where τ_w was also used as an estimate of imposed stress. The authors found an E_{app} of 17 to 40 Pa for the mixed and pure culture biofilms (Stoodley, Lewandowski, Boyle, *et al.*, 1999). Similarly, Blauert, Horn and Wagner (2015) employed the same methods and found an E_{app} of 36.0 ± 2.6 Pa and a G of 29.7 ± 1.7 Pa for mixed species biofilms. In the latter study, in place of a high-speed camera, OCT was used to visualise biofilm deformation during fluid shear experiments in a flow cell (Figures 3-5 and 3-6).

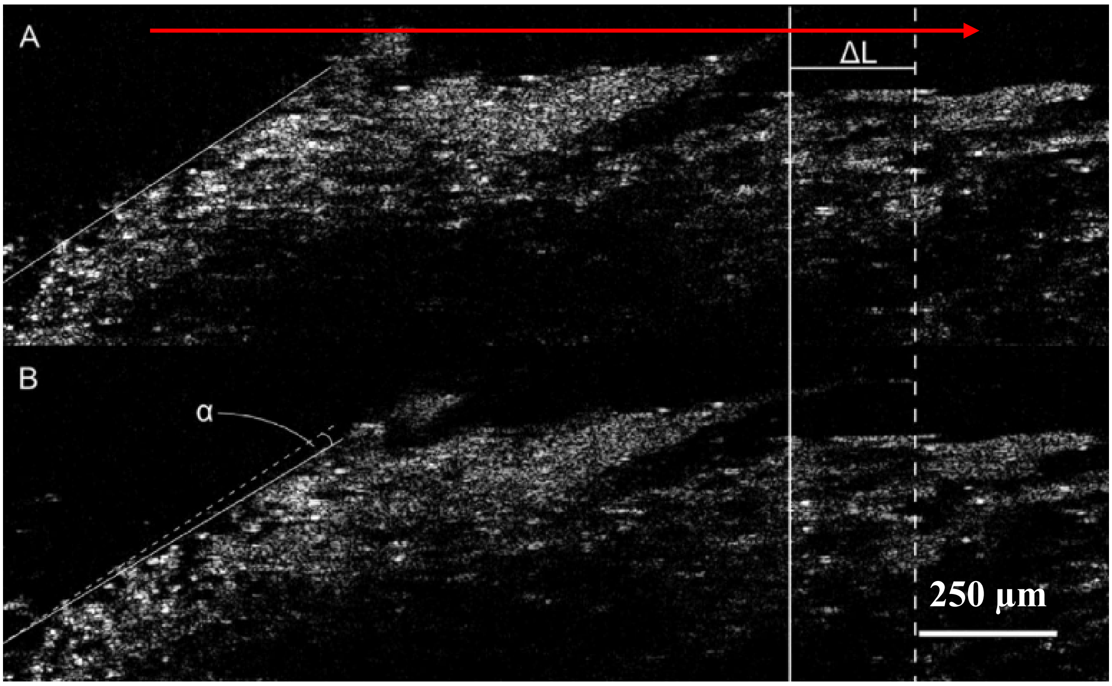

Figure 3-6. *An example of using biofilm images to estimate shear modulus (G) and elastic modulus (E). This figure has been taken from (Blauert, Horn and Wagner, 2015) where an OCT was used to capture biofilm deformation. A) OCT 2D-scan taken at 0 m* s^{-1} *and B) was taken as 2100 m* s^{-1} *after changing the shear stress to 1.64 Pa. The angle of deformation (α) is indicated and shows a difference between the two images. Also, ΔL is shown which is the change in length of the streamer between the two images. Flow was from left to right (red arrow) and the scale bar indicates 250 µm.*

Strain can be estimated from images by measuring the relative change in L compared to the original length of a biofilm feature, as shown in Figure 3-6; yet it is more challenging to quantify shear stress acting on a biofilm. As a result, τ_w is often used as an estimate of imposed shear stress, but by using smooth wall theory the fact that shear stress is affected by viscoelastic fluid-structure interactions exhibited by a biofilm (which could cause greater shear effects) is neglected (Picioreanu *et al.*, 2018). By installing a pressure drop system in a flow cell, shear stress associated with biofilm presence could be measured directly. Another assumption of smooth-wall theory is that the imposed shear force is consistent across the entire biofilm, which is unlikely due to their dynamic nature (Ochoa *et al.*, 2007; Paul *et al.*, 2012). Picioreanu *et al.*, (2018) coupled OCT with computer modelling and revealed that fluid forces exerted over a biofilm was not homogenous, with the front of a biofilm experiencing larger deformations and greater internal stress than the biofilm further downstream. Although a pressure drop system would produce more accurate bulk estimations of G and E, the shear forces exerted on the overall biofilm would still be assumed homogeneous (Mathias and Stoodley, 2009).

3.2.3 Viscoelasticity of biofilms

In the current literature, E and G, can range from a few Pa to several kPa (Kim, Kwon and Kim, 2017; Tallawi, Opitz and Lieleg, 2017) (Table 3-1). In part this is explicable by the array of methods used to study biofilm mechanics (Figure 3-4), each working at different scales and implementing different conditions, such as growth conditions, type of applied stress and type of biofilm, to name a few (Paul *et al.*, 2012; Araújo *et al.*, 2019).

Stoodley *et al.,* (1999) found biofilms grown under laminar and turbulent flow to exhibit different mechanical properties (Dunsmore *et al.*, 2002; Lemos *et al.*, 2015; Fanesi *et al.*, 2021) and Souza-Egipsy *et al.*, (2021) uncovered how biofilms with different dominant species varied in their responses to stress. The latter point is also supported by work by Winston *et al.*, (2003) who determined a G of 63.9 Pa for a *Streptococcus mutans* biofilm, but for mixed species pondwater biofilms G was much lower at 1.2 Pa. The variability that biofilms exhibit is further exemplified by studies that have shown how the same bacterial strain can produce very different mechanical results (Hohne, Younger and Solomon, 2009; Barai, Kumar and Mukherjee, 2016; Kim, Kwon and Kim, 2017). Collectively, the listed studies magnify the challenges related to studying biofilm mechanics caused by biofilm heterogeneity and adaptability.

3.2.3.1 Streamers and ripples

Streamers are viscoelastic filamentous structures of biofilms (Karimi *et al.*, 2015) that generally develop under turbulent flow (Lewandowski and Stoodley, 1995; Stoodley *et al.*, 1998; Taherzadeh *et al.*, 2010), although some studies have shown streamer production at lower Re too (Rusconi *et* *al.*, 2010; Das and Kumar, 2014; Hassanpourfard *et al.*, 2015; Scheidweiler *et al.*, 2019). It has been suggested that streamers developing under turbulence are an adaptive response of a biofilm to high shear stress (Stoodley *et al.*, 2002) which could be explicable by the physical structure of the streamer itself. Streamers interact with the flow field surrounding a biofilm by dissipating energy via oscillatory movements which can limit the fluid forces acting on the biofilm structure (Taherzadeh *et al.*, 2010) and could reduce biofilm detachment.

However, it must also be noted that streamers can establish secondary oscillatory flows, believed to be caused by vortex shedding (Stoodley *et al.*, 1998). This behaviour was confirmed using computational methods (Taherzadeh *et al.*, 2010) and can cause higher drag due to an increase in fluid-structure interactions. Research concerning the Deepwater Horizon oil rig explosion revealed how streamers could form directly on a sheared oil-water interface (White, Jalali and Sheng, 2019; White *et al.*, 2020). The study concluded that streamers formed a 'wake region' behind the droplet which increased drag by up to 80 % which consequently lowered the rising-velocity of the oil-droplet (White *et al.*, 2020). This increase in drag seems high, but streamers have been reported to induce greater disruption to fluid flow than a surface-attached biofilm (Drescher *et al.*, 2013). Evidently, streamers are free-moving, streamlined and flexible structures and although their presence can deter fluid flow from the bulk biofilm, due to their oscillatory behaviour they could also increase the risk of biofilm detachment (Taherzadeh, Picioreanu and Horn, 2012).

As well as fluid-structure interactions existing with streamers, biofilms have been shown to 'flow' in the form of wrinkle- or ripple-like structures when exposed to shear (Stoodley, Lewandowski, Boyle, *et al.*, 1999; Fabbri *et al.*, 2017). Using methods such as CLSM and SEM, it has biofilm ripples have been shown to migrate downstream (Fabbri *et al.*, 2017) which enables parts of a biofilm to resist detachment from a surface (Stoodley, Boyle and Lappin-scott, 2000; Rupp, Fux and Stoodley, 2005). As a result, ripple-behaviour has been recognised to play a role in biofilm survival (Peterson *et al.*, 2015; Gloag *et al.*, 2021) but also has implications with drag (Stoodley *et al.*, 1999; Schultz *et al.*, 2011).

3.2.3.2 Hardening, compression, and consolidation

Under increasing shear stress, OCT images have captured a range of biofilm phenomena occurring in real time, that otherwise may not have been discovered (Wagner and Horn, 2017). Increasing shear stress can induce biofilm compression, and is typically observed alongside a reduction in thickness as it can cause the collapse of pores within the biofilm structure (Paul *et al.*, 2012; Blauert, Horn and Wagner, 2015; Majumdar *et al.*, 2017). A reduction in porosity, in turn, invokes a mechanical response referred to as hardening or stiffening which involves an increase in the elasticity of a biofilm (Lembre, Lorentz and Di, 2012) which partly explains the high levels of resistance to stress biofilms can exhibit (Laspidou et al., 2014; Jafari et al., 2018; Picioreanu et al., 2018). Hardening has been observed by rheological techniques (Hohne, Younger and Solomon, 2009; Gloag *et al.*, 2018) and imaging techniques (Jafari *et al.*, 2018; Picioreanu *et al.*, 2018), where a decrease in thickness has further been identified as a characteristic of the hardening process (Valladares Linares *et al.*, 2016; Jafari *et al.*, 2018) although is not always observed (Desmond, Morgenroth and Derlon, 2018). Hardening behaviour has also been observed in streamers, using imaging techniques, where a decrease in streamer porosity led to an increase in resistance to fluid flow (Scheidweiler et al., 2019). Note that hardening is a property that has been found to increase hydraulic resistance (Paramanova, 2009; Rmaile *et al.*, 2013; Jafari *et al.*, 2018) and therefore implicates drag.

In addition to the phenomena already described, biofilm consolidation also exists and is when an elasticity gradient is present within a biofilm - the surface demonstrates a lower elasticity than the base layers which are denser (Alpkvist *et al.*, 2006) and have a lower porosity (Masuda, Watanabe and Ishiguro, 1991; Zhang and Bishop, 1994; Laspidou et al., 2014). Laspidou and Aravas (2007) theorised that the E of a biofilm was inversely related to porosity and found inconsistencies in mechanical behaviour across a biofilm. The authors found that during biofilm compression the porosity of the base layers were 50 % lower than the surface layers (Laspidou and Aravas, 2007), which were more ‘fluffy’ and more vulnerable to erosion. Using OCT, Blauert et al, (2015) also showed that when a biofilm was exposed to shear forces, compression occurred predominantly around the upstream section of the biofilm (Picioreanu *et al.,* 2018) and was shown as a decrease in thickness and reduction in porosity, whereas downstream surface features were elongated and the biofilm maintained its original thickness. It is evident that compression and consolidation are interlinked, and both are features of the hardening process (Alpkvist *et al.*, 2006; Paramonova *et al.*, 2009; Picioreanu *et al.*, 2018). The research around biofilm compression and hardening, suggest that there is spatial heterogeneity with regards to shear stress imposed on a biofilm and the mechanical properties because of this variation.

Biofilm viscoelasticity evolves over time and is dependent on flow conditions (velocity, pressure etc.) and additional biofilm properties, such as porosity. Also the age of a biofilm can affect it’s mechanical profile, for example consolidation is particularly notable in older biofilms (Laspidou *et al.*, 2014). From the evidence presented in the literature, a single value for the elastic or shear modulus cannot be assumed for an entire biofilm, as is often the case in biofilm models (Möhle *et al.*, 2007; Picioreanu *et al.*, 2018).

3.2.4 Modelling biofilm viscoelasticity using artificial systems

Similarities exist between the microstructure of a biofilm and polymeric gels (McCarthy *et al.*, 1999; Stoodley, Lewandowski, Boyle, *et al.*, 1999; Even *et al.*, 2017; Di Martino, 2018) which has partly been attributed to the high-water content both possess (Berlanga and Guerrero, 2016). As a result, polymeric gels or hydrogels are often selected as the basis for many artificial biofilm systems. Artificial biofilms can be split into two types: the most common is generated by embedding live bacterial cells within a polymeric gel, such as a hydrogel (Strathmann, Griebe and Flemming, 2000; Huang *et al.*, 2019) which have previously been used for studying physicochemical characteristics of biofilms (Strathmann, Griebe and Flemming, 2000). Alternatively, fully artificial biofilms have no living component, they are simply a material.

Although artificial systems typically exhibit mechanical and geometric homogeneity, which biofilms do not, some studies have found that they successfully display deformation comparable to natural biofilms (Stewart *et al.*, 2015; Di Martino, 2018; Gloag *et al.*, 2018; Snowdon *et al.,* 2022). Li, Matouš and Nerenberg, (2020) produced an alginate-based artificial biofilm with embedded bacterial cells; although the artificial system did not mimic biofilm surface topography, rheometer data determined that *E* was comparable to a *Pseudomonas aeruginosa* biofilm. On the other hand, Strathmann, Griebe and Flemming (2000) introduced structural complexity by creating a micro-scale model system with pores and channels to study physico-chemical characteristics of the biofilm matrix. Similarly, Stewart *et al.*, (2015) studied the contribution physico-chemical factors to biofilm elasticity by comparing *Staphylococcus epidermidis* biofilms to artificial biofilms. The authors found that artificial biofilms of chitosan and bacteria could simulate the structure and micro-rheology of a natural biofilm under specified conditions; the *E* reported for the artificial system was approximately 2.6 Pa and for the natural biofilm it was 3.7 Pa (Stewart *et al.*, 2015). The benefits of utilising artificial systems include the reproducibility of data, which is near impossible in biofilm studies, and material parameters can be controlled (Strathmann, Griebe and Flemming, 2000; Stewart *et al.*, 2015). An artificial system could further uncover important behaviour applicable to biofilms (Macedo *et al.*, 2014; Pabst *et al.*, 2016; Kandemir *et al.*, 2018).

Interestingly, many studies have demonstrated that biofilms behave like viscoelastic gels without the live component (Christensen and Characklis, 1990; De Beer, Stoodley and Lewandowski, 1997; Wloka *et al.*, 2004; Yan *et al.*, 2018). Kandemir *et al.*, (2018) found the stiffness of specific hydrogels with and without encapsulated bacteria to be comparable to each other which suggests that the encapsulation of living components is not required for a biofilm model to be produced. The benefit of using fully artificial systems is that the complexities that are inevitable when working with living organisms, whether it be bacterial cells incorporated into hydrogels or cultivated biofilms, are removed. Also, results are even more reproducible, and experiments can have a higher through-put. These benefits were demonstrated by Macedo *et al.*, (2014) who produced a novel and controllable, gelatin-based hydrogel biofilm model for endodontic research. The authors validated the use of a hydrogel by using a rheometer to characterise the viscoelastic properties of the gel and comparing the results to biofilm data in the literature (Böl *et al.*, 2013; Macedo *et al.*, 2014; Swimberghe *et al.*, 2019). Biofilm viscoelasticity, in general, is not well understood and through using artificial biofilms and synthetic materials to simplify complex biological systems we could begin to further our knowledge on biofilm mechanics under controlled conditions.

3.2.5 Modelling biofilm viscoelasticity using computational methods

Mathematical modelling is a powerful technique that is becoming increasingly popular for studying biofilm-fluid interactions (Böl and Ehret, 2012; Tierra *et al.*, 2015; Desmond, Morgenroth and Derlon, 2018). Models are often used to compliment laboratory biofilm experiments where imaging methods have been utilised to capture deformation (Jafari *et al.*, 2018; Picioreanu *et al.*, 2018) and rheometry analysis has been used produce mechanical parameter inputs for models (Li, Matouš and Nerenberg, 2020).

By generating models based on real biofilm geometries, which is possible thanks to the union between imaging techniques and computational methods (Hartenberger *et al.*, 2020; Li, Matouš and Nerenberg, 2020) surface heterogeneity can be introduced. Picioreanu *et al.,* (2018) generated a biofilm deformation model to estimate biofilm mechanical properties and used real biofilm geometries captured using OCT. The authors relaxed typical model assumptions such as homogeneity and constant elasticity, and instead implemented the following conditions: a non-constant shear stress over the biofilm (Ochoa *et al.*, 2007), any biofilm structure could be investigated (it was not limited to the popular and unrealistic mushroom structure that is historically used for biofilm studies (Costerton, 1995) and non-linear mechanical behaviour was considered. The authors concluded that the model determined a more accurate estimation of biofilm elastic moduli and could be used to quantify behaviour such as biofilm stiffening or hardening (Picioreanu *et al.*, 2018). Modelling techniques can also simulate specific biofilm geometries such as oscillating streamers (Taherzadeh *et al.*, 2010) which will further our understanding around these viscoelastic drag-producing features.

The collaborative effort of computational and experimental methods have developed understanding of biofilm phenomena where little is known, such as hardening and compression (see Section 3.2.3.2 for more details) (Wilking *et al.*, 2011; Barai, Kumar and Mukherjee, 2016; Jafari *et al.*, 2018). But, despite improvements in biofilm modelling there are still limitations. Perhaps the most important is the lack of experimental data on biofilm mechanical properties (Alpkvist *et al.*, 2006), which means many biofilm simulations typically presume rigidity and surface homogeneity

(Picologlou, Zelver and Characklis, 1980; Fortunato *et al.*, 2017; Picioreanu *et al.*, 2018). Also, there has been little research on the effects of mechanical heterogeneity on biofilm deformation (Pavissich, Li and Nerenberg, 2021) which means single values for mechanical parameters (such as E) typically estimated using a rheometer, are used as the inputs to computer models. Single input values are a disadvantage of current biofilm models as it is known that biofilms are mechanically heterogenous. Elasticity (Alpkvist *et al.*, 2006) and porosity gradients (Laspidou and Aravas, 2007; Blauert, Horn and Wagner, 2015) have been observed in biofilms grown and tested under an array of conditions. Pavissich, Li and Nerenberg (2021) investigated the spatial distribution of mechanical properties in a biofilm using magnetic tweezers, a micro-scale technique. The authors applied a complimentary computational model to predict the effects of mechanical heterogeneity on biofilm deformation and concluded that the mechanically heterogenous biofilm deformed up to 64 % more than the homogenous counterpart (Pavissich, Li and Nerenberg, 2021). The study executed by Pavissich, and co-authors suggests that mechanical heterogeneity (at the micro-scale) plays a critical role in deformation, which as a result would inevitably affect drag.

3.3 **Biofilm-associated drag**

Rigid and homogenous structures, such as sandpaper, or embedded sand grains, are often used to calibrate drag equipment (Fabbri *et al.*, 2019), and are also utilised for modelling flow around and over biofilms (Perkins *et al.*, 2012; Yusim and Utama, 2017). In part, rigid structures are frequently adopted as biofilms as they have displayed roughness profiles comparable to sandpaper roughness (Dennington *et al.*, 2015; Yusim and Utama, 2017; Hartenberger *et al.*, 2020) and sand-grains (Walker, Sargison and Henderson, 2013); and have demonstrated drag indicative of rigid surfaces (Hartenberger *et al.*, 2020). Despite parallels, biofilms naturally exhibit heterogeneity and display deformation when exposed to hydrodynamic shear which rigid structures do not (Figure 3-1). Deformation has been observed using rheological methods, where viscous and elastic (viscoelastic) behaviour is evident in response to shear stress (Vinogradov *et al.*, 2004; Pavlovsky, Younger and Solomon, 2013; Barai, Kumar and Mukherjee, 2016) and using imaging techniques where streamer and ripple behaviour has been identified (Stoodley, Lewandowski, Boyle, *et al.*, 1999; Wagner *et al.*, 2010; Depetris *et al.*, 2019; Gloag *et al.*, 2020). Therefore, whilst rigid structures can successfully simulate roughness, they neglect biofilm heterogeneity and viscoelasticity (Picologlou, Zelver and Characklis, 1980; Stoodley, Boyle and Lappin-Scott, 1999; Wilking *et al.*, 2011; Peterson *et al.*, 2013). It is acknowledged that drag is implicated by biofilm physico-mechanics, namely viscoelasticity (Picologlou, Zelver and Characklis, 1980; Schultz and Swain, 2000; Blauert, Horn and Wagner, 2015), yet there is a wide gap in the literature regarding the nature of this relationship. This lack of knowledge and methodology leads to the continued use of rigid structures for modelling biofilms.

3.3.1 Measuring biofilm-associated drag using flow cells

Due to the size and long service periods of ships (~ five years), laboratory experiments are often used to better inform our understanding of ship-related drag and the role of biofilms in its production. To date several methods have been used for examining marine biofilm-associated drag, including tow tanks, flow tunnels, flow cells and rotating discs (Schultz and Myers, 2003; Dennington *et al.*, 2015; Fabbri *et al.*, 2019). Yet, minor differences in methodology causes wide variation in efforts to relate biofilm characteristics to drag (Walker, Sargison and Henderson, 2013; Schultz *et al.*, 2015; Hartenberger *et al.*, 2020). The lack of method standardisation is, in part, attributed to high levels of diversity that biofilms exhibit, making them difficult to work with experimentally and computationally. Also, biofilms display sloughing or detachment when exposed to flow, which can skew drag data collected.

Flow cells are a popular method for studying biofilm-associated drag as hydrodynamic conditions can be controlled. The advantages of studying biofilm mechanics in a flow cell was discussed in Section 3.2.2.2. To characterise fluid flow in relation to flow velocity Reynolds number (*Re*) is often used:

$$Re = \frac{uD_h}{v_k} \qquad \textit{Equation 3-5}$$

where v_k, is the kinematic viscosity of water ($m^2\ s^{-1}$) for a given temperature, and is calculated using absolute viscosity, μ ($kg\ m^{-1}\ s^{-1}$) and density, ρ ($kg\ m^{-3}$):

$$v_k = \frac{\mu}{\rho} \qquad \textit{Equation 3-6}$$

and D_h is the hydraulic diameter of the flow cell, calculated using the cross-sectional area and wetted perimeter of the flow cell test section:

$$D_{\mathrm{h}} = \frac{2(HW)}{H+W} \qquad \textit{Equation 3-7}$$

where, H is the flow cell height and W is the flow cell width. Briefly, *Re* is dimensionless and describes the flow condition within a system. It is simply the ratio between inertial and viscous forces scaled to a relevant system length such as channel geometry or, length of an object moving relative to the surrounding fluid. When viscous forces dominate (at low flow) then the flow is constant and is classified as laminar, but when inertial forces dominate there is turbulent flow which can be characterised by irregular fluid motion. Typically, the transition from the laminar to turbulent regime occurs at approximately 2000 to 4000 *Re*.

If pressure sensors are incorporated into a flow cell then pressure drop (ΔP) can be measured which allows a proxy for drag to be estimated – the coefficient of friction, C_f (Fabbri *et al.*, 2019; Li *et al.*, 2019; Hartenberger *et al.*, 2020). C_f is a dimensionless number calculated using the following equation:

$$C_\mathrm{f} = \frac{D_h}{2\rho u^2}\frac{\Delta P_f}{L} \qquad \textit{Equation 3-8}$$

where, C_f is the Fanning friction factor, L is the distance between pressure ports and ρ is the water density (kg m^{-3}). Pressure drop is typically measured using a differential pressure sensors and flow velocity (u) is also recorded. In a turbulent flow regime, ΔP and u^2 can exhibit a linear dependence, and therefore the slope of this line can be substituted into Equation 3-8 as $\Delta P_\mathrm{f}/u^2$ to give a single C_f value across an entire flow regime (Fabbri et al., 2019). Similarly, a rotating disk can be used, where instead of pressure drop, torque is used to calculate Cm as a proxy for drag (Loeb et al., 1984; Holm et al., 2004; Dennington et al., 2015, 2021).

In conjunction to measuring drag, an optical window can be installed as the flow cell top-plate to allow deformation to be visualised, tracked, and measured using imaging techniques (see section 3.2.2 for more details) such as OCT (Figure 3-5). If pressure drop is measured simultaneously to deformation, shear stress values that consider the effect of the biofilm can be measured. As a result, this could mean then when measuring G of a biofilm using τ_w in Equation 3-2 the actual shear stress values can be quantified.

It is worth noting that an optical 'window' which is made by inserting a smooth clear top plate into a flow cell may lead to an asymmetric velocity profile, which could lead to underestimations of C_f as roughness is not equivalent on all walls (Parthasarathy and Muste, 1994; Pimentel et al., 1999). The compromise of having an optically smooth 'window' wall has been recognised in studies, where asymmetry has been corrected for using techniques such as Particle Image Velocimetry (PIV) to characterise the flow field (Hartenberger *et al.*, 2020). It may be beneficial for future work to incorporate a small optical window into a flow cell top-plate as opposed to a full transparent top-plate. A smaller optical window would allow majority of the flow cell sides to be rough as required and assumes that the effects of the smaller window would be negligible.

3.3.2 The effects of biofilm roughness and viscoelasticity on drag

It is widely accepted that an increase in roughness will increase drag (Andrewartha *et al.*, 2010; Fabbri *et al.*, 2019) and that it is a dominant factor in effecting biofilm-associated drag (Schultz and Swain, 2000; Song, Demirel and Atlar, 2019). This has been captured using laboratory experiments (Yusim and Utama, 2017), computational methods and numerical simulations (Schultz, 2007; Chung *et al.*, 2021; Song *et al.*, 2021). Although, a recent study by Murphy *et al.*, (2022) showed that drag associated with a uniform biofilm with high coverage, as opposed to a patchy biofilm with greater roughness elements, produced a higher drag coefficient. The authors suggested that viscoelastic effects over a greater area could be responsible for the increase in drag and would likely be in the form of streamers (Murphy *et al.*, 2022).

It is often reported that biofilms induce greater drag than rigid structures of equivalent roughness (such as sandpaper), consequent to physico-mechanical properties (Picologlou, Zelver and Characklis, 1980), namely viscoelasticity (Rupp, Fux and Stoodley, 2005; Peterson *et al.*, 2015). This has been found true for laboratory scale studies, for example using pressure drop techniques in flow cells (Hartenberger *et al.*, 2020), and at ship scale (Demirel, Turan and Incecik, 2017).

Picologlou, Zelver and Characklis (1980), experimented with biofilms and turbulent pipes and concluded that when biofilm viscoelasticity was considered, as opposed to assuming rigidity (in the form of sand grains), the resultant frictional resistance was significantly higher (Lewkowicz and Das, 1986). This is supported by research by Hartenberger *et al.*, (2020) who found that biofilms experienced roughly double the drag increase when compared to their rigid 3D-printed replicas. Therefore, it is evident that even though biofilm topography and surface heterogeneity was successfully captured by the replicas the viscoelastic response to shear was not; deviation between the datasets was accounted for as 'compliance effects' such as streamers and mat vibrations (Hartenberger *et al.*, 2020). Note that Hartenberger *et al.*, (2020) did find some agreement in drag caused by a ten-week-old biofilm and a rigid surface of equivalent roughness, which fits in line with an earlier study by Murphy *et al.,* (2018) who found a uniform ten-week-old biofilm to produce a velocity profile like a rigid structure. On the other hand, for young patchy biofilms (three-week-old) produced in the Hartenberger study, compliance appeared to play a significant role in drag production and no correlation with the rigid biofilm replicas was found (Hartenberger, 2019). This single study is evidence that there are inconsistencies in drag data produced by biofilms, which makes it challenging to link roughness and compliance effects to drag, as well as to predict biofilm-associated drag. It has been stated that if the effects of compliance on drag can be uncovered then this would facilitate better predictions of biofilm-related pressure drop and biofilm-associated drag on ships (Towler *et al.*, 2003).

Due to biofilms exhibiting high diversity there is no doubt that some are dense and firm, or even homogenous (like sandpaper) (Jafari *et al.*, 2018); for example, Wagner *et al.*, (2010) visualised repeating units in the structure of a biofilm using an OCT suggesting homogeneity. With respect to rigidity, biofilms can display rigid-like behaviour under shear in the form of hardening (or stiffening) (Rupp, Fux and Stoodley, 2005; Laspidou *et al.*, 2014; Picioreanu *et al.*, 2018) but also dependent on their growth conditions. Biofilms grown under high shear have been found to display greater cohesion (Dunsmore *et al.*, 2002; Stoodley *et al.*, 2002; Rupp, Fux and Stoodley, 2005; Fanesi *et al.*, 2021) which can increase density (Lemos *et al.*, 2015) and makes them more mechanically robust (Gloag *et al.*, 2020). Biofilms grown under low shear, however, have been described as having ‘fluffy’ less dense surface layers (Derlon *et al.*, 2008; Paul *et al.*, 2012) that are quickly deformed or even eroded under increasing shear stress (Fanesi *et al.*, 2021). Using OCT and a flow cell, Shen *et al.*, (2017) visualised the detachment of biofilms under a range of flow velocities and observed rigid biofilms that resisted deformation and detachment when exposed to high shear stress; the authors concluded that in part this was explicable by low nutrient conditions during growth. As a result of the mentioned studies, it could be expected that sandpaper or sand-grains could capture specific biofilm behaviour, perhaps at higher *Re* or those grown under certain conditions, however it must be considered that biofilms are still viscoelastic, even if under specified conditions rigidity is observed.

The roles that biofilm characteristics play in biofilm-associated drag and the interactions they demonstrate are evidently unclear. Due to many experimental parameters: growth conditions and testing conditions, that implicate biofilm morphological and structural properties, efforts made to link physico-mechanics to drag penalty are complicated. Rigid structures as biofilm models, although useful in initial steps for characterising fluid-structure interactions, cannot be used to capture the viscoelasticity of natural biofilms as undoubtedly deformation is neglected and drag values are being mis-estimated (Picioreanu *et al.*, 2018; Hartenberger *et al.*, 2020).

3.3.3 Modelling biofilm-associated drag

Using computational or artificial systems to model biofilm-associated drag is a natural extension of systems used to model biofilm physico-mechanics in flow, as described in Sections 3.2.4 and 3.2.5. With an aim to simplify studies on biofilm-associated drag, experimental and computational models have been adopted which typically assume rigidity and/ or homogeneity (Picioreanu *et al.*, 2018; Hartenberger *et al.*, 2020). To date, experimental biofilm-associated drag systems have involved focussing on specific biofilm features, by producing artificial streamers composed of wool or nylon threads (Lewkowicz and Das, 1986; Andrewartha and Sargison, 2011; Ng and Walker, 2012) or have utilised synthetic materials to produce artificial biofilms (El-Labbad, 1987; Macedo *et al.*, 2014).

3.3.3.1 Modelling biofilm-associated drag using fully artificial biofilms

To better understand biofilm drag-production mechanisms, artificial streamers have been investigated as an alternative to using sandpaper or sand-grains which are used to model the bulk biofilm (Yusim and Utama, 2017). Artificial streamers have involved generating surface protrusions in the form of nylon or woollen strands (Andrewartha and Sargison, 2011; Ng and Walker, 2012) that have the ability to move under flow. Lewkowicz and Das (1986), utilised nylon tufts to model drag production mechanisms of biofilms and found that C_f calculated when using nylon tufts as oppose to a rigid control was 18 % higher. Andrewartha and Sargison (2011) adopted a similar approach using woollen strands. The drawback of these models is that although artificial protrusions are individual free moving structures, perhaps mimicking biofilm streamers, the materials themselves are hard and mechanical properties cannot be readily manipulated as they can be for a synthetic material (Macedo *et al.*, 2014).

Stoodley *et al.*, (1998) studied natural biofilms with streamers and found a loss coefficient (*k*) 2.2 times higher than that of a clean flow cell. Although there is variability between percentage increase in artificial and natural streamer studies, collectively they show how specific biofilm features possess drag production mechanisms that cannot be ignored when studying drag. Efforts to link mechanical response to drag have largely involved the representation of streamers, yet they cannot account for the viscoelastic response demonstrated by the bulk biofilm, which has been visualised using OCT (Wagner *et al.*, 2010; Wagner and Horn, 2017; Jafari *et al.*, 2018; Picioreanu *et al.*, 2018). Interestingly, Stoodley *et al.*, (1998) stated that streamer motion could be limited by biofilm flexibility, where Scheidweiler *et al.*, (2019) discovered the alternative, that upon reduced flexibility of the biofilm (determined by reduced porosity), streamer behaviour dominated the flow field. This perhaps leads to a conclusion that streamers and bulk biofilm properties should be looked at independently and once understood fully can be united. As a final remark, streamers are ubiquitous, they can form under a variety of conditions, and therefore like whole biofilms, they are challenging to model (Ghosh *et al.*, 2021).

3.3.3.2 Modelling biofilm associated drag using numerical simulations and computational models

Over the last few decades, the numerical study of roughness effects on drag has been dominated by well-established work on roughness functions by Nikuradse (1933) and Colebrook (1939) and similarity law analysis by Granville (1958). For a detailed review of these methods please refer to Chung *et al.*, (2021). Nikuradse (1933) pioneered research on the effects of uniform sand grain roughness on turbulent flow in a cylindrical pipe (Grigson, 1992), and Colebrook (1939) built on this work by studying commercial pipes where irregular surface roughness is common (Schultz and Myers, 2003). The latter work became the basis of the Moody diagram (Moody, 1944) which is used to determine friction factor for a given relative roughness and *Re*.

Granville similarity law analysis facilitates the prediction of the effect of roughness on frictional resistance by using roughness functions (Granville, 1958). Therefore, to be applied successfully in biofilm studies, roughness functions are required for biofilms (Schultz and Flack, 2007; Flack and Schultz, 2010). Determining roughness functions for biofilms is challenging as biofilms can display dynamic roughness under flow (Perkins *et al.*, 2012; Hartenberger *et al.*, 2020). Also, biofilms are unique, so a roughness function for one biofilm may not describe the behaviour of another.

Nevertheless, roughness functions have been determined in biofilm research (Schultz and Flack, 2007) and have been implemented in simulation studies using CFD to predict the effect of fouling (hard and soft) on ship resistance (Demirel *et al.*, 2014; Demirel, Turan and Incecik, 2017; Song, Demirel and Atlar, 2019; Hakim *et al.*, 2021; Song *et al.*, 2021; Suastika *et al.*, 2021). Experimental drag data can be collected using flow cells (Lambert *et al.*, 2009; Perkins *et al.*, 2012), rotating discs (Dennington *et al.*, 2021) or towing tanks (Turan *et al.*, 2016; Demirel *et al.*, 2017) and can be evaluated using Granville; roughness function data can then be compared to values predicted using Colebrook or Nikuradse (Schultz and Myers, 2003).

Whilst these numerical simulations can successfully capture roughness effects on fluid flow, they do not consider additional biofilm properties. This is highlighted by Schultz and Swain, (2000), who studied the influence of biofilms on drag by applying Granville similarity law analysis to determine roughness functions. The authors found that none of the biofilms investigated produced data that could be collapsed to the Colebrook or Nikuradse and concluded that properties such as shear modulus of a biofilm needs to be considered to accurately predict drag. A similar conclusion was met by Perkins and co-authors (2012) who studied biofilms in hydropower pipes and found a dynamic relationship between Re and C_f that was not comparable to Colebrook-type behaviour. The authors found that drag initially increased with increasing Re followed by a sudden decline in C_f, which was perhaps caused by detachment of the biofilm or mechanical behaviour such as compression (Lambert *et al.*, 2009; Perkins *et al.*, 2012). On the contrary, Hartenberger *et al.*, (2020) studied filamentous biofilms and found that five and ten-week-old biofilms did not fully collapse but were close to the Colebrook roughness function. In the same study, rigid biofilm replicas were generated and perhaps unexpectedly appeared to fit to the Nikuradse roughness correlation, despite possessing an inhomogeneous surface topography usually akin to Colebrook (Hartenberger *et al.*, 2020). The non-conformity of different biofilms in comparison to Nikuradse and Colebrook is perhaps expected due to the dynamic nature of biofilms.

Despite some similarities between experimental and computational datasets, dynamic mechanical and surface heterogeneity needs to be incorporated into models for accurate predictions of biofilm-associated drag to be made (Hartenberger *et al.*, 2020; Song *et al.*, 2021; Suastika *et al.*, 2021). Furthermore, the observations made using computational and numerical methods are study-specific, which means that although correlations may be discovered in one study, they cannot be applied to all biofilms due to high variability amongst biofilms.

Collectively, the models presented in this section, from artificial to computational and numerical highlight how:

1) Rigid structures, homogenous or heterogenous, cannot capture total biofilm behaviour when subject to stress, even if they are allowed to flex (Schultz and Swain, 2000; Hartenberger *et al.*, 2020)
2) How focussing on specific structures, such as streamers, may neglect the biofilm response of different structures such as relatively flat continuous films or heterogenous mound-like patches.

Biofilm viscoelasticity has been attributed with increasing biofilm mechanical integrity (Flemming and Wingender, 2010; Peterson *et al.*, 2013; Even *et al.*, 2017; Gloag *et al.*, 2020) and with dictating deformation behaviour (Das and Kumar, 2014; Barai, Kumar and Mukherjee, 2016) (Das and Kuman, 2014; Barai et al., 2016). Also, it has been suggested that viscoelasticity is an adaptation of biofilms to fluctuating mechanical stress (Rupp, Fux and Stoodley, 2005; Gloag *et al.*, 2020). Collectively, these statements lead to the assumption that viscoelasticity contributes to the high tolerance biofilms can demonstrate in high stress environments (Shaw *et al.*, 2004; Cense *et al.*, 2006; Peterson *et al.*, 2013; Fortunato *et al.*, 2017), such as the side of ship (Dennington *et al.*, 2015; de Carvalho, 2018). It is accepted that viscoelasticity implicates drag yet robust experimentally derived relationships between these two factors is lacking. Before artificial, physical, or computational systems can be used to model these complex fluid-structure interactions, viscoelasticity needs to be experimentally characterised. While several medically relevant biofilms have begun to be characterised, to our knowledge there are no data on mechanical properties of typical marine ship-fouling biofilms, which contain both microalgae and bacteria.

4 Chapter 4: General methodology

Although a methodology section is provided in each chapter, this section intends to provide contextual information of equipment and scientific method that may not be within the working knowledge of a general technical audience. Further information is provided that may not be outlined in an academic paper where a certain level of understanding within a specific scientific discipline is assumed.

Three main pieces of equipment were utilised throughout this research, a marine biofouling flow cell (MBFC), an OCT, and a parallel-plate rheometer. A MBFC was used to estimate drag associated with synthetic materials and marine biofilms; the design and hydrodynamic characterisation of the MBFC are provided in Section 4.1. To visualise deformation behaviour and topographical changes of synthetic materials and marine biofilms in the MBFC an OCT was used; in Section 4.2 the design of the OCT is provided, and calculations used to quantify structural properties of synthetic materials and marine biofilms are given. Finally, to rheologically characterise marine biofilms grown on different surfaces a parallel-plate rheometer was adopted and methods are outlined in Section 4.3.

4.1 The Marine Biofouling Flow Cell (MBFC)

As detailed in Section 3.2.2.2 flow cells are often used for estimating drag associated with marine biofilms and synthetic systems. Here, an enclosed meso-scale MBFC, with a recirculating tank of artificial seawater (ASW), was used to measure drag associated with synthetic surfaces of different roughness' and real marine biofilms (Figure 4-1). The ASW had a pH of ~ 8.0 and salinity of 35‰. Methods associated with the preparation of a synthetic system or cultivation of marine biofilms can be found in subsequent chapters. This section presents the general flow cell design and methods used for estimating biofilm-associated drag using pressure drop.

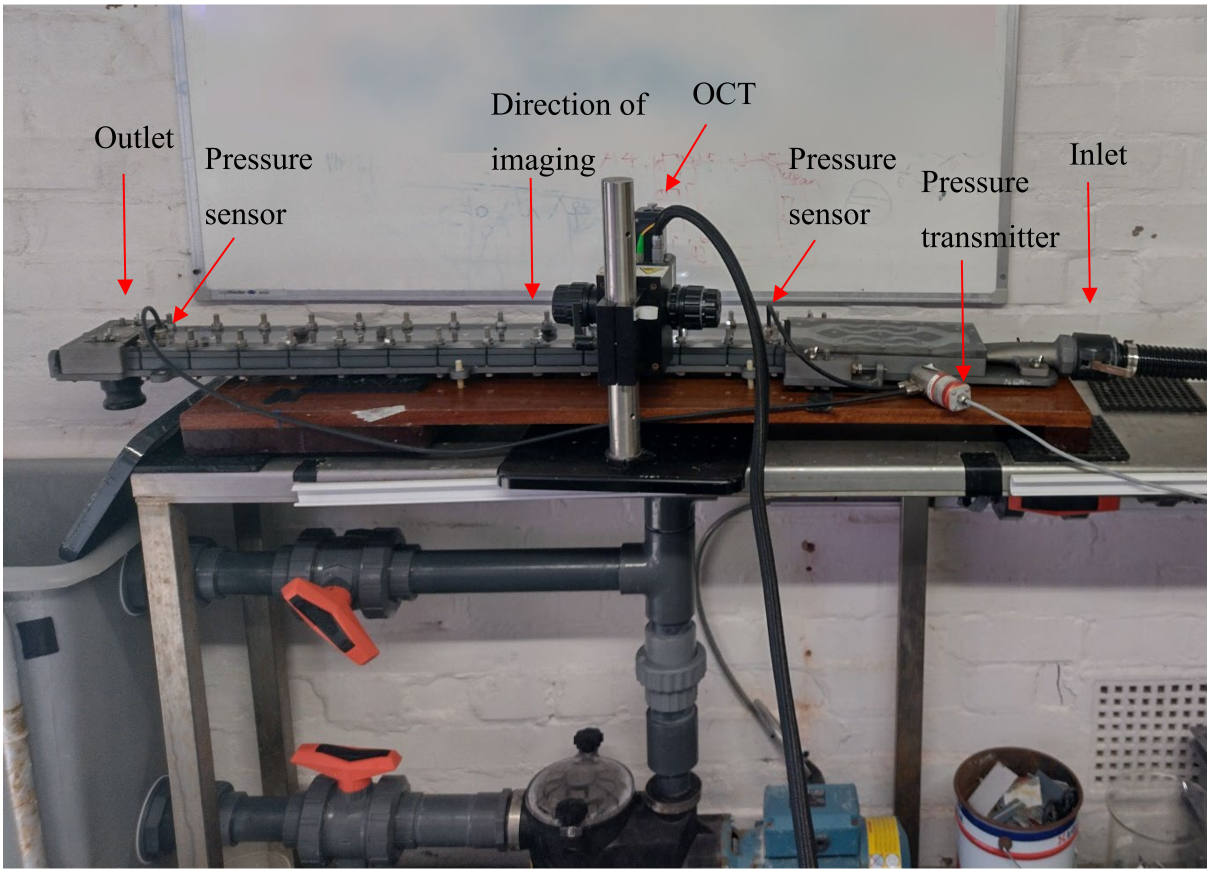

Figure 4-1. *Annotated diagram of the OCT set up with the MBFC (AkzoNobel, Gateshead, UK) for in-situ visualisation and data capture of biofilm structure and deformation during a flow cycle. Adapted diagram from Snowdon et al., (2022).*

4.1.1 Flow cell design

The flow cell was constructed of three main sections: inlet, test section, and an outlet (Figure 4-1) and the base was made of anodized aluminium. The rectangular test section was composed of a rigid PVC base followed by clear acrylic side panels and a clear, smooth, acrylic top-plate, each separated with rubber gaskets and measured 0.85 m (L) × 0.01 m (H) × 0.05 m (W) (giving an aspect ratio of 5:1). Pressure sensor ports were machined into the top plate 0.03 m and 0.83 m from the inlet and differential pressure sensors with a pressure differential range of 0 to 600 millibar (PL-692 Huba Control) were installed (Figure 4-1).

The location of the pressure sensors provided a pressure drop test length of 0.8 m. It has previously been reported that an entry-length of at least 30 × flow cell height is required to guarantee fully developed flow at the first pressure sensor (Hong, Katz and Schultz, 2011). The criteria outlined in the literature for a suitable entry-length was not achieved here and was, in part, explicable by the flow cell design. The flow cell was designed for culturing and testing biofilms under hydrodynamic conditions with an aim to assess their structure, growth and removal using OCT (Fabbri *et al.*, 2018); therefore, a long entry-length was not prioritised. To aid flow development a maze-like baffle was incorporated at the inlet (Figure 3-5) (Fabbri *et al.*, 2019). Further, pressure sensors were placed to facilitate the location of the OCT (Figure 4-1), which enabled biofilm behaviour to be studied *in-situ* in real-time, whilst providing maximum pressure drop length and high pressure drop sensitivity. Despite the short entry-length of the flow cell, flow was confirmed to be turbulent in the system as ΔP was proportional to flow velocity^2 (u^2) (Massey and Ward-Smith, 1998; Fabbri *et al.*, 2019; Snowdon *et al.*, 2022). The relationship between ΔP and u^2 was also observed throughout the current Thesis.

Although the flow cell geometry is smaller than others used in the literature for estimating biofilm associated drag (Schultz *et al.*, 2015; Hartenberger *et al.*, 2020), it offers high throughput experiments and enables a greater focus on understanding the relationship between physico-mechanical properties and drag as methods such as OCT, which operate at a centimetre scale working distance, can be used in conjunction with the flow cell.

4.1.2 Hydrodynamic characterisation of the MBFC

Test pieces, whether synthetic or natural biofilms, were inserted into the MBFC and exposed to a flow cycle. Unless otherwise stated, the flow cycle involved incrementally increasing the flow velocity of ASW, which was controlled by pump setting (centrifugal pump, 1.1 kW, Calpeda, Italy), up to approximately 3.5 m s^{-1} (loading cycle) followed by stepwise decreases in flow velocity back to 0 m s^{-1} (unloading cycle) (Figure 4-2). In the MBFC a flow velocity of 3.5 m s^{-1} was equivalent to a *Re* of approximately 5.2×10^4. At the start of every flow cycle, ASW was ran through the flow cell at < 1 m s^{-1} so that the pressure sensor tubing could be bled of any bubbles in the system.

Note that across a ship hull a *Re* on the magnitude of 10^6 and higher can develop (Moody, 1944; Demirel *et* al., 2014; Demirel, Turan and Incecik, 2017) which is significantly higher than the maximum *Re* reached in the MBFC employed here. To verify the use of this system for predicting ship-related drag experiments would need to be executed at a higher *Re* and equipment limitations would need to be considered. Despite this, for reasons already provided, the MBFC was used across all investigations in this Thesis.

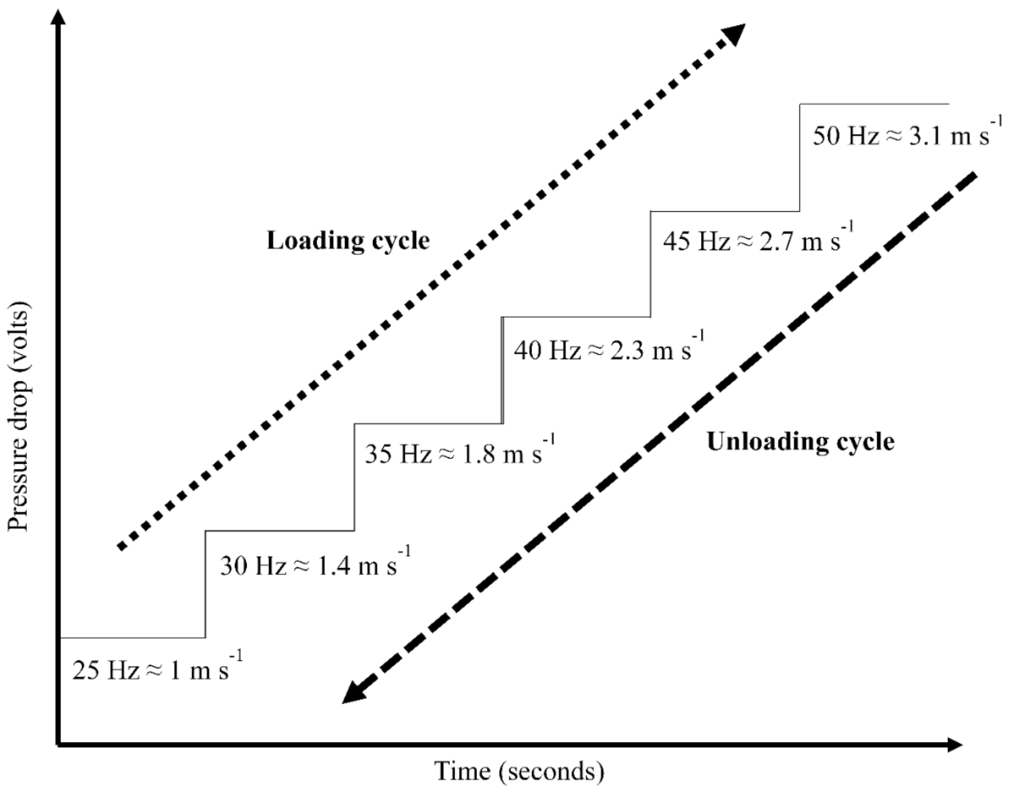

Figure 4-2. *Diagram detailing the steps of a flow cycle executed in the flow cell (AkzoNobel, Gatehead, UK). The steps were determined by a change in the pump setting (Hz) which altered the pressure in the flow cell. The loading cycle moved from 25 to 50 Hz and the unloading cycle was the reverse. For each step, an approximation of the flow velocity has been indicated. Each step was held for two minutes to allow for OCT images to be taken.*

Flow velocity was recorded using a digital flow sensor (Perfect Reef Systems Corrente+ 2”) with a working range of 0 to150 L h^{-1} (with a water pressure of < 1.5 MPa) and was used to calculate *Re* as defined in Equation 3-5 (Fabbri et al., 2018; Li et al., 2019; Stoodley et al., 2001). As μ and ρ are affected by temperature which in turn affects ν_k (Equation 3-6), temperature was also recorded at every stage during the flow cell cycle (Figure 4-2).

ΔP was measured continuously throughout the flow cycle using differential pressure sensors attached to the top-plate. By measuring ΔP, C_f was calculated using Equation 3-8 and was used as a proxy for drag (Fabbri *et al.*, 2019). For the MBFC used in this throughout this work, *L* was the distance between the pressure ports (0.8 m) and ρ was the density of ASW (kg m^{-3}) calculated at the relevant temperature.

In a turbulent flow regime, ΔP and u^2 can exhibit a linear dependence (Massey and Ward-Smith, 1998). Therefore, as well as calculating C_f for every stage in the flow cycle (Figure 4-2), a single average C_f could be calculated across an entire flow regime by substituting the slope of the line exhibited by ΔP and u^2 into Equation 3-8 as $\Delta P_f/u^2$ (Fabbri *et al.*, 2019; Snowdon *et al.*, 2022). This instantaneous drag value will be henceforth referred to as $C_{f,\text{I.}}$

4.1.3 Asymmetric flow cell system

The MBFC used throughout these investigations was installed with a smooth clear top-plate which could lead to an asymmetric flow velocity profile. As an aim of the following investigations was to study deformation behaviour of synthetic and natural biofilms the clear smooth top-plate was necessary to allow real-time imaging of test pieces using OCT (Blauert, Horn and Wagner, 2015; Fabbri *et al.*, 2018; Picioreanu *et al.*, 2018) (Figures 3-5 and 4-1). The compromise of using a top-plate with a different roughness to the base-plate has been recognised in other studies and has previously been accounted for using methods such as PIV (Hartenberger *et al.*, 2020). During this research, however, asymmetry was accounted for by conducting flow cell experiments on synthetic biofilms in a symmetric (equivalent roughness top-plate) and asymmetric flow cell (smooth top-plate).

As rigid structures are often used as the benchmark for studying drag in the literature, experiments utilised rigid synthetic biofilms (rigid filler, sandpaper, and smooth PVC) for comparing drag calculated in a symmetric and an asymmetric system. For the rigid materials there was a strong linear relationship between C_f calculated for an asymmetric and symmetric system of increasing roughness (Figure 4-3). However, due to viscoelastic behaviour exhibited by marine biofilms and the disruption this can cause to the boundary layer (Murphy *et al.*, 2018, 2022) it could be expected that a linear relationship would not be found for a deformable synthetic structure or for natural marine biofilms. Future work should aim to characterise C_f in the MBFC for an elastomeric system.

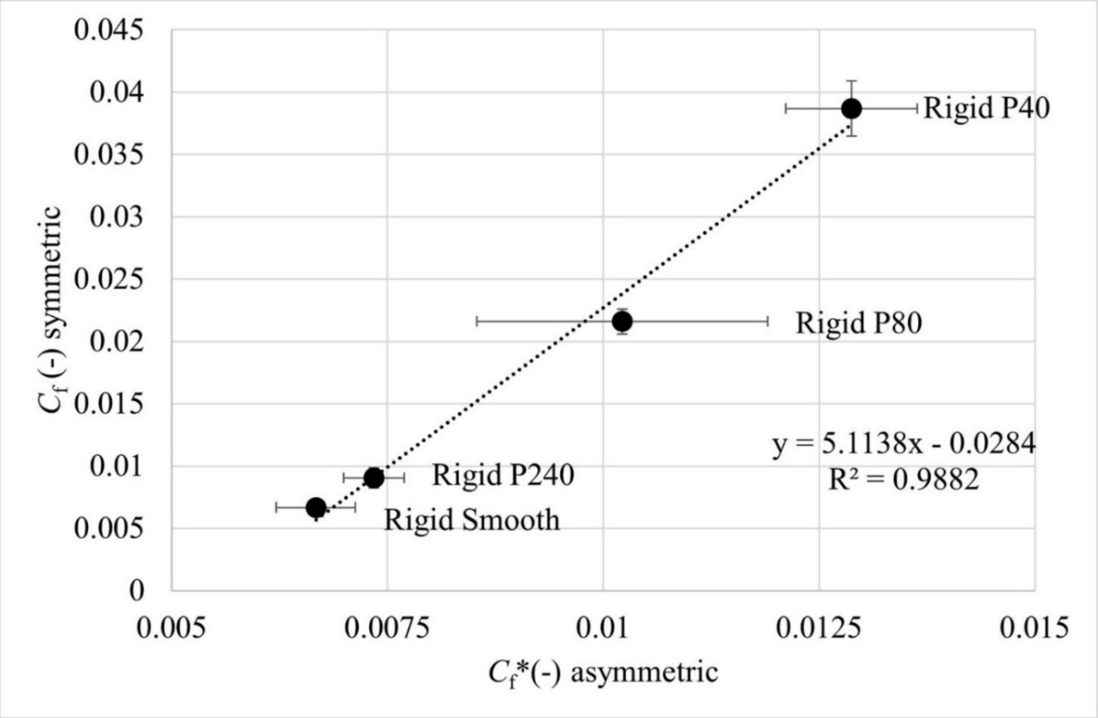

Figure 4-3. *Average $C_f \pm SD$ calculated for a symmetric and asymmetric (*) flow cell set up for a rigid system of varying roughness' (where rigid includes data for a rigid filler material and sandpaper). A line of best fit has been added to the figure.*

4.1.4 Uncertainty analysis on flow cell data

4.1.4.1 Experimental uncertainty analysis

Experimental uncertainty provides an indication of the uncertainty surrounding a variable based on the uncertainty associated with its component parts. As estimating drag associated with marine biofilms was an aim of the current work, uncertainty was calculated for C_f^* using the root of the sum of the squares (RSS) method outlined in Cimbala (2013). It was expected that uncertainty would decrease with an increase in *Re* (Lorenzini *et al.*, 2009) and therefore analysis was executed at 2.2 × 10^4 and 4.0 × 10^4 *Re* (both of which were within the capability of the flow cell). Average C_f^* was calculated at the different *Re* using Equation 3-8 for an elastomeric and rigid sandpaper system (as outlined in Chapter 5). Mean ± standard deviation (SD) was then calculated for each of the variables in Equation 3-8; the standard deviations were then transformed to a 95 % confidence interval which was used to calculate experimental uncertainty for C_f^*:

$$\frac{\partial C_{f*}}{C_{f*}} = \sqrt{\left(\frac{\partial \Delta P}{\Delta P}\right)^2 + \left(\frac{\partial D_h}{D_h}\right)^2 + \left(\frac{\partial \rho}{\rho}\right)^2 + \left(\frac{\partial L}{L}\right)^2 + \left(2\,\frac{\partial u}{u}\right)^2} \qquad \textit{Equation 4-1}$$

where, ∂ is the uncertainty of a variable at a 95 % confidence. The outcome of Equation 4-1 is then multiplied by average C_f^* (calculated for a given set up) to give a numerical value for $\partial\ C_f^*$. To get percentage error the outcome is multiplied by 100.

Although uncertainty analysis was not executed on marine biofilms, the outcome of the analysis for drag related to elastomeric system, shown in Table 4-1, provides useful insight into the effects of deformation behaviour on drag calculations in the MBFC. As biofilms are dynamic and heterogeneous, they would likely complicate efforts to perform accurate uncertainty analysis.

Table 4-1. *Average* C_f^* *measured using a pressure drop system in an MBFC and calculated for material replicas at* $Re = 2.2 \times 10^4$ *and* 4.0×10^4 *± uncertainty error using Equation 4-1. All measurements were calculated using 95 % confidence limits.*

	$Re = 2.2 \times 10^4$	$Re = 4.0 \times 10^4$
Elastomer		
Smooth	0.0102 ± 0.00422	0.00858 ± 0.00144
P240	0.0131 ± 0.000595	0.0102 ± 0.000467
P80	0.0160 ± 0.00478	0.0138 ± 0.00373
P40	0.01333 ± 0.00199	0.0125 ± 0.00148
Filler		
Smooth	0.00699 ± 0.000634	0.00617 ± 0.0000827
P240	0.00854 ± 0.00342	0.00718 ± 0.00230
P80	0.0100 ± 0.00569	0.00853 ± 0.00488
P40	0.01487 ± 0.00121	0.0128 ± 0.000949

4.1.4.2 Elemental uncertainty analysis

Elemental uncertainty is the overall uncertainty of a variable and can be defined as precision or bias uncertainties as it incorporates systemic error (from the manufacturer) and random error through measurements taken. Here, it was calculated for each of the component variables in the C_f^* equation (Equation 3-8) using the error provided by the manufacturers of different pieces of equipment; for example the error of the flow metre used to measure flow velocity and the error of the pressure sensors used to measure pressure drop. Variable uncertainty (∂x) was calculated using

$$\partial x = \sqrt{(\partial_{measurement})^2 + (\partial_{manufacturer})^2} \quad \text{Equation 4-2}$$

And was measured for every component variable in Equation 3-8 as shown in Table 4-2. To calculated uncertainty surrounding the collected measurements and manufacturer limits the RSS method outlined in Cimbala, (2013) was applied.

Table 4-2. *Average elemental uncertainty error (%) for the component parts of Equation 3-8 used to measure drag. Uncertainty surrounding drag for an elastomeric sandpaper system, a rigid filler sandpaper system and sandpaper at Re = 2.2 × 10^4 and 4.0 × 10^4 are presented using equations from Cimbala, 2013. All measurements are taken at 95 % confidence limits.*

	***u* (m s^{-1})**	**ΔP (Pa)**	**ρ (kg m^{-3})**	**D_h (m)**	**L (m)**
Elastomer 2.2 × 10^4	4.87	17.19	1.00	3.34	0.05
Elastomer 4.0 × 10^4	4.87	7.45	1.01	3.34	0.05
Filler 2.2 × 10^4	10.11	19.82	1.01	2.23	0.05
Filler 4.0 × 10^4	10.11	15.08	1.01	2.23	0.05
Sandpaper 2.2 × 10^4	2	32.50	1.01	1.75	0.05
Sandpaper 4.0 × 10^4	2	26.74	1.01	0.03	1.75

4.2 Optical Coherence Tomography (OCT)

To quantify structural properties of synthetic and natural biofilms, namely thickness (mm), roughness coefficient (R_a^*) and cover, an OCT (Ganymede, ThorLabs, Germany) was used. To simultaneously measure biofilm structure, mechanics and drag, the OCT was set up in conjunction with the flow cell (Figures 3-5 and 4-1).

An OCT scanner measures a point reflection signal from the test piece surface and produces a depth-resolved intensity profile along the scan axis (z-direction, flow-cell height) this is called an "A-scan". By acquiring several scans along-stream (x-direction, flow-cell length), a cross-sectional image is produced in the xz-plane (two-dimensional scan, 2D) and is otherwise known as a "B-scan". Consecutive "B-scans" along the other lateral axis (y, the flow-cell width) generates a full volumetric representation (three-dimensional scan, 3D), as detailed previously (Xi *et al.*, 2006; Haisch and Niessner, 2007; Wagner *et al.*, 2010). Importantly, the OCT used in this research had a 3D imaging probe (PR3-09-A0) which housed a LK3- LSM03(BB) objective lens with a working distance of 25.1 mm. The lens provided a central wavelength of 930 nm and gave an axial resolution of 5.8 μm and a lateral resolution of 8.0 μm in air (refractive index = 1). The OCT could capture a 3D-image of 10.0 mm × 10.0 mm × 2.7 mm (x-y-z). For more details on OCT and its advantages over alternative methods, namely CLSM, refer to Section 3.2.2.2.

ThorLabs software, version 5.8.3, (Ganymede, ThorLabs, Germany) was used to control the OCT light settings, focusing and imaging. Milferstedt et al., (2009) determined that 3.4 mm^2 was the minimum area required for representative analysis of biofilm mesoscopic features, but also stated that an increase in area image led to higher precision (Wagner *et al.*, 2010). Based on these recommendations, x-z cross-sections of 9.0 mm × 2.0 mm (9211 × 1024 pixels) with a resolution of 0.98 μm in the x-direction and 2.75 μm in the z-direction, were acquired. As images were taken *in-situ* (in ASW or natural seawater) the refractive index for water, 1.34, was applied. Unless otherwise stated, 3D-scans were also acquired and typically measured 9.0 mm × 9.0 mm × 2.0 mm (x-y-z). All OCT scans were manually exported as .tiff files from ThorLabs for further analysis. For 2D-scans this involved using Fiji, ImageJ (https://imagej.net/Fiji) and is detailed in the relevant chapters; for 3D-scans MATLAB was utilised as described in Section 4.2.1.

4.2.1 Processing of 3D-scans for structural characterisation of marine biofilms

To assess the surface topography and structure of marine biofilms grown statically and dynamically, OCT 3D-scans (C-scans) were exported as .oct files into MATLAB. Custom scripts produced by Fabbri et al., (2018) were ran and produced data on average biofilm thickness (mm), R_a^* and percent coverage (%) (Blauert, 2017). Briefly, the process in MATLAB involved thresholding and manual detection of the panel and biofilm surfaces.

Figure 4-4 shows an example of the MATLAB output when quantifying biofilm thickness (mm). Across the images vertical blue lines can be seen (Figure 4-4) which is indicative of a loss in the boundary surface between the biofilm and the surrounding fluid. This could be consequence to errors in thresholding leading to pixel removal or by signal interference during testing, which could be caused by the presence of bubbles in the MBFC system or by reflection from the test surface.

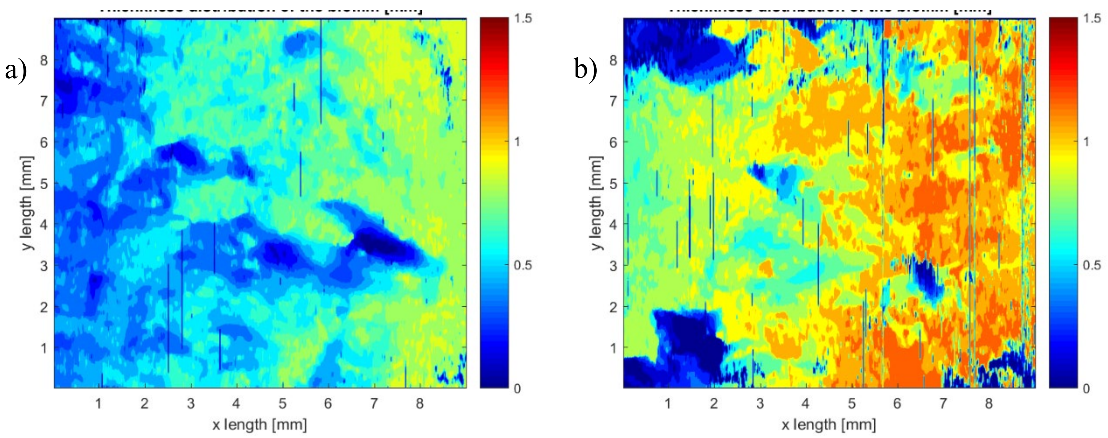

Figure 4-4. *Aerial heat maps showing the thickness distribution (mm) of biofilms grown in flow cells in Hartlepool Marina (UK) under a) a low flow rate and b) a high flow rate. The heat maps are produced from processing OCT 3D-scans in MATLAB and using Equation 4-3.*

4.2.1.1 Average thickness (mm)

Average thickness (mm) was calculated from the individual scans (A-scans and B-scans) within a C-scan:

$$\bar{T}_{B-scan} = \frac{1}{N}\sum_{N}^{j=1} T_{A-scan,j} = \frac{1}{N}\sum_{N}^{j=1}(z_b - z_c)_j \qquad \textit{Equation 4-3}$$

where $T_{A-scan,j}$ is the thickness at a single point, j (A-scan) within a B-scan and N is the total number of j's (A-scans) within the B-scan. At each A-scan, thickness was measured by subtracting the position of the coated surface, z_c, from the biofilm surface position, z_b. Once the biofilm surface and coating surface were detected at each A-scan, an average thickness could be calculated across all B-scans and subsequently the overall C-scan. An example of the output is depicted in Figure 4-4.

4.2.1.2 Roughness coefficient (R_a^*)

The following equation, based on Murga et al., (1995) and referenced in Fabbri *et al.*, (2018), was used to calculate the surface roughness coefficient:

$$R_a *= \frac{1}{N}\sum_{i=1}^{N}\frac{\left|L_{F,i}-\bar{L}_F\right|}{\bar{L}_F} \qquad \textit{Equation 4-4}$$

where, i indicates an A-scan and N is the total number of i's (A-scans) within a B-scan. The equation is based on biofilm thickness, where $L_{F,i}$ is the maximum thickness and L_F is average thickness. If a biofilm is relatively homogenous with few variations from the mean thickness, then R_a^* will be closer to zero. Alternatively, a heterogenous biofilm with high variation around the mean will lead to a higher R_a^* value.

4.2.1.3 Percent cover (%)

Biofilm coverage on a surface was measured using the following equation, as stated in Fabbri *et al.*, (2018):

$$Coverage(\%) = \frac{A_b}{A_s}\ x\ 100 \qquad \textit{Equation 4-5}$$

where, A_b is the area covered by a biofilm and A_s is the imaging area (9 mm^2).

4.3 Rheological characterisation of marine biofilms

A Discovery Hybrid rheometer (HR10) (TA Instruments, Delaware, USA) was used to rheologically characterise marine biofilms grown on 40 mm PVC coupons under different conditions. Further details on cultivating marine biofilms for testing, specific experimental procedures are provided in the subsequent relevant chapters. The sensitivity of a rheometer is generally not great enough for measuring soft, fragile, and thin biofilms (relative to materials that are usually tested on a rheometer) which complicates efforts to rheologically characterise biofilms and, in part, explains why no standard methods of testing exist. Despite this rheometer testing of biofilms has been achieved in the literature and for information of its benefits see Section 3.2.2.1.

The rheometer used throughout these investigations was constructed of a rigid cast aluminium frame (Figure 4-5) and possessed a gap position resolution of 0.02 µm which was beneficial for measuring biofilms ~ < 1 mm thickness. Further, the rheometer was designed to measure low stress with a torque range of 5.0×10^{-9} to 2.0×10^{1} N m and a torque resolution of 1.0×10^{-10}. For characterising marine biofilms, a parallel-plate set up was adopted and consisted of a smart-swap geometry 40 mm stainless-stell sandblasted top-plate (TA Instruments, Delaware, USA) to generate roughness for grip and to avoid slippage during testing. For the baseplate a clear PVC immersion well and Peltier-plate heat exchanger were used (Figure 4-5). The well was carefully filled with 4 mL of seawater taken from the location of biofilm cultivation and the Peltier-plate ensured that the biofilms were kept at the same temperature they were grown at to avoid thermal shock.

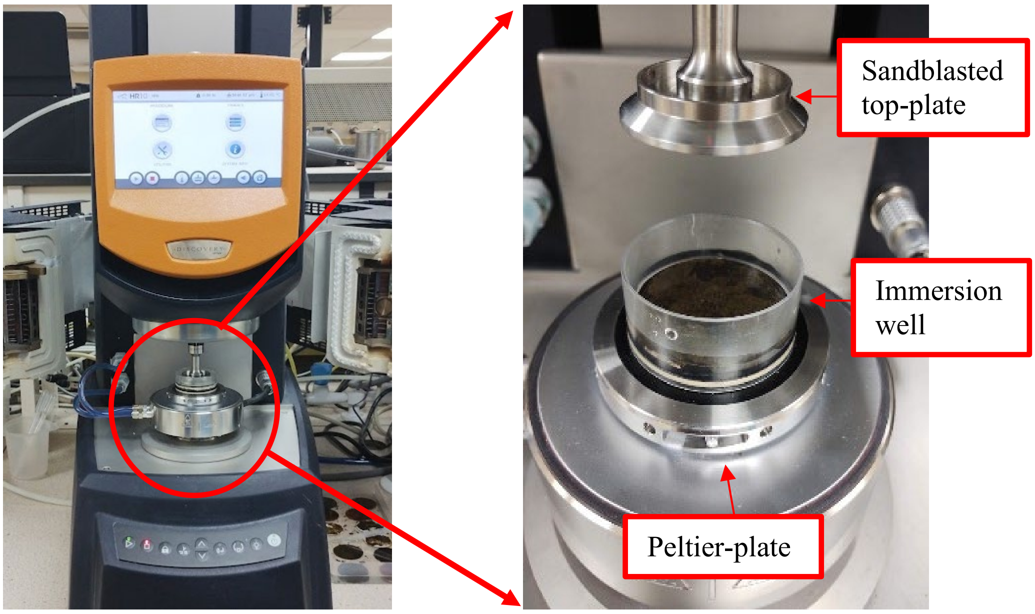

Figure 4-5. *Annotated diagram of a Discovery Hybrid (HR10) rheometer set up for parallel-plate testing of a marine biofilm grown on a smooth surface in Hartlepool Marina (UK). A Peltier-plate and immersion well are also labelled.*

To normalise for differences in biofilm thickness across a coupon, the biofilms were compressed to a normal force of 0.1 N (± 0.01 N) before testing began. By controlling normal force the gap thickness could change based on differences in thickness across biological replicates and ensured contact with the top-plate (Towler *et al.*, 2003). It has been suggested that by using normal force as opposed to gap thickness when characterising marine biofilms there could be reduced variability in rheological data, as well as a reduction in slippage during testing, as demonstrated by multiple published biofilm studies (Towler *et al.*, 2003; Winston *et al.*, 2003; Vinogradov *et al.*, 2004).

4.3.1 Amplitude sweeps

An amplitude sweep is executed by incrementally increasing oscillatory strain at a constant frequency. For these experiments strain was increased from 10^{-5} to 10^{-1} at an oscillation frequency of 1 Hz, which was within the frequency limits of the rheometer of 10^{-7} to 10^{2} Hz. The tests were performed to identify the linear viscoelastic region (LVR) which is determined as the region where storage (G') and loss modulus (G'') are plateaued at the start of an experiment (Figure 4-6). The LVR could then be used to inform the experimental conditions applied during frequency sweeps and creep-recovery tests. Yield stress (σ_y) could also be calculated and is taken as the intersect of *G′* and *G′′* (Figure 4-6).

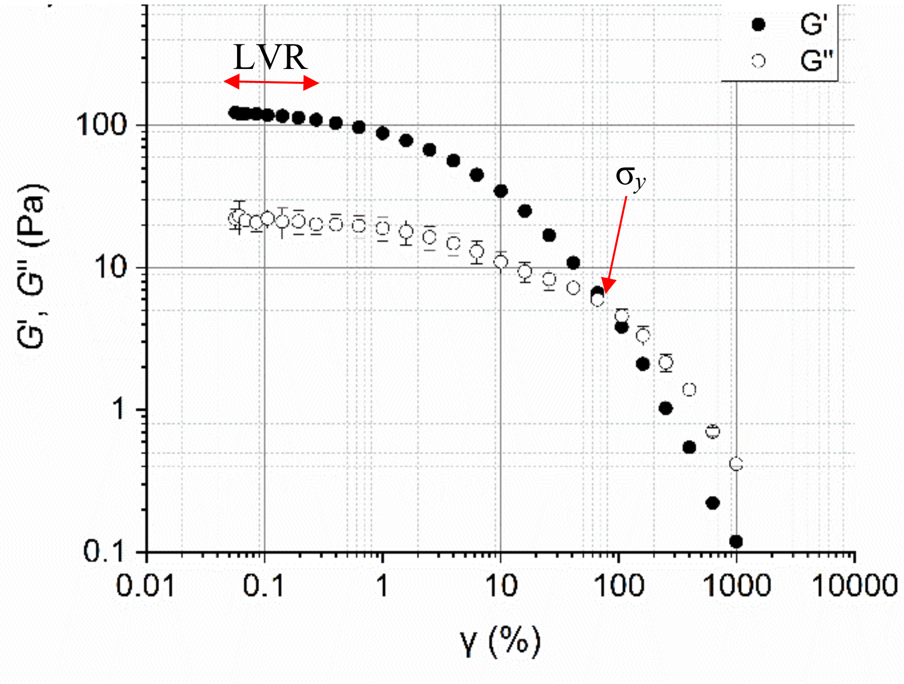

Figure 4-6. *Representative amplitude sweep data for a marine biofilm grown on a smooth surface at the Dove Laboratory (UK). The red arrows indicate the linear viscoelastic region (LVR) and the yield stress (σ_y).*

4.3.2 Frequency sweeps

To determine the dynamic behaviour of a material, such as biofilms, frequency sweeps can be used. The oscillatory frequency was increased incrementally from 0.1 to 10 Hz, at a constant strain from within the LVR. Note that the oscillatory frequency corresponded to an angular frequency (ω) 0.63 to 63 rad s^{-1}.

4.3.3 Creep-recovery

Creep-recovery experiments are performed to characterise the viscoelasticity of a material, such as biofilms. By applying a constant shear stress over a set time period (creep) deformation can be captured, the stress is then removed, and the relaxation of a material can be studied. Throughout this study, creep-recovery tests were performed at different shear stress values ranging from 0.25 to 20 Pa. Unless otherwise stated, a constant stress was applied for 60 seconds and then removed (0 Pa); recovery of the biofilm was then followed for 60 seconds. Strain was plotted as a function of time which allowed effective shear modulus (*G*) and effective viscosity (η) to be quantified (Figure 4-6) (Gloag *et al.*, 2018). As biofilms naturally display mechanical and structural spatial heterogeneity (Wagner *et al.*, 2010; Pavissich, Li and Nerenberg, 2021) *G* and η can only be considered as estimates of the overall biofilm properties, hence the term ‘effective’ is applied (Shaw *et al.*, 2004).

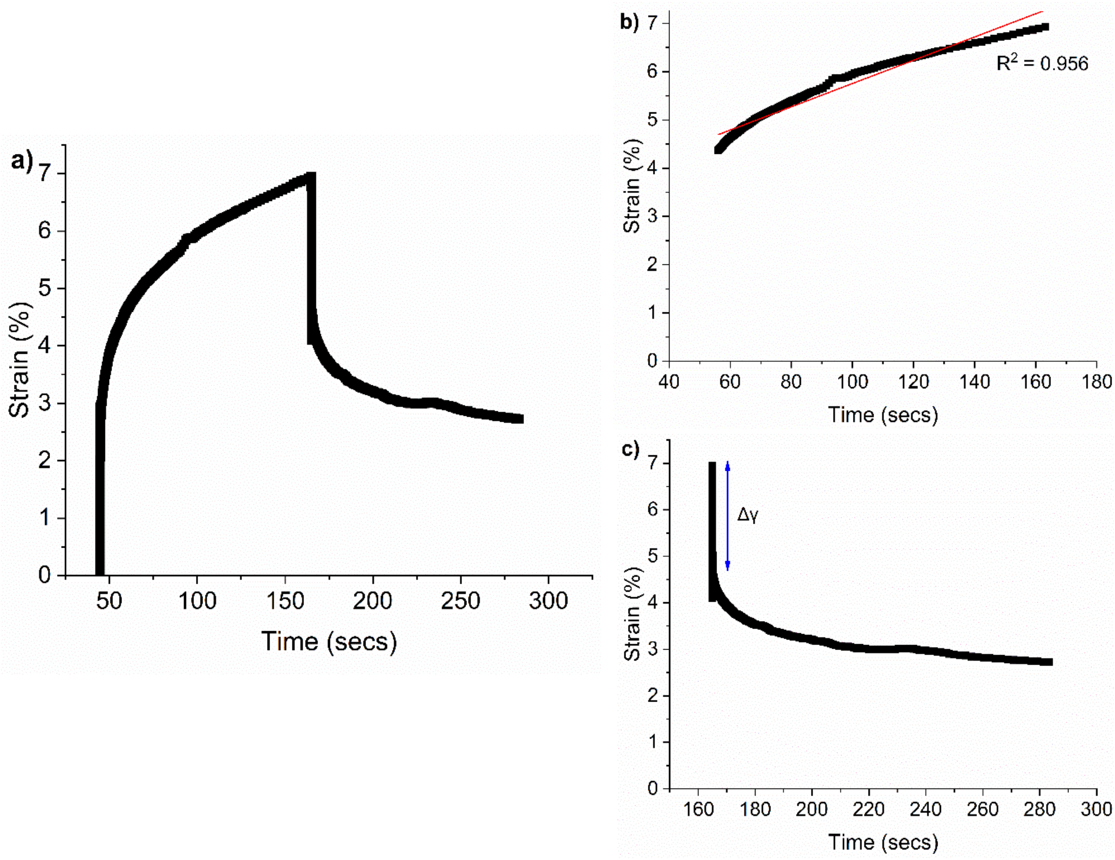

Figure 4-7. *a) Representative creep-recovery data for a marine biofilm grown on PVC coupons in Hartlepool Marina (UK) showing how b) η can be calculated using the slope of the linear viscous region (red line) and c) G can be calculated using the length of the elastic recovery response ($\Delta\gamma$) (blue line). Adapted from Snowdon et al., (2023).*

During the creep portion of the experiment effective η can be calculated:

$$\eta = \frac{\sigma}{slope} \qquad \text{Equation 4-6}$$

where, σ is shear stress (Pa) and *slope* is the slope of the linear viscous region of the creep curve. The linear viscous region is taken as the section of the slope where $R^2 > 0.95$ as depicted by the red line in Figure 4-7b. From the recovery part of the experiment effective *G* was calculated using:

$$G = \frac{\sigma}{\Delta\gamma} \qquad \text{Equation 4-7}$$

where, Δγ is the elastic recovery response and is measured as the immediate vertical drop in strain when the shear stress is removed (Figure 4-7c). Note that the strain value inputted into Figure 4-7 must be in a dimensionless format, not a percentage (i.e., 10 % would be 0.1). From *G* and η, elastic relaxation time (λ) could also be calculated, which is the time it takes for a biofilms response to shear to transition from elastic- to viscous-dominated.

$$\lambda = \frac{\eta}{G} \qquad \textit{Equation 4-8}$$

5 Chapter 5: Elastomeric sandpaper *replicas* as model systems for investigating elasticity, roughness and associated drag in a marine biofilm flow cell

ABSTRACT

Biofilm heterogeneity and adaptability complicates efforts to link biofilm structural and mechanical properties to frictional drag. As a result, rigid structures are typically used as the benchmark for studying biofilm-associated drag. Elastomeric sandpaper replicas were generated to be used as model systems for investigating the effect of roughness and elasticity on drag, over the *Re* range of approximately 2.0×10^4 to 5.2×10^4 using a marine biofilm flow cell. To control for roughness parameters and surface topography the replicas were created for sandpaper grit numbers: P40, P80 and P240 with average measured roughness (S_a) of 108, 49 and 16 µm, respectively. Profilometry confirmed that there was no significant difference between the roughness of the rigid sandpaper sources and the material replicas. The marine biofilm flow cell was fitted with a clear lid, which allowed real-time visualisation of the replicas' surface topography using OCT. Pressure drop measurements, expressed as a friction coefficient, revealed that the elastomeric sandpaper replicas had a significantly higher associated drag, of up to 52 %, when compared to the rigid counterparts. From statistical analysis it was confirmed that material mechanical properties, such as elasticity, and surface roughness both significantly affect drag. Elastic model systems can be used to enhance our understanding of biofilm physico-mechanics and their role in marine drag.

5.1 **Introduction**

Biofilms are composed of a community of sessile microorganisms embedded within a viscous exudate (the matrix). The matrix is dominated by extracellular polymeric substances (EPS) (Flemming and Wingender, 2010; Di Martino, 2018) and water (Berlanga and Guerrero, 2016), and offers protection to microbial cells from external stressors, such as environmental, chemical or mechanical factors (Peterson *et al.*, 2013).

In the shipping industry, the presence of biofilms on ship hulls can increase frictional drag which has significant economic and environmental consequences, such as higher fuel consumption and correspondingly greater greenhouse gas emissions (Townsin, 2003). An increase in ship shaft power between 1 % and 18 % due to the presence of a biofilm is a frequently cited figure in the current literature (Haslbeck and Bohlander, 1992; Schultz *et al.*, 2011; Yeginbayeva *et al.*, 2020). Due to the complexity of measuring drag at ship-scale, the majority of marine biofilm drag studies are executed at a laboratory scale, for example using flow cells on the order of 1 m; results can then be extrapolated to predict ship-scale drag (Schultz *et al.*, 2015; Yeginbayeva *et al.*, 2020). Importantly, care must be taken when extrapolating data to ship-scale as ship relevant *Re* are typically orders of magnitude higher than the *Re* range covered using smaller flow cells (Fabbri *et al.*, 2019). Operating at a smaller scale is useful for screening since more replicates can be ran providing greater rigor; further, environmental conditions can be controlled, and physico-mechanical properties can be studied more closely (Fabbri *et al.*, 2018). It is known that biofilm morphological properties, such as surface roughness (Andrewartha *et al.*, 2010; Li *et al.*, 2019), and physico-mechanical (combined physical and mechanical) properties are significant in influencing drag (Watanabe, 1969; Schultz *et al.*, 2015); yet, the relative contribution of these properties is poorly understood (Blauert, Horn and Wagner, 2015; Picioreanu *et al.*, 2018; Hartenberger *et al.*, 2020). In part, this is attributed to the high level of heterogeneity and adaptability that biofilms exhibit, which leads to wide variations in efforts to relate biofilm characteristics to drag (Schultz and Swain, 2000).

To study biofilm-associated drag, experimental and computational models have been adopted which use homogenous and rigid structures to mimic biofilm behaviour (Yusim and Utama, 2017; Hartenberger *et al.*, 2020). A benefit of utilising a synthetic system as a biofilm substitute is that the material has reproducible properties that can be controlled, which is a challenge when using natural biofilms. Rigid and homogenous structures, such as embedded sand grains or sandpaper, can approximate average biofilm roughness profiles and have been reported to cause similar, if not equivalent, drag to biofilms under specified experimental conditions (Murphy *et al.*, 2018; Hartenberger *et al.*, 2020). However, in many other studies, drag associated with biofilms greatly exceeds that which would be anticipated for a rigid equivalent (Picologlou, Zelver and Characklis, 1980; Hartenberger *et al.*, 2020).

Biofilms are viscoelastic materials, which typically exhibit a time-dependent response when under applied stress, such as hydrodynamic shear (Shaw *et al.*, 2004; Gloag *et al.*, 2018). The deformation behaviour of viscoelastic materials, for example wide-ranging lab and environmental biofilms, has been repeatedly captured using mechanical methods, such as rheology, indentation (Peterson et al., 2013; Stoodley et al., 1999) and imaging methods (Blauert, Horn and Wagner, 2015; Picioreanu *et al.*, 2018; Depetris *et al.*, 2019). Biofilm material properties have long been hypothesised as a major reason for why biofilm fouling causes high frictional drag (Picologlou, Zelver and Characklis, 1980; Schultz and Swain, 2000). Therefore, whilst conventional methods used to physically model biofilms involve implementing rigid materials of different roughness', they generally do not account for viscoelastic physico-mechanical properties, which could alter fluid-structure interactions and possibly lead to the mis-estimation of drag (Picologlou, Zelver and Characklis, 1980; Picioreanu *et al.*, 2018; Hartenberger *et al.*, 2020).

To investigate differences in drag associated with a rigid and deformable material, Lewkowicz and Das (1986) introduced a compliant drag-production mechanism into a biofilm-associated drag model using nylon tufts. They revealed a significant increase in drag when comparing the drag induced by the compliant system to the rigid controls, which was explained by fluid-structure interactions caused by the surface protrusions. Andrewartha and Sargison (2011) adopted a similar approach using woollen strands. The drawback of these models is that although artificial protrusions are individual free moving structures the mechanical properties and the roughness patterns cannot be varied independently as they could be with synthetic material models.

Alternatively, artificial biofilms which involve embedding bacterial cells in a hydrogel (Strathmann, Griebe and Flemming, 2000; Körstgens *et al.*, 2001b), have been implemented as models for studying biofilm mechanics and deformation behaviour as they can mimic biofilm-like responses to shear (Stewart *et al.*, 2015; Di Martino, 2018). Yet, Kandemir *et al*., (2018) found that under specified conditions there was no difference observed between a hydrogel with and without embedded bacteria. A benefit of a model with no living component is that natural variability as well as structural and biological complexity observed in biofilms is removed (Macedo *et al.*, 2014). Moreover, a synthetic material can be manipulated to simulate an array of physico-mechanical characteristics. El-Labbad, (1987) utilised smooth panels of agar gels of different concentrations to mimic different levels of biofilm 'slime': 0.5 % was used to represent light to moderate slime and 1 % was implemented for heavy slime. The denser slime equivalent (1 % agar) caused a greater increase in drag (El-Labbad, 1987), which suggests that differences in drag between the agar gels were driven by material mechanical properties.

Due to the species and mechanical property diversity of biofilms there is no doubt that some can be characterised as rigid and rough, much like sandpaper structures, or even uniform with repeating units (Wagner *et al.*, 2010) – yet this is likely the exception as opposed to the rule. The aim of this study is to build upon and extend rigid conventional methods by introducing a tailored elastic component. The objective of the present work is to determine the relative contribution of elasticity and roughness to drag using elastomeric and rigid *replicas* of the surfaces of sandpapers of various roughness grades. Although biofilms are spatially heterogenous, a defined and repeatable surface profile was incorporated into the *replicas* to simplify the system and to allow physico-mechanical properties to be the focus of the study. Drag was measured using pressure drop sensors installed into a flow cell and was expressed as C_f (Fabbri *et al.*, 2019; Li *et al.*, 2019). It was hypothesised that the elastomeric structures would induce a significantly greater drag than rigid structures of comparable roughness. Topographical change in response to hydrodynamic shear was simultaneously measured using OCT, a non-invasive imaging technique that has been previously implemented for studying biofilm mechanics at the meso-scale (Wagner *et al.*, 2010; Blauert, Horn and Wagner, 2015; Wagner and Horn, 2017). By utilising a fully synthetic tailored system, such as the one proposed in the present study, the effects of surface geometry and mechanical properties on drag can be studied in isolation. If we can determine under which conditions physical and/or mechanical properties are most influential to drag then better insights into the efficiency of coating technologies for the prevention and management of biofilms can be gained (Fabbri *et al.*, 2018, 2019; Hartenberger, 2019). These findings will help advance the development of a more accurate experimental marine biofilm models and can be used to further study the contribution of physico-mechanical properties on biofilm-associated drag.

5.2 Materials and Methods

5.2.1 *Cast and replica preparation*

The casting and moulding process involved three groups of materials, referred to as *source*, *intermediate*, and *replica* (see Table A-1). Two *sources* (either sandpaper or smooth PVC) were used to create an impression in the *intermediate* material to produce a negative mould (Figure 5-1c). Materials (elastomeric or rigid when set) were then poured into the *intermediate* moulds to generate *replicas* of the *source* materials (Figure 5-1d-f). The *replicas* were generated to be compatible with the flow cell and measured 85 cm × 5.5 cm. Between all steps (Figure 5-1) polytetrafluoroethylene (PTFE) release spray was used to ensure easy removal from surfaces.

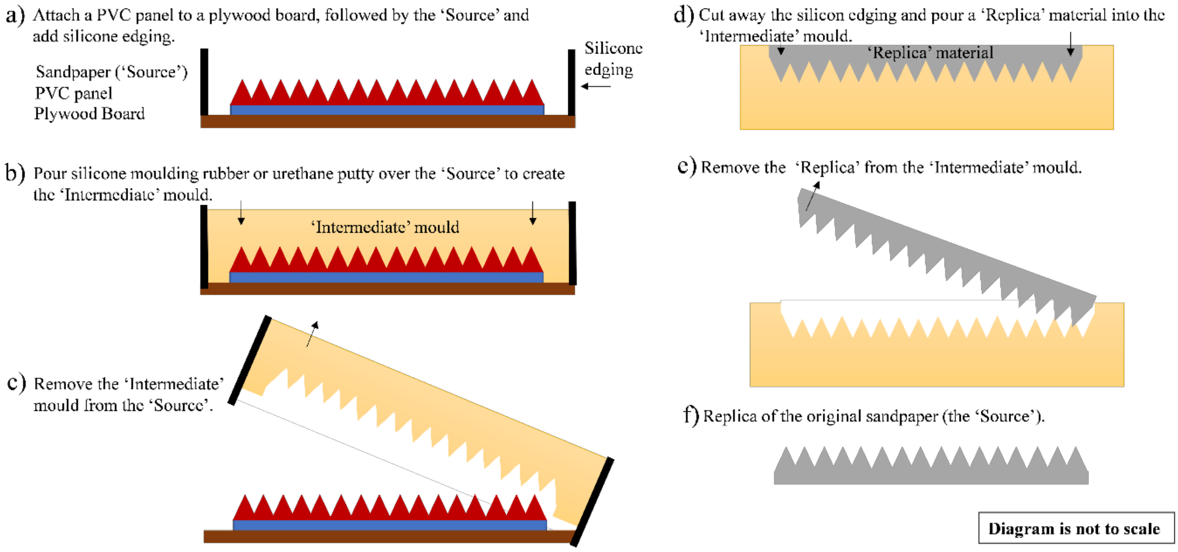

Figure 5-1. *Method for generating rough and smooth replicas of the sources. For illustrative purposes the example uses sandpaper as a source, silicone moulding rubber as the intermediate material and epoxy filler as the replica material.*

5.2.1.1 *Source* materials

Replicas were generated from two source materials: sandpaper (3M, Bracknell, UK) and PVC panels (Chemical Process Solutions, Seaham, UK). Sandpaper of three different grit numbers: P40, P80 and P240, classified as per the Federation of European Producers of Abrasives (FEPA), were used as uniform rough surfaces for modelling biofouled surfaces. The listed roughness grades were selected as they have been previously used for drag experiments in the flow cell (Fabbri *et al.*, 2019) and to cover a roughness range comparable to biofilm surface roughness values (Li *et al.*, 2019). PVC panels were used as a smooth control for modelling an 'unfouled' surface.

To create the smooth source surface, a PVC panel (85 cm × 5.5 cm) was bonded to a plywood board, which formed a stable base when casting. For the rough sandpaper sources an individual sandpaper sheet (85 cm × 5.5 cm) was bonded to the PVC panel (Figure 5-1a). For the sandpaper source, the PVC panel was necessary so that the resultant sandpaper replicas were flush with the channel walls when inserted into the flow cell.

5.2.1.2 *Intermediate* materials

Intermediate materials were poured over source materials to create negative moulds. There were two *intermediate* materials used. Silicone rubber (10:1 weight mix ratio of part a:b, ACC silicones, Somerset, UK) (Figure 5-2) was used to cast the epoxy filler *replicas* (see Section 5.2.1.3) and urethane putty (2.52:1 weight mix ratio of part a:b, ITW Devcon, Massachusetts, US) was used for the elastomer *replicas* (Table A-1). The different *intermediate* materials were required as the elastomer *replica* material adhered to the silicone rubber *intermediate* material. In total seven *intermediate* moulds were generated: silicone-P40, silicone-P80, silicone-P240, silicone-smooth, urethane-P40, urethane-P80 and urethane-P240 (Table A-1). For the smooth elastomer *replicas*, the self-levelling material was simply brushed onto a prepped PVC panel as opposed to using a urethane-smooth *intermediate* mould.

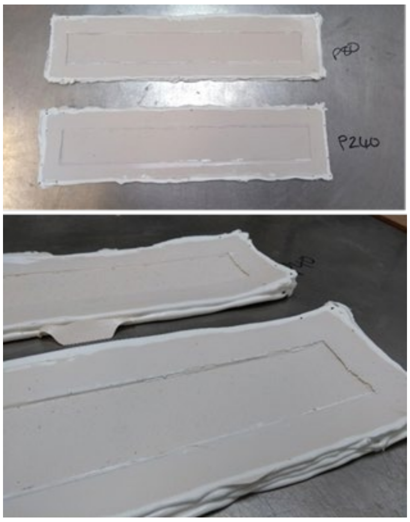

Figure 5-2. *Intermediate silicone negative moulds of P80 and P240 sandpaper sources, taken from Snowdon et al., (2022).*

Since the uncured silicone *intermediate* material was a liquid with a 48-h setting time, a silicone edging was built up 5 cm away from the sandpaper panel in all directions (resultant size of the *intermediate* material mould = 95 cm × 15.5 cm) (Figures 5-1 and 5-2). The white silicone edging was removed from the silicone *intermediate* mould once it had set to ensure flat surface for the epoxy filler *replica* material to set.

5.2.1.3 *Replica* materials

Two *replica* materials were investigated: a polydimethylsiloxane (PDMS)-based elastomer and an epoxy filler with 25 % extra curing agent added. The extra curing agent was required as epoxy filler alone was too brittle for moulding and casting. Also, the epoxy filler is a commercial coating and was prepared according to manufacturer instructions for Interfill 830 (AkzoNobel, Gateshead, UK). A palette knife was used to fill the *intermediate* silicone mould with the epoxy filler and the elastomer was prepared and poured into the *intermediate* urethane mould.

Upon setting in the moulds, the final *replicas* were removed with care to avoid tearing (Figure 5-1e-f). As mentioned previously, a urethane-smooth *intermediate* mould was not required to generate the smooth elastomeric *replicas*.

In total, eight *replica* types were produced: elastomer-P40, elastomer-P80, elastomer-P240, elastomer-smooth, filler-P40, filler-P80, filler-P240 and filler-smooth (n = 2 to 4) that were tested in the flow cell. The *sources*: sandpaper-P40, sandpaper-P80, sandpaper-P240 and smooth PVC (n = 2 to 4) were also tested in the flow cell to allow comparison with their material *replicas*.

5.2.1.4 Surface roughness measurements of sources and replicas

To confirm successful and accurate transfer of surface roughness between the *sources* and the *replicas* a blue-light interferometer (MikroCAD premium, LMI technologies, Burnaby, Canada) was used to measure arithmetical mean surface roughness height (S_a). Six area scans were taken at random sections across every 85 cm × 5 cm replicate for the *replicas* and *sources* (n = 2 to 4). A single area scan measured 10 cm × 2 cm, had an *x-z* resolution of 50 µm × 5 µm and was quantitatively analysed using ODSCAD software (GFMesstechnik GmbH, Berlin, Germany) (Figure A-1). A cut-off wavelength of 10 mm was implemented (Medhurst, 1990; Howell and Behrends, 2006). For the *sources* and *replicas,* S_a was measured both before and after exposure to a flow cell cycle (Figure 4-2). This allowed detection of any changes in roughness consequent to flow.

5.2.2 Preparation and mechanical characterisation of materials

Mechanical profiles were generated for both *replica* materials.

5.2.2.1 Tensile properties

An Instron 5969 material test instrument with a 1 kN load cell and an 87.5 mm gauge length was used for testing the mechanical properties of each material (Zou, Qu and Zou, 2007). The loading speed applied during testing was dependent on the material and ranged from 25 mm min^{-1} to 50 mm min^{-1}. Samples were prepared by pouring the *replica* materials into a dumbbell-shaped silicone mould. Among other calculated properties, tensile strength (MPa), failure strain (%) and elastic modulus (MPa) were of interest.

5.2.2.2 Wetting properties

A Data Physics optical contact angle (OCA) system was paired with SCA20 contact angle measurement software (Data Physics, GmbH, Berlin, Germany). A test material was applied to a clean 15 cm × 10 cm glass plate using a 400 µm draw-down and was exposed to drying at ambient room temperature. The OCA for each material was calculated using sessile drop testing: a 4 µL deionised water droplet was dropped onto the coated glass plate, through air, from a syringe (n = 6). For each droplet, two angle measurements were taken per second for a total of 120 seconds. As a reference point, the measurements taken at 60 seconds for each drop were used to give an average OCA for each test material.

5.2.2.3 Microhardness

A Fisherscope H100C hardness measurement system (Helmut Fischer, GmbH, Berlin, Germany) was used in conjunction with a WIN-HCU software. Test samples were prepared by coating PVC microslides with a test material using a 400 µm draw-down. Indentation tests were executed, and results of interest included modulus of indentation (E_{IT}), Marten's hardness (H_M) and elastic deformation percentage of indentation energy (n_{IT}).

5.2.3 MBFC drag experiments

An enclosed meso-scale flow cell (Figure 4-1), with a rectangular test section of 0.85 m (L) × 0.01 m (H) × 0.05 m (W) and a recirculating tank of artificial seawater (ASW) was used for testing drag associated with sandpaper *replicas*. The ASW had a pH of 8.1 and salinity of 35‰. Although the flow cell implemented is smaller than others used in the literature (Schultz *et al.*, 2015; Hartenberger *et al.*, 2020), it offers high throughput experiments and enables a greater focus on understanding physico-mechanical properties of a material by allowing methods such as OCT to be used in conjunction with the flow cell, which operates at a centimetre-scale working distance. The base of the flow cell was a rigid PVC panel with acrylic side panels. A clear acrylic window panel was installed as the top plate to allow real-time OCT imaging of the *source* and *replica* surfaces in response to flow (Fabbri *et al.*, 2018) (Figure 4-1). Pressure drop sensor ports were positioned in the clear top plate 0.03 m and 0.83 m from the inlet, giving a pressure drop test length of 0.8 m. An entry length of at least 30 × flow cell height has been referenced to guarantee fully developed flow at the first pressure sensor (Hong, Katz and Schultz, 2011), which due to the design of the flow cell could not be adopted here. The pressure sensors were located at the maximum pressure drop length to facilitate the location of the OCT and to increase pressure drop sensitivity. To aid flow development a baffle was added at the flow cell inlet. The hydrodynamic characteristics have previously been investigated using sandpaper of different roughness grades (Fabbri *et al.*, 2019).

The *source* and *replica* materials were inserted into the flow cell and exposed to a flow cycle for a duration of up to 22 minutes. The flow cycle involved incrementally changing the flow velocity of ASW up to approximately 3.5 m s^{-1} (loading cycle) followed by stepwise decreases in flow velocity back to 0 m s^{-1} (unloading cycle) (as detailed in Figure 4-2). During the flow cycle, temperature was measured at each step and ranged between 18°C to 24°C. Flow velocity was recorded using a digital flow meter which allowed *Re* to be calculated using Equation 3-5 (Fabbri et al., 2018; Li et al., 2019; Stoodley et al., 2001). Due to the change in temperature over the flow cycle, the kinematic viscosity of ASW (m^2 s^{-1}) was calculated also for each step (Figure 4-2) as defined by Equation 3-6. For more details on the equipment and equations used during flow cell testing see Section 4.1.

Importantly, the thickness of *sources* and *replicas* were measured using a ruler before being inserted into the flow cell; the thickness was then used to calculate the flow cell height which is used to calculate D_h as defined in Equation 3-7. The maximum flow velocity of approximately 3.5 m s^{-1} corresponds to a maximum *Re* in these experiments of about 5.2×10^4.

5.2.3.1 Calculating drag from pressure drop measurements

Pressure drop (ΔP) was measured throughout the flow cycle using differential pressure sensors that were attached to the top-plate. By measuring ΔP drag could be calculated and expressed as C_f using Equation 3-8 (Fabbri *et al.*, 2019). C_f is a dimensionless number and was calculated for all flow cell runs to allow for statistical comparison.

In a turbulent flow regime, ΔP and u^2 can exhibit a linear dependence (Massey and Ward-Smith, 1998). Therefore, as well as calculating C_f for every stage in the flow cycle (Figure 4-2), $C_{f,\,I}$ was also calculated to represent drag across an entire flow regime (Fabbri et al., 2019). For more details see Section 4.1.2.

It is important to note that since the calculated C_f was based on an asymmetric flow cell set up (roughness was not equivalent on all walls) and there is an insufficient entry length for fully developed flow, the values reported are specific to the system used in this study. Hence, from this point C_f will be referred to as C_f^* to signify that care should be taken when interpreting the C_f data. To assess the relative influence of asymmetry on C_f, flow cell experiments were also executed using a rigid rough symmetric flow cell set up, where roughness was equivalent on the top and bottom of the flow cell (Figure 4-3).

5.2.4 Surface visualisation using OCT 2D-scans

An OCT (Ganymede, ThorLabs, Germany) was set up in conjunction with the flow cell (Figure 4-1) for non-invasive real-time imaging of the *sources* and *replicas* under flow conditions. For more details on OCT design and methodology see Section 4.2.

In this study, three 2D-scans (duration 1.2 seconds each, OCT scan-rate = 30 kHz) were taken at every incremental and decremental step in the flow cycle, for each replicate. ThorLabs software, version 5.8.3 (Ganymede, ThorLabs, Germany) was used to control the OCT and with respect to light, focus and imaging the same settings were applied to all replicates. Based on previous reports, *x-z* cross-sections of 18 mm^2 (9211 pixels × 1024 pixels) were acquired which corresponds to a resolution of 0.98 μm in the *x*-direction and 2.75 μm in the *z*-direction (Milferstedt, Pons and Morgenroth, 2009). As images were taken *in-situ* the refractive index for water, 1.34, was used. All

OCT images were manually exported as .tiff files from ThorLabs for analysis in Fiji, ImageJ (https://imagej.net/Fiji).

5.2.4.1 OCT image processing and analysis

OCT datasets were processed using the open-source image analysis software, Fiji (Schindelin *et al.*, 2012). Before processing, the 2D-scans were cropped to the area of interest containing the topographical surface features (Figure 5-3). The 'Shanbhag' method was then used to threshold and binarise the images (Shanbhag, 1994) and an implemented plugin 'Find connected regions' for the factor 'Tubeness' was used to identify connected structures. The plugin 'MorphoLibJ' was used for morphology segmentation and measurements (Legland, Arganda-Carreras and Andrey, 2016). Particle geometries in the 2D-images were characterised using perimeter and elongation (where a value of 1 indicates roundness, and anything higher indicates elongated structures). The same processing method was applied to all images.

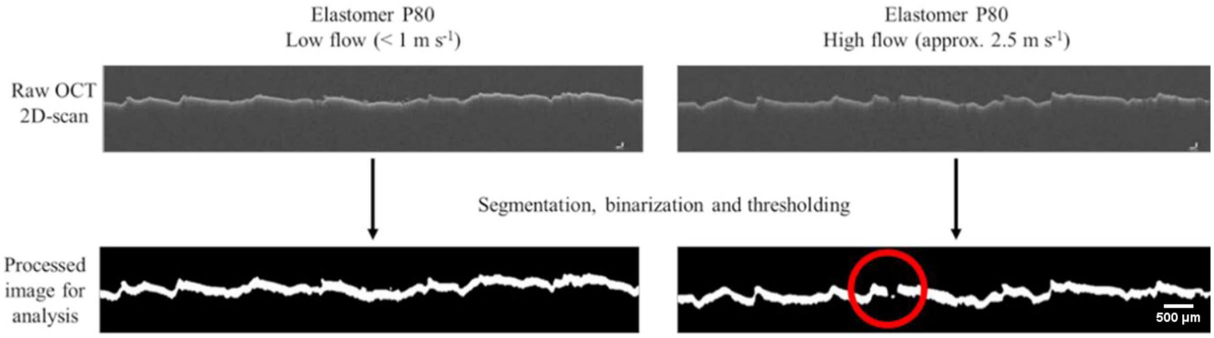

Figure 5-3. *Raw and processed OCT 2D-scans taken at different stages in the flow cycle. The scans for the elastomer P80 replicas are shown as an example. The processed images are post-application of the segmentation, binarization and thresholding methods which allows for analysis of shape. The red circle shows an example of gaps in the processed images which could skew shape data.*

5.2.5 Statistical analysis

R Studio (R Core Team, 2019) was used for statistical analysis. For all statistical outcomes a *P*-value of < 0.05 was deemed statistically significant.

To determine differences in the mechanical profiles of the filler and elastomeric material ANOVA and post-hoc Tukey tests (95 % confidence interval) were executed on the individual data sets (contact angles, tensile testing etc.). To confirm successful transfer of roughness from *sources* to *replicas,* and to determine any changes in the surface topography of *sources* and *replicas* under increasing flow, ANOVA and Post-hoc Tukey tests (95 % confidence interval) were performed. For the data that did not meet the assumptions for these tests, such as non-normal distribution (Shapiro-Wilk) and unequal variance (Levene's), the non-parametric Kruskal Wallis test was used.

To determine the contribution of roughness (smooth, P240, P80 and P40) and material (rigid, elastomeric) on C_f^* at different *Re*, two-way ANOVA and Post-hoc Tukey tests were executed. The sum of squares of one variable was divided by the total sum of squares of all variables (elasticity, roughness, and the interaction effect) and this was multiplied by 100 to give percentage contribution.

5.2.6 Uncertainty analysis

Uncertainty analysis was performed on C_f^* values calculated for the elastomer and filler *replicas*, sandpaper sources and smooth PVC. The uncertainty around C_f^* was calculated by combining the associated uncertainty of the individual measured variables and taking the root of the sum of the squares (Cimbala, 2013). It was expected that uncertainty would decrease with increasing *Re* (Lorenzini *et al.*, 2009; Schultz *et al.*, 2015; Hartenberger, 2019) and therefore analysis was performed at a *Re* of 2.2×10^4 and 4.0×10^4 (as seen in Table 4-1). The systemic and random uncertainties related to instrumental error were also calculated and are summarised in Table 4-2.

5.3 Results

5.3.1 Mechanical properties of synthetic materials

Two *replica* materials, a PDMS-based elastomer and epoxy filler, were mechanically characterised using an array of methods. The elastomeric material possessed a low elastic modulus and high strain to failure when compared to the epoxy filler (P-value < 0.05) (Table 5-1). The filler became torn and snapped when pulled lengthwise, as opposed to stretching as the elastomer did. This reflects the hardness of the epoxy filler which had a measured mean H_M of 21.08 ± 36.03 MPa compared to the elastomer which was 1.52 ± 0.28 MPa. Water contact angles were used to determine material wettability. The contact angle of the filler was in the range normally associated with hydrophilic behaviour (OCA $< 90°$) whereas the contact angle of the elastomer was on the border of the ranges normally associated with hydrophilic and hydrophobic behaviour (OCA $\sim 90°$) (Law, 2014) (Table 5-1). As expected, the mechanical properties determined for the two materials were significantly different (P-value < 0.01) (Table 5-1). As a result, the *replica* materials were classified as elastomeric or rigid, where the rigid group comprised epoxy filler *replicas* and both *sources* (smooth PVC and sandpapers) and the elastomeric group was composed of PDMS-based elastomer *replicas* (Table 5-1).

Table 5-1. *Summary of roughness and mechanical properties of the source and replica materials. The intermediate material is that which was used to create a replica of the source using a mould. A dash indicates that data was not collected, or it was not applicable.*

	S_a (FEPA standards)	***S_a pre-flow (µm)***	***E (MPa)***	***Ultimate tensile strain (%)***	***Tensile strength (MPa)***	***OCA (°)***	***H_M (MPa)***	***Group***	***Intermediate material***
Source									
PVC	Smooth	6.8 ± 0.9	~ 3500 [1]	-	-	-	-	Rigid	-
Sandpaper	P240	16.3 ± 1.7	~ 200,000 - 400,000	-	-	-	-	Rigid	-
Sandpaper	P80	48.9 ± 1.3							-
Sandpaper	P40	107.7 ± 3.5							
Replica									
Elastomer	Smooth	6.3 ± 1.2	1.54 ± 0.26	135.3 ± 23.3	1.04 ± 0.15	87.8 ± 15.1	1.52 ± 0.28	Elastomer	Urethane putty
	P240	16.0 ± 1.4							
	P80	44.9 ± 1.3							
	P40	93.7 ± 5.5							
Filler	Smooth	4.9 ± 1.7	63.23 ± 11.06	14.14 ± 2.2	2.91 ± 0.14	78.1 ± 12.8	21.07 ± 6.03	Rigid	Silicone moulding rubber
	P240	14.8 ± 2.0							
	P80	42.7 ± 2.3							
	P40	92.4 ± 6.6							

[1] value taken from Titow (1984) for rigid PVC

5.3.2 *Successful transfer of surface roughness from source to replica*

A homogenous surface roughness for the *replicas* was achieved using sandpaper of varying roughness grades. As desired, all sandpaper roughness grades used as *sources*: P40, P80 and P240 and the PVC panel, possessed significantly different S_a values (Table 5-1 and Figure 5-4).

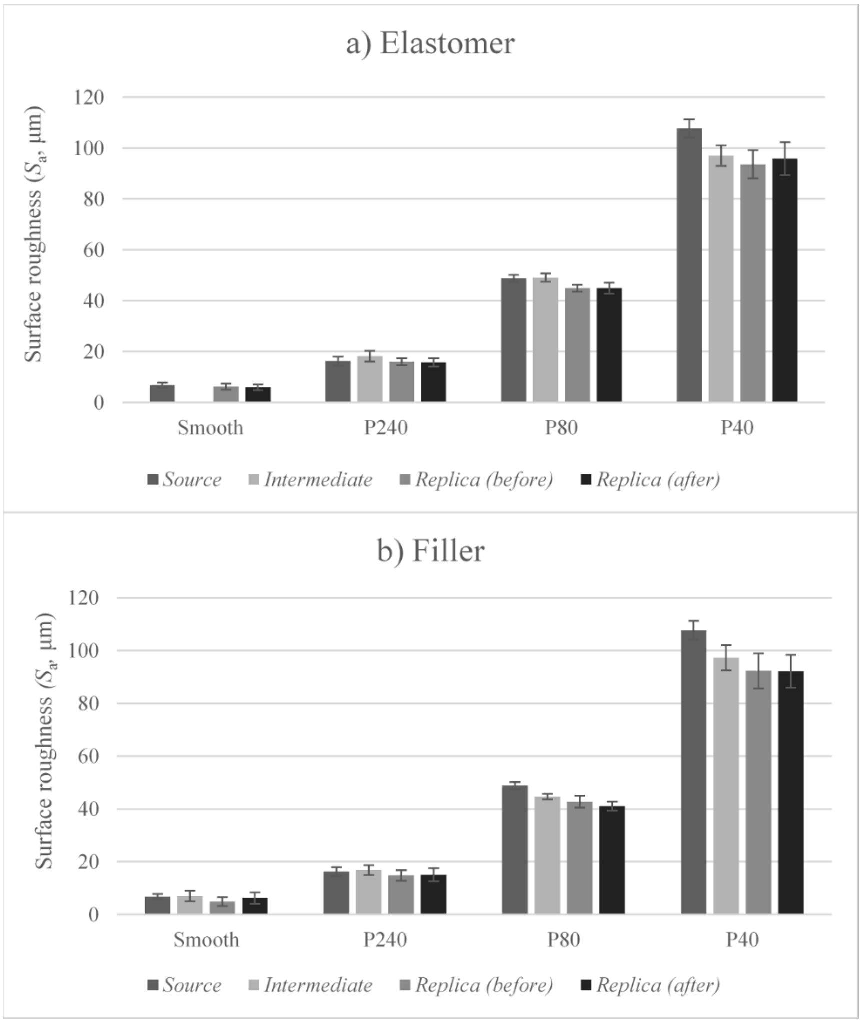

Figure 5-4. *Surface roughness (µm) measured using a blue-light interferometer for a) elastomer replicas and b) filler replicas before and after a flow cycle on the flow cell. The S_a of their counterpart sources and intermediates is also shown, for all roughness' investigated: smooth, P240, P80 and P40.*

Blue light interferometry was used to measure S_a at all stages during the casting and moulding process, see Figure 5-4. There was some evidence of a reduction in S_a during casting and moulding for some of the rougher *replicas*, for example filler-P40 and elastomer-P40 *replicas* displayed lower S_a than their *source* and *intermediate* counterparts (Figure A-1). Nevertheless, there were no statistically significant differences in S_a of the filler-P40 and elastomer-P40 *replicas* (Table 5-1). S_a was also measured before and after the *sources* and *replicas* were exposed to flow in the flow cell. Statistical analysis confirmed that for all test pieces (n = 2 to 4) there were no significant differences in surface roughness before and after flow had been applied (*P*-value > 0.05) (Figure 5-4).

5.3.3 Changes to surface topography of material replicas in response to applied flow

OCT 2D-scans were taken of the *sources* and *replicas* under increasing flow in the flow cell. Raw images were then processed to quantify topographical features at the mesoscale. Note that in some OCT images the boundary surface was lost (Figure 5-3) which influenced data output, therefore images with missing sections were excluded from statistical analysis. Also, although roughness was consistent across all *source* and *replica* replicates (*n* = 2 to 4), shape data produced significantly different numeric results between replicates. Therefore, to study changes in shape parameters with increasing flow velocity, averages could not be meaningfully taken, and individual structures in fields of view for each replicate were analysed separately.

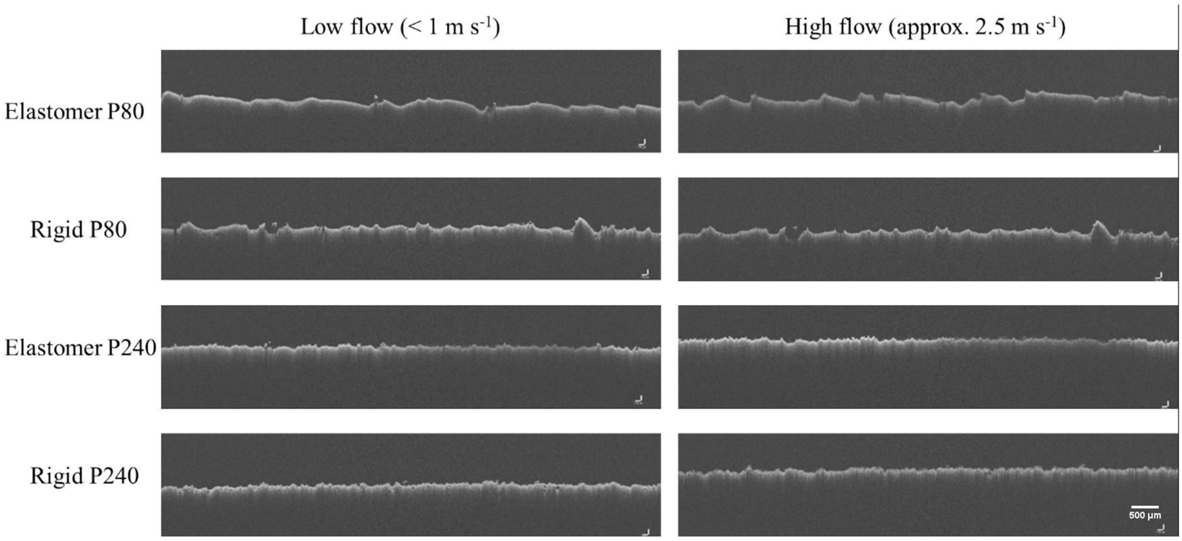

Figure 5-5. *Photographs of OCT 2D-scans taken at low and high flow during a flow cell cycle. The elastomer-P80, elastomer-P240, filler-P80 and filler-P240 have been used as examples to show changes in the surface topography. The scale bar represents 500 µm.*

Image analysis revealed that despite roughness profiles being substantially similar between elastomeric and filler *replicas* of the same roughness category (Table 5-1), the surface shape was significantly different (*P*-value < 0.05), especially at higher roughness grades (P40 and P80) (Figure 5-5). The elastomer *replicas* appeared wave-like whereas the filler *replicas* more closely resembled a sandpaper surface (Figure 5-5). Similarities between the sandpaper *sources* and filler *replicas* were enhanced when assessing structural changes consequent to changing flow velocity as both datasets exhibited a linear relationship between elongation and flow velocity. In contrast, the elastomer *replicas* showed fluctuations in elongation values with increasing flow velocity as the surface appeared roughened and surface peaks moved (Figure 5-6).

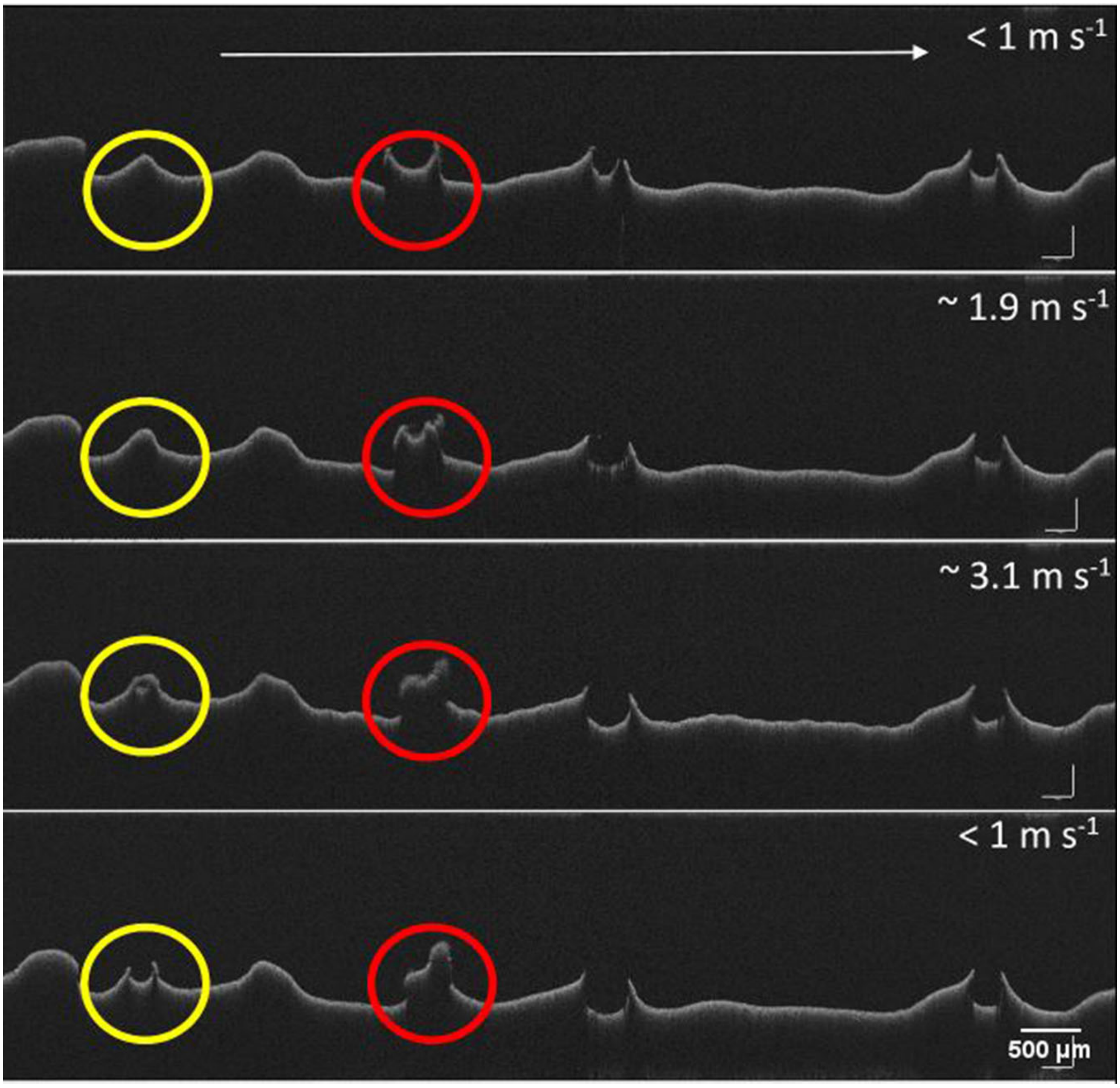

Figure 5-6. *OCT 2D-scans taken at different flow velocities during a flow cell cycle. An elastomer-P40 replicate (n = 2) has been used to show a change in surface topographical features at different stages. A flow velocity of < 1m* s^{-1} *indicates the start and end of the flow cell cycle. Maximum elongation was determined at ~ 1.9 m* s^{-1} *(~ Re = 3.0 x* 10^4*) and the maximum flow velocity reached was 3.1 m* s^{-1} *(~ Re = 5.2 x* 10^4*). Changes of two prominent features are circled (red and yellow rings) at each flow stage. The scale bar represents 500 µm.*

Interestingly, the elastomer-P40 *replicas* showed signs of permanent deformation, as illustrated by 2D-scans taken of the elastomer-P40 after cessation of flow (Figure 5-6). A relaxation period was not included during the experiments, yet it does not seem likely from the example depicted in Figure 5-6 that there would be full recovery of the initial structure. From the elongation data collected during the loading and unloading cycle there is evidence of some elastic rebound which is indicative of a viscoelastic response to applied flow. However, further experimentation would be required to confirm these observations.

5.3.4 *Drag induced by sources and replicas in an asymmetric flow cell system*

5.3.4.1 Elasticity

Loading cycle data were obtained for all the elastomeric and rigid test pieces (smooth, P240, P80 and P40, see Table 5-1 and Figure 5-7). The ΔP measurements were expressed as C_f and were plotted against *Re* (Figure 5-7).

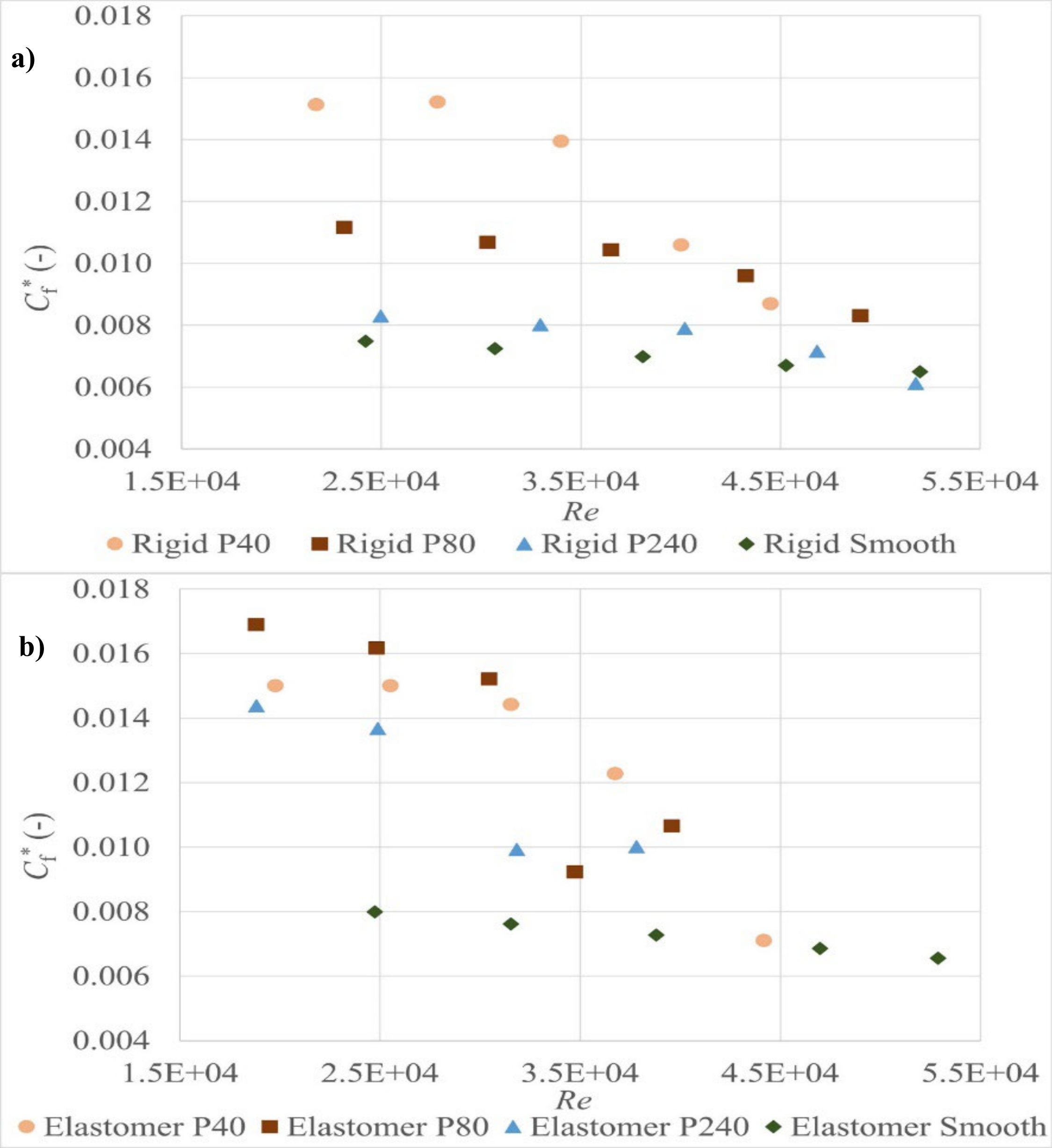

Figure 5-7. *C_f^* plotted against Re for all sources and replicas tested in the flow cell (n = 2 to 4); a) shows data for the elastomeric replicas and b) is the rigid dataset; where circles represent the P40 data, squares are P80, triangles are P240, and a dash is for the smooth data. Only loading data is plotted in both figures. Re and C_f^* were calculated for every step in the flow cell loading cycle (Figure 4-2) using Equations 3-5 and 3-8.*

For most test pieces the general shape of the drag curves was broadly similar; with increasing *Re* there was a slowing decrease in C_f^* (Figure 5-7). However, under closer inspection of the data points in Figure 5-7, filler-P40, elastomer-P40, -P80 and -P240 data demonstrate longer *Re* dependence where at a *Re* of approximately 3.0×10^4, C_f^* experiences a marked decrease. It is known from profilometry (Figure 5-4) and OCT-scans (Figure 5-5) that S_a was not affected by flow and therefore this dependence was linked to a mechanical response to increasing shear stress, which is not demonstrated by the rigid test pieces.

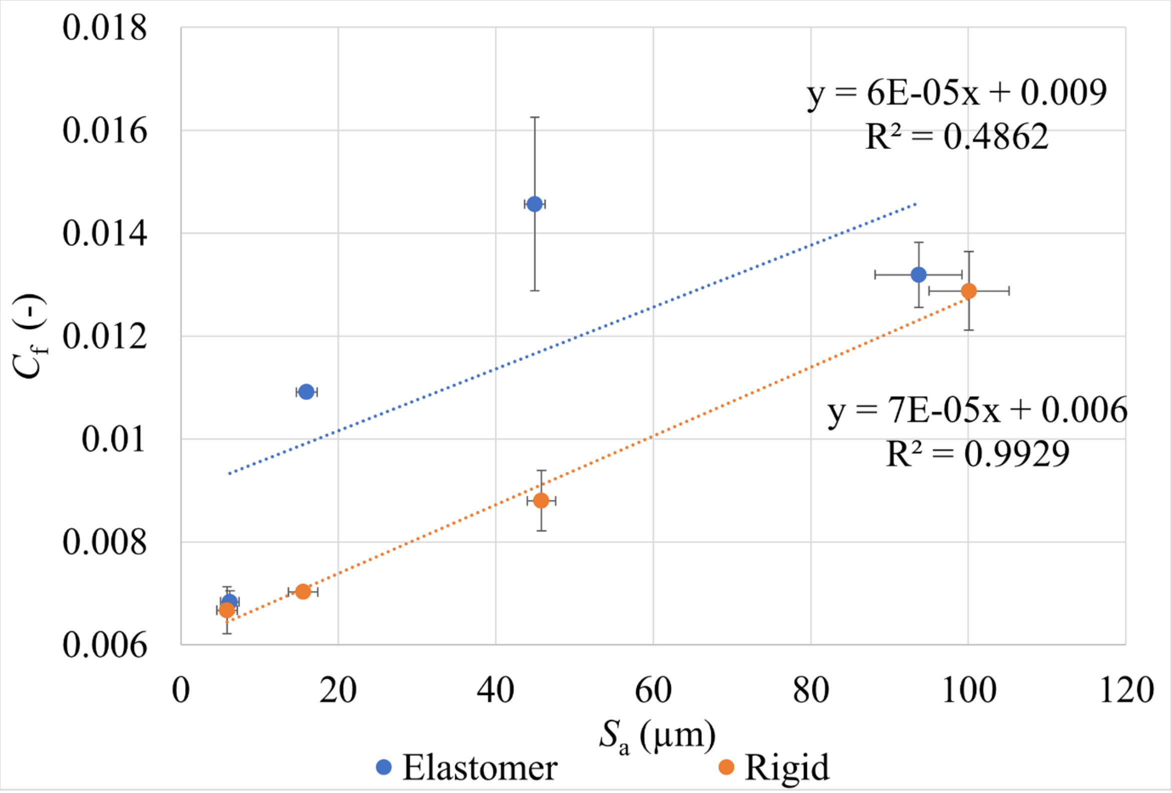

Figure 5-8. *Average S_a (µm) ± SD plotted against average $C_{f,\,I}$ (-) ± SD (n = 2 to 4) for the elastomeric and rigid material categories, where rigid includes the filler replica data and source data. Data for four roughness' are shown: smooth, P240, P80 and P40 (as per FEPA standards). A linear line of best fit has been applied.*

More specifically, $C_{f,\,I}$ was calculated for all replicas and sources ran on the flow cell using the slope of the line when ΔP was plotted against u^2 using Equation 3-8. This was possible as the relationship between ΔP and u^2 was linear for all flow cell runs. The elastomer-P80 and -P240 led to a 52 % and 48 % increase in $C_{f,\,I}$ when compared to the rigid counterparts of substantially similar roughness (Figure 5-8). Despite a significant increase in roughness elastomer-P40 displayed a drop in $C_{f,\,I}$ when compared to elastomer-P80 and was only 2 % higher than rigid-P40 (Figure 5-8). Also, elastomer-smooth, and rigid-smooth replicas demonstrated little to no *Re* dependence (Figure 5-7) and possessed only a 6 % difference in $C_{f,\,I}$ (*P*-value > 0.05) (Figure 5-8).

5.3.4.2 Roughness

The drag data calculated for the elastomeric *replicas* was significantly higher than that of the rigid counterparts up to a roughness of approximately 45 µm (P80 data) (Figures 5-7 and 5-8), and both data sets exhibited a positive relationship between S_a and $C_{f,\,I}$ (Figure 5-8). The $C_{f,\,I}$ calculated for the rigid-P240, -P80 and -P40 test pieces were 14 %, 59 % and 100 % higher than the rigid-smooth *replicas* and for the elastomeric data set these values were 60 %, 127 % and 93 %, respectively. It is important to note that although there was a strong linear relationship between average S_a and $C_{f,\,I}$ for the rigid data set ($R^2 = 0.99$), it was poor for the elastomeric data set, due to the P40 *replica* drag data ($R^2 = 0.49$) (Figure 5-8).

The non-linearity between S_a and $C_{f,\,I}$ of the elastomer *replicas* suggests that the elastic material properties enhanced the effects of roughness (Figure 5-8), as elastomer *replicas* showed comparable drag values to filler *replicas* in the next roughness category: elastomer-P240 and -P80 displayed behaviour comparable to filler-P80 and -P40 (Figures 5-7 and 5-8). It was concluded that material properties and surface roughness influenced drag, taken as a single C_f^* value, both independently (P-value < 0.01) and combined (P-value < 0.01). This conclusion was supported using interaction plots produced in R studio (P-value < 0.001). Importantly, the parameter of shape was not introduced into the ANOVA as it showed co-linearity with the roughness values.

5.3.4.3 Contribution of elasticity and roughness to drag

To assess the contribution of material properties and roughness on C_f^* with increasing Re, C_f^* was calculated for specified Re and two-way ANOVAs were carried out. For all Re investigated (covering the Re range of about to 2.0×10^4 to 5.2×10^4), roughness, material-type, and an interaction between the two factors was significant in effecting average C_f^* (P-value < 0.01). Table 5-2 shows how the effect of both roughness and material evolved with increasing Re (measured as percentage contributions) at specified Re, for example the roughness contribution appears to increase and plateau, and the material contribution fluctuates.

Table 5-2. *The contribution of material, roughness, and the interaction of the two on* C_f^* *calculated at three different Re using the power lines of best fit from Figure 5-7. All values are presented as percentages (%).*

	Re = 2.2 × 10⁴	***Re = 3.0 × 10⁴***	***Re = 4.0 × 10⁴***
Material	18.5	12.6	18.6
Roughness	55.9	76.7	75.6
Interaction	25.6	10.7	5.8

5.3.4.4 Uncertainty analysis of C_f^*

Uncertainty analysis was performed on the average C_f^* values taken at $Re = 2.2 \times 10^4$ and 4.0×10^4 for all material *replicas* and *sources* using methods proposed by Cimbala (2013). Using Equation 4-1, the overall uncertainty bounds for the elastomeric *replicas* ranged from ± 22 % at 2.2×10^4 *Re* and ± 15 % at 4.0×10^4 *Re*. For the filler *replicas* the uncertainty values were ± 28 % and 25 % and for the *source* data (sandpaper and smooth PVC) uncertainty was ± 33 % and 28 %. The uncertainty bounds reported here are higher than those reported by Hartenberger (2019) which could be a consequence of the asymmetric boundaries and small aspect ratio of the channel. For further details on the uncertainty error around C_f^* taken at different *Re* see Table 4-1 and for elemental uncertainty see Table 4-2.

5.4 Discussion

5.4.1 The mechanical characterisation and visualisation of the elastomer and filler material

As intended, the PDMS-based elastomer and epoxy filler displayed significantly different mechanical properties (Table 5-1) and from these results it is suggested that the elastomer would be better suited to modelling biofilm behaviour than rigid structures. For example, the elastomer demonstrated a high tensile strain, within the range of between 150 % and 320 % recorded for natural biofilms (Ohashi *et al.*, 1999), and possessed a lower elastic modulus than the rigid counterparts (Table 5-1). In addition, whilst the filler demonstrated hydrophilic behaviour (OCA <

90°) (Table 5-1), the contact angles for the elastomer sat either side of the 90° threshold, which is comparable to the wetting behaviour observed for natural biofilms (Werb *et al.*, 2017).

Biofilms are known to exhibit different degrees of elasticity, ranging from Pa to kPa (Table 3-1). To date, rheological data does not exist for ship-relevant marine biofilms. Souza-Egipsy et al., (2021) however, compared mechanical properties for eukaryotic and prokaryotic biofilms obtained from an acidic stream, and found that the elastic modulus for the eukaryotic biofilms was significantly lower than the prokaryotic biofilms. Marine biofilms incorporate eukaryotic organisms and therefore it is possible that they would possess a different elastic modulus to what has been reported in the literature for biofilms found in other environments, for example medical and wastewater treatment (Table 3-1). It is of interest to mechanically characterise marine biofilms to inform future design of materials that could be used in the proposed synthetic replica system for modelling biofilm physico-mechanical responses to applied flow.

5.4.2 Drag induced by rough elastomeric sandpaper replicas

Typically, computational and experimental studies have utilised rigid, rough surfaces such as sandpaper or sand-grains for studying drag, namely biofilm-associated drag (Yusim and Utama, 2017). In part, this is explicable by work that has shown parallels between drag induced by rigid structures and biofilms (Flack, Schultz and Connelly, 2007; Hartenberger *et al.*, 2020).

Flow cells are widely used to study impacts of surface roughness on skin friction and drag. A symmetric flow cell set up is often implemented, where the top and base plate are of equivalent surface roughness. However, in this study, C_f^* was calculated in an asymmetric flow cell, where the smooth top plate acted as a window into the flow cell and the base plate was rough; this was necessary to allow real-time visualisation and *in-situ* measurements of surface deformation. The side walls were also smooth since it was impractical to line these with *source* or *replica* materials due to the narrow dimensions. The compromise of having an optically clear window wall to allow observation has been recognised in other studies (Blauert, 2017; Picioreanu *et al.*, 2018) and has been corrected for using techniques such as PIV (Hartenberger *et al.*, 2020). It is acknowledged that the C_f^* calculated in the present study for the rough surfaces will likely be underestimations of the values obtained in a flow cell where roughness is equivalent on all walls. Nevertheless, despite this limitation we believe C_f^* is a useful metric for comparing relative effect of drag by the different materials, at least over the *Re* range of 2.0×10^4 to 5.2×10^4 studied here.

It would be of interest to determine a relationship between C_f^* for a symmetric and asymmetric flow cell system using the elastic and rigid materials (Figure 4-3) with the purpose of calculating roughness-functions and predicting drag at a ship-relevant scale.

5.4.2.1 Surface Roughness and Drag

It is well known that a surface with higher roughness will induce greater drag due to increased friction; this has been observed at laboratory and ship scale (McEntee, 1916; Moody, 1944; Townsin, 2003; Oliveira, Larsson and Granhag, 2018). As expected, this trend was observed for the elastomeric and rigid datasets collected here (Figures 5-7 and 5-8). The calculated drag for elastomer-smooth, rigid-smooth and the PVC-smooth was broadly consistent (P-value > 0.05) (Figures 5-7 and 5-8), showing little to no impact from the different mechanical properties.

For the rigid and elastic data sets, once roughness was introduced there was a jump in the C_f^* values (Figures 5-7 and 5-8). This increase was different depending on the material. As is characteristic for a rigid structure the rigid data set displayed a strong positive linear relationship between S_a and $C_{f,\,I}$ (Figure 5-8) (Fabbri *et al.*, 2019). The elastomer *replica* $C_{f,\,I}$ data, however, demonstrated a non-linear relationship with increasing S_a which was partly explicable by the 15 % decrease in $C_{f,\,I}$ between elastomer-P80 and -P40 (Figure 5-8). As roughness was controlled, the deviation was attributed to mechanical properties, namely elasticity and the response of topographical features under flow (Figure 5-6). This conclusion is supported by ANOVA which indicated a significant relationship between static roughness (before and after flow) and material type on C_f^* at specified *Re* (P-value < 0.001). Hartenberger et al., (2020) similarly interpreted their experimental comparisons between living biofilms and their rigid replicas where they concluded that differences in drag were driven by compliance, namely mat vibrations, and streamer flutter.

The differences observed between the elastomeric and rigid data sets highlight how rigid structures are limited for studying drag associated with softer materials. For example, if the line of best fit for the rigid dataset had been utilised to predict drag for the elastomeric system (Figure 5-8), then $C_{f,\,I}$ would have been significantly underestimated. Further, Fabbri *et al.*(2019) found a linear relationship between rigid roughness and drag, yet if this had been used to extrapolate drag associated with an elastomeric surface, the resultant drag values would have also been underestimated. The results presented over our *Re* range of 2.0×10^4 to 5.2×10^4 demonstrate how not only roughness but physico-mechanical properties must be considered when predicting drag (Jafari *et al.*, 2018; Picioreanu *et al.*, 2018); and that physico-mechanical properties could have a larger impact on C_f than initially expected.

5.4.2.2 Elasticity and Drag

Viscoelastic structures such as biofilms will induce a greater pressure drop, and therefore drag, than rigid structures such as sandpaper or sand grains, as a consequence of their physico-mechanical properties (Hansen and Hunston, 1974; Peterson et al., 2015). An early study by Picologlou, Zelver and Characklis (1980) experimented with biofilms and turbulent pipes and concluded that when the viscoelasticity of biofilms was considered, as opposed to assuming rigidity (in the form of sand grains), the resultant frictional resistance was higher. More recently, Hartenberger et al., (2020) reached a similar conclusion when comparing natural biofilms to 3D-printed rigid replicas; biofilms displayed a significantly higher drag than their rigid replicas and displayed a different trend in drag with increasing *Re.* This implies the behaviour of a biofilm under increasing flow velocity cannot be fully captured by rigid replicas even if equivalent surface topography is achieved. Similarly, Yeginbayeva *et al.,* (2020) studied the combined effect of mimicked 'hull' roughness and biofilms and found biofilm presence to be significant in affecting drag. The data presented in the current study supports these conclusions as differences in drag curves were observed between the elastomeric and rigid *replicas* (Figure 5-7).

Perkins *et al.,* (2012) studied biofouled hydropower pipes and determined that with increasing *Re,* C_f either increased or plateaued until a critical *Re* was reached. After this critical point, C_f experienced a sudden drop with increasing *Re* that eventually levelled out again (Lambert *et al.*, 2009; Perkins *et al.*, 2012). The authors reasoning for this behaviour was that the biofilm had been sheared, had detached from the surface or was being flattened against the pipe wall. Interestingly, a similar drag curve to those presented for biofouled pipes by Perkins *et al.,* (2012) was observed for the homogenous, rough elastomer *replicas*, where up to a *Re* of 3.0×10^4 the elastomeric drag curves were plateaued and past this *Re* the value of C_f^* experienced a sudden decline. This decline is assumed to be due to a physico-mechanical response, such as streamlining or flattening out, as unlike real biofilms, detachment was not possible, and roughness remained unchanged before and after the surfaces were subject to flow (Figure 5-4). This is supported by results of a two-way ANOVA that showed distinct changes to the contributions of roughness and material-type to C_f^* at a *Re* of 3.0×10^4. Also, the elastomeric drag curves did not level out at higher *Re* (Figure 5-7), therefore future flow cell runs could be set up to operate at greater *Re* which would perhaps identify a *Re* at which the elastomer *replicas* responses plateau and show no *Re* dependence. It is worth noting that in Perkins *et al.*, (2012) shearing and flattening behaviour was not physically observed during flow and therefore it is important to consider that the trend between C_f^* and *Re* observed for the elastomeric data, which was attributed to compliance, could explain what has been observed in the heterogeneous biofilm study.

The conclusion that differences in C_f^* induced by the elastomeric and filler *replicas* was consequence to different mechanical profiles and therefore physico-mechanical responses to flow is supported by analysis of the OCT images. The filler and elastomeric *replicas* experienced different responses to increasing flow velocity as shown by changes to their surface topography (Figure 5-5). When tested on the flow cell, the elastomeric *replicas* did not deform to the same degree as natural biofilms, which are generally softer and more elastic (Table 3-1) and removal was not observed, yet there was evidence of a viscoelastic response to increasing flow velocity (Figure 5-6). It would be beneficial to use an OCT to measure deformation quantitively using angles of deformation, as did Blauert (2017), or alternative image analysis methods, such as Digital Image Correlation (DIC) (Mathias and Stoodley, 2009). DIC could provide information on 2D and 3D-interactions between a compliant surface and surrounding fluid which would inevitably alter C_f. Nevertheless, the results presented in the current study demonstrate how fluid structure interactions vary depending on material mechanical properties (Figure 5-5) and can evolve with increasing flow velocity (Figure 5-6 and Table 5-2).

This study is the initial basis for addressing questions such as: what happens to a biofilm surface under flow, and how do the physical and mechanical properties respond? A successful quick and easy moulding and casting process has been detailed for generating material replicas and would be suited to experimental up-scaling. It is acknowledged that the synthetic model is in its primary stages, but by controlling roughness and mechanical properties of different materials it is easier to separate out the relative contribution of these properties on drag than if a heterogeneous surface had been incorporated, or one that allowed sloughing and detachment. Despite this, future work should add structural and mechanical complexity to better mimic real biofilms. Also, future studies should look to compare the data obtained from the meso-scale flow cell to that collected for a larger flow cell (with a suitable entry length to guarantee fully developed flow), to validate its use.

5.5 Conclusion

Surface roughness and physico-mechanical properties influence drag. What is unknown is how they interact with each other, and how this relationship influences drag. A method for generating a fully synthetic model system for studying the effects of physico-mechanical properties on drag has been presented. Sandpaper of varying roughness grades was chosen as the template for moulding, as it is a readily available rigid roughened surface with homogenous coverage and controlled roughness characteristics.

Although biofilms have not been investigated here, the *replica* data produced supports the hypothesis that elastomeric surfaces are better substitutes than rigid structures for modelling elastic or viscoelastic responses to drag. This was captured by a pressure drop system and OCT 2D-scans, where the movement of topographical features was detected under flow. The combination of studying mesoscopic structural parameters (such as elongation) extracted from OCT 2D-scans, and the mechanics of elastomeric materials allows us to represent natural biofilm physico-mechanics more closely, within a dynamic environment (a flow cell).

The rigid data showed significantly lower C_f^* values than the elastomeric counterparts (Figure 5-8) and would have been ineffective in predicting C_f^* associated with the elastomeric *replicas*. As the elastic modulus of the materials was significantly different (P-value < 0.001) (Table 5-1), while S_a was the same (Figure 5-4 and Table 5-1), it was concluded that the elasticity played a significant role in influencing the drag (Figures 5-7 and 5-8), as it may be expected to do in natural biofilms (Rupp, Fux and Stoodley, 2005; Hartenberger, 2019). This was confirmed by statistical analysis that deemed roughness and elasticity (independently and combined) were both significant in affecting C_f^*.

Our results showed that elasticity is significant in influencing drag and shares a significant interaction with surface roughness and thus material properties should not be neglected in predicting drag caused by viscoelastic biofilms or in model systems. This knowledge serves as a basis for future study into the effect of physico-mechanical properties of compliant materials on drag, it should be used to inform future models and is relevant to the coating industry with respect to targeting specified biofilm properties for reducing biofilm presence on ship hulls.

6 Chapter 6: Surface properties influence marine biofilm rheology, with implications for ship drag

ABSTRACT

Marine biofilms on ship hulls increase frictional drag, which has economic and environmental consequences. It is hypothesised that biofilm mechanics, such as viscoelasticity, play a critical role in biofilm-associated drag, yet is a poorly studied area. The current study aimed to rheologically characterise ship-relevant marine biofilms. To combat marine biofilms on ship hulls, fouling-control coatings are often applied; therefore, the effect of different surfaces on marine biofilm mechanics was also investigated. Three surfaces were tested: a non-biocidal, chemically inert foul-release coating (FRC), an inert anti-corrosive primer (ACP) and inert PVC. Physical properties of biofilms were explored using OCT and a parallel-plate rheometer was used for rheological testing. Image analysis revealed differences in the thickness, roughness, and percent coverage between the different biofilms. Rheological testing showed that marine biofilms, grown on FRC and ACP acted as viscoelastic materials, although there were differences. FRC biofilms had a lower shear modulus, a higher viscosity, and a higher yield stress than the ACP biofilms, suggesting that the FRC biofilms were more readily deformable but potentially more robust. The results confirmed that surface treatment influences the structural and mechanical properties of ship-relevant marine biofilms, which could have implications for drag. A better understanding of how different surface treatments affect marine biofilm rheology is required to improve our knowledge on biofilm fluid-structure interactions and to better inform the coating industry of strategies to control biofilm formation and reduce drag.

6.1 Introduction

Marine biofilms are multi-cellular communities composed of micro-algal and bacterial components encased within a protective and hydrated matrix. The matrix is mainly comprised of extracellular polymeric substances that the organisms exude, which aids in attachment of a biofilm to a surface (Zargiel, Coogan and Swain, 2011; Zargiel and Swain, 2014). The EPS can be considered as a crosslinked polymer gel (Kavanagh and Ross-Murphy, 1998; Wilking *et al.*, 2011; Mazza, 2016), and is arranged with a system of pores and channels that contribute to the elastic and viscous behaviour of a biofilm (Lembre, Lorentz and Di, 2012; Quan *et al.*, 2022). Biofilms are viscoelastic entities, which exhibit a time dependent response when exposed to mechanical stress or strain that demonstrates both elastic and viscous elements. This behaviour has been reported as partly responsible for the recalcitrance of biofilms to external challenges, such as mechanical, chemical and medical (Peterson *et al.*, 2015; Charlton *et al.*, 2019), since although biofilms are typically soft and deformable materials, they can dissipate imposed stresses through viscoelastic responses (Grillet, Wyatt and Gloe, 2012; Sun *et al.*, 2013; Souza-Egipsy *et al.*, 2021). For example, biofilms have been shown to ‘flow’ in the form of ripple-structures when exposed to increased shear enabling parts of the biofilm to resist detachment from a surface (Stoodley, Boyle and Lappin-scott, 2000; Rupp, Fux and Stoodley, 2005) demonstrating that the viscoelastic nature of a biofilm has a role to play in biofilm survival (Peterson *et al.*, 2015; Gloag *et al.*, 2021).

Marine biofilms induce significant economic and environmental consequences within the shipping industry (Townsin, 2003) and can induce a 1 - 18 % penalty in ship shaft power (Haslbeck and Bohlander, 1992; Schultz *et al.*, 2011). It is widely accepted that biofilms increase surface roughness of a ship hull which consequently increases biofilm-associated drag (Moody, 1944; Andrewartha and Sargison, 2011). Yet, it has also been hypothesised that biofilm viscoelasticity increases drag too by dissipating energy through viscoelastic motion as well as disrupting the laminar boundary layer by means such as streamer oscillation (Stoodley *et al.*, 1998; Hartenberger *et al.*, 2020). A deeper understanding of how marine biofilm physico-mechanical properties interact with one another and how these complex systems respond to external forces is required. To do this an important step is to characterize and quantify the elasticity and viscosity of marine biofilms.

The elasticity of medical and dental biofilms is reasonably well documented, ranging between a few Pa and several kPa (Kim, Kwon and Kim, 2017; Tallawi, Opitz and Lieleg, 2017). In part, the large range is understandable given biofilm heterogeneity which makes it difficult to apply standard test methods (Böl *et al.*, 2013). It could be expected that marine biofilms would have a similar elasticity range, although it is important to note that the biological composition of a marine biofilm can differ considerably from medical or wastewater biofilms. Marine biofilms incorporate not only bacteria, but diatoms and microalgae, which add to their structural and EPS chemical complexity. Winston *et al.*, (2003) studied pond water biofilms with a micro-algal presence and found that they possessed a significantly lower shear modulus than that for bacterial biofilms. More recently, Souza-Egipsy *et al.*, (2021) studied prokaryotic and eukaryotic biofilms in an acidic stream and found significant differences between the structural and mechanical properties.

To combat biofilm formation and macrofouling on ship hulls fouling-control coatings are often applied. Traditionally, fouling-control coatings have routinely employed toxic biocides, which deter the settlement and growth of biofouling organisms (Finnie and Williams, 2010). Although often highly effective, such biocidal coatings release biocides and concerns about the potential harmful impact on the aquatic environment mean that the use of this type of coating is increasingly regulated on a national and international basis (Galvão De Campos *et al.*, 2022). Therefore, the industry is moving towards non-biocidal alternatives, such as foul-release coatings (Finnie and Williams, 2010). In simple terms, FRCs act as ‘non-stick’ elastomeric surfaces due to a low surface energy which makes it challenging for marine fouling organisms (such as diatoms) to bond to a surface and are substantially chemically inert (Atlar *et al.*, 2003; Candries, Atlar and Anderson, 2003). Importantly, due to differences in the chemical composition, wettability, and surface roughness of different coatings different biological communities thrive on different coated surfaces (Salta *et al.*, 2013; Zargiel and Swain, 2014; Papadatou *et al.*, 2021). In turn, a different microbial community could constitute a change in structural (Donlan, 2002; Schiebel *et al.*, 2020) and mechanical properties due to changes in EPS composition, concentration of bacterial cells and cohesiveness etc. (Souza-Egipsy *et al.*, 2021), which would consequently impact drag (Hunsucker *et al.*, 2018). Therefore, to better understand how surface coatings alter the mechanical properties of a biofilm, rheological characterisation of marine biofilms grown on different surfaces was investigated.

The aims of the present study were, firstly, to determine the structural and mechanical properties of marine biofilms, using OCT and a rotational parallel-plate rheometer. A rotational rheometer is perhaps the most cited equipment used for rheological characterisation of biofilms (Gordon *et al.*, 2017) as it can capture complex viscoelastic behaviour (Charlton *et al.*, 2019; Gloag *et al.*, 2020; Jana *et al.*, 2020). Modern rheometers allow both dynamic measurements in shear as well as axial indentation. Also, a rheometer offers high throughput experiments due to small test pieces and ease of application (Boudarel *et al.*, 2018). Furthermore, OCT is a non-invasive method for visualising biofilms at the meso-scale and was employed to characterise the structural properties of the biofilms before and after rheological testing. The second aim was to compare the structural and mechanical profiles of biofilms grown on different surfaces.

6.2 Methodology

6.2.1 *Coupons and surface treatments*

Circular PVC coupons with a 40 mm diameter and 1 mm thickness (Chemical Process Solutions Ltd.) were abraded with P80-grade sandpaper to promote the adhesion of paint to the coupon surface.

The paints used were commercial coatings provided by AkzoNobel:

- Intershield® 300 (ACP, *n* = 10) – a grey universal primer with long-term anti-corrosive properties and no anti-fouling properties (ACP).
- Intersleek® 1100SR (FRC, *n* = 10) – a grey non-biocidal, advanced fluoropolymer foul-release coating

The paints were prepared according to manufacturer instructions (AkzoNobel) and a synthetic paint brush was used to ensure a smooth coated surface, as confirmed using blue light interferometry (Figure B-1). The ACP coupons were single coated whereas the FRC coupons followed a scheme of first an anticorrosive primer (ACP), then silicone tie-coat and finally the FRC top-coat was applied. Inert grey PVC coupons (PVC, *n* = 10) that had been abraded with P80-grade paper were used as a control surface for the rheometer experiments. It was important to keep surface colour consistent across all coupons to eliminate the potential impact of colour on the rheological properties of biofilms (Dobretsov, Abed and Voolstra, 2013; Gambino *et al.*, 2018) (Figure 6-1). For each surface type, ten coupons were prepared for fouling (total = 30 coupons).

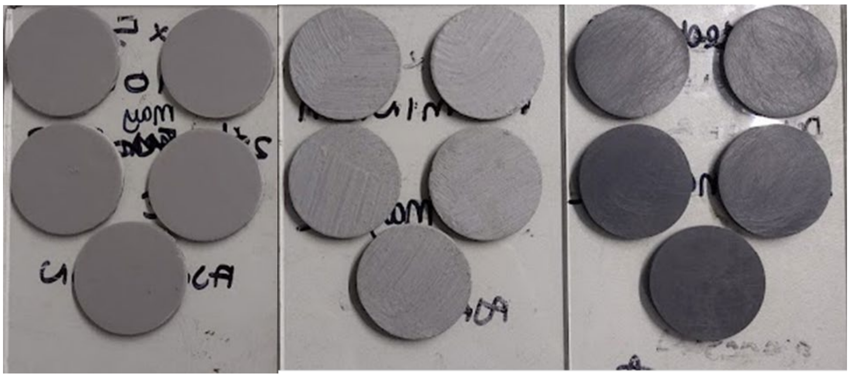

Figure 6-1. *Coupons (40 mm dia.) were attached to a glass plate before being immersed in a natural seawater tank at the Dove Laboratory (Cullercoats Bay, UK). From left to right there are FRC coupons, ACP, and uncoated, sanded PVC coupons (control).*

6.2.2 *Exposure to marine fouling*

The coupons were attached to 15 cm × 10 cm glass plates (Figure 6-1) and were immersed in a shallow indoor recirculating tank of natural seawater at Newcastle University's Dove Marine Laboratory (Cullercoats Bay, UK) under static conditions, so that no downstream effects of one coupon position influencing another was expected. Each glass plate held five identical coupons (Figure 6-1). The glass plates were immersed horizontally (in random positions) at the same depth in the tank to avoid differences in the biofilms driven by light availability. The seawater was filtered of larger particles and marine organisms and was lit naturally by a skylight window situated above the tank. The coupons were deployed on 24th February 2022 and were removed on 19th April 2022. Over this period, the seawater temperature was 7 to 10 °C. The coupons were removed carefully from the tank to avoid disruption to the biofilm structure and were transported to AkzoNobel (Gateshead, UK) for testing on a rheometer. Biofilms were kept hydrated during transportation by misting them with water taken from the Dove Laboratory tank.

Although marine biofilms in a real-world scenario are typically exposed to flow conditions, those tested here were cultivated under static conditions. This enabled the focus of the study to be on assessing the relationship between structural and mechanical properties of marine biofilms. Further, marine ships experience idle periods and are typically more vulnerable to biofilms and other fouling organisms during this time (Davidson *et al.*, 2020); as biofilms are typically the first colonisers of a ship hull it would be useful to rheologically characterise them under both static and dynamic conditions.

6.2.3 Structural characterisation of biofilms using OCT

Before rheological testing the coupons covered with biofilm were characterised using OCT (Ganymede, ThorLabs). An OCT is a non-invasive, high throughput method for visualising and quantifying biofilm properties in-situ at the meso-scale (Wagner and Horn, 2017). For additional information on OCT design please refer to Section 4.2.

In the present study, each coupon was immersed in a shallow dish filled with seawater taken from the tank at the Dove Laboratory and was then placed under the OCT. Three B-scans measuring 9.0 mm × 2.1 mm (*xz*) with an acquisition time of 0.14 seconds were taken of each coupon. In addition, a single C-scan measuring 9.0 mm × 9.0 mm × 2.1 mm (*x, y, z*) with an acquisition time of 36.5 seconds was taken of each coupon. The A-scan averaging was set to three to remove noise from the images and the OCT scan rate was 30 kHz. ThorLabs software, version 5.8.3 (Ganymede, ThorLabs), was used to control the OCT light, focus and imaging.

To quantify biofilm structural properties the C-scans were exported as .oct files from ThorLabs into MATLAB (version 2021b) and were processed using custom MATLAB scripts produced by Fabbri *et al.*, (2018). OCT analysis was conducted before and after rheological testing to assess the effect of stress on the structural characteristics of the biofilms. This also allowed a comparison between biofilms grown on different surfaces that had been exposed to comparative rheological testing procedures.

For all coupons covered with biofilms, mean biofilm thickness (mm), percent coverage (%) and R_a^* were calculated (Blauert, Horn and Wagner, 2015; Fabbri *et al.*, 2018). For more details on calculations please refer to Section 4.2.1.

6.2.4 Rheometer

A HR10 rheometer was used to rheologically characterise the marine biofilms. A parallel-plate set-up was adopted with a 40 mm stainless-steel sandblasted top-plate to create roughness for grip and to avoid slippage. All measurements were performed at 10 ºC using a Peltier-plate heat exchanger (Figure 6-2). It was important to test the biofilms at the temperature they had been cultivated to avoid thermal shock. The biofilms were kept hydrated during testing by immersing them in a well filled with 4 mL of the seawater taken from the tank they were cultivated in.

Biofilms typically exhibit structural heterogeneity which could be expected to cause variability in rheometer measurements. Hence, we report the values for the whole biofilms (cells, EPS, trapped debris and water channels within the structure). In the open literature it has been suggested that controlling the gap thickness between the parallel plates using a constant normal force as opposed to biofilm thickness ensures sufficient contact between the biofilm and the rheometer top-plate, regardless of original heterogeneity, as evidenced by non-slippage using this strategy (Towler *et al.*, 2003). In this study, biofilms were compressed to a normal force of 0.1 N before testing. For each rheometer experiment three biological replicates were prepared. As rheometer tests can disrupt the mechanical integrity of a biofilm each replicate was tested once.

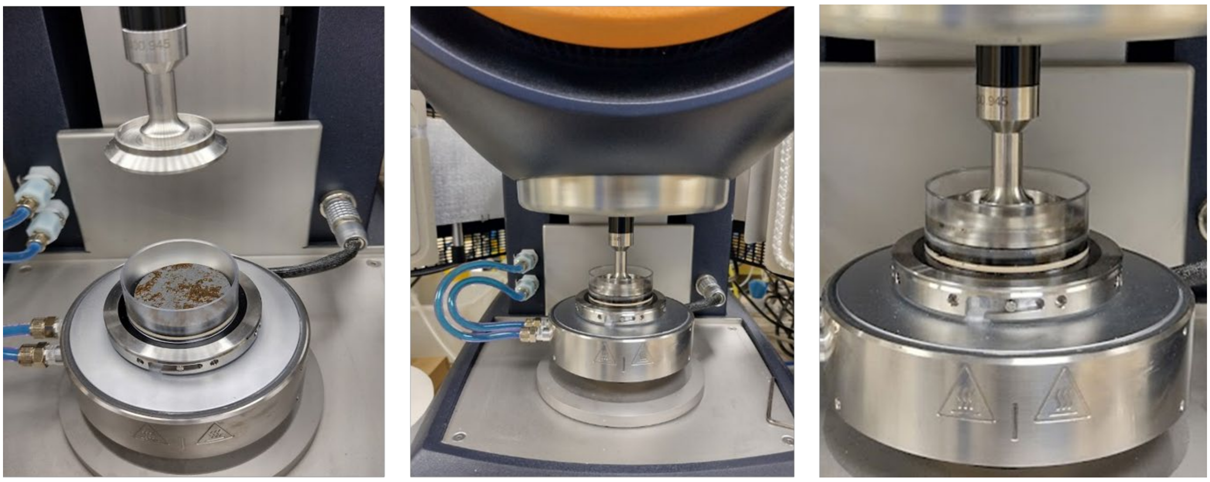

Figure 6-2. *The parallel-plate rheometer was set up with a Peltier plate and clear PVC well. The well was loaded with a coupon covered with biofilm (a) and seawater was added for testing (b, c).*

6.2.4.1 Amplitude sweeps

Amplitude sweeps were performed by incrementing oscillatory strain from 10^{-5} to 10^{-1} at an oscillation frequency of 1 Hz. The linear viscoelastic region (LVR) for the biofilms was determined from stress-strain curves where the stress was linear as a function of strain with an R^2 value > 0.95. The yield stress was taken as the intersect of the storage (G') and loss moduli (G'') (Figure 4-6).

6.2.4.2 Frequency sweeps

Frequency sweeps were executed by incrementing the oscillatory frequency from 0.1 to 10 Hz at a constant strain of 2.5×10^{-4} which was determined as being in the LVR for the biofilms grown on all coupons.

6.2.4.3 Creep-recovery

Creep-recovery tests were performed at different shear stress values ranging from 0.25 to 20 Pa. A constant stress was applied for 60 seconds at which point the stress was removed (0 Pa) and recovery of the biofilm was then followed for an additional 60 seconds. Strain was plotted as a function of time and effective G and effective η were quantified (Gloag *et al.*, 2018). From the creep portion of the experiment η was calculated as defined in Equation 4-6 (Figure 4-7b) and from the recovery G was calculated using Equation 4-7 (Figure 4-7c). λ was also calculated as the ratio of G to η as defined by Equation 4-8 (Shaw *et al.*, 2004).

6.2.5 Statistical analysis

Statistical analysis was executed in R Studio (version 1.1.423, R version 4.2.1) (R Core team, 2020) and a P-value of < 0.05 was deemed significant for all statistical outcomes.

To study the effect of rheological testing on the roughness coefficient (R_a^*), mean thickness (mm) and percent coverage (%) of biofilms grown on each surface a Welch's two sample T-test was executed. A one-way ANOVA and a post-hoc Tukey test was used to determine significant differences in the mechanical characteristics, namely G, η and λ, of biofilms grown on different surfaces. A Kruskal-Wallis and post-hoc Dunn test was used as the non-parametric alternative if data did not fit the assumptions of an ANOVA. To measure differences between the physical characteristics of biofilms grown on different surfaces a Kruskal-Wallis was required.

6.3 Results

6.3.1 Characteristics of biofilms grown on different coupons

To test the hypothesis that ship-relevant marine biofilms grown on different coupons would display a variety of structural properties the biofilm characteristics were captured using an OCT. The effect of shear was also tested by using OCT before and after testing on the rheometer. Qualitatively, the biofilms grown on the FRC coupons ("FRC biofilms") were thin with sparse small clumps in comparison to the 'fluffy' and thick biofilms covering the surface of the PVC and ACP coupons

("PVC biofilms" and "ACP biofilms", respectively), see Figure 6-3. Overall, all biofilms were brown in colour which signified a high diatom presence, confirmed by microscopy.

Note that although three biological replicates were prepared for each rheometer test, some coupons were discarded due to disturbances during transfer from the growth tank to the rheometer. Also, as there is no standard method of testing for rheologically characterising marine biofilms (Böl *et al.*, 2013; Boudarel *et al.*, 2018) some coupons had to be utilised for method optimisation.

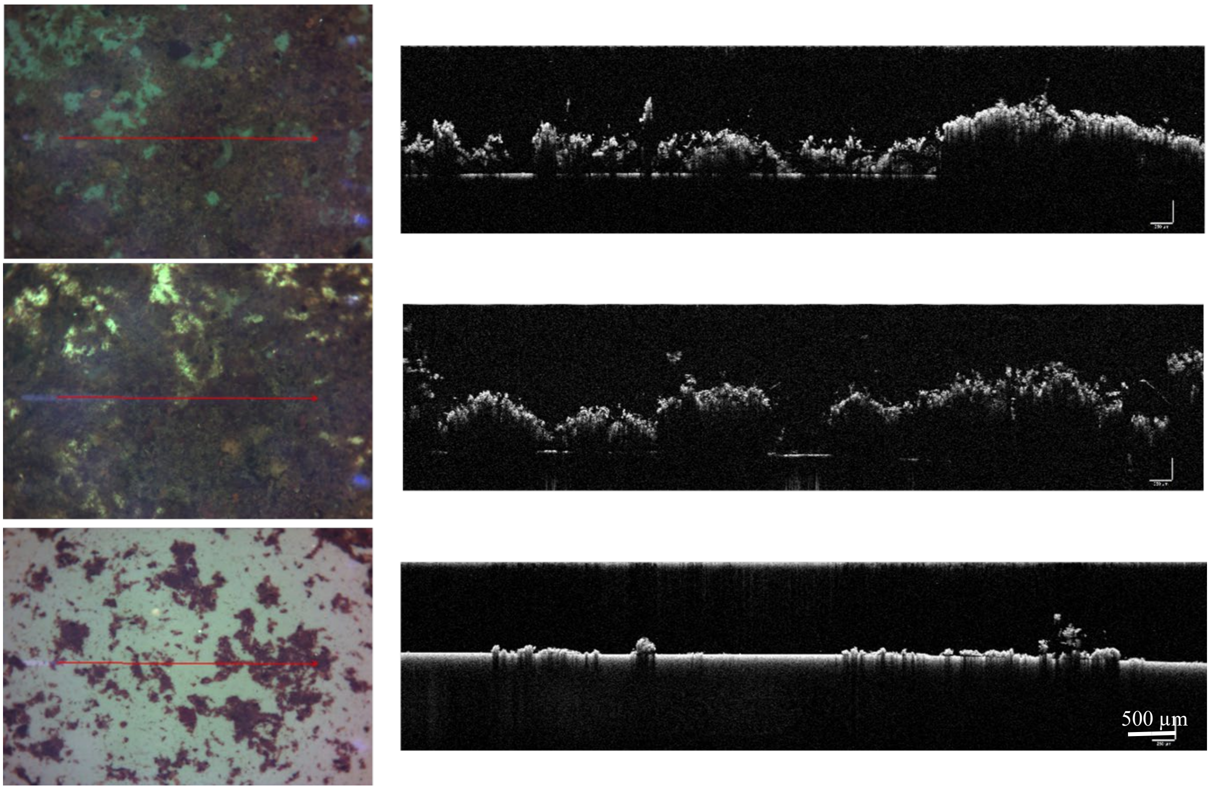

Figure 6-3. *Optical microscopy (left) and cross-sectional OCT 2D- scans (right) taken using an OCT, of the biofilms grown on different surfaces: top = PVC, middle = ACP, bottom = FRC. The red line in the photographs shows the direction of the 2D-scan on the right. The scale bar represents 500 µm.*

Physical differences were confirmed by statistical analysis as shown in Figure 6-4. Significant differences were found between the thickness (before testing) of the biofilms grown on the three coupon types (P-value < 0.05) (Figures 6-3 and 6-4). The ACP biofilms had a significantly higher pre-testing R_a^* and a significantly lower pre-testing coverage than the PVC biofilms. Between ACP: FRC and PVC: FRC there were no significant differences in percent coverage and R_a^* (P-value > 0.05). Across all variables, the biofilms grown on FRC coupons showed the lowest change when comparing structural properties pre- and post-testing, which suggests that the FRC biofilms are robust under testing conditions. For the ACP and PVC biofilms there was a significant difference between thickness before and after testing (P-value < 0.05) (Figure 6-4b), which could be linked to the removal of 'fluffy' surface layers when exposed to shear stress.

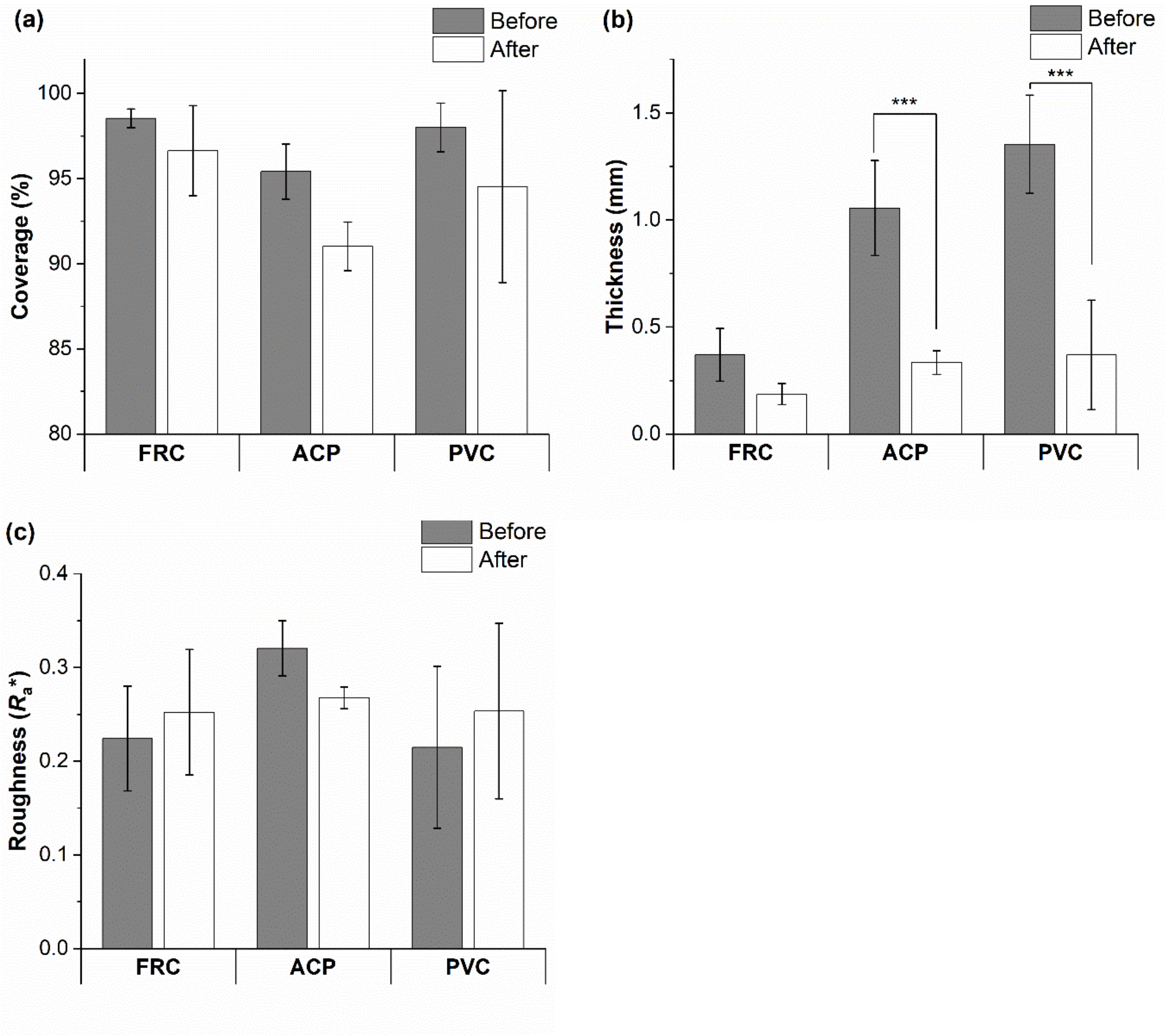

Figure 6-4. *Biofilm (a) coverage (%), (b) mean thickness (mm) and (c) roughness coefficient (R_a^*) calculated from OCT 3D-scans before and after rheological testing on a rheometer. Data is presented as mean ± SD. A '***' indicates a significant difference ($P < 0.001$) identified using a Welch's two sample T-test.*

6.3.2 *Rheological characterisation of marine biofilms*

6.3.2.1 Amplitude sweeps

Oscillatory strain sweeps were performed by incrementally increasing strain (-) from 10^{-5} to 10^{1} at a controlled frequency of 1 Hz. The storage modulus (G', Pa), loss modulus (G'', Pa) and stress (σ, Pa) were calculated and are displayed in Figure 6-5. The LVR was taken as the section where the stress-strain slope had an $R^2 > 0.95$; for all coupon types the LVR was comparable with respect to length and strain range (Figure B-2).

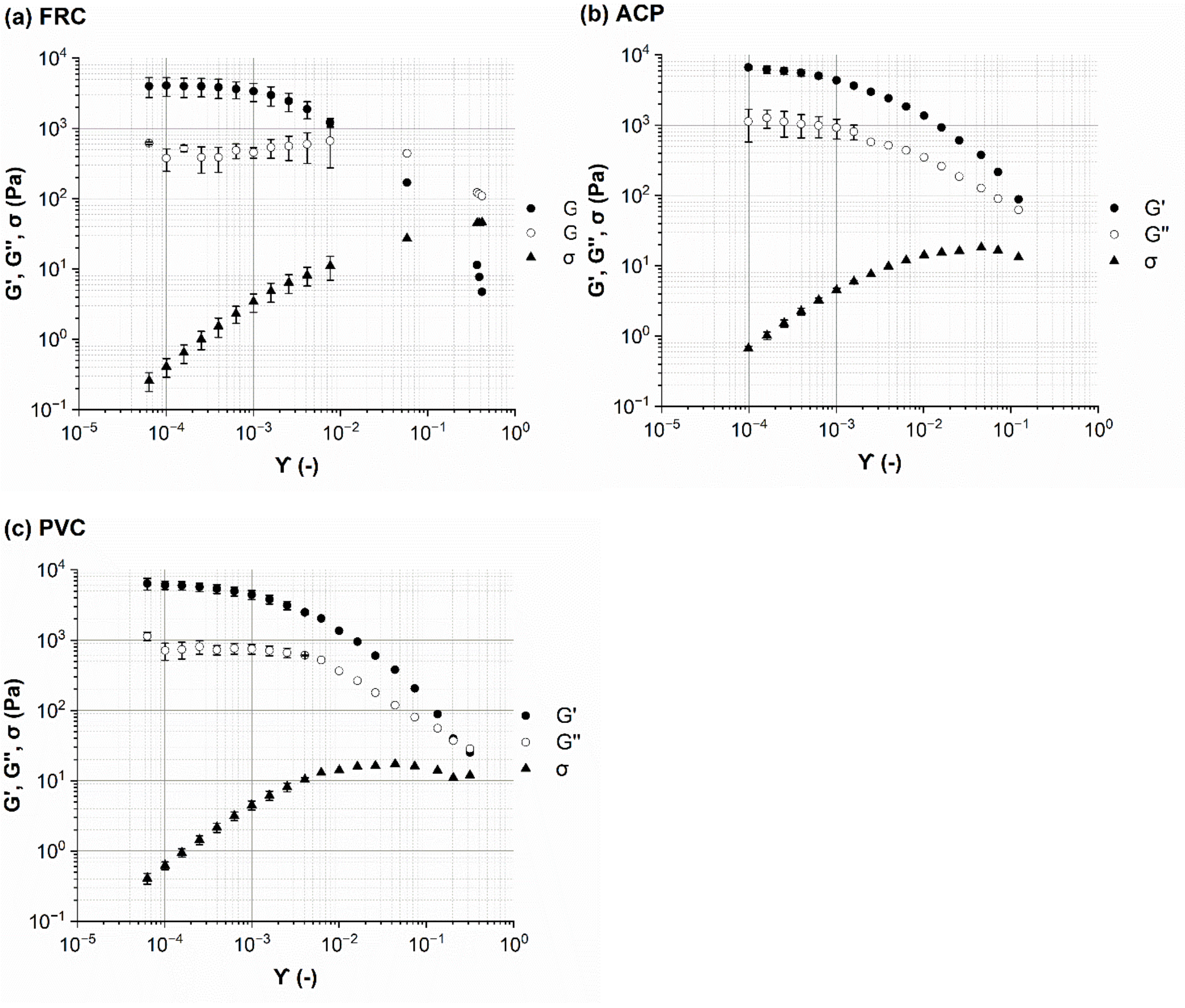

Figure 6-5. *G' (closed circles), G'' (open circles) and σ (closed triangles) vs γ for biofilms grown on: (a) FRC (n = 2), (b) ACP (n =2) and (c) PVC (n = 3) coupons. Data presented as mean ± SD.*

The intersect of G' and G'' was taken as the yield stress, which indicates a shift from an elastic-response to a viscous-dominated response. The FRC biofilms displayed the greatest yield stress of 15 ± 4 Pa (n = 2), compared to 13 Pa (n = 1), for ACP biofilms and 11 Pa (n = 1) for the PVC biofilms, which suggests that the FRC biofilms were stronger than the others. The shape of the G'

and G'' curves of PVC and ACP biofilms were comparable; after the LVR both showed a steady decline in G' and G'' with an increase in strain which continued past the yield stress point (shear thinning behaviour) (Figure 6-5). Shear thinning behaviour has often been reported for biofilms (Vinogradov *et al.*, 2004; Prades *et al.*, 2020; Souza-Egipsy *et al.*, 2021) and is indicative of disruption within the biofilm structure which would be expected as the biofilm is transitioning towards a more viscous-like response Alternatively, for FRC biofilms, after the LVR, G'declined but G'' showed a slight increase until the yield stress was reached. This behaviour is often described as a weak strain overshoot (Hyun *et al.*, 2011; Souza-Egipsy *et al.*, 2021) which occurs when there is a local maximum of G''(Hyun and Kim, 2011), as was found for the FRC biofilms (Figure 6-5). After the G'' maximum the yield stress was reached and was followed by a slow decline in G'' with increasing strain. Unlike the other biofilms, the FRC biofilms also experienced an eight-fold increase in phase angle after the yield stress, which indicates a rapid shift from elastic-dominated to viscous-dominated behaviour.

6.3.3 Frequency sweeps

Fresh biofilm coupons were used to test the dynamic behaviour of marine biofilms over a range of frequencies, from 0.1 to 10 Hz or angular frequencies (ω) of 0.63 to 63 rad s-1. G' was consistently higher than G'' for all coupons tested and both parameters were relatively independent of increasing frequency (Figure 6-6). Collectively the behaviour displayed by the biofilms, across the conditions applied, is indicative of an elastic-solid material.

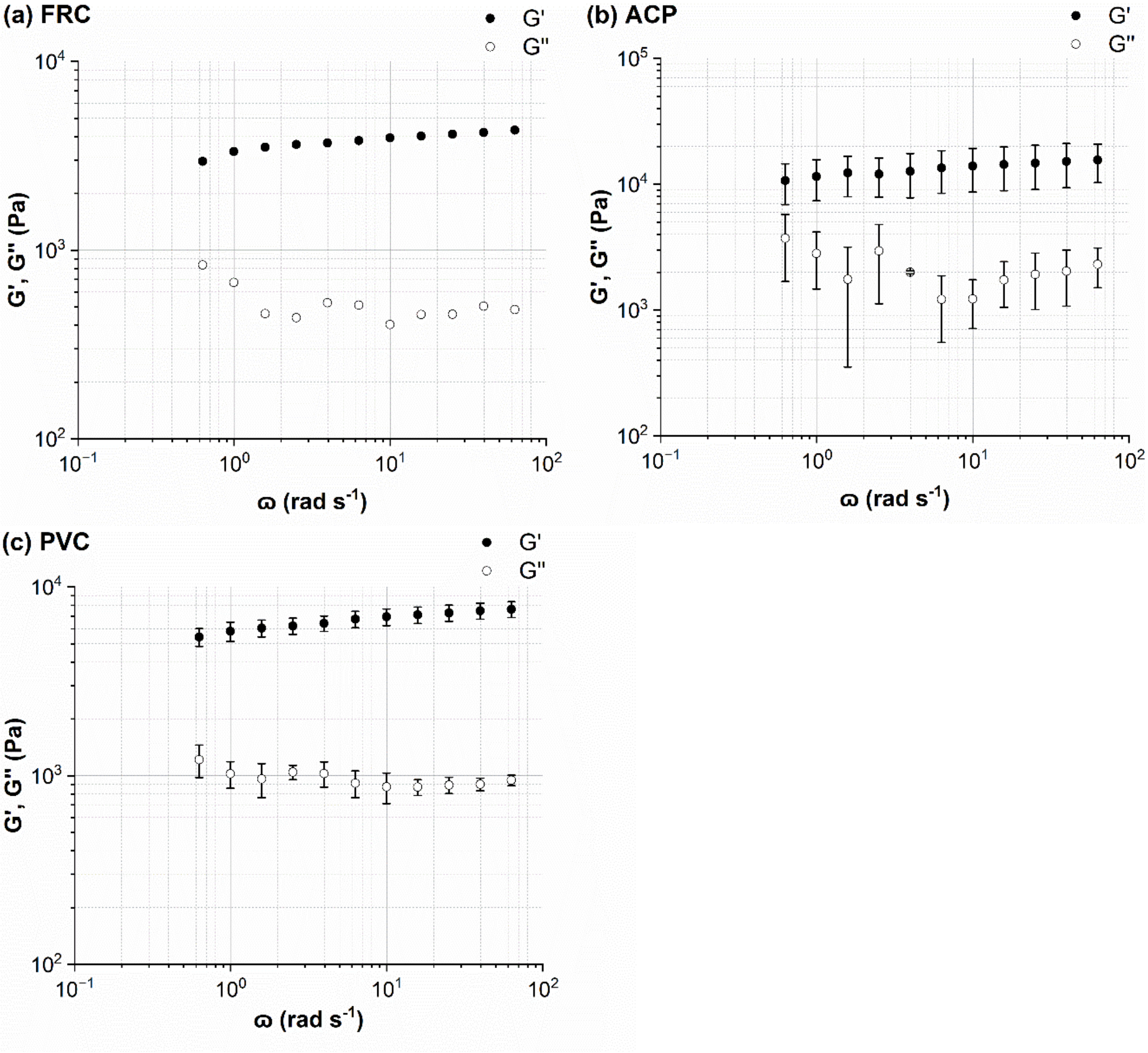

Figure 6-6. *Frequency sweeps performed on: (a) FRC (n =1), (b) ACP (n =2) and (c) PVC (n = 3). Angular frequency was incrementally increased from 0.63 to 63 rad s^{-1}. G′ (closed circles) and G″ (open circles) are plotted. Data presented as mean ± SD.*

6.3.4 3.2.3 Creep-recovery

Effective *G* and effective *η* were calculated from creep-recovery curves. The biofilms grown on FRC coupons possessed the lowest *G* and highest *η* when compared to the biofilms grown on ACP and PVC coupons (Figure 6-7). All measurements were taken within the LVR region for each surface, as identified by the amplitude sweeps (Figures 6-5 and B-2).

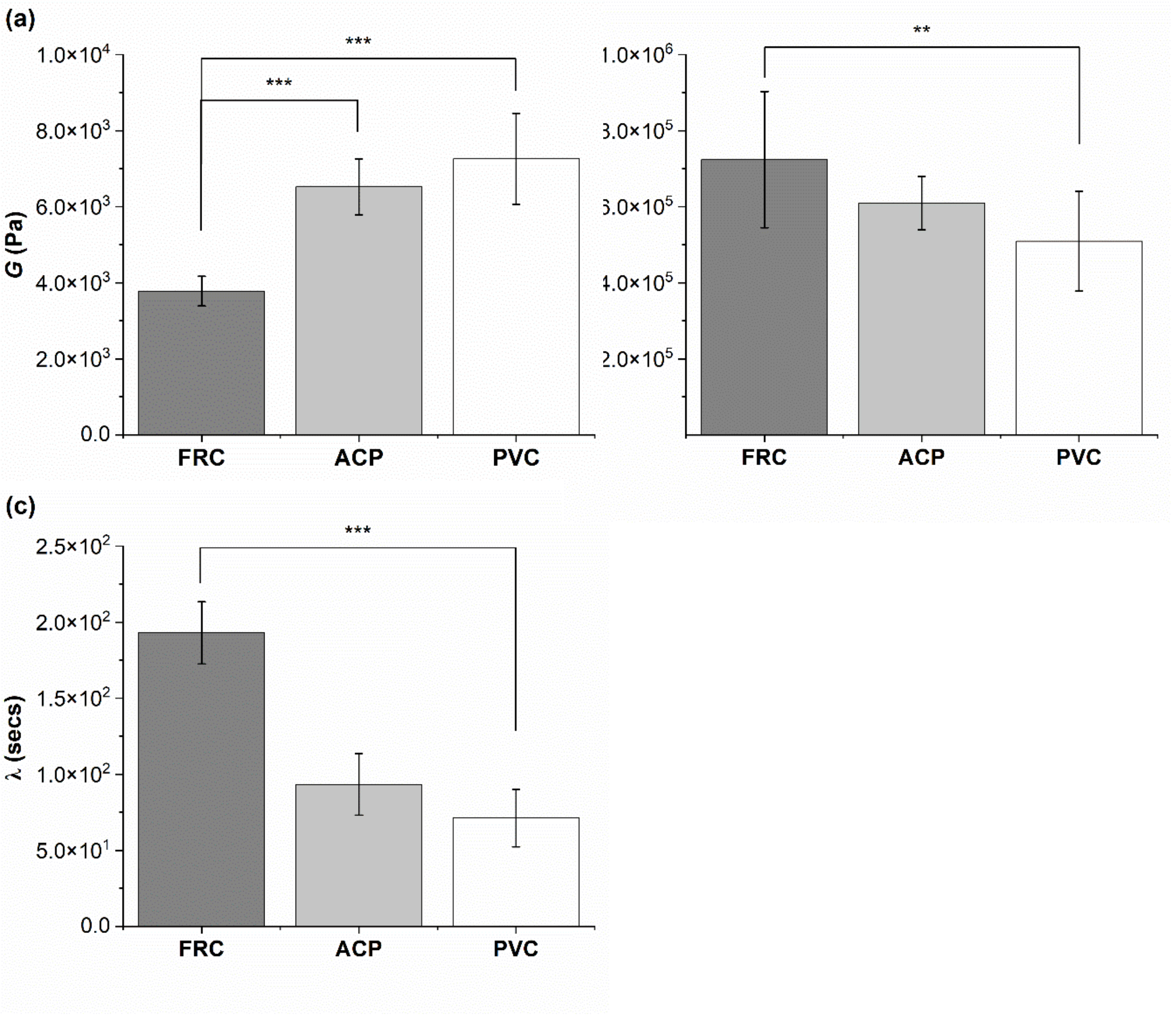

Figure 6-7. *Mechanical characterisation of marine biofilms grown on: FRC (n = 1), ACP (n = 1) and PVC (n = 3) coupons using creep-recovery measurements. (a) G was calculated using Equation 4-7; (b) η using Equation 4-6 and (c) λ using Equation 4-8. Statistical analysis was conducted using one-way ANOVA or Kruskal Wallis tests. Data presented as mean ± SD and P-values are represented as *** = 0.001, ** = 0.01.*

A shear stress of 1.5 Pa was identified as within the LVR region for all coupons tested (Figures 6-5 and B-2) and was therefore used to compare the creep-recovery data (Figure 6-8). The biofilms present on all coupon types showed similarity in the creep curves; each displayed an instantaneous elastic response (Figure 6-8a), time-dependent viscous response (Figure 6-8b) and instantaneous elastic recovery (Figure 4-6c).

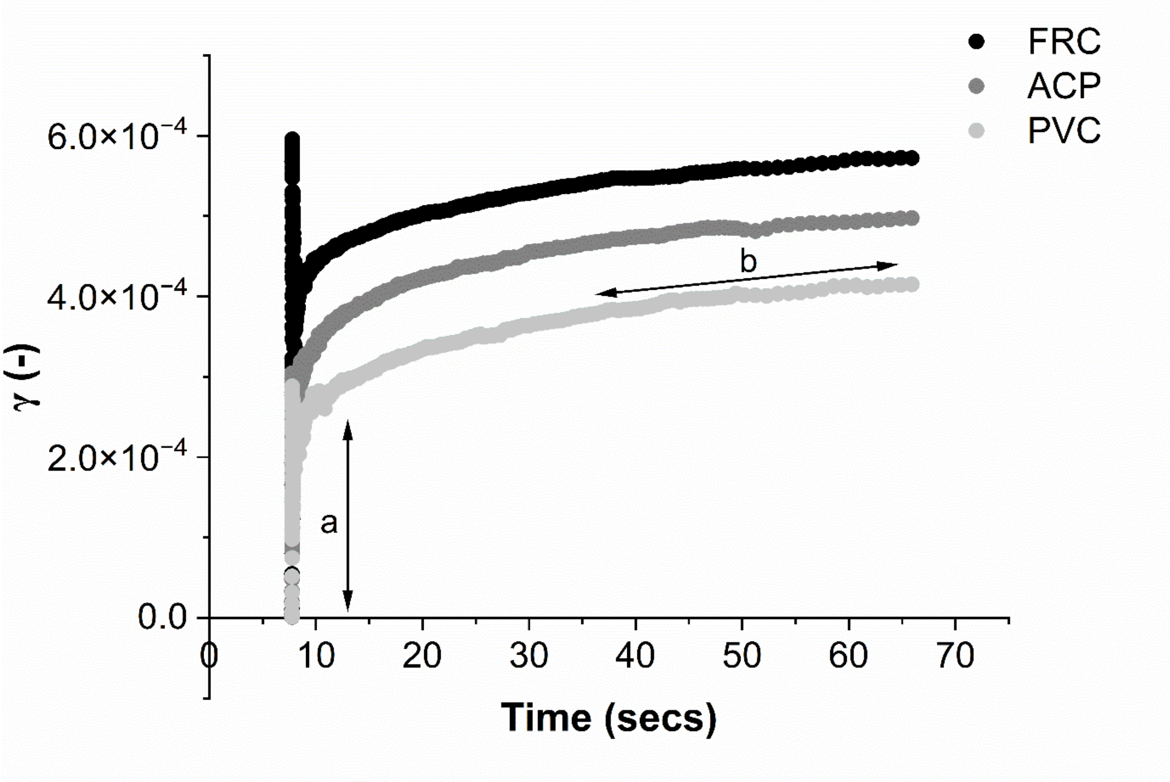

Figure 6-8. *Strain, γ (-) vs. time for each of the coupon types: FRC (black), ACP (dark grey) and PVC (light grey). A stress of 1.5 Pa was applied for 60 seconds at which point stress was set to 0 Pa and recovery was plotted for 60 seconds. The creep curve for PVC (light grey) has been annotated (black arrows) to show the two classic sections of a viscoelastic creep response: a) instantaneous elastic response, b) time-dependent viscous response.*

The suggestion that the FRC biofilms are the most compliant biofilms studied here is supported by the creep curves. Figure 6-8 shows how the FRC biofilms deform more readily than the ACP and PVC biofilms with a greater instantaneous elasticity when strain was applied. Using the instantaneous elastic recovery portion (Figure 4-7) λ was calculated and revealed that FRC had the longest λ which was more than a factor of two greater than the alternative biofilms (Figure 6-7).

It important to highlight that biofilms will display a different response under different stressors (Stoodley, Lewandowski, Boyle, *et al.*, 1999). For example, within the LVR the FRC biofilms displayed stability and viscoelasticity, but at a higher shear stress structural integrity diminished. At 20 Pa the FRC biofilms showed no viscoelastic strain recovery which is characteristic of a liquid, where the ACP biofilms maintained a time-dependant viscoelastic recovery response with some elastic recovery and permanent deformation (Figure 6-9).

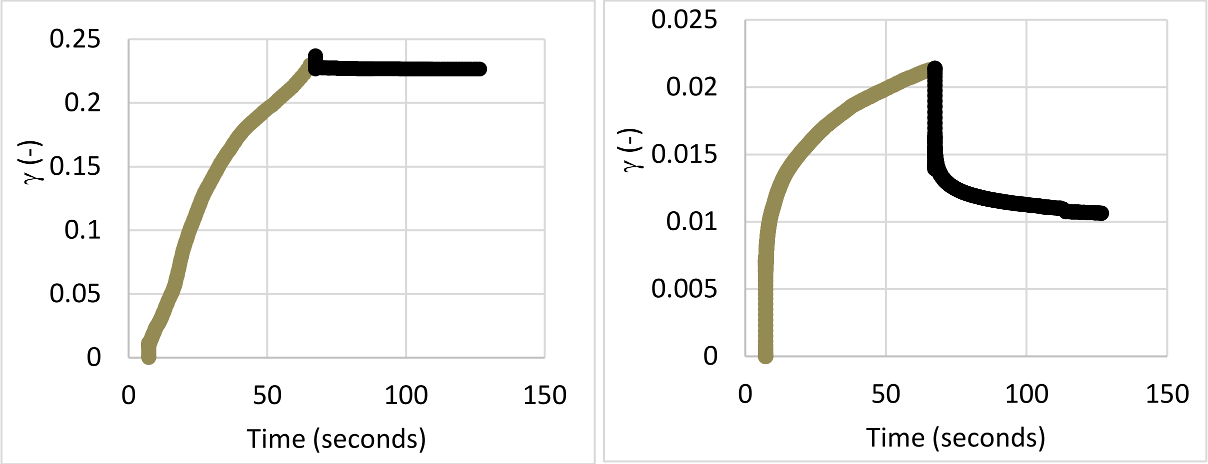

Figure 6-9. *Creep recovery data for: (a) FRC (b) ACP biofilms tested at a shear stress of 20 Pa. This shear stress was out of the LVR for both biofilms which react very differently.*

6.4 Discussion

In this study ship-relevant marine biofilms have been rheologically characterised for the first time. The marine biofilms, grown at the Dove Laboratory, showed rheological behaviour analogous to viscoelastic materials which has been reported previously for alternative biofilm types (Stoodley, Lewandowski, Boyle, *et al.*, 1999; Körstgens *et al.*, 2001b; Rupp, Fux and Stoodley, 2005; Vadillo-Rodriguez and Dutcher, 2009). Some similarities were anticipated between the biofilms as they were grown under the same environmental conditions (temperature, pH, salinity, water depth) and the surface colour was kept consistent to avoid colour-driven changes to the biological communities. Despite some similarities, our observations show that there were significant differences, physically and mechanically, between biofilms grown on substantially chemically inert and biocide-free different surfaces. This was perhaps driven by differences in biological communities across the surfaces (Papadatou *et al.*, 2021), which would inevitably alter the physical structure and mechanical profile of a biofilm.

It is important to note that an aim of this investigation was to assess the physico-mechanical properties of marine biofilms and therefore no taxonomic identification was executed. It would be of interest to carry out microbiological analysis of the biofilm components and community composition to determine whether differences observed in mechanical properties are caused by structural differences and/or biological ones.

6.4.1 Structural characterisation of marine biofilms using OCT

From optical microscopy and OCT cross-sectional scans (Figure 6-3) it is shown how biofilms cultivated on different inert surfaces possess structural variability, thickness, and percent coverage (Fabbri *et al.*, 2018). The biofilms grown on ACP and PVC coupons could be described as thick and ‘fluffy’ (Figure 6-4), where a ‘fluffy’ biofilm has loose surface layers and stiff consolidated base layers (Zhang and Bishop, 1994; Towler *et al.*, 2003; Laspidou and Aravas, 2007; Paramonova *et al.*, 2009; Picioreanu *et al.*, 2018; Gloag *et al.*, 2021). When a ‘fluffy’ biofilm is exposed to external stress the surface layers can be quickly sheared, whereas the base layers display a greater resistance (Zhang and Bishop, 1994). Differences in OCT scans before and after testing on the rheometer showed that the ACP and PVC coupons displayed a 68 % decline in biofilm thickness (Figure 6-4) (P-value < 0.05). Similar results were found for biofilms grown statically on an inert coating by Fabbri et al., (Fabbri *et al.*, 2018) where there was approximately a 70 % decline in thickness after exposure to applied shear, coupled with a 40 % reduction in coverage. In the present study, despite a significant reduction in thickness, percent coverage was comparable before and after rheological testing (Figure 6-4) which suggests that the base layers of the biofilms were, in fact, more resistant to imposed shear than the surface layers. Interestingly, Zhang and Bishop noted that the base layers of a ‘fluffy’ biofilm can be 50 % less porous than the surface layers which is important as a reduction in porosity leads to a less viscous, stiff, and dense biofilm (Zhang and Bishop, 1994; Laspidou *et al.*, 2014; Lembré, Di Martino and Vendrely, 2014; Jafari *et al.*, 2018). Although, density and porosity were not investigated, it could be concluded that the ACP and PVC biofilms demonstrate characteristics akin with a ‘fluffy’ biofilm. The creep-recovery data further revealed that the ACP and PVC biofilms had a higher G, a lower η and shorter λ than the FRC biofilms (Figure 6-7) which could be expected given the structural characteristics.

Alternatively, the biofilms grown on FRC coupons were much thinner than the ACP and FRC biofilms, measuring 0.37 ± 0.19 mm (Figures 6-3 and 6-4b). Also, the FRC biofilms were sparse and displayed clumped coverage (Figure 6-3). Like the ACP and PVC biofilms, the coverage of the FRC biofilms remained consistent before and after rheological testing; however, the FRC biofilms also showed no significant change in average biofilm thickness (Figure 6-4). The FRC biofilms were not ‘fluffy’ like the other biofilms, and therefore it could be that differences in the physico-mechanical properties are driven by surface properties which are responsible for resistance of FRC biofilms. To confirm this, the rheological characterisation of marine biofilms on different coatings is required.

6.4.2 Viscoelasticity of marine biofilms

The effective G of marine biofilms ranged from 3780 to 7257 Pa, based on surface type, which fits comfortably within the range quoted in the open literature for other biofilms (Böl *et al.*, 2013; Kim, Kwon and Kim, 2017; Tallawi, Opitz and Lieleg, 2017). The biofilms grown on FRC coupons possessed a significantly lower G and higher η than the PVC and ACP biofilms (Figure 6-7) and could be described as soft and viscous. Tierra *et al.*, (2015) created a multicomponent model for studying biofilm deformation and determined that a biofilm with high viscosity and low elasticity is required for a stable and compliant biofilm structure. A compliant biofilm can readily deform in response to imposed shear stress due to viscoelastic behaviour; the elastic elements store energy via reversible deformation whereas viscous forces dissipate energy and reduce the risk of cohesive failure and detachment (Rupp, Fux and Stoodley, 2005; Gloag *et al.*, 2021). On the other hand, the ACP and PVC biofilms were stiff, possessed a lower yield stress and demonstrated significant removal of the biofilm surface layers. The reduction in thickness of the ACP and PVC biofilms could be responsible for the higher G exhibited due to consolidation effects (Valladares Linares *et al.*, 2016). From results presented, it can be concluded that the FRC biofilms were more compliant than the ACP and PVC biofilms as they adapted to changing conditions without removal (Figure 6-4) and resisted imposed shear to a greater extent, as determined by the higher yield stress.

Souza-Egipsy *et al.*, (2021) reported that an increase in G correlated with an increase in λ, due to a greater interconnectivity within the structure of biofilms collected from acidic environments. However, in the present study ACP and PVC biofilms possessed a significantly higher G but a λ more than half that for the FRC biofilms (Figure 6-7). Peterson *et al.*, (2015) found that a biofilm with a greater concentration of bacterial cells had a longer elastic relaxation time as cells are the heaviest component of the EPS, on the other hand, in the same study, it was noted that a longer λ could also be consequence to polymers re-arranging within the EPS. It is expected that polymeric structural rearrangement is responsible for the longer relaxation time exhibited by the softer FRC biofilms as an increased presence of bacterial cells within the EPS would produce a stiffer biofilm (Barai, Kumar and Mukherjee, 2016; Cao *et al.*, 2016).

The resistance of the FRC biofilms to applied stress was further highlighted in the amplitude sweeps where a weak strain overshoot was identified (Figure 6-5a). A weak strain overshoot occurs during the yielding of a material and is a non-linear viscoelastic phenomenon caused by a shift from solid-like deformation in the LVR to fluid-like, plastic flow (Donley *et al.*, 2020). The FRC biofilms demonstrated viscoelastic solid behaviour at low stresses (Figures 6-5 and 6-6) and showed evidence of plasticity past the LVR (Figure B-2a). A weak strain overshoot is characteristic of soft glassy materials such as emulsions, colloidal gels and soft hydrogel spheres dispersed in water (Hyun *et al.*, 2011; Donley *et al.*, 2020) and has recently been observed in mono-species biofilms (Jana *et al.*, 2020) and diatom-dominated biofilms found in an extreme acidic environment (Souza-Egipsy *et al.*, 2021). It is challenging to determine the structural cause of this behaviour as it material dependent (Hyun *et al.*, 2011), and as biofilms are largely heterogeneous another level of complexity is added. It is likely that for the marine biofilms grown on FRC coupons the weak strain overshoot is caused by viscous dissipation and structural rearrangement as the biofilm adapts to increasing shear stress; as the critical stress is reached, the biofilm yields and alignment in the direction of flow occurs. This latter point fits with the phase-angle data that revealed an eight-fold decline after the yield stress was reached, which shows that the FRC biofilms were fluid-like past this point. Future work should incorporate the study of large amplitude oscillatory shear as although differences in mechanical response can be visualised from amplitude sweeps and creep-recovery, Lissajous plots provide a deeper insight into the mechanical state of a material during testing (Hyun *et al.*, 2011; Jana *et al.*, 2020).

6.4.3 Marine biofilm viscoelasticity and drag

Drag measurements were not studied here, however it could be expected that at low shear stress the FRC biofilms would produce a greater drag than the stiffer PVC and ACP biofilms due to greater compliance (Snowdon *et al.*, 2022). This is based on studies that have found compliant structures to generate a significantly higher drag compared to rigid alternatives (Picologlou, Zelver and Characklis, 1980; Hartenberger *et al.*, 2020), particularly at lower shear (Snowdon *et al.*, 2022). Alternatively, rough and thick biofilms with good coverage are expected to provide a greater drag than thin and sparse biofilms (Hartenberger *et al.*, 2020; Murphy *et al.*, 2022), which instead suggests that the PVC and ACP biofilms could produce a greater drag than the FRC biofilms. Valladares Linares *et al.*, (2016) determined that a decline in thickness was coupled with an increase in elasticity and consequently an increase in resistance to shear, which could be explicable by denser base-layers that have consolidated over time under a thicker biofilm. On the other hand, Desmond, Morgenroth and Derlon, (2018) found no correlation between thickness, roughness and increased resistance to shear and Jafari *et al.*, (2018) concluded that porosity influences resistance more than thickness. Collectively, these previous studies highlight the complexity of biofilms and how different growth, and testing conditions alter the physico-mechanical responses to imposed stress and making it challenging to link these properties to drag.

The ACP and PVC surfaces were chemically inert, they had no antifouling capabilities and the resultant biofilms shared similar structural and mechanical properties (Figures 6-3 to 6-5 and 6-7). However, the FRC surfaces, which are also chemically inert but whose surface properties are designed to minimise adhesion of fouling organisms, appeared to select for patchy and compliant biofilms, and, for the most part, these had significantly different properties to the ACP and PVC biofilms. It is important to highlight that the experiments were executed at low shear stressors that are not comparable to those experienced on a ship or boat hull and therefore do not reflect in-service performance of different surfaces. Instead, the results highlight how different surfaces affect biofilm physico-mechanical properties and from the results presented it could be suggested that biofilm thickness plays a critical role in determining biofilm mechanics (Fabbri *et al.*, 2018).

Marine biofilms are likely affected by a multitude of environmental conditions, such as seasonality and temperature and, testing conditions such as growth duration and surface type (i.e., toxic vs non-toxic coatings). Future work should endeavour to study how changing growth and testing conditions effects community structure and how this could cascade down to altering biofilm viscoelasticity and inevitably drag. For example, although the shipping industry is moving away from toxic based antifouling coatings it would be of interest to see how these coatings influence biofilm physico-mechanics since they are still widely used. Although a parallel-plate rheometer may not mimic real-world conditions with respect to the shear forces a biofilm could experience on a ship hull (Karimi *et al.*, 2015), it offers high throughput experiments for characterising marine biofilms on different surfaces and provides a benchmark for studying marine biofilm viscoelasticity. It would be of interest to execute longer-term experiments that can capture seasonal variability and possibly represent biofilms on ship-hulls more appropriately. Nevertheless, in the current study questions have started to be answered on how marine biofilm structure interacts with mechanical properties and suggestions have been made as to how this could implicate drag.

To date, it is unknown how surface coating and biofilm structure alter the mechanical response of biofilms to stress, but also how different biological communities influence these relationships. Before these questions can be answered, it is critical that the mechanical properties of marine biofilms are first studied in isolation to enable a better fundamental understanding of marine biofilm viscoelasticity and the role of biofilm structure in this behaviour (Peterson *et al.*, 2015). This is an important step towards generating better informed coating formulation choices for improved fouling control properties and reduced drag.

6.5 Conclusion

To conclude ship-relevant marine biofilms, grown in natural seawater at the Dove Laboratory (Cullercoats Bay, UK) are viscoelastic and their physico-mechanical properties differ depending on the surface type. Here, the first viscoelastic characterization of different marine biofilms using creep-recovery experiments on a parallel-plate rheometer has been done. The viscoelastic biofilms grown on ACP and PVC coupons displayed similarities in their structural properties and in their mechanical response to imposed shear as shown by the amplitude sweeps (Figure 6-5). The FRC biofilms, however, had a higher yield stress, significantly lower G, higher η, and a λ more than double that of the alternative biofilms. Collectively, the FRC biofilms could be described as soft and viscous and were more compliant than the ACP and PVC biofilms. Structurally, the ACP and PVC biofilms could be described as ‘fluffy’ and thick, whereas the FRC biofilms were thinner and did not show a significant decline in thickness before and after rheological testing. It would be beneficial to determine a correlation between biofilm physico-mechanical properties and biofilm composition as a function of coating type, as it is likely that differences observed across the biofilms grown on different coupons are partly explicable by microbiological differences. We acknowledge that there are additional properties that could have altered the biofilm physico-mechanics that have not been studied here, such as the wettability and chemical composition of the coatings, as well as biofilm community. Nevertheless, new results have highlighted how different surface treatments produce biofilms with different physico-mechanical properties which is an important research area for the shipping and coatings industry.

7 Chapter 7: The Effect of Surface Colour on the Physcio-mechanics of Marine Biofilms

ABSTRACT

The presence of marine biofilms on ship hulls causes an increase in frictional drag. The physico-mechanical properties of marine biofilms influence drag, yet the relative contribution of biofilm viscoelasticity remains an understudied area. To combat biofilms antifouling coatings are often applied to ship hulls, yet the effect of colour on drag-causing properties, such as biofilm physico-mechanics, is overlooked. In the present study it is demonstrated how surface colour affects the structure and mechanical properties of marine biofilms. Furthermore, new results reveal how marine biofilm structure and mechanics may be correlated. Using OCT and a parallel-plate rheometer biofilms grown on red and black surfaces were similar whereas biofilms grown on white surfaces were thicker and displayed a significantly different mechanical profile. A better understanding of how surface coating properties influence drag-causing properties of biofilms (such as structure, composition, and viscoelasticity) is required to improve antifouling coating efficiency and to improve our knowledge on fluid-structure interactions.

7.1 Introduction

Any surface immersed in non-sterile water will be quickly colonised by microfouling organisms that have the potential to generate biofilms. Marine biofilms are heterogeneous systems comprised of microalgae (such as diatoms) and bacteria encased within a gel-like matrix of EPS. The EPS is predominantly composed of water (Berlanga and Guerrero, 2016) and contributes to biofilm viscoelasticity, which means they exhibit both viscous and elastic behaviour in response to external stimulation (Snowdon *et* al., 2023). The viscoelastic nature of biofilm, is in part, responsible for the resistance biofilms exhibit when under mechanical, chemical (for example biocidal) and environmental stress (Peterson *et al.*, 2015; Fabbri *et al.*, 2019; Gloag *et al.*, 2020), such as on the side of a ship hull.

In the shipping industry, marine biofilms cause environmental and economic implications. Biofilm presence alone can increase ship drag by up to 18 % (Schultz *et al.*, 2011) and, in part this is attributed to biofilm viscoelasticity (Picologlou, Zelver and Characklis, 1980; Snowdon *et al.*, 2022). Despite this, there are few studies in the literature that have investigated how different surfaces effect marine biofilm viscoelasticity (Snowdon *et* al., 2023) or how this behaviour contributes to drag (Snowdon *et al.*, 2022). In part, this is due to the complexity of the system including biofilm spatial and structural heterogeneity, the fact that they are surface attached and generally very thin presents a challenge for applying standard rheological methods (Böl *et al.*, 2013).

To combat biofouling, antifouling coatings are often applied to ship hulls. These can either be toxic, or non-toxic. Briefly, toxic (or biocidal) coatings contain harmful chemical which deter the settlement of fouling organisms (Finnie and Williams, 2010). The use of biocidal coatings has become highly regulated due to the suspected harmful effects on the marine environment (Galvão De Campos *et al.*, 2022) and therefore non-toxic coatings are increasingly applied - 'non-stick' elastomeric materials with a low surface energy and are substantially chemically inert (Atlar *et al.*, 2003; Finnie and Williams, 2010). Due to differences in chemical composition, wettability and surface finish, marine biofilms colonising different antifouling coatings are varied in community composition and species diversity (Salta *et al.*, 2013; Papadatou *et al.*, 2021), which in turn influences the macrofouling communities (Dobretsov, Abed and Teplitski, 2013; Camps *et al.*, 2014). To improve the efficiency of anti-fouling coatings against biofilms (and to decrease drag), a better understanding of how marine biofilms interact with fluid flow and how they change in response to different surfaces is required.

As well as coating differences in surface properties, surface colour influences biofilm formation and structure. Dobretsov, Abed and Teplitski, (2013) studied both marine micro- and macrofouling communities and found black surfaces to promote a higher density of fouling compared to white. A similar conclusion was met by Swain *et al.*, (2006) who studied macrofouling communities on black and white surfaces. More recently, Gambino *et al.*, (2018) investigated the effects of red, white, black and blue surfaces on cyanobacterial biofilms and concluded that colour is vital in determining the bioreceptivity of a surface; the authors found that white surfaces produced the greatest biomass due to the quality and quantity of light available for phototrophs, thus simulating growth. Alternatively, black and blue surfaces promoted EPS production as a potential response to low light availability which causes high levels of oxidative stress (Gambino *et al.*, 2018). These studies have highlighted how colour influences biofilm community, yet little is known on how colour alters the physical structure of biofilms and even less is known on how colour influences biofilm mechanics.

The main aim of this investigation was to determine whether different colours, of the same antifouling coating, influences marine biofilm structure and mechanical properties. The results will contribute knowledge into improving the efficiency of antifouling coatings against potential biofilm targets using surface colour as a driver.

7.2 Materials and Methods

7.2.1 Coupons and surface treatments

Test coupons were fabricated from 1 mm thick grey PVC and had a 40 mm diameter (Chemical Process Solutions Ltd., Seaham, UK). Preparation of coupons (total = 108 coupons) for painting involved abrading the surface with P80-grit sandpaper.

The coupons were coated using a three-part scheme, according to manufacturer instructions (AkzoNobel, Gateshead, UK). First, an anti-corrosive primer was applied, followed by a tie-coat and finally the topcoat. The topcoat used was Intersleek® 700, which is a non-biocidal silicone-based foul release coating and was applied in three different colours: red, white, and black (Figure 7-1). The colours were selected based on previous studies investigating the impact of colour on biofilm formation and characteristics (Dobretsov, Abed and Voolstra, 2013; Gambino *et al.*, 2018).

Figure 7-1. *40 mm PVC coupons attached to a square pipe before being immersed in Hartlepool Marina (Hartlepool, UK).*

7.2.2 Surface properties of coated coupons

Pre-field deployment in Hartlepool Marina (UK), the surface properties of the three types of coupons were tested. This was to ensure that any differences in biofilm characteristics were not consequent to variations in surface roughness or wettability (Salta *et al.*, 2013).

7.2.2.1 Blue light interferometry

A Blue-light Interferometer (MikroCAD premium, LMI technologies, Burnaby, Canada) paired with ODSCAD software (GFMesstechnik, Berlin, Germany) was used to measure S_a of red ($n = 9$), white ($n = 7$) and black ($n = 8$) coupons. A single scan with a 10 mm cut-off wavelength and measuring 20 mm × 20 mm was taken per coupon (Medhurst, 1990).

7.2.2.2 Optical Contact Angles (OCA)

A Data Physics OCA machine, paired with SCA20 software (Data Physics, Berlin Germany) was used to measure water droplet (4 µL) contact angles on red ($n = 2$), white ($n = 3$) and black ($n = 3$) coupons. For each biological replicate, three technical replicates were taken. Two OCA measurements were taken per second for a total of 120 seconds; the measurements taken at 60 seconds were used as a reference point used for statistical comparison of OCA across the three colour types.

7.2.3 Exposure to marine fouling

Coloured coupons ($n = 18$ of each colour) were attached to one external side of a 1 m square downpipe (Wickes, 65 × 65 mm) using double-sided sticky tape. In total, two pipes were prepared for immersion (Figures 7-1 and 7-2). The pipes were deployed horizontally, with the coupons orientated upwards, at the side of a raft in Hartlepool Marina (Hartlepool, UK), at a depth of 1 m on 4th October 2022 (Figure 7-2). It was important to immerse the pipes at the same depth and to position the coupons the same way to avoid differences in biofilm growth due to sunlight exposure (Swain *et al.*, 2006).

Figure 7-2. *Deployment of pipes at Hartlepool Marina (UK): a) the pipes were tied to the railings using white ropes (yellow arrows) and b) the pipes were immersed at the same depth with the coupons facing upwards to maximise sunlight.*

The pipes were carefully removed from the Marina over two separate weeks (23rd and 30th November 2022) to allow for structural and rheological testing of each set of 54 coupons. Over the immersion period the seawater temperature was 10 to 13 °C. For transportation to AkzoNobel, a single pipe was placed carefully into a large plastic bag, pulled taught and tied at each end with a cable tie, to retain the biofilm moisture. At AkzoNobel, the coupons were detached from the pipe surface, using a palette knife, and were placed into a container filled with water taken from Hartlepool Marina. The pH and temperature of the water was tested daily to ensure consistency. Further, tests requiring unpreserved (live) biofilm were conducted over two days (retrieval +1) to minimize breakdown of the biofilm structure.

7.2.4 Structural characterisation of biofilms using OCT 3D-scans

OCT was used to characterise the structure of marine biofilms grown for 7- and 8-weeks in Hartlepool Marina. To investigate how mechanical testing influences biofilm structure, OCT was also applied after biofilms had been exposed to a testing regime on a parallel-plate rheometer. Briefly, OCT is a non-invasive, high throughput method for measuring mesoscopic biofilm properties *in-situ* (Wagner *et al.*, 2010). For more details on the OCT used refer to Section 4.2.

Six randomly selected coupons of each coupon type were carefully placed into a shallow dish, filled with seawater taken from Hartlepool, under the OCT (ThorLabs software version 5.4.8). Since the samples were immersed in natural seawater a refractive index of 1.34 was applied to correct for refraction. For each biological replicate, a B-scan measuring 9.0 mm × 2.1 mm (acquisition time = 0.66 seconds) and a C-scan measuring 9.0 mm × 9.0 mm × 2.1 mm (acquisition time = 33.20 seconds) was taken. To limit noise, A-scan averaging was set to three and the scan rate was 30 kHz (Fabbri *et al.*, 2018).

To quantify biofilm structure, C-scans were exported as .oct files into MATLAB version 2021B (MATLAB, 2021). Custom scripts produced by Fabbri *et al.,* (2018) were applied to quantify three structural parameters: mean biofilm thickness (mm), roughness coefficient (-) and cover (%) as defined in Section 4.2.1.

7.2.5 Qualitative microscopy

To determine if surface colour affected biofilm community, coupons were swabbed for microscopic analysis. For both 7- and 8-week biofilms, three coupons were randomly selected for samples to be taken. Samples were collected using an inoculation loop and were placed in individual Eppendorf tubes with 2 mL of Hartlepool seawater. Samples were placed in a fridge at 4 ºC until testing on the microscope.

A Keyence VHX-6000 digital microscope, fitted with a Z100 lens, was used to visualise the prepared biofilms. Preparation involved pipetting a small amount of biofilm in seawater onto a glass microscope slide and covering it with a glass coverslip. A small amount of clear nail varnish was used to seal the coverslip in place to avoid dehydration of the biofilm sample under the heat of the microscope lamps. To provide optimum contrast between the biofilm sample and the microscope a white stage was installed, and lighting settings involved full ring and epi-illumination. A magnification range of x100 to x1000 was used.

7.2.6 Rheometer

A HR-10 rheometer with a Peltier-plate heat exchanger (10 ºC) and 40 mm stainless-steel sand-blasted top-plate (to avoid slip) was used to rheologically characterise marine biofilms grown on coloured coupons (Figure 7-3). Prior to all tests on the rheometer, biofilms were compressed until a normal force of 0.1 N was detected. This step was necessary to normalise for heterogenous biofilm thickness and to ensure contact with the sand-blasted top-plate (Towler *et al.*, 2003). For more information on the rheometer used see Section 4.3.

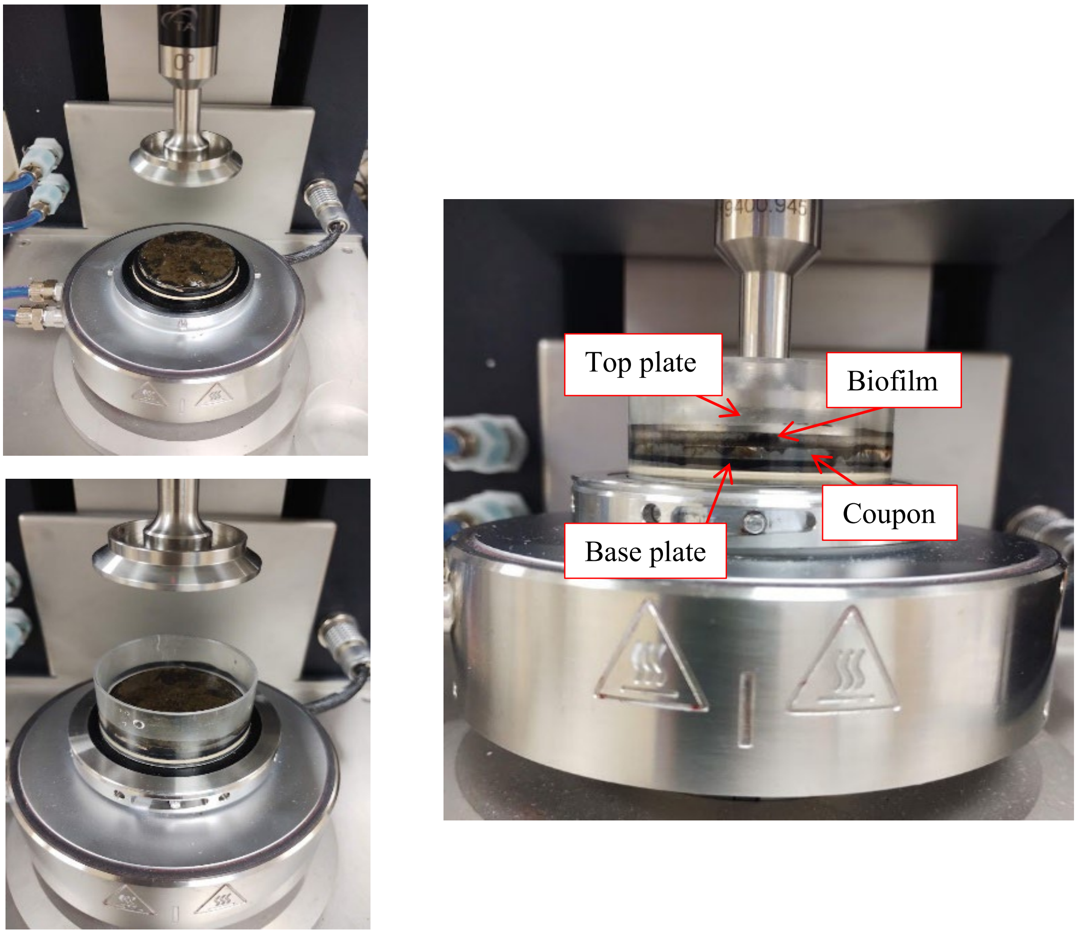

Figure 7-3. *Rheometer apparatus loaded with a biofilm grown on a black coupon with a) a Peltier-plate heat exchanger set to 10°C, b) an immersion well filled with 4mL Hartlepool seawater and c) a sand-blasted 40 mm top-plate for testing the mechanics of the biofilm.*

7.2.6.1 Amplitude Sweeps

Amplitude sweeps were performed by incrementing oscillatory strain (γ) from 10^{-2} to 10^{3} and keeping frequency constant at 1 Hz. The tests were used to identify the linear viscoelastic region (LVR) which was subsequently used to inform the testing conditions of the frequency sweeps and creep recovery experiments. The LVR was determined as the region where G' and G'' had an R^2 value > 0.95 when plotted against strain. The intersection of G' and G'' was taken as the yield stress (σ_y) as exemplified in Figure 4-6.

7.2.6.2 Frequency Sweeps

Frequency sweeps were conducted by incrementing oscillatory frequency from 10^{-1} to 10^{1} Hz or an angular frequency (ω) of 0.62 to 62 rad s^{-1}. A constant strain of 0.1 % was applied as this was identified as being within the LVR during the amplitude sweeps.

7.2.6.3 Creep-recovery

Creep-recovery was performed at different shear stress values: 0.5, 1, 2 and 4 Pa. From the amplitude sweeps all these values were within the LVR. A constant stress was applied for 120 seconds which was then removed for the recovery portion of the experiment. Strain (%) was plotted as a function of time and effective G, effective η and λ were quantified from the curves as depicted in Figure 4-7 (Gloag *et al.*, 2018). The same method for quantifying biofilm mechanics was used in Chapter 6 (Snowdon *et* al., 2023).

7.2.7 Comparative Statistics

R studio (R Core team, 2020) was used for statistical analysis. A P-value < 0.05 was deemed statistically significant for all test outcomes.

To determine differences in the surface properties of coated coupons before the fouling period a one-way ANOVA was applied. Once fouled, biofilm structure and mechanics were quantified. To test for differences in structural properties: thickness, R_a^*, cover, and mechanical properties: σy, G, η, λ, based on colour and growth period a two-way ANOVA and Post-hoc Tukey test was used. As an indicator of biofilm strength, biofilm structure was quantified before and after testing on the rheometer and a Welch's T-test was applied to determine any significant changes. Finally, a Spearman's correlation was used to identify any relationships between biofilm structure and mechanics, irrespective of colour and growth period.

7.3 Results

Coated coupons were tested pre-field deployment for surface roughness and wettability. Roughness, measured as S_a, was comparable across all coated coupons irrespective of colour (P-value > 0.05). However, one-way ANOVA revealed that the white surfaces had a significantly lower contact angle of 92.6°, compared to the red and black surfaces which were 101.3° and 102.5°, respectively. Despite these differences, the average OCA for all surfaces was within the range associated with hydrophobic surfaces (OCA > 90°).

7.3.1 Microscopy

Visually, the biofilms grown on red, white, and black coupons were green-brown in colour, which suggests a high diatom presence and was confirmed using digital microscopy (Figure 7-4). Microscopy revealed an array of different unicellular organisms, namely diatoms (pennate to chain) and *Euglena sp.* across all different coloured substrates (Figure 7-4).The same was found for multicellular organisms, where although taxonomic analysis was not executed, algae (red and green seaweed), amphipods, copepods and nematodes were identified (Figure 7-4).

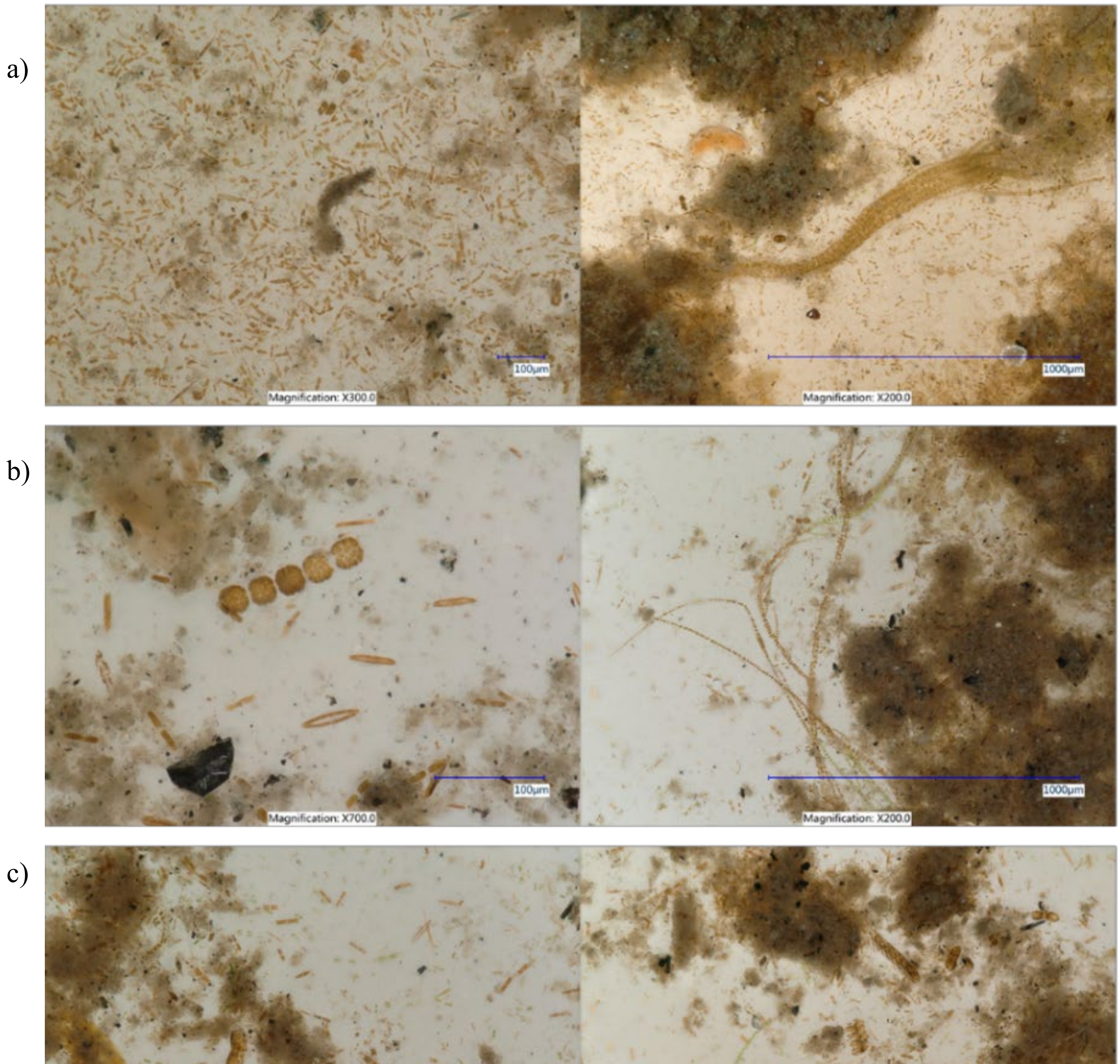

Figure 7-4. *Example microscopy photographs of biofilm samples taken from a) red, b) white and c) black coupons. On the left the scale bars = 100 µm and on the right the scale bars = 1000 µm. Magnification is noted at the bottom of every photograph.*

7.3.2 Structure of marine biofilms

A two-Way ANOVA was used to assess the effect of growth period (7- and 8-weeks) and coupon colour on biofilm thickness (mm), R_a^* and cover (%). For each colour there were no significant differences in structural properties based on growth period (P-value > 0.05). Visually, the biofilms grown on red, white, and black coupons displayed similar structural properties (Figure 7-5).

Figure 7-5. *Sample of biofilms grown on red, white, and black coupons in Hartlepool Marina (UK).*

OCT image analysis revealed that biofilms grown on white coupons were thicker, had greater surface coverage and were more homogenous (lower R_a^*) when compared to biofilms on alternative coupons (Figure 7-6). Biofilms grown on red, white, and black coupons had an average thickness of 0.76 mm, 1.24 mm and 0.95 mm and an average cover of 96.5 %, 98.8 % and 98.0 % (Figure 7-6). Differences in thickness observed between biofilms on red: white and red: black coupons were deemed significantly different (P-value < 0.05) (Figure 7-6), as were differences in biofilm cover on red: white coupons (P-value < 0.05). Interestingly, there were no significant differences in R_a^* across all coloured surfaces. (Figure 7-6).

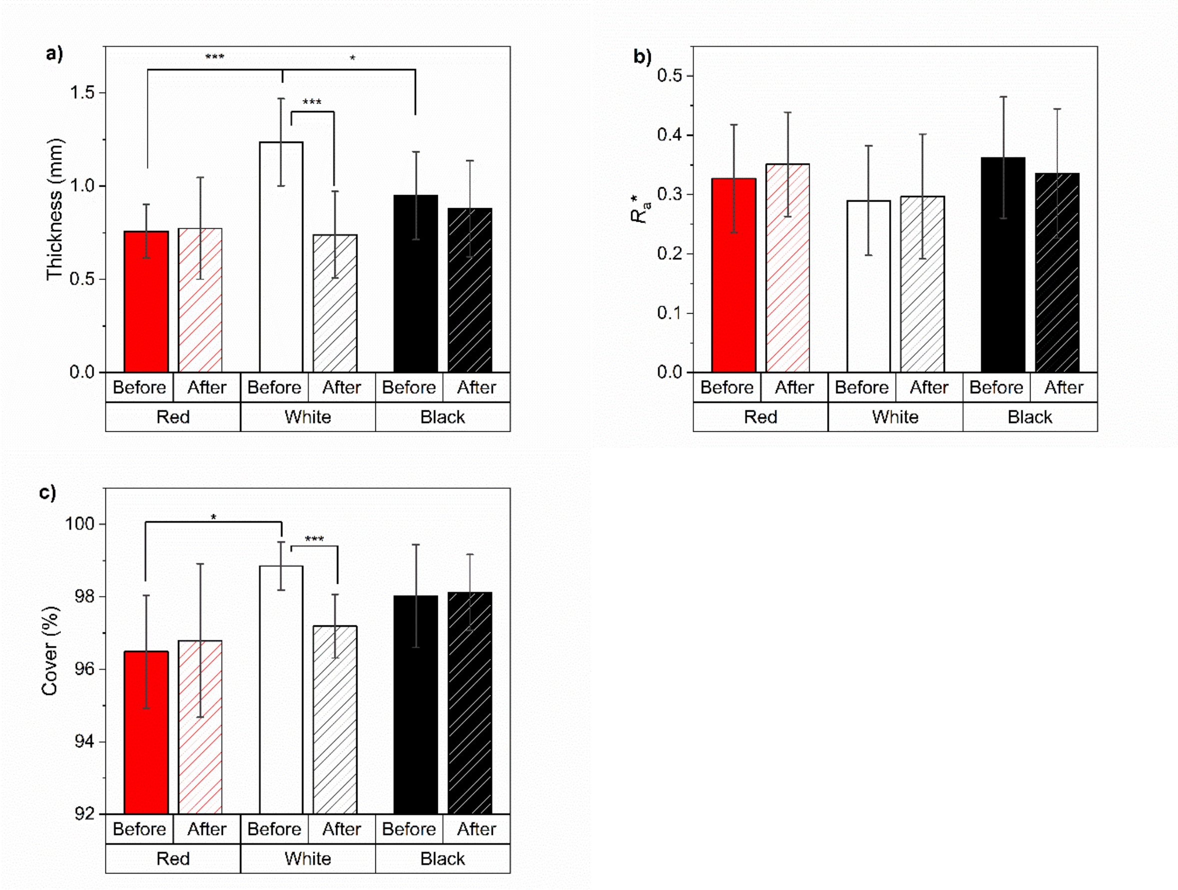

Figure 7-6. *Biofilm a) mean thickness (mm), b)* R_a^* *and c) cover (%) calculated from 3D OCT-scans before and after testing on a rheometer. P-values are shown as: * < 0.05, ** < 0.01, *** < 0.001, calculated using Kruskal Wallis and Dunn's test for colour comparisons and Welch's T-test for before-after data.*

The effect of dynamic rheometer testing on biofilm structure was also tested and acted as an indicator of biofilm strength. Biofilms on white coupons showed a significant decline in thickness and cover after rheometer testing (*P*-value < 0.01) (Figure 7-6). On the other hand, biofilms on red and black coupons remained unchanged, which suggests they are more robust. Again, R_a^* displayed no significant change for all colours (*P*-value > 0.05) (Figure 7-6).

7.3.3 Mechanical properties of marine biofilms

7.3.3.1 Colour and growth period did not affect yield stress

Across all coupons the LVR and σ_y was comparable, irrespective of colour and growth period (*P*-value > 0.05) (Figure 7-7). The LVR was identified using amplitude sweeps and was between 0.05 to 1 % strain (Figure 7-7a-c). For biofilms grown on red coupons σ_y was 7.0 ± 4.8 Pa, for white: 5.1 ± 2.8 Pa and for black: 6.0 ± 2.8 Pa (Figure 7-7d). After σ_y, a decline in *G′* and *G″* was observed for all biofilms, which is indicative of shear thinning behaviour (Souza-Egipsy *et al.*, 2021).

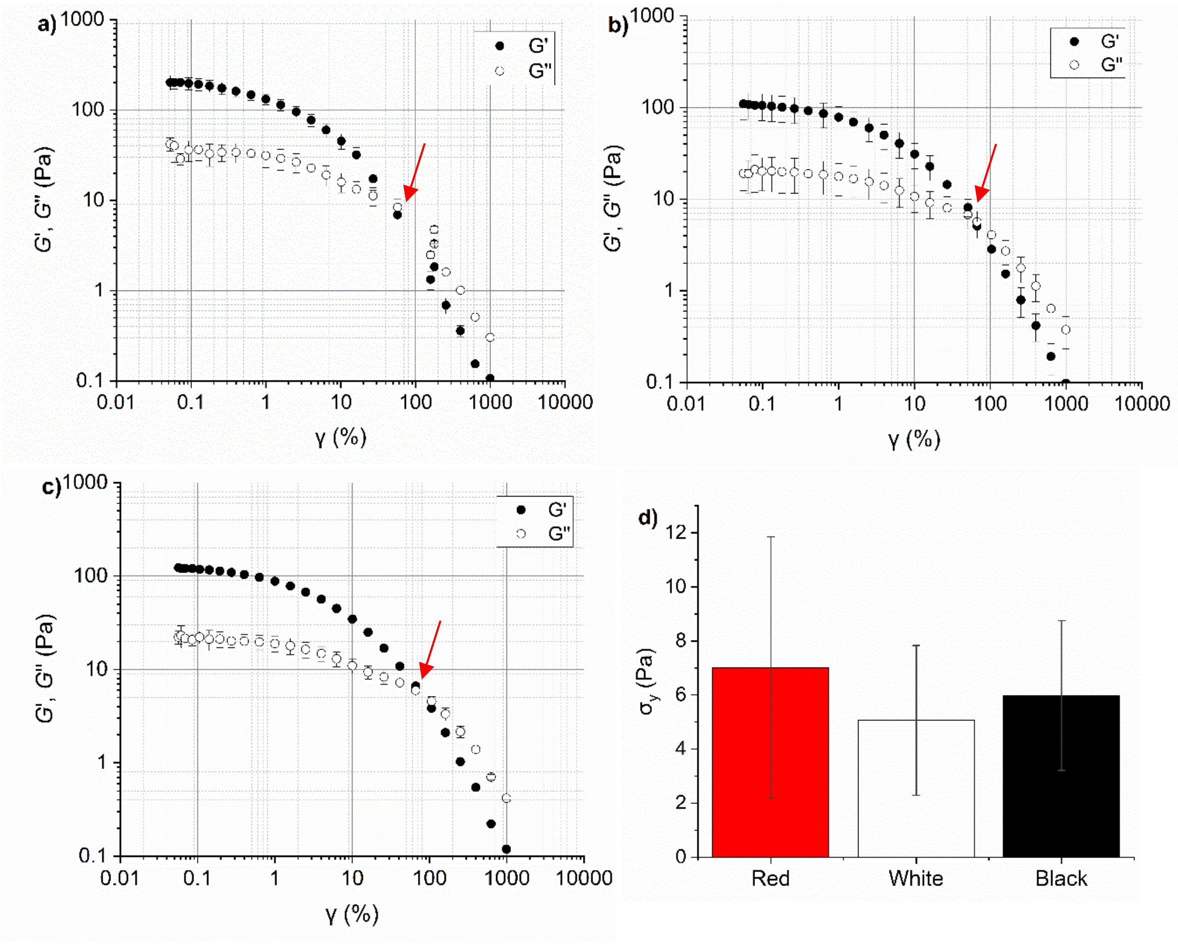

Figure 7-7. *Amplitude sweeps for biofilms grown on a) red (n = 8) b) white (n = 8) and c) black (n = 9) coupons. The red arrows indicate σ_y which is shown in d) as mean ± SD. Data were grouped by colour irrespective of growth period.*

7.3.3.2 Frequency sweeps

Frequency sweeps were executed at an oscillation strain of 0.1 %, which was within the LVR for all coloured coupons (n = 3 to 4) as shown in Figure 7-7. For biofilms grown on red coupons G' and G'' approximately doubled when comparing 7-week and 8-week data (P-value < 0.05) (Figure 7-8). Whereas for biofilms grown on black and white coupons at 8-weeks G' and G'' was approximately half that calculated for 7-weeks (P-value < 0.05) (Figure 7-8). After 8-weeks there were no significant differences in G' or G'' as a function of coupon colour (P-value > 0.05) (Figure 7-8).

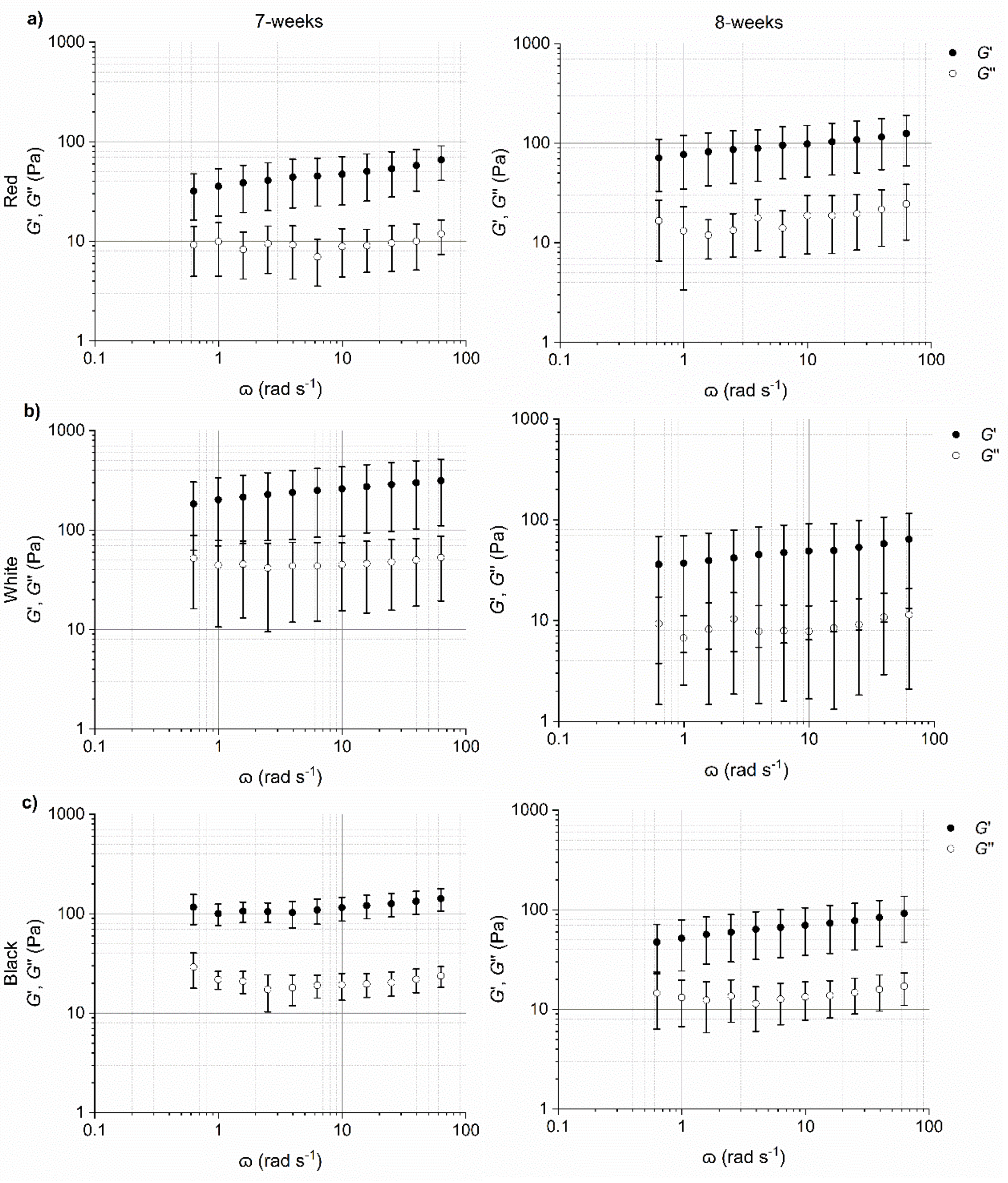

Figure 7-8. Frequency sweeps of biofilms grown on a) red, b) white and c) black coupons for 7- and 8-weeks. Data is presented as average ± SD (n = 3 to 4).

Overall, *G′* and *G″* were on the magnitude of 10^1 to 10^2 for all coupon colours (Figure 7-8). The biofilms grown on red, white, and black coupons showed comparable behaviour across the entire frequency range; *G′* dominated *G″* and phase angles remained below 15° which is indicative of a predominantly elastic response (Figure 7-8). Further, *G′*, *G″* and phase angle was relatively independent of increasing frequency which suggests behaviour analogous with gels (Stefano *et al.*, 2009; Souza-Egipsy *et al.*, 2021). A negative correlation between increasing frequency and η^* was observed which is indicative of shear thinning behaviour (Vinogradov *et al.*, 2004).

7.3.3.3 Shear modulus and viscosity are influenced by colour and time

The creep curves for biofilms grown on red, white, and black coupons demonstrated the characteristic, time-dependent behaviour of a viscoelastic material (Figure 7-9) (Rupp, Fux and Stoodley, 2005; Karimi *et al.*, 2015). The biofilms showed some elastic recovery once stress was removed, however fluid-like behaviour and permanent deformation was experienced as depicted in Figure 7-9e as unrecoverable strain.

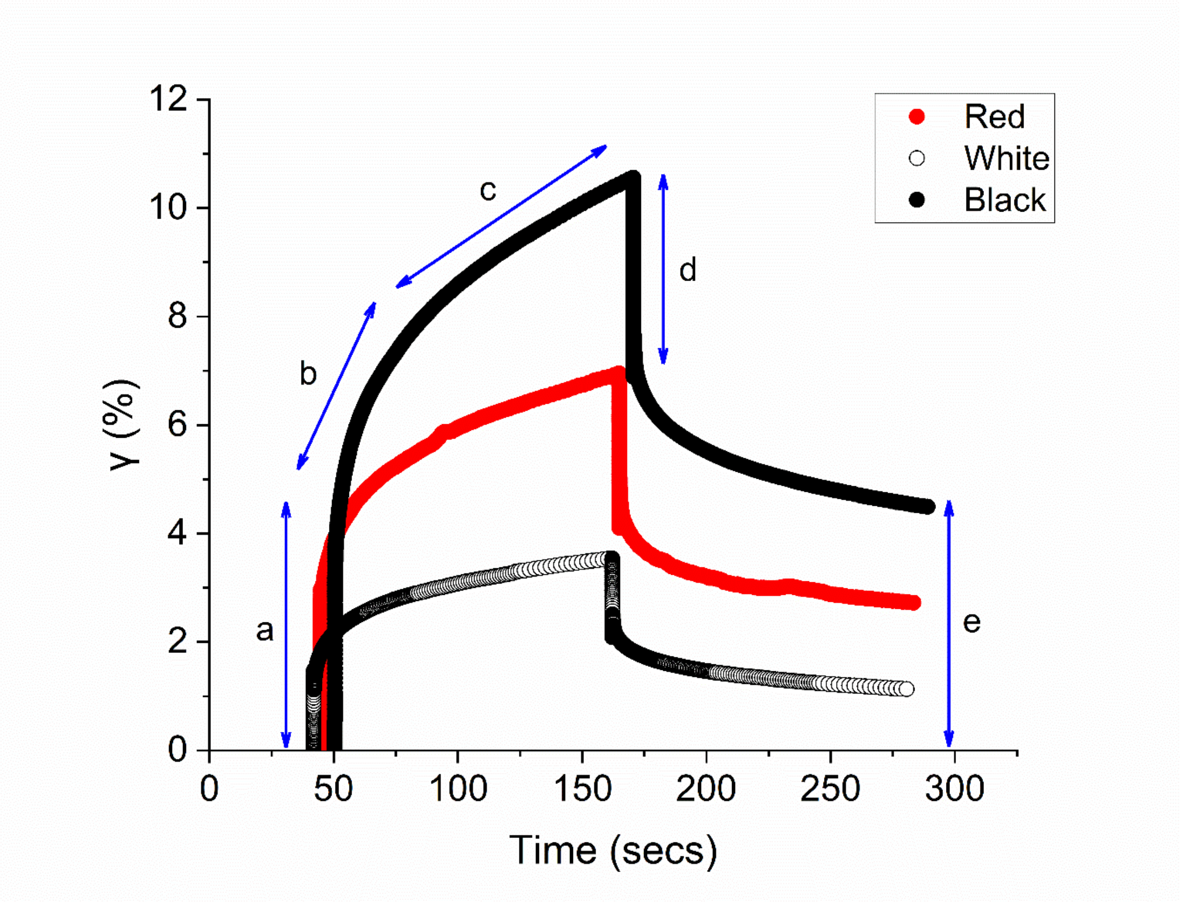

Figure 7-9. *Creep-recovery of biofilms grown on red (n = 4), white (n = 4), and black coupons (n = 4) at a stress of 1 Pa. The five stages of viscoelastic response are annotated (blue arrows), a) instantaneous elastic response to stress, b) transient viscoelastic behaviour, c) linear viscous response, d) elastic recoil and e) unrecoverable strain. Data from 8-weeks has been used as an example.*

Figure 7-10 shows estimates for the effective shear modulus (G) and effective viscosity (η) of biofilms calculated using creep curve data from across the LVR for each coupon type. Despite structural continuity between biofilms cultivated for 7- and 8-weeks, there was mechanical variation for biofilms grown on white coupons (P-value < 0.05). Biofilms grown on white coupons for 8-weeks possessed a significantly higher G and η when compared to the 7-week counterparts

(Figure 7-10). For the red and black coupons, no significant variation in biofilm mechanical properties based on time was observed (*P*-value > 0.05).

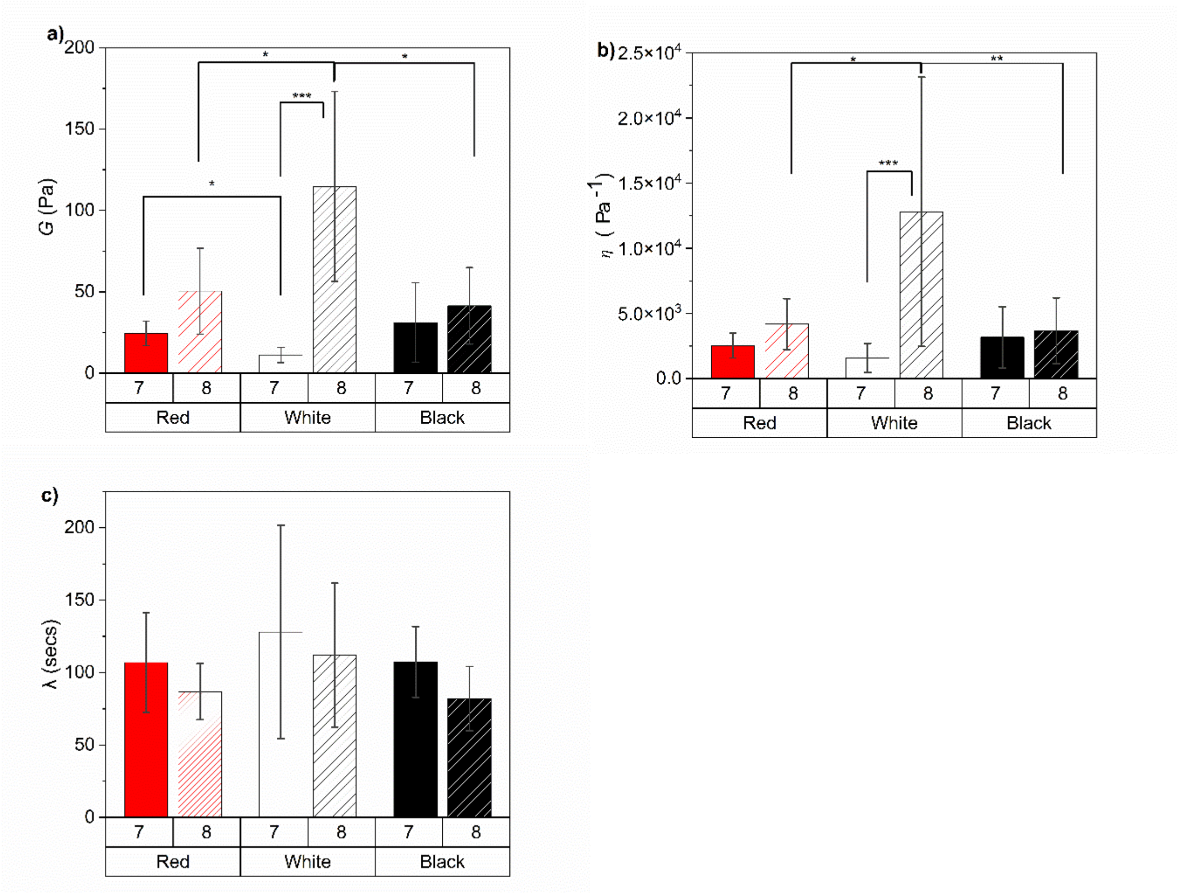

Figure 7-10. *Mechanical properties from the creep curves (Figure 7-9) a) G, b) η and c) λ, were calculated using the creep-recovery curves for red, white, and black coupons. Data is presented as mean ± SD (n = 3 to 4) and is shown for biofilms grown for 7 weeks (a, solid colour) and 8 weeks (b, striped). P-values calculated using a Kruskal Wallis and Dunn Test are shown as: * < 0.05, ** < 0.01, *** < 0.001.*

Differences in mechanics driven by colour were also observed. After 7-weeks of growth, biofilms on red coupons were stiffer, (possessed a significantly higher *G*) than biofilms on white coupons (Figure 7-10). Despite being the softest biofilms after 7-weeks growth, in week 8, biofilms on white coupons had a higher *G* and η than biofilms on red and black coupons (Figures 7-9 and 7-10). Interestingly, despite structural and mechanical differences, the elastic relaxation time of the marine biofilms were not affected by colour or time (Figure 7-10).

Studying the relationship between structural and mechanical biofilms across all coupons, irrespective of colour and week, revealed a significant inverse relationship between *G*: cover and *G*: thickness (*P*-value < 0.05). A lower thickness and coverage correlated with a higher *G* as seen for the red and black coupons when compared to the white coupons (Figure 7-10). A relationship between marine biofilm thickness and *G* was also suggested in Chapter 6 (Snowdon *et* al., 2023) and has been recognised for other biofilms in the open literature (Valladares Linares *et al.*, 2016).

7.4 Discussion

The results from this study suggest that marine biofilm physico-mechanics are significantly influenced by surface colour. The biofilms grown on white coupons were thicker, showed greater coverage and possessed a different mechanical profile to those grown on red and black coupons. As the white coupons possessed a significantly lower OCA than the red and black coupons it must be considered that biofilm differences, in part, are due to surface wettability (Zheng *et al.*, 2021). Huggett, Nedved and Hadfield (2009) studied biofilms in Pearl Harbour and found that although there were differences in initial surface wettability the bacterial community composition after 10-days was comparable. Further, Dexter *et al.*, (1975) concluded that the greatest differences in biofilm attachment on surfaces with different wettability occurred in the first 10 hours of exposure in Woods Hole Harbour. As the biofilms in the present study were grown over 8-weeks it could be that the effects of surface wettability on long-term biofilm architecture is minimal.

Biofilms grown on red and black coupons exhibited comparable structural and mechanical profiles that were not affected by time (Figure 7-10). The similarities are likely explained by the presence of comparable dominant species in the biofilms (Souza-Egipsy *et al.*, 2021) or by surface properties, such as lightness of the coating and reflectivity. For example, Gambino *et al.*, (2018) found that red, blue and black surfaces had similar lightness ratings and oxidative stress levels due to limited light availability for phototrophs.

7.4.1 Colour effects the structure of marine biofilms

Biofilms grown on coloured coupons showed consistent structure over 7- and 8-weeks of growth and were all relatively homogenous (Figure 7-6). Overall, white surfaces simulated thick biofilms than black and red surfaces and showed greater coverage than biofilms grown on red surfaces (Figure 7-6). Gambino *et al.*, (2018) examined cyanobacterial biofilms and found that white surfaces produced thick biofilms with more biomass than red and black surfaces after 30-days of growth. The authors concluded that white surfaces maximised available light for biofilm formation and development due to photosynthetic components in the matrix. Although the present study had a longer growth period, from the results depicted in Figure 7-6 it could be argued that surface colour alters marine biofilm architecture on white surfaces over a longer period. To address this longer and shorter time points should be investigated.

To determine structural stability of marine biofilms, OCT scans were taken before and after rheometer testing. OCT showed that white coupon biofilms experienced a significant decline in thickness and cover of 50.2 % and 1.7 % respectively (Figure 7-6). OCT has been previously used to measure changes in marine biofilm structure as a result of dynamic testing and similar loss in cover and thickness has been determined (Fabbri *et al.*, 2018). Snowdon *et* al., (2023), for example, found that ACP and PVC biofilms grown statically, experienced a 67 % decline in thickness due to rheometer testing. It is often reported that biofilms develop 'fluffy' top layers during growth that can be 50 % more porous than the base layers and are therefore less resistant to shearing (Laspidou *et al.*, 2014; Jafari *et al.*, 2018); the base layers on the other hand are denser as they have been consolidated over time (Zhang and Bishop, 1994; Laspidou and Rittmann, 2004). As the white coupon biofilms were the thickest studied (1.2 mm) base layers could have become more consolidated than the biofilms on red and black coupons resulting in a stiff and dense structure (Zhang and Bishop, 1994) that could lead to greater resistance to shear (Valladares Linares *et al.*, 2016). The creep-recovery data for 8-week biofilms on white coupons, which shows a significant increase in *G*, supports this statement (Figure 7-9).

7.4.2 Colour and growth period effects the mechanical properties of marine biofilm on white surfaces

All biofilms investigated were viscoelastic (Figures 7-9 and 7-10). The effective *G* of marine biofilms grown on different coloured coupons ranged from 11.3 to 31.2 Pa after 7-weeks growth and increased to 41.4 to 114.8 Pa after 8-weeks growth. The data fits within the *G* range often quoted in the literature of a few Pa to several kPa (Tallawi, Opitz and Lieleg, 2017), yet it sits a few orders of magnitude lower than previously reported values for ship-relevant marine biofilms (Chapter 6). Differences in values can be explained by biofilm growth conditions, community composition (Souza-Egipsy *et al.*, 2021) and surface properties (Swain *et al.*, 2006; Qian *et al.*, 2007; Salta *et al.*, 2013).

Although biofilm structure was unaffected by one extra week of growth, the mechanical profile of those on white coupons was altered. At 7-weeks, biofilms were soft with a low viscosity (Figure 7-10), as expected from the relationship identified between structure and *G*. However, after 8-weeks *G* had increased by a factor of 10 and η a fraction of 8, making the white coupon biofilms the stiffest and most viscous biofilms investigated here (Figures 7-9 and 7-10). The change in viscoelasticity of biofilms on white coupons is highlighted in the frequency sweeps (Figure 7-8). Stiff and viscous biofilms typically possess a higher internal cohesiveness (Souza-Egipsy *et al.*, 2021) and are less readily deformable than softer biofilms, as shown in Figure 7-9; this rigidity could explain the structural disruption in the 8-week biofilms observed after rheometer testing. In part, the increase in *G* could be explained by a thicker consolidated base layer in the biofilms on white coupons after 8-weeks of growth, whereas after 7-weeks the softer 'fluffy' top layers may have been dominant hence a lower *G*. To confirm this, biofilm porosity and consolidation would have to be investigated.

Although there were no visual differences in biofilm communities on the coloured coupons (Figures 7-4 and 7-5), a shift in dominant species present could also be driving differences in biofilm mechanics. Biofilms cultivated on black and white surfaces for 40-days in the Sea of Oman showed comparable community composition but significant variation in bacterial and diatom species diversity (Dobretsov, Abed and Voolstra, 2013), which could further impact biofilm mechanics and resistance. For example, it has been shown that an increase in the concentration of bacterial cells increases elastic modulus (Barai, Kumar and Mukherjee, 2016); and a softer biofilm has been attributed to mobile organisms creating an open and deformable micro-structure (Souza-Egipsy *et al.*, 2021). Alternatively, a shift in EPS composition and production could also be responsible for a change in the viscoelasticity of a biofilm (Peterson *et al.*, 2013; Tallawi, Opitz and Lieleg, 2017) and could explain the spike in *G* and η for white coupons biofilms depicted in Figure 7-10 (Gloag *et al.*, 2018). It would be of interest to carry out taxonomic analysis and analysis of EPS composition to confirm this and to determine a link between colour, composition, and physico-mechanics of biofilms.

Despite variation in structural properties and mechanical behaviour of biofilms grown on white surfaces compared to red and black, a λ of approximately 103 seconds was reported across all coupons (Figure 7-10); this data was similar to that reported in Chapter 6 which was within the range of 100 to 200 seconds depending on surface treatment. A similar conclusion was met by Shaw *et al.*, (2004) who rheologically characterised 44 biofilms and found that although creep data was significantly different there was a commonality in λ.

7.4.3 Marine biofilms, drag and antifouling coatings

It is widely accepted that the physico-mechanics of marine biofilms influence drag. In fact, many studies have demonstrated how viscoelastic materials induce a greater drag when compared to rigid structures (Picologlou, Zelver and Characklis, 1980; Hartenberger *et al.*, 2020; Snowdon *et al.*, 2022). Therefore, although drag was not measured in the present study, it could be expected that biofilms on red and black coupons would induce a higher drag than biofilms on white coupons due to their compliance (Figure 7-9) and structural stability in response to dynamic testing (Figure 7-6).

Dobretsov, Abed and Voolstra (2013) advised that antifouling screening should be executed on darker surfaces (namely blue and black) as they promote the presence of fouling compared to white surfaces (Swain *et al.*, 2006). In the present study no significant differences were found in the biofilm coverage of white and black coupons (Figure 7-6); yet due to differences in their structural and mechanical profiles it could be argued that the red and black coupons simulated a 'stronger' biofilm which would be preferred when testing antifouling coating efficiency. For example, the structure of biofilms grown on black and red coupons were unaffected by rheometer testing (Figure 7-6). The resistance exhibited in response to imposed shear suggests that the biofilms grown on black and red coupons were more structurally robust as they adapted to changing conditions without removal (Figure 7-6). As EPS is partly responsible for biofilm resistance to external stressors such as biocidal, mechanical and environmental (Peterson *et al.*, 2015; de Carvalho, 2018), a higher structural stability in biofilms could be due to greater EPS production (Gambino *et al.*, 2018) or production of particular EPS elements, such as extracellular DNA (eDNA) (Tuck *et al.*, 2022). Gambino *et al.*, (2018) showed that black surfaces maximised EPS production during early growth (< 14 days) of cyanobacterial biofilms due to oxidative stress caused by limited light availability. Although EPS production was not studied here, it could explain the robustness of biofilms on red and black surfaces, and in part, is supported by the creep-recovery data collected after 8-weeks of growth (Figure 7-10).

Dobretsov, Abed and Voolstra (2013) also advised that white surfaces are best suited for maximising anti-fouling properties. Although there was > 94 % biofilm coverage across all coupons studied here, the data, in part, support this statement. Biofilms on white surfaces experienced the greatest structural disruption after being exposed to rheological testing (Figure 7-6) which could be expected to aid in removal. Of note, Dobretsov, Abed and Voolstra (2013) conducted their study over 40-days in the subtropical Sea of Oman, whereas the coupons in the present study had a fouling period of up to 8-weeks under temperate and seasonal conditions.

There is a need to better understand how structure influences marine biofilm viscoelasticity so that biofilm-associated drag can be better estimated. It can be concluded that structural properties of marine biofilms, namely thickness and coverage, significantly influenced G which would subsequently alter drag. However, despite structural continuity across biofilms on white coupons, the mechanical properties showed a significant shift which highlights how additional biofilm properties must be considered to have a role in driving biofilm mechanics (and consequently drag). Overall, these results signify how multiple biofilm characteristics are closely intertwined and demonstrates the complexity of studying biofilm-associated drag.

7.5 Conclusions

It is understood that the physico-mechanical properties of marine biofilm influence drag (Picologlou, Zelver and Characklis, 1980; Snowdon *et al.*, 2022). However, few studies have quantified ship-relevant marine biofilm viscoelasticity (Snowdon *et* al., 2023) and fewer still have investigated how marine biofilm physico-mechanics are affected by surface properties, such as colour. OCT image analysis confirmed that surface colour affects biofilm structural properties; white surfaces simulated a thicker biofilm than biofilms grown on red and black surfaces. Whilst structure was consistent with growth, creep-recovery revealed that G and η was affected by both colour and growth period. At 7-weeks biofilms grown on white surfaces were the softest biofilms investigated, yet at 8-weeks G and η significantly increased indicating a stiff and viscous biofilm. It is evident that there are colour driven changes to structure and mechanics of marine biofilms and that there is a complex relationship between the two properties; however, it must be acknowledged that differences could also be driven by changes in EPS composition or by dominant species present within the biofilm communities. Future work should endeavour to include these parameters, nevertheless, new results produced here have shown how surface colour alters biofilm physico-mechanics, with specific reference to white coatings, which could help inform future anti-fouling coating development.

8 Chapter 8: Impact of hydrodynamics on biofilm physico-mechanics and the overall effect on drag penalty

ABSTRACT

Marine biofilms were grown on smooth coated panels in flow cells at Hartlepool Marina (UK) from April to August 2022. To determine whether hydrodynamic conditions alter the physical and mechanical (physico-mechanical) properties of marine biofilms, they were grown under two different flow rates: low flow 2,000 L h^{-1} (LF) and high flow 4,000 L h^{-1} (HF). After four-months, a clean MBFC (with an integrated pressure drop system) was set up with OCT to allow simultaneous measurements of drag (expressed as a friction coefficient, C_f) and biofilm physico-mechanics through tracking structural deformation as a function of varying shear stress *in-situ*. Over a *Re* range of 1.2×10^4 to 5.2×10^4 it was concluded that hydrodynamic conditions significantly influence biofilm physico-mechanical properties and associated-drag. Overall, the LF biofilms were softer, thinner, displayed lower coverage and produced a significantly lower drag than the HF counterparts. Structural properties were strongly correlated with shear modulus (*G*) yet did not directly influence C_f, whereas *G* significantly affected C_f. Further, statistical analysis revealed that viscoelasticity alone could be used to predict $C_{f,\,I}$ over the *Re* range investigated. The novel approach of quantifying biofilm structure, viscoelasticity and drag simultaneously has highlighted the role viscoelasticity plays in marine-biofilm associated drag and has emphasised the need for new deformable models for making drag estimations.

8.1 Introduction

Marine biofilms cause an array of issues in the shipping industry. Perhaps the most recognised being an increase in frictional drag caused by the accumulation of biofilm, often referred to as slime, on a ship hull (Schultz and Swain, 2000; Schultz *et al.*, 2015) which further leads to an increase in fuel consumption and greenhouse gas emissions (Townsin, 2003; Schultz *et al.*, 2011). As a result, there is a need to better understand the role biofilms play in drag production as well as the contribution of individual properties on drag.

Marine biofilms are diverse assemblages of bacteria, diatoms and algae encased within a viscoelastic exudate referred to as the matrix (Salta *et al.*, 2013). The matrix provides protection to the biofilm from external stressors, such as chemical or mechanical (Peterson *et al.*, 2015) and is primarily composed of EPS (Flemming and Wingender, 2010). Marine biofilms also display a high level of heterogeneity, adaptability, and resistance to changing hydrodynamic conditions, such as those experienced on the side of a ship. Studies have demonstrated the adaptability of biofilms by studying how their attachment or detachment processes (Saur *et al.*, 2017), architecture and structure (Pereira *et al.*, 2002; Paramonova *et al.*, 2009), community composition and mechanical behaviour (Souza-Egipsy *et al.*, 2021), change when cultivated under varying conditions (Dunsmore *et al.*, 2002). For example, biofilms grown under higher shear are typically more cohesive than those grown under lower shear (Stoodley *et al.*, 2002; Vieira, Melo and Pinheiro, 2009; Fanesi *et al.*, 2021) which leads to a stiff structure (Paramonova *et al.*, 2009) with greater resistance to mechanical stress (Simões *et al.*, 2022). Although relationships have been reported across biofilm properties, the effect this may have on drag has been poorly studied. As a result, there is a need to characterise the physico-mechanical properties of marine biofilms under different hydrodynamic conditions as this will further our understanding of how properties interact with one another and further implicate drag (Fabbri *et al.*, 2019; Hartenberger *et al.*, 2020; Snowdon *et al.*, 2022).

The dynamic and resistant behaviour of biofilms make it challenging to link biofilm properties to drag, yet there is some consensus across the literature. It is widely accepted that structural properties, such as biofilm roughness is a dominant factor in drag-production mechanisms (Schultz, 2007; Andrewartha *et al.*, 2010; Murphy *et al.*, 2018). Also, viscoelastic behaviour is known to play a role in marine biofilm-associated drag (Picologlou, Zelver and Characklis, 1980; Schultz and Swain, 2000). Viscoelastic drag production has been demonstrated by studies that have compared drag induced by rigid structures to viscoelastic structures, such as natural biofilms (Picologlou, Zelver and Characklis, 1980; Hartenberger *et al.*, 2020) and elastomeric materials (Snowdon *et al.*, 2022). Woollen strands (Andrewartha and Sargison, 2011) and nylon threads (Ng and Walker, 2012) have also been adopted with an aim to mimic complex fluid-structure interactions of streamers -'finger-like' filamentous protrusions from the biofilm surface (Stoodley *et al.*, 1998) - thus effecting drag (Hartenberger *et al.*, 2020). Despite evidence of viscoelasticity increasing drag, rigid and homogenous structures are often adopted as the benchmark model system for studying biofilm-associated drag. In part, the continued use of rigid systems is because they offer reproducibility and have been shown to display comparable roughness profiles and drag penalty to naturally occurring biofilms (Murphy *et al.*, 2018). Despite some reported similarities, rigid structures cannot capture deformation and viscoelastic behaviour that biofilms are known to exhibit; as a result rigid models could be leading to inaccurate estimations and predictions of drag (Picioreanu *et al.*, 2018; Hartenberger *et al.*, 2020; Snowdon *et al.*, 2022).

Although it is recognised that biofilm viscoelasticity alters drag, to our knowledge, this relationship has not been verified *in-situ*. OCT has often been used to visualise biofilm deformation (Wagner *et al.*, 2010; Blauert, Horn and Wagner, 2015; Picioreanu *et al.*, 2018) and can be installed in conjunction with a flow cell (Figure 3-5) which offers the ability to determine deformation and drag simultaneously (Fabbri *et al.*, 2019; Snowdon *et al.*, 2022). This investigation aimed to quantify biofilm structure: thickness, cover and roughness (in the form of a roughness coefficient, R_s^*) and deformation using OCT whilst simultaneously measuring drag. Secondly, the effect of hydrodynamic conditions during growth on biofilm physico-mechanics and drag was investigated. The findings will help advance our understanding of biofilm drag-production mechanisms and could therefore aid the development of anti-fouling coatings. Further, our results should advance the development of experimental models used to estimate biofilm-associated drag (Snowdon *et al.*, 2022).

8.2 Materials and Methods

8.2.1 Preparation of panels

Four PVC panels measuring 85 cm (L) × 5.5 (W) × 0.1 (D) cm were prepared by applying a commercial marine coating scheme provided by AkzoNobel. Three layers of paint were applied; first, an anticorrosive primer, followed by a silicon tie coat and finally a topcoat. The topcoat was Intersleek ®1100 in grey. Coating layers were applied by spraying paint on one panel face and each coat had an average dry thickness of approximately 125 μm.

8.2.2 Dynamic biofilm growth in a MBFC

Two PVC panels were inserted into the top and bottom of a meso-scale MBFC designed for *in-situ* biofilm culturing under flow (Fabbri *et al.*, 2018, 2019). Briefly, the MBFC was comprised of a rigid, opaque PVC base and top plate, followed by clear acrylic side panels (Figure 8-1). Clear side panels were necessary to allow light into the system for biofilm growth and development. For more details on flow cell design please refer to Section 4.1 and Fabbri *et al.*, (2019).

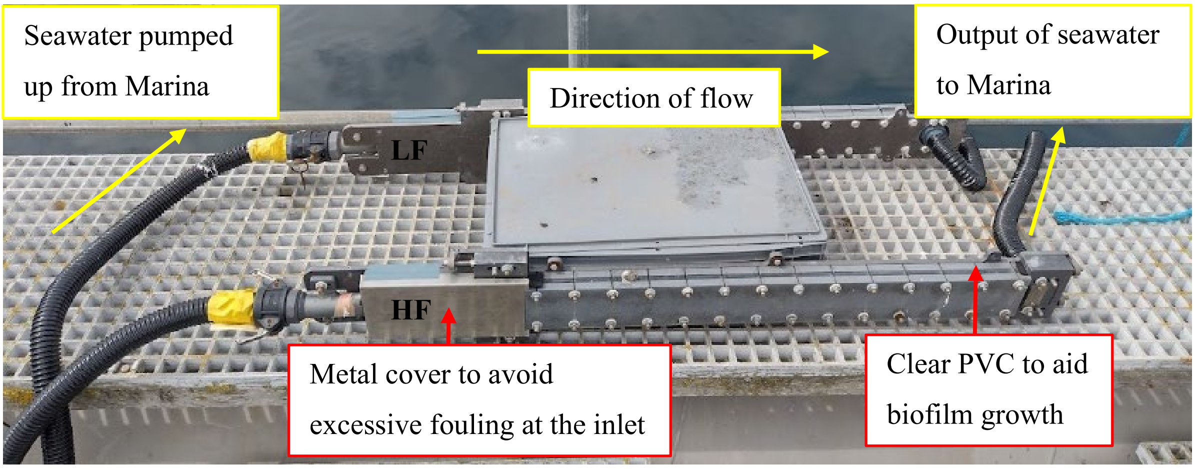

Figure 8-1. *Two MBFC's orientated on their sides at Hartlepool Marina (UK) set to run at two different flow rates, labelled as LF (top) and HF (bottom). Each MBFC housed two coated PVC panels facing each other. Yellow arrows show the direction of flow and red arrows provide extra information.*

Two MBFC's (2 panels in each) were set up at Hartlepool Marina (Hartlepool, UK) and each were operated from 4th April to 8th August 2022 to ensure sufficient biofilm coverage. Figure 8-1 shows how the MBFC's were set up; notably, the flow cells were orientated on their sides to reduce the risk of bubble scouring and disruption across the biofilms (Jang, Rusconi and Stocker, 2017) as well as for differences in gravitational settling of sediment across the panels. A submersible pump was attached to each flow cell via a flexible PVC hose that pumped fresh seawater through the flow cells (Figure 8-1). To test the hypothesis that biofilms grown under different flow conditions would result in different physico-mechanical properties and drag, the flow cells were set to run at different flow rates. One MBFC was set to run at ~ 2000 L h^{-1} (low flow, LF), and the other at ~ 4000 L h^{-1} (high flow, HF) (Aqua Medic DC Runner 9.2, max flow rate = 9000 L h^{-1}) which equated to ~ 2.0×10^4 *Re* and 3.5×10^4 *Re*. Maintenance occurred every two weeks to check that the systems were running smoothly. Over the fouling period the seawater temperature covered a range of 5 to 18 °C.

After 4-months, the MBFC's were removed from Hartlepool Marina (UK) and were carefully transported to AkzoNobel (Gateshead, UK) for hydrodynamic testing. To ensure the biofilms kept hydrated during transportation a bag was cable tied around each end of the flow cells to maintain a moist environment within. Once at AkzoNobel, the panels were carefully removed from the MBFC's and placed into a shallow container filled with Hartlepool seawater; pH and salinity were tested daily to ensure that the integrity of the biofilm samples before testing.

8.2.3 MBFC drag experiments

A clean MBFC with a recirculating tank of artificial seawater (ASW) was set up for testing biofilm-associated drag (Figure 4-1). A fouled panel was loaded into the base plate of the MBFC, and a clear top-plate was installed to act as a window for imaging using OCT (Figure 4-1). Fouled panels were exposed to a flow cell cycle for a duration of up to 40 minutes (which was an adaptation of the method outlined in Figure 4-2). ASW was slowly pumped through the MBFC before the cycle began so that the pressure sensors could be bled of any air in the system. The flow cycle involved incrementally increasing flow velocity by ~ 0.2 m s^{-1} (controlled by increasing the pump setting by 2.5 Hz) every two minutes until a maximum value of ~ 3.5 m s^{-1} was reached, followed by an incremental decrease back to 0 m s^{-1}. Two-minute steps were used so that the biofilm could adapt to the new flow velocity before OCT images were taken.

During the flow cycle, temperature and flow rate were monitored using a flow meter. Temperature ranged from 21 to 23 °C during testing. In conjunction, ΔP was continuously measured at a sampling rate of 180 per second using a DataQ data acquisition unit (Model DI-149) and WinDaq software (DataQ Instruments, Ohio, USA). By measuring ΔP, C_f could be calculated for every step in the flow cycle using Equation 3-8. L was taken as 0.8 m (distance between pressure ports) and ρ was the density of seawater (kg m^{-3}) calculated for every incremental stage in the flow cycle to account for temperature changes. In addition, D_h was calculated at every incremental stage to account for changes in flow cell height caused by changes in biofilm thickness.

A strong linear relationship between ΔP and u^2 is indicative of the turbulent regime (Massey and Ward-Smith, 1998; Fabbri *et al.*, 2019) and was exhibited in this study. Therefore, the slope of this relationship was substituted into Equation 3-8 to give an average instantaneous value for drag across the loading regime ($C_{\mathrm{f, I}}$).

As mentioned in Section 4.1 the MBFC was designed for culturing biofilms (Figure 8-1) (Fabbri *et al.*, 2018) and therefore had a shorter entry length and was overall smaller than flow cells typically used for measuring drag (Schultz *et al.*, 2015; Hartenberger *et al.*, 2020). Despite this, previous studies have shown that the MBFC used across these investigations provides fully turbulent conditions (Fabbri *et al.*, 2019; Snowdon *et al.*, 2022) as was also confirmed in the present study by studying the relationship between ΔP and u^2. For additional information on the design and hydrodynamic characterisation of the MBFC see Section 4.1. As ΔP and u^2 shared a strong linear relationship $C_{\mathrm{f, I}}$ was calculated for LF and HF biofilms.

It is important to note that all flow cell experiments were executed in an asymmetric system where the top-plate and side-plates were smooth, and the base plate possessed biofilm roughness. As this geometry could alter the flow velocity profile, it is acknowledged that C_f values could be system specific and henceforth will be referred to as C_f^*. As the focus of this work was to determine biofilm viscoelasticity (using OCT) in conjunction with drag (using an integrated pressure drop system) a smooth top-plate was considered an acceptable compromise. For further information on this experimental set up please refer to Snowdon *et al.*, (2022).

8.2.4 Optical Coherence Tomography (OCT)

An OCT was used to quantify and visualise biofilm structure and deformation during the flow cycle experiment as described in Section 4.2. In the present study, 2D-scans ($n = 3$) and a single 3D-scan were taken at every stage in the flow cycle. The 2D-scans had an acquisition rate of 0.14 seconds and measured 9 mm × 2 mm in the *xz*-plane whereas the 3D-scan was taken over 36.5 seconds and measured 9 mm × 9 mm × 2 mm volume (81 mm^2, 162 mm^3). Scan sizes were determined by previous studies that had specified an area of 3.4 mm^2 as the minimum required to provide representative data on biofilm mesoscopic features (Morgenroth and Milferstedt, 2009). ThorLabs software version 5.4.8 (Ganymede, ThorLabs, Germany) was used to control lighting, focus, and image settings.

8.2.4.1 Quantifying structural properties using 3D-scans

To quantify structural properties of LF and HF biofilms, 3D.oct files were exported into MATLAB (Version 2021B, MATLAB, 2021) and custom scripts produced by Fabbri *et al.*, (2018) were ran. Mean thickness (mm), R_a^* and cover (%) were calculated for all 3D-scans taken. For calculations see Section 4.2.1.

8.2.4.2 Quantifying rheological properties using 2D-scans

OCT 2D-scans were exported from ThorLabs as .tiff files for analysis in Fifi, ImageJ (Schindelin *et al.*, 2012). Average G was estimated from three OCT 2D-scans taken at every stage in the flow cycle using:

$$G = \frac{\tau_w}{\alpha} \qquad \textit{Equation 8-1}$$

where α is the angle of deformation and τ_w is shear stress calculated using Equation 3-4.

To calculate α for every velocity increment in the flow cycle, a prominent biofilm feature was randomly selected from OCT 2D-scans taken before the flow cycle began. Using the first set of images ($n = 3$) before the flow cycle began an initial angle was measured manually using Fiji, ImageJ (Figure 8-2a). Subsequent angles (Figure 8-2b) were then subtracted from the initial angle to give α. All angles were measured relative to zero and were converted to radians. As well as calculating G using Equation 8-1, stress-strain plots were produced to give a single G estimate for each fouled panel over the loading cycle.

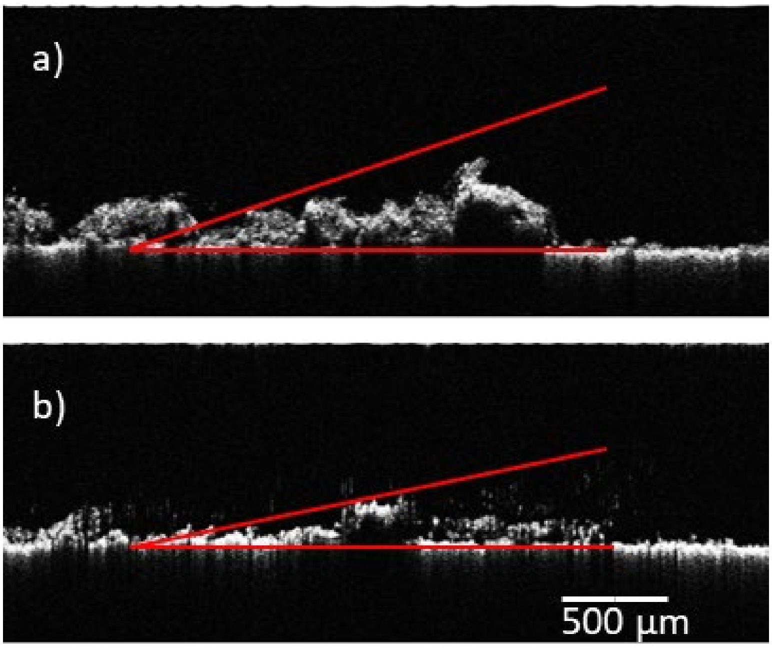

Figure 8-2. *Example OCT 2D-scans taken at a) before the flow cycle began (Re ~ 0) and b) during the flow cycle (Re < 5.2 × 10^4). The red lines show the manually measured angles that would be used to calculate the angle of deformation.*

8.2.5 Qualitative microscopy

Before performing the flow cycle experiments, biofilms samples were collected from all four fouled panels by carefully swabbing the edges. A single sample was transported to an Eppendorf tube with 2 mL of fresh Hartlepool seawater and was then stored in a fridge at 4 °C. Swabs were also taken after the biofilms had been exposed to a flow cell cycle to determine whether the communities were affected by applied shear stress.

A small amount of a biofilm sample (immersed in Hartlepool seawater) was pipetted onto a glass microscope slide and covered with a glass coverslip. Clear nail varnish was used to seal the coverslip edges to slow the biofilm dehydration process due to the heat of the microscope lamp. The prepared sample was then loaded onto a Keyence VHX-6000 digital microscope, fitted with a Z100 lens and white stage, which was used to qualitatively analyse the LF and HF biofilms before and after hydrodynamic testing. Full-ring and epi-illumination were applied to the samples for optimum lighting.

8.2.6 Statistical analysis

For statistical analysis R Studio (R Core Team, 2019) was used. To assess whether growing conditions had a significant effect on biofilm structure, mechanics and drag an ANOVA was implemented. If assumptions of an ANOVA were not met, such as normality and equal variance, a Welches T-Test or Kruskal Wallis was used.

As structural and mechanical properties of biofilms were continuously measured throughout the flow cycle, correlation analysis (Pearson's or Spearman's) could be applied to study whether a relationship existed between the properties. Correlation analysis was also used to determine relationships, if any, between structure or mechanics and C_f^*. If a significant relationship was found, linear regression was used to test whether C_f^* could be estimated from known structural and mechanical properties.

8.3 Results

8.3.1 Marine biofilm structure

An OCT was used to measure the structure of biofilms grown under low and high flow in Hartlepool Marina (UK). Both conditions lead to high biofilm coverage and showed evidence of animal fouling (Figure 8-3), specifically amphipods, which were particularly prevalent in the HF biofilms (Figure 8-3a). Amphipods are common in coastal waters and construct mud tubes that may have contributed to the overall biofilm structure and mechanical profile. Furthermore, there were visible differences between the LF and HF biofilms; the HF biofilms were thicker and more homogenous (Figure 8-3a) which could be confirmed using OCT analysis (Figure 8-4).

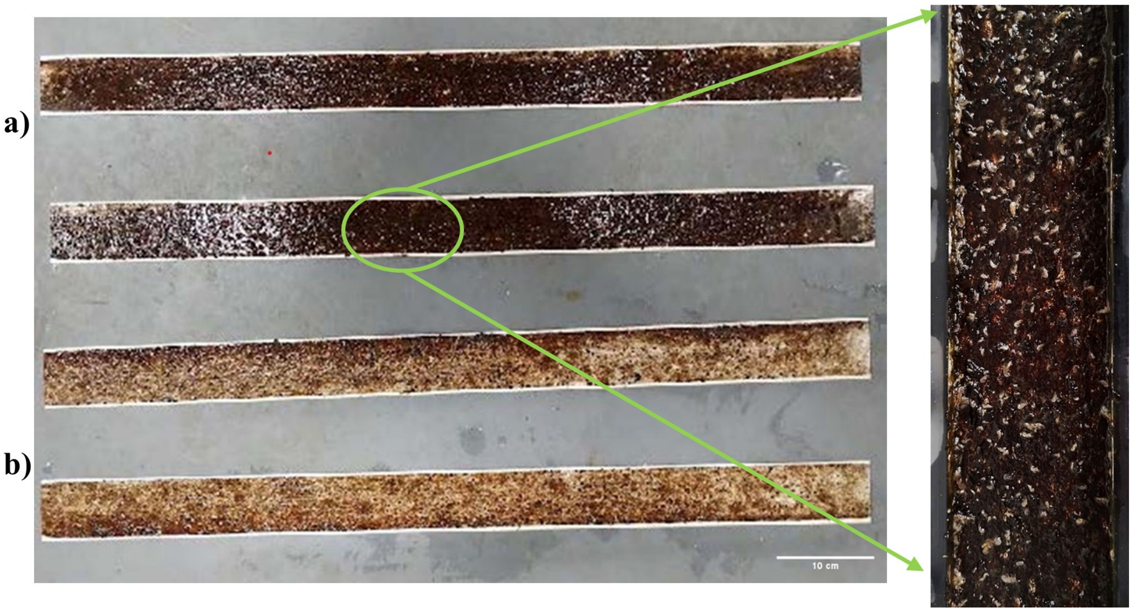

Figure 8-3. *Photographs of fouled panels (each measuring 85 cm × 5.5 cm) removed from Hartlepool Marina (UK) where biofilms were grown under a) high flow and b) low flow. The zoomed in area shows evidence of animal fouling, specifically amphipods (white specs), on a HF biofilm.*

To assess whether increasing shear altered biofilm structural properties the OCT was set up in conjunction with the MBFC (Figure 4-1). Over the entire flow cycle, statistical analysis confirmed that there were differences in cover, thickness, and R_a^* when comparing LF and HF biofilms (P-value < 0.05). As flow velocity increased, both HF and LF biofilms experienced a decrease in thickness and coverage and an increase in R_a^* (Figure 8-4). A higher R_a^* indicates that the biofilm is becoming more heterogeneous which could be expected as biofilm is sloughed or removed from a surface. Interestingly, both biofilms show an increase in thickness at lower *Re* stages (Figure 8-4b). From studying the OCT 2D-scans the change in thickness coincides with behaviour that could be described as inflation of the biofilm structure or streamer production, an example of which can be seen in Figure 8-5. After this point, both LF and HF biofilms showed a gradual loss in thickness as *Re* increased (Figure 8-4b).

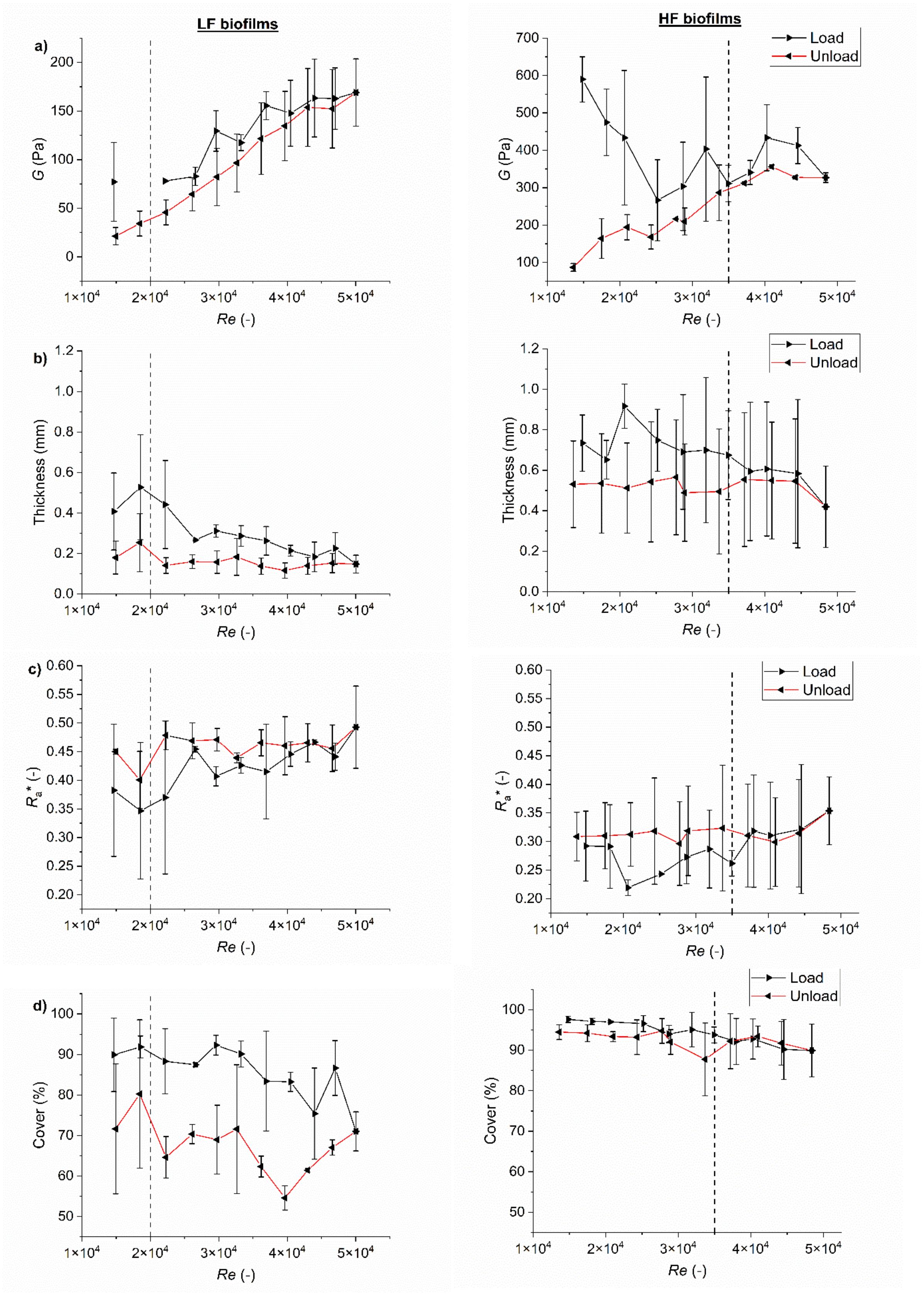

Figure 8-4. *Structural and mechanical properties of LF biofilms (left) and HF biofilms (right) plotted against Re and quantified using 2D and 3D-OCT scans: a) shear modulus, G (Pa); b) thickness (mm); c)* R_a^**; and cover (%). The loading regime (black line) and unloading regime (red line) are plotted and data are presented as mean ± SD (n = 2). The dotted vertical lines indicate the Re at which the biofilms were grown.*

LF and HF biofilms both experienced a change in thickness, cover and R_a^* around the *Re* at which they were grown, ~ 2.0×10^4 *Re* and 3.5×10^4 *Re,* respectively (Figure 8-4) yet the disruption experienced by LF biofilms was greater than that observed in HF biofilms (Figure 8-4). Disruption to the LF biofilms was also evident in the OCT 2D-scans depicted in Figure 8-5a; when a low level of flow was applied a lift response was seen, this quickly turned into streamer behaviour and removal events as higher *Re* are approached. Alternatively, for the HF biofilms there was less removal (Figure 8-4) and higher levels of streamer production (Figure 8-5b).

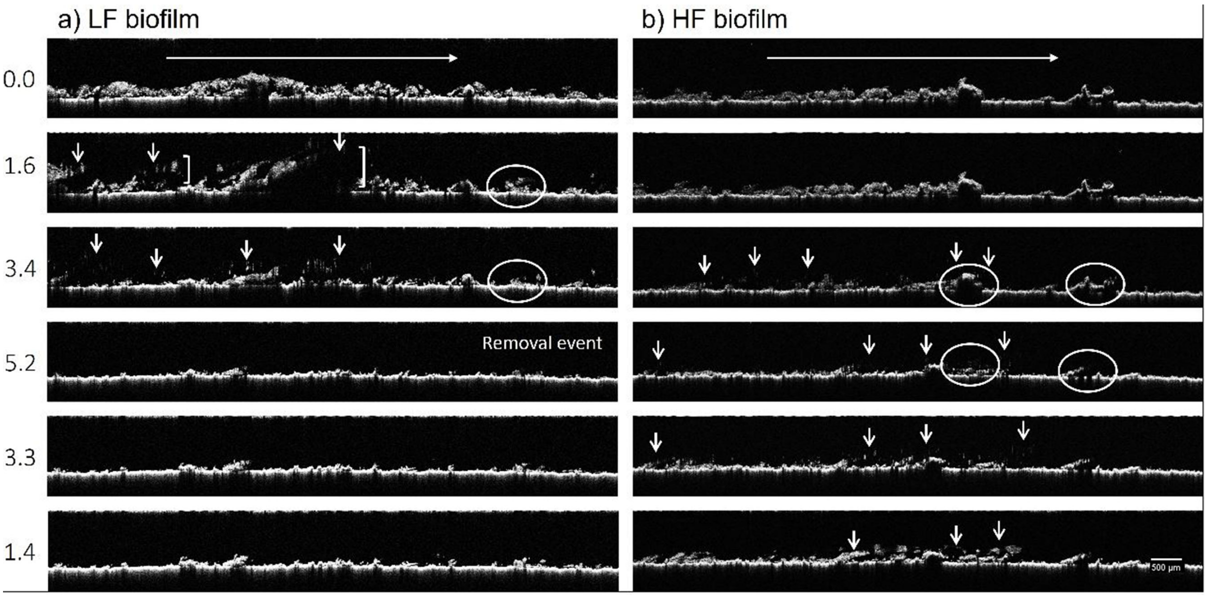

Figure 8-5. *Example OCT 2D-scans taken of a a) LF biofilm and b) HF biofilm. The numbers to show the direction of flow; white vertical arrows show areas of streamer production; white circles show specific areas of removal between scans and the brackets in a) 1.6 indicate lift behavior. The scale bar represents 500 µm.*

8.3.2 Rheological characterisation of marine biofilms

8.3.2.1 Using 3D-scans to calculate shear modulus, *G*

Angles of deformation (α) were measured from consecutive OCT 2D-scans in Fiji, ImageJ, to allow shear modulus to be calculated at every step in the flow cycle. The results showed that there was a significant difference in *G* calculated for LF and HF biofilms over the flow cycle (P-value < 0.05) which on average were 132.5 ± 50.6 Pa and 324.4 ± 19.0 Pa ($n = 2$), respectively. From OCT image analysis it was further confirmed that LF and HF biofilms were viscoelastic (Figures 8-5 and 8-6). As HF biofilms were stiffer than LF biofilms it could be suggested that the HF biofilms were more resistant to increasing shear. This was confirmed by analysing OCT 2D-scans taken throughout the flow cycle which showed how some HF biofilm features from the start of the cycle were still present at the end (Figure 8-5b) and is likely consequence to HF biofilms being cultivated under higher shear (Donlan, 2002; Krsmanovic *et al.*, 2021; Simões *et al.*, 2022).

Differences between the mechanical profiles of LF and HF biofilms were further depicted in the average stress-strain curves produced from α data (Figure 8-6). For the LF biofilms there was evidence of hysteresis as the loading and unloading curves do not coincide (Figure 8-6a); this behaviour is indicative of permanent deformation through viscous behaviour during the cycle (Figure 8-6a). Further, the stress-strain curves of the LF biofilms cover a longer and higher strain range compared to the HF biofilms which demonstrates the stiffness of HF biofilms under increasing shear conditions. Despite resistance, the HF biofilms still showed some evidence of permanent deformation although it was to a smaller degree than that observed for the LF biofilms (Figures 8-5 and 8-6). Note that OCT 2D-scans were not taken after the flow cycle ended and therefore biofilm recovery could not be measured.

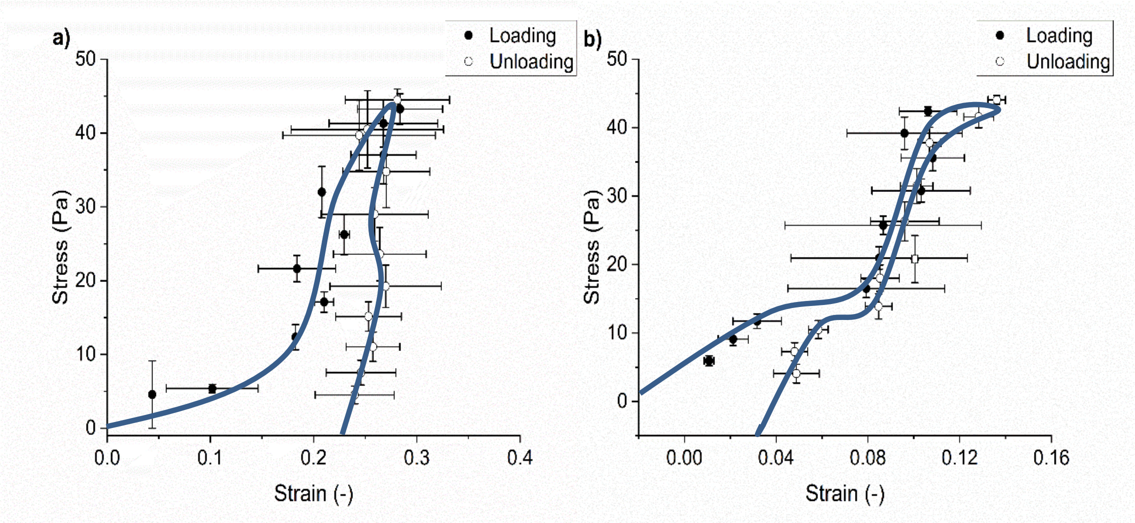

Figure 8-6. *Average stress-strain ± SD for a) LF biofilms and b) HF biofilms. Averages were taken from two biological replicates, where for each stage within the cycle for each replicate there were three OCT 2D-scans. The blue lines show the general stress-strain trend.*

8.3.3 Drag calculations from the flow rate pressure drop relationship

Drag, expressed as C_f^*, was calculated using pressure drop measurements and was plotted against *Re* (Figure 8-7). Despite the difference in cultivation conditions, LF and HF biofilms produced similar drag curves across a *Re* range of approximately 1.2×10^4 to 5.2×10^4. Both showed an initial jump in C_f^* followed by a gradual decline up to a *Re* of approximately 4.0×10^4 at which point there was a steep decline in C_f^* as *Re* continued to increase. From a *Re* of 2.0×10^4 to 4.0×10^4 there was a deviation between the LF and HF curves which could be explicable by changes to physico-mechanical properties, such as streamer action, sloughing or removal, as seen in

Figure 8-5. Note that a PVC panel was used as a smooth, unfouled control and is also presented in Figure 8-7.

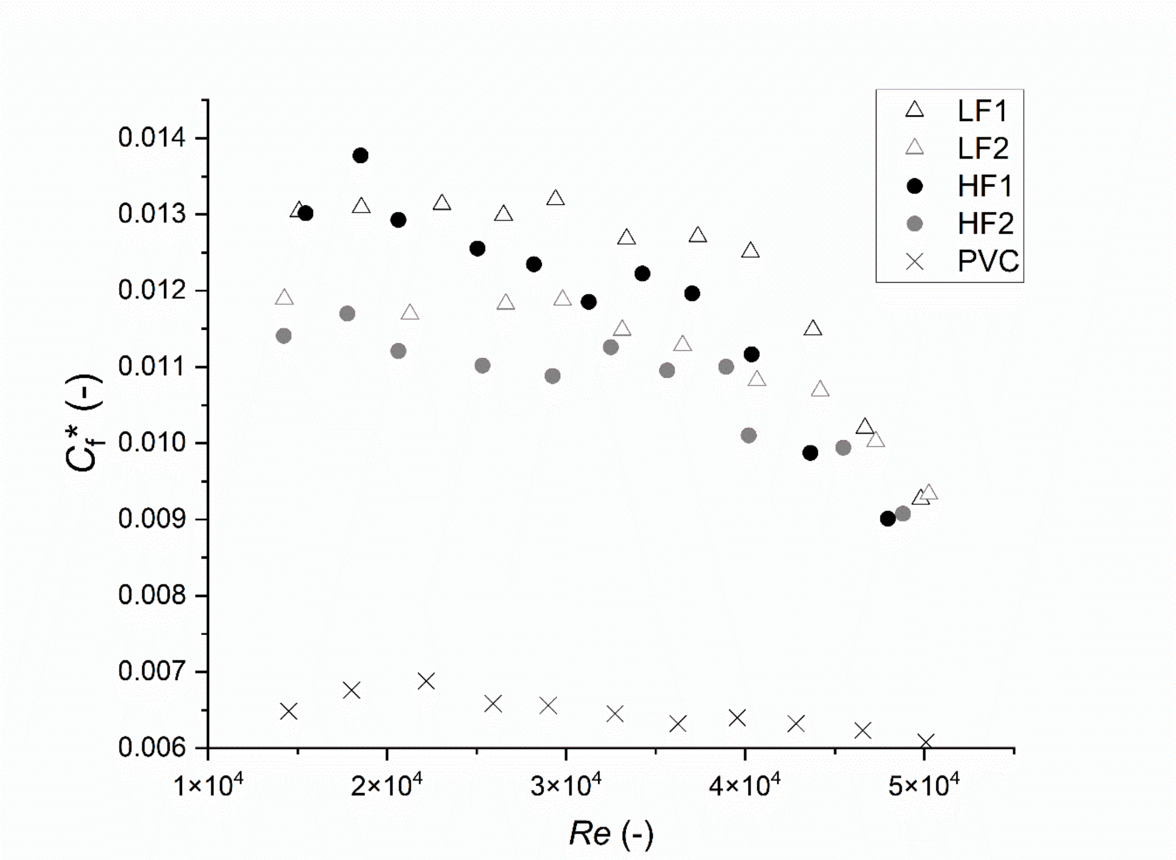

Figure 8-7. *C_f* plotted against Re for LF biofilms (open triangles) and HF biofilms (closed circles). Individual replicates are labelled as 1 and 2. Data for an unfouled smooth PVC panel is also plotted as a comparative control (crosses). Only loading data is plotted.*

For LF and HF biofilms ΔP vs u^2 showed a strong linear relationship, therefore a single $C_{f,\,I}$ value could be calculated (Fabbri *et al.*, 2019; Snowdon *et al.*, 2022). The average $C_{f,\,I}$ for LF biofilms was 5.7 % higher than that calculated for HF biofilms which was 0.0099 ± 2E-05 and 0.0094 ± 6E-05 ($n = 2$) respectively; and was deemed significantly different (ANOVA, *P*-value < 0.05).

8.3.3.1 Correlations between structural parameters, *G*, and C_f^*

Over the entire flow cycle, consecutive OCT-scans were taken to enable quantification of structural and mechanical properties. From correlation analysis, it was concluded that relationships existed between structural and mechanical properties of biofilms. Overall, a lower thickness and coverage and a higher R_a^* (more heterogeneous biofilm) correlated with a lower *G* (softer biofilm) (Figure 8-5).

Over the flow cycle the effect of structure and mechanics on C_f^* was studied. Data after $Re = 2.5 \times 10^4$ was used in calculations as this was the point at which *G* stabilised with respect to increasing *Re* (Figure 8-4). As expected, an increase in *Re* was correlated with a decrease in C_f^* (Figure 8-7 and

Table 8-1) (Moody, 1944; Fabbri *et al.*, 2019; Snowdon *et al.*, 2022). Despite relationships existing between structure and mechanics, cover, thickness, and R_a^* showed no significant relationship with C_f^* during loading, whereas G did (Table 8-1); a lower G correlated with a higher C_f^* (P-value < 0.05). This relationship was also determined for the average values of G and $C_{f,\,I}$ calculated for LF and HF biofilms (P-value < 0.05). Further, a linear regression revealed that average G could be used to estimate and predict average $C_{f,\,I}$ (P-value < 0.05, $R^2 = 0.92$).

Table 8-1. *R^2 values taken from correlation analysis executed on marine biofilm structural, mechanical and drag data calculated over the loading regime of the flow cycle (starting from Re = 2.5 × 10^4).*

	Re	**Thickness**	$\boldsymbol{R_a^*}$	**Cover**	$\boldsymbol{G}$	$\boldsymbol{C_{f,\,I}}$
Re	x	**-0.51**	-0.32	**-0.48**	0.14	**-0.73**
Thickness	**-0.51**	x	**-0.84**	**0.96**	**0.36**	0.31
$\boldsymbol{R_a^*}$	-0.32	**-0.84**	x	**-0.82**	**-0.43**	-0.04
Cover	**-0.48**	**0.96**	**-0.82**	x	0.23	0.3
$\boldsymbol{G}$	0.14	**0.36**	**-0.43**	0.23	x	**-0.42**
$\boldsymbol{C_f^*}$	**-0.73**	0.31	-0.04	0.3	**-0.42**	x

8.3.4 *Qualitative microscopy*

As biofilm community can play a role in structural and mechanical properties, qualitative microscopy was executed (Paramonova *et al.*, 2009; Souza-Egipsy *et al.*, 2021). Visually, biofilms were similar in colour and had an amphipod presence which was confirmed using qualitative microscopy (Figure 8-9). Diatom chains and red and green algae were also prevalent in both LF and HF biofilms.

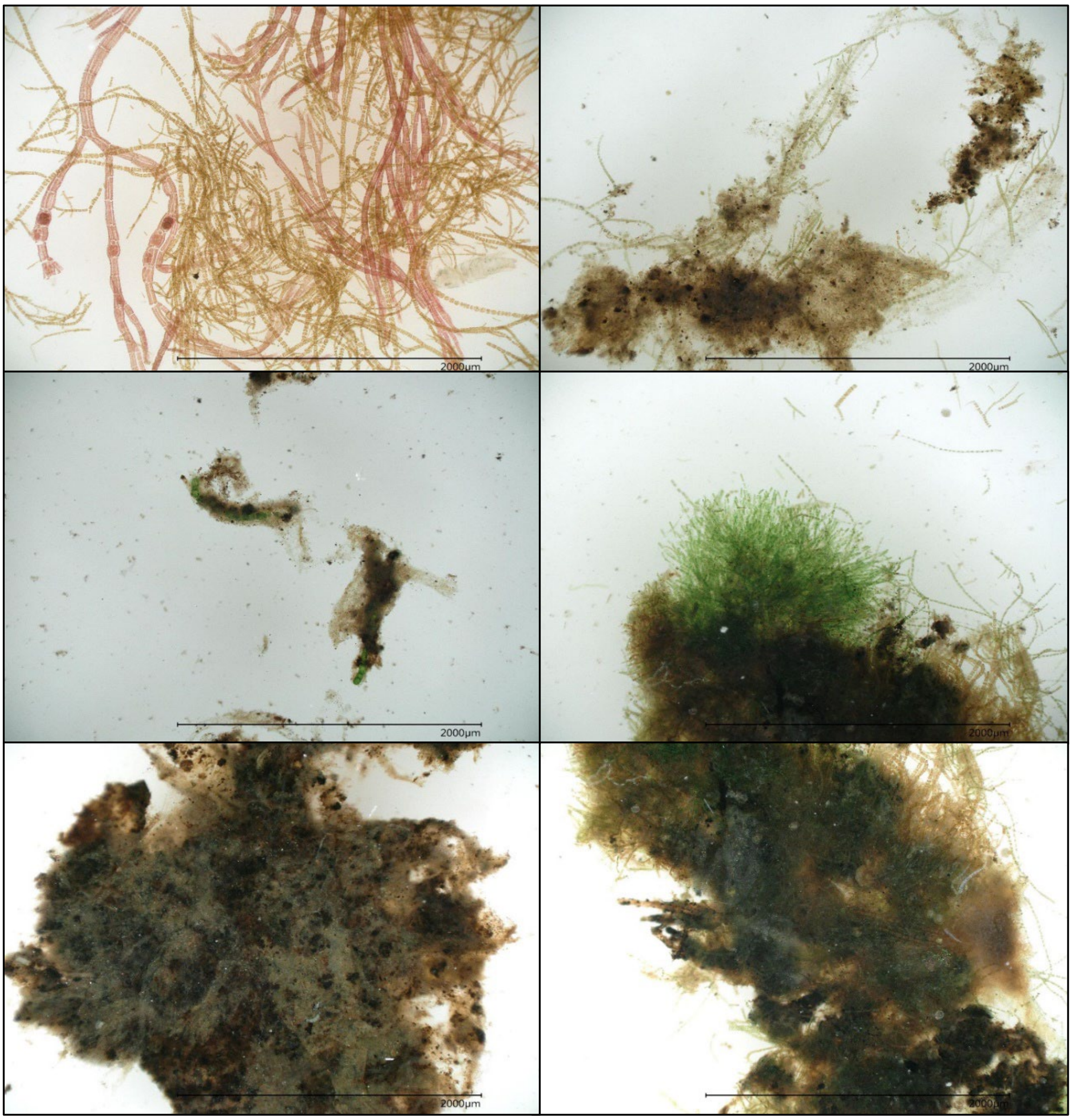

Figure 8-8. *Example photographs of a) LF biofilms and b) HF biofilms, taken using a digital microscope. The scale bar in every photo represents 2000 µm.*

8.4 Discussion

LF and HF biofilms housed diatoms and seaweed, but they also had an animal presence in the form of amphipods (Figures 8-3 and 8-8) which are common in coastal waters. Amphipods construct and inhabit mud tubes and as they were more prevalent in HF biofilms (Figures 8-3), it must be considered that some differences in biofilm physico-mechanics could be consequent to their presence. As biofilms on ships do not grow in isolation the community observed in the present study could, in fact, be more representative of real-world scenarios where biofilm fouling interacts with animal fouling.

8.4.1 In-situ determination of biofilm physico-mechanical properties using OCT

By measuring α as a function of increasing shear stress, viscoelasticity could be determined and expressed as G. Over the same range structural properties, namely thickness, cover and R_a^*, were also calculated. This allowed relationships between structural and mechanical properties to be statistically determined (Figures 8-4 and 8-6 and Table 8-1).

The LF and HF biofilms both exhibited viscoelastic behaviour (Figures 8-5 and 8-6). The LF biofilms were softer, with a G of 132.5 ± 19.0 Pa, than the HF biofilms which measured 324.4 5 ± 50.6 Pa. The G values reported in this study fit well within the range often cited in the literature for biofilms (Tallawi, Opitz and Lieleg, 2017) and concur with previously reported values for ship-relevant marine biofilms (see Chapters 6 and 7). Cultivating biofilms under a high flow velocity has been associated with a greater resistance to applied stress when compared to biofilms grown under lower flow (Stoodley, Boyle, Cunningham, Dodds, *et al.*, 1999; Simões *et al.*, 2022). In part, the resistance to shear is explicable by structure (Paramonova *et al.*, 2009; Desmond, Morgenroth and Derlon, 2018). During growth, biofilms adapt to hydrodynamic conditions by altering their structural properties (Fanesi *et al.*, 2021) and as a consequence their mechanics change (Paramonova *et al.*, 2009; Simões *et al.*, 2022). A significant relationship between biofilm structure and mechanics is exemplified in the present study for both LF and HF biofilms.

Generally, a higher shear stress promotes a dense, thin and cohesive biofilm with good coverage (Stoodley, Lewandowski, Boyle, *et al.*, 1999; Krsmanovic *et al.*, 2021; Soares *et al.*, 2022) that is structurally strong (Pereira *et al.*, 2002) and mechanically resilient (Simões *et al.*, 2022). Although the HF biofilms displayed a high coverage and greater resistance to shear, they were almost twice as thick (0.73 mm) as the LF biofilms (0.41 mm) across the flow cycle (Figures 8-4 and 8-5). Paramonova *et al.*, (2009) assessed the impact of hydrodynamic conditions on biofilm architecture and compressive strength of different types of dental biofilm: single- and dual-species biofilms and a wild-type biofilm grown from dental plaque. The authors concluded that regardless of biofilm type, an increase in thickness when grown under higher shear was observed (Paramonova *et al.*, 2009). Applying flow during biofilm development has been shown to promote thicker biofilms than those grown under static conditions due to greater mass transfer and nutrient availability through the biofilm (Stoodley *et al.*, 1999; Fernandes *et al.*, 2021). In the present study, and in Paramonova *et al.*, (2009) biofilms were not grown statically; yet, the thcikness of the HF biofilms could be explicable by an optimal balance existing between shear induced detachment and biomass accumulation due to high mass transfer and nutrient availability (Stoodley *et al.*, 1999; Stoodley, Boyle, Cunningham, Dodds, *et al.*, 1999). In support of this point, HF biofilms had a greater concentration of streamers than LF biofilms (Figure 8-5); the development of streamers has been previously suggested as a survival strategy for biofilm communities as their oscillatory actions can optimise nutrient availability and mass transfer whilst reducing the risk of detachment (Taherzadeh *et al.*, 2010). Alternatively, as biofilms grown under lower shear are often softer, such as the LF biofilms here (Figure 8-6), they could perhaps experience greater removal or sloughing resulting in a thin and patchy biofilm. The OCT-scans (Figure 8-5) and quantitative analysis (Figure 8-4) confirmed that LF biofilms experienced greater structural disruption than HF biofilms in response to increasing stress.

Using OCT to visualise biofilms in membrane systems Valladares Linares (*et al.*, 2016) concluded that a decline in biofilm thickness was coupled with an increase in G. In part, this behaviour could be explained by removal of ‘fluffy’ top layers which reveal denser base layers that have been consolidated over time and are subsequently more rigid (Desmond, Morgenroth and Derlon, 2018; Jafari *et al.*, 2018). Above a *Re* of approximately 2.0×10^4, LF and HF biofilms showed a reduction in thickness and an increase in *G* but at lower *Re* they deviated (Figure 8-4). LF biofilms maintained a relatively consistent *G* at lower *Re* although it is worth noting that LF biofilms were cultivated at approximately $Re = 2.0 \times 10^4$ and therefore could be expected to display stability up to this point (Stoodley, Lewandowski, Boyle, *et al.*, 1999). HF biofilms, however, were cultivated at approximately $Re = 3.5 \times 10^4$ yet showed a strong decline in *G* at *Re* lower than the cultivation *Re* and an increase in *G* at higher *Re.* As OCT scans were taken throughout the flow cycle, they were used to visualise behaviour at different stages; HF biofilms experienced greater streamer action than LF biofilms (Figure 8-5) (Stoodley, Lewandowski, Boyle, *et al.*, 1999) which could explain the apparent softening at lower *Re* as streamers are typically much softer than the bulk biofilm (Murphy *et al.*, 2018).

The OCT scans allowed visualisation of dynamic biofilm behaviour and also offered insights into the structural and mechanical heterogeneity exhibited by biofilms (Milferstedt, Pons and Morgenroth, 2009; Pavissich, Li and Nerenberg, 2021). For example, although the LF biofilms were generally softer than the HF biofilms there were structural features which possessed a significantly higher *G* and demonstrated resistance to removal over the flow cycle (Figure 8-5a).

However, it must be noted that although heterogeneities can be visualised the OCT only offered a 9 mm^2 view into a much larger biofilm area. OCT-scans were captured close to the flow cell inlet where pressure was as its highest, it could be expected that the downstream sections of biofilm would possess very different physico-mechanical properties to those quantified here (Picioreanu *et al.*, 2018; Fabbri *et al.*, 2019) due to variation in water pressure, nutrient availability and mass transfer. In addition biofilm clusters have been known to detach from a surface, migrate downstream and reattach (Dunsmore *et al.*, 2002; Nguyen *et al.*, 2021), this behaviour could be expected to alter drag yet may not be captured as biofilms clusters move out of the OCT field of view. Similarly, biofilm clusters could 'roll' into the field of view and was possibly observed here for the LF biofilms where an increase in cover was recorded at multiple stages in the flow cycle (Figure 8-4). Ideally, the OCT field of view would be larger however the test conditions were selected to optimise resolution, area covered and acquisition time during dynamic testing. Despite these limitations, OCT is a powerful tool and in conjunction with the MBFC offers new insights into biofilm viscoelastic behaviour, such as streamer production, and could be used to study biofilm development and detachment.

8.4.2 Biofilm physico-mechanical properties and drag

Flow cells are often utilised for measuring biofilm-associated drag (Schultz, 2007; Hartenberger *et al.*, 2020) and have been previously used in conjunction with imaging methods, such as OCT, for measuring mechanical deformation of viscoelastic entities, such as biofilms or synthetic materials (Blauert, Horn and Wagner, 2015; Picioreanu *et al.*, 2018; Snowdon *et al.*, 2022). Fabbri *et al.*, (2019) used the same flow cell employed in the present study and demonstrated how biofilms could be cultured under flow and then assessed for drag, whilst simultaneously using an OCT to capture biofilm structure. The data produced here highlights the advantages of the techniques used by Fabbri *et al.*, (2019) whilst also progressing them by introducing simultaneous measurements of viscoelasticity as a function of shear stress.

Despite a 5.7 % difference in $C_{f,I}$, the drag curves for LF and HF biofilms exhibited a similar trend under increasing *Re* (Figure 8-7). Below a *Re* of 2.0×10^4 there was a small spike in the experimentally determined C_f^* followed by a relatively plateaued region where C_f^* showed little change with increasing *Re*. At approximately $Re = 4.0 \times 10^4$ there was a marked decline in C_f^* as *Re* continued to increase. Perkins *et al.*, (2012) investigated naturally grown biofilms in hydropower pipes and found a plateau in C_f at lower *Re* which was followed by a sharp decline that was attributed to shearing of the biofilm; it was also suggested that flattening of the biofilm against the pipe walls could cause the observed trend (Lambert *et al.*, 2009; Perkins *et al.*, 2012). A similar trend was also found by Snowdon *et al.*, (2022) who studied drag associated with an elastomeric sandpaper surface, but as removal and shearing was not possible the C_f^* vs *Re* trend was attributed to deformation (Chapter 5). Instead of assuming biofilm deformation is responsible for changes in C_f an OCT was employed to capture viscoelastic behaviour in real time (Figure 8-5). Here, flattening was not observed, however both LF and HF biofilms exhibited deformation, shearing and streamer action before $Re = 4.0 \times 10^4$ (Figure 8-5). After this point, LF biofilms experienced high levels of removal which could explain the significant decline in C_f^* (Figure 8-7). For the HF biofilms, however, little removal was observed (Figures 8-4d and Figure 8-5b). Instead, the decline in drag could be explicable by hardening of the biofilm structure, shown as an increase in G in response to increasing Re past the conditions applied during growth (approximately $Re = 3.5 \times 10^4$) (Figure 8-4a). Collectively, the results suggest that although there are similarities in the drag curves, different fluid-structure interactions could be driving the trends in LF, and HF biofilm associated-drag. Furthermore, it is evident that drag curves associated with viscoelastic structures, whether natural or synthetic, do not coincide with those seen for rigid materials due to deformation behaviour (Hartenberger *et al.*, 2020; Snowdon *et al.*, 2022). As a result, using rigid models to estimate and predict biofilm-associated drag could lead to large under estimations.

It was concluded that biofilms grown under a lower flow velocity were thinner, more heterogeneous, and softer, determined by a lower G, than biofilms grown at a higher flow velocity and over a Re range of 2.5×10^4 to 5.2×10^4 induced a greater drag. Note that although LF biofilms induced a greater drag they also experienced greater removal, therefore at higher Re ($> 5.2 \times 10^4$) the more resistance HF biofilms may produce a greater drag due to higher biofilm coverage (Murphy *et al.*, 2022). Overall, our findings concur with the open literature which recognises that viscoelastic structures, namely biofilms, increase drag (Picologlou, Zelver and Characklis, 1980; Schultz *et al.*, 2015). By using a MBFC and an OCT the dynamic nature of marine biofilms in response to increasing shear has been successfully captured in real-time and could be related to drag. Our results highlight the complexity of marine biofilms in response to flow but also how different hydrodynamic conditions lead to varying properties (Figures 8-4 and 8-5). Due to the heterogeneity of biofilms, future models should endeavour to incorporate viscoelastic replicas of naturally grown biofilms to capture deformation and topographical changes with increasing flow velocity.

8.5 Conclusion

It is widely accepted that viscoelastic structures influence drag, expressed as C_f^* here. This has been confirmed by studies that have compared drag associated with viscoelastic and rigid materials. In the present study, a novel approach was adopted where physico-mechanical properties of ship-relevant marine biofilms were characterised *in-situ* whilst also measuring pressure drop to enable C_f^* to be calculated as a proxy for drag. Over a Re range of 1.2×10^4 to 5.2×10^4, it was confirmed that hydrodynamic conditions significantly influence biofilm structure and mechanics which consequently effects drag. The LF biofilms were softer than the HF biofilms (with a lower G) and showed evidence of permanent deformation and significant removal from the surface. The HF biofilms, however, were more rigid, displayed elastic recovery and structural stability. From OCT image analysis it was confirmed that structural characteristics of biofilms, namely thickness, cover and R_a^* correlated with G yet did not directly impact C_f^*. The LF biofilms caused a 5.7 % higher $C_{f,\mathrm{I}}$ than the HF biofilms which was correlated with differences in G. This study demonstrates how G should not be neglected when estimating or predicting drag and highlights the need for the development of surrogate viscoelastic models which more closely reflect real biofouling. It can be concluded that the hydrodynamic conditions during biofilm growth alters the physico-mechanical properties of marine biofilms which in turn influences drag. By relating drag to the physical structure and mechanical properties of marine biofilms under different *Re* we can better understand the role biofilms play in drag production and better inform the coating industry of biofilm targets for more efficient antifouling coatings.

9 Chapter 9: General Discussion

Although each chapter, structured as a paper, presents a comprehensive discussion this section compiles the results and key insights from Chapters 5 to 8 to provide an overarching discussion and outlines the links between the various research questions studied.

9.1 Beyond rigid conventional systems for modelling marine biofilm-associated drag

In Chapter 5 rigid conventional models used to estimate biofilm-associated drag were developed by introducing a tailored system with respect to surface roughness and mechanical properties. Over a *Re* range of 1.2×10^4 to 5.2×10^4 it was concluded that an elastomeric structure induced a drag up to 52 % higher than a rigid structure, depending on surface roughness. This conclusion supports the present literature which states that biofilm compliance plays a critical role in drag production (Picologlou, Zelver and Characklis, 1980; Hartenberger *et al.*, 2020; Snowdon *et al.*, 2022). Furthermore, it has been highlighted how an elastomeric material possesses a different relationship between increasing *Re* and C_f when compared to a rigid material, which was assumed to be consequence to viscoelastic behaviour and could be more representative of natural biofilm behaviour (Lambert *et al.*, 2009; Perkins *et al.*, 2012). Biofilm viscoelasticity and the role it plays in drag was successfully observed in Chapter 8 by installing an OCT alongside the flow cell for real-time visualisation of deformation as a function of increasing shear stress. Statistical analysis further revealed that a significant relationship existed between roughness and elasticity that changed with increasing *Re*; these new results emphasise how neither property can be studied in isolation when estimating or predicting biofilm-associated drag. The relationships discussed in Chapter 5 highlight how deformable materials, such as biofilms, exhibit dynamic behaviour under increasing *Re* and that this behaviour needs to be better characterised if we are to understand its role in drag production.

9.2 Surface treatment affects marine biofilm physico-mechanical properties

To tackle the negative consequences that biofilms present to the shipping industry (among others) we need to understand the underlying mechanisms implicating drag. Although marine biofilm viscoelasticity is hypothesised to have a critical role in drag production, it has not been characterised in the open published literature. In Chapter 5 it was demonstrated that roughness and elasticity of an elastomeric material interact to significantly influence drag, and therefore it could be further expected that a relationship between physico-mechanical properties plays a role in marine biofilm drag production. Consequently, in Chapters 6 and 7 marine biofilms were rheologically characterised, for the first time, as was the relationship between structural and mechanical properties.

Biofilms on ships are exposed to different coatings which act to prevent or manage their growth (Finnie and Williams, 2010). It has been previously shown that different ship coatings can affect biofilm community and species (Salta *et al.*, 2013; Papadatou *et al.*, 2021) which in turn could be expected to alter the physico-mechanics of a marine biofilm (Souza-Egipsy *et al.*, 2021). For example, Souza-Egipsy *et al.*, (2021) demonstrated that biofilms with a higher concentration of motile organisms (eukaryotes) possessed a more open biofilm architecture and exhibited greater deformation than biofilms dominated by prokaryotes (i.e., bacteria). Therefore, as marine biofilms incorporate both eukaryotic and prokaryotic species they could be expected to sit at the lower end of the shear or elastic modulus spectrum quoted in the literature (Table 3-1). In this present study, marine biofilms were rheologically characterised for the first time and were observed to be viscoelastic with a shear modulus range of 11 Pa to 7500 Pa; this data supports the notion that marine biofilms could be softer than alternative biofilms. The shear modulus range reported covers a few orders of magnitude which was expected as marine biofilms were cultivated under different conditions with respect to location (Hartlepool Marina or Dove Laboratory, UK), time, surface colour (red, black, or white), coating type (FRC or ACP) and method of data collection (OCT or rheometer testing). Although taxonomic identification of organisms was not executed in this current investigation, qualitative microscopy confirmed the presence of motile organisms within all marine biofilms tested (Chapters 6, 7 and 8) which could explain the low shear modulus (Souza-Egipsy *et al.*, 2021).

To test the hypothesis that biofilms grown on different surfaces would possess diverse physico-mechanical properties, biofilm were cultivated first on coupons painted with different grey commercial coatings (Chapter 6). A rheometer has often been applied for studying biofilm mechanics (Charlton *et al.*, 2019) yet coupling OCT to characterise biofilm structure as an indication of structural stability in response to shear testing on a rheometer has not been reported. From using OCT to quantify thickness, roughness and cover, and a parallel-plate rheometer to measure G, η and λ, it was shown that although coupon surface roughness and colour were comparable the resultant biofilms exhibited different physico-mechanical profiles. ACP and PVC biofilms were thick, 'fluffy' and exhibited structural disruption when exposed to shear stress during rheometer testing as shown by a 68 % reduction in thickness. Alternatively, biofilms cultivated under the same conditions but on FRC coupons were significantly thinner, exhibited a clumped coverage and showed little change in structural properties when exposed to shear. The mechanical properties between the ACP: FRC and PVC: FRC were also deemed significantly different, which was, in part, attributed to structural differences (Snowdon *et* al., 2023).

In the shipping industry, marine coatings come in a variety of colours and therefore it is important to understand the role colour could play in drag-producing properties of marine biofilms, such as viscoelasticity. Given that different surface colours have been shown to alter biofilm community composition by simulating greater biomass or promoting EPS production (Gambino *et al.*, 2018), and differences in community composition can alter biofilm architecture (Souza-Egipsy *et al.*, 2021) it was hypothesised that surface colour could also influence biofilm physico-mechanics. From the new results presented in Chapter 7 it was concluded that surface colour significantly affects thickness, R_a^*, and coverage of marine biofilms as well as viscoelastic behaviour. Biofilms on red and black surfaces were thinner and were more structurally robust than biofilms cultivated on white surfaces. Gambino *et al.*, (2018) studied the effect of surface colour on cyanobacterial biofilm development and concluded that darker surfaces maximised EPS production, which could perhaps explain the structural robustness of biofilms on red and black surfaces in the current investigation. A link between biofilm structure and mechanics was also determined which emphasises the conclusions from Chapter 5 that roughness and elasticity are linked and those in Chapter 6 where it was suggested that physico-mechanical links could exist.

These novel findings, on the effects of colour on biofilm viscoelasticity and the role structure has in this behaviour, offer key insights for the coatings industry. The results highlight the complexity of marine biofilms - different surfaces and conditions can stimulate biofilms with very different structural and mechanical properties which can be expected to implicate drag in different ways. A better understanding of how surface coating properties influence drag-causing properties of biofilms (such as structure, composition, and viscoelasticity) is required to improve antifouling coating efficiency and to improve our knowledge on in-field fluid-structure interactions.

9.3 Hydrodynamic conditions affect marine biofilm physico-mechanical properties and drag production

Within the open literature it is well documented that biofilms cause a higher drag than rigid structures, even if surface topography is kept consistent (Hartenberger *et al.*, 2020). It is often assumed that the higher drag caused by biofilms is due to compliant behaviour under shear (Picologlou, Zelver and Characklis, 1980), as was also the case in Chapter 5 for the elastomeric system (Snowdon *et al.*, 2022). In Chapter 8, the approach from Chapter 5 was successfully developed by installing an OCT alongside the flow cell to enable simultanoues measurements of pressure drop, biofilm structure and biofilm mechanics under increasing *Re*. Using OCT, inflation, streamer production and removal processes were observed (Figure 8-5), all of which could be linked back to drag and structural changes. As relationships between structural and mechanical properties were determined throughout Chapters 5 to 7 for an elastomeric system and statically grown biofilms, it was expected that this conclusion would also be met for marine biofilms grown in-field under dynamic conditions.

Biofilms grown under different flow regimes have been shown to display different physico-mechanical properties which lead to differences in resistance to shear forces (Stoodley *et al.*, 1999; Soares *et al.*, 2022), for example a biofilm grown under higher shear is typically more rigid and displays structural and mechanical robustness (Fanesi *et al.*, 2021). As a result of the different physico-mechanical properties and findings in Chapter 5 showing how a rigid structure produces a lower drag than a compliant one, it was hypothesised that a biofilm grown under higher shear would be stiffer (measured as a higher G), structurally stable and therefore produce a lower drag than a compliant structure over the same Re range. Although the structure of mechanical properties of biofilms cultivated under different shear has been previously reported, by using the OCT and an MBFC current methods were developed by enabling simultaneous measurements of C_f^*. In Chapter 8 the hypothesis was demonstrated by showing that HF marine biofilms experienced little structural disruption in response to increasing Re (Figure 8-7), possessed a G more than double that of the LF biofilms and had a significantly lower $C_{f,\text{I}}$.

In addition, it was found that the structural properties shared a significant correlation with biofilm mechanics which was, in part driven, by hydrodynamic conditions during growth. The HF biofilms were thicker, had a high coverage and were more homogenous than the LF biofilms, which correlated with a higher G and lower C_f^*. Fanesi *et al.*, (2021) reported similar conclusions, with respect to physico-mechanical properties, for single-species biofilms (*Chlorella vulgaris*) cultivated under different hydrodynamic conditions (using microscopic techniques) and suggested that microalgal biofilms display structural rearrangement in response to different shear with repercussions for mechanical properties and 3D structure. Single-species and multi-species biofilms (as studied in this work) present different biological complexities, for example Paramonova *et al.*, (2009) studied both types (relevant to dentistry) and concluded that multi-species biofilms are more resistant to compressive environmental forces than single-species; in part, this is likely consequence to inter-species interactions (Joshi, Gunawan and Mann, 2021). Additionally, multi-species biofilms are more representative of real-life scenarios. Despite inevitable differences, from the data gathered it be concluded that structural rearrangement under increasing shear alters mechanical properties at the meso-scale in marine biofilms. Overall, these findings emphasise the interactions between physical structure and mechanical properties revealed in Chapters 6 and 7 using a parallel-plate rheometer and OCT to characterise biofilms grown on different surfaces.

9.3.1 Beyond conventional methods of assuming viscoelasticity effects drag

Marine biofilms have been shown to be viscoelastic structures, and softer biofilms overall induce a greater drag. Although biofilms grown under a higher flow rate were more rigid, they still showed a comparable relationship between Re and C_f^* to that observed for biofilms grown under lower shear

– at lower *Re* (Figure 8-7). C_f^* showed little to no change but as *Re* increased above ~ 4.0 × 10^4 there was a sudden decline in C_f^*. The trend observed was like that observed in Chapter 5 for the elastomeric model biofilm system and therefore verifies the use of the system as a more appropriate substitute for estimating biofilm-associated drag. In the open published literature the same trend has also been observed for natural biofilms and was attributed to flattening of the biofilm against a pipe wall or shearing events (Lambert *et al.*, 2009; Perkins *et al.*, 2012), yet no imaging methods were utilised.

For this current study, instead of assuming viscoelastic behaviour was responsible for trends observed between *Re* and C_f^* it was tracked in real-time using OCT. OCT revealed that although drag trends were comparable between the biofilms grown under different conditions, different viscoelastic behaviours were responsible. From quantifying structural and mechanical properties alongside drag, it is believed that for the HF biofilms a hardening response was responsible for a drop in C_f^*. In Chapter 5 a rigid material of equivalent roughness to a compliant material produced up to a 52 % lower drag, therefore if a biofilm becomes more rigid under increasing *Re* it could be expected that drag would drop. Hardening is typically exhibited in conjunction with pore closure which can be observed as an increase in shear or elastic modulus (as was observed in Figure 8-4) due to extrusion of water (Jafari *et al.*, 2018; Picioreanu *et al.*, 2018). As HF biofilms were cultivated under greater shear than LF biofilms, which experienced low structural disruption and detachment at higher *Re* (Figure 8-5), the hardening response could be a survival mechanism of HF biofilms to promote resistance to shear forces. Although an increase in shear modulus was also measured for LF biofilms from OCT 2D-scans large removal events were also evident (Figure 8-5) and coincided with a rise in *G*, therefore surface detachment was deemed responsible for the observed drop in C_f^*. This data perhaps suggests that coverage should be considered when estimating biofilm-associated drag, as suggested recently by Murphy *et al.*, (2022), as HF biofilms with significantly greater coverage than LF biofilms presented a significantly different $C_{f,\,I}$. Recently, Murphy *et al.*, (2022) concluded that percent coverage could be a more powerful metric for measuring biofilm associated drag than surface roughness after showing that relatively homogenous biofilms with greater coverage possessed a greater drag. This study demonstrated that at lower *Re* the softer LF biofilms had a lower coverage and greater surface heterogeneity than HF biofilms, and induced a higher $C_{f,\,I}$. However, it must be considered that at higher *Re* HF biofilms could cause a higher drag than the LF alternatives as they displayed a greater resistance to removal than the softer LF biofilms leading to greater coverage (Figure 8-5).

The biofilm-associated drag data, Chapters 5 and 8, exemplify the dynamic behaviour exhibited by biofilms under increasing *Re* using OCT and an MBFC. Although this behaviour has been captured, it must be noted that biofilms are largely heterogenous with respect spatial and temporal structural and mechanical properties. For example, it is often cited that vertical density gradients exist within biofilms and that rigid basal layers can exhibit a 50 % lower porosity than the ‘fluffy’ surface layers which are more vulnerable to shear and removal events (Zhang and Bishop, 1994). Furthermore, the viscoelastic nature of biofilms inevitably alters their overall structure and response to shear; greater removal could be exhibited as the biofilm transitions towards a viscous-dominated response as was seen for the LF biofilms in Chapter 8 where lift followed by streamer action and removal was observed (Figure 8-5a). For the HF biofilms however, streamer action, along with structural stability, were partly responsible for little removal from the surface (Figure 8-5b). The comparison of the HF and LF biofilms successfully demonstrates the variability that exists within marine biofilms. Across this investigation, the heterogeneity of marine biofilms has been emphasised and the results show that a ‘one size fits all’ approach to modelling biofilm-associated drag is perhaps not possible – biofilm properties and inter-property relationships change under increasing *Re*. As a result, it could be hypothesised that viscoelastic behaviour has a greater effect on drag at lower *Re* and that at higher *Re* (or flow higher than the hydrodynamic conditioning velocity of a biofilm) rigid structures could, in fact, be suitable for modelling biofilm associated drag as hardening behaviour or removal occurs. Further experiments would be required to test this hypothesis and would involve testing over greater *Re* ranges (above $Re = 5.2 \times 10^4$).

Overall, the observations highlight the complexity of studying marine biofilm-associated drag. An OCT and a MBFC have been successfully employed for studying biofilm physico-mechanics *in-situ* whilst simultaneously measuring drag using an integrated pressure drop system. By employing these methods, the dynamic behaviour that biofilms exhibit under flow has been captured and quantified. The results have revealed how biofilm thickness, cover and roughness significantly influence the mechanical profile of a biofilm which in turn significantly influences C_f. OCT has confirmed assumptions made in the literature by revealing how viscoelastic behaviour does implicate drag and that although drag curves may look comparable, the underlying viscoelastic mechanisms driving drag under increasing *Re* could be very different and need to be better understood. Despite differences in the underlying drag-production mechanisms of biofilms cultivated under different conditions, the general trend in *Re* and C_f^* was similar and was successfully captured by the elastomeric system proposed in Chapter 5. Consequently, it can be concluded that the artificial biofilm system is a better substitute for studying biofilm-associated drag. Finally, a relationship between structural and mechanical properties, using both the elastomeric systems and biofilms grown under different conditions was observed.

10 Chapter 10: Conclusions and Future Recommendations

10.1 Conclusions

The primary aim of this research was to determine the effects of physico-mechanical properties on biofilm-associated drag using an artificial system, validated with real marine biofilm data. The original work presented in this thesis achieved this aim by expanding on the previous literature that has used rigid rough structures to estimate and predict biofilm-associated drag and that has assumed differences in drag between rigid structures and biofilms is due to compliance effects. The main conclusions and novel contributions of this work are presented below.

10.1.1 A novel elastomeric system for measuring marine biofilm-associated drag

A novel elastomeric sandpaper system has been proposed for studying the effects of structure and viscoelasticity on biofilm-associated drag. As surface topography and mechanical properties of a material can be controlled the effects of each on drag can be determined independently. Combined effects can also be studied. The model was verified by studying marine biofilm viscoelasticity and marine biofilm-associated drag. The main conclusions are as follows:

- Drag associated with elastomeric structures was up to 52 % higher than that associated with rigid structures (sandpaper and filler) of equivalent roughness over a *Re* range of 1.2×10^4 to 5.2×10^4.
- The C_f^* vs. *Re* relationship for the elastomeric system accurately represented the trends exhibited by marine biofilms (Chapter 8): a plateau in C_f^* at lower *Re* was followed by a marked decrease in C_f^* at a *Re* of approximately 3.0×10^4.
- New results showed that roughness and elasticity significantly influence drag independently, but also that they share a significant interaction effect on drag.
- The contribution of roughness and elasticity changed under increasing *Re*. Although contributions were not quantified when studying marine biofilms (Chapter 8) OCT showed highly dynamic behaviour of biofilms which would likely alter the dominant contributing factor to drag.

10.1.2 Surface treatment effects marine biofilm physico-mechanical properties

For the first time, marine biofilms have been rheologically characterised. Marine biofilms were cultivated under different conditions by changing surface colour or surface chemistry and G, η and λ were quantified. The main conclusions are as follows:

- Marine biofilms are viscoelastic, as shown using a parallel-plate rheometer (Chapters 6 and 7) and an OCT in conjunction with a flow cell (Chapter 8).
- The shear modulus range for marine biofilms was 11 Pa to 7500 Pa (dependent on the growth conditions). These values fit well within that reported in the current literature yet sit towards the lower end of the spectrum.
- Biofilm structure and mechanics are affected by surface conditions, such as coating type (Chapters 6) and colour (Chapter 7).
- Biofilm structure and mechanics are linked, and this relationship changes dependent on surface conditions.

10.1.3 Hydrodynamic conditions effect marine biofilm physico-mechanical properties and drag

Previous work has employed an OCT for measuring biofilm viscoelasticity and an MBFC for measuring drag, here, the open literature was extended by using these methods in conjunction. This novel approach allowed *in-situ* determination of viscoelasticity, structure and drag associated with marine biofilms grown under different hydrodynamic conditions.

- HF biofilms were thicker, more homogenous, and more structurally robust when compared to LF biofilms. In addition, HF biofilms were rigid and had a shear modulus of 324.4 ± 19.0 Pa compared to 132.5 ± 50.6 Pa for LF biofilms.
- LF biofilms produced a 5.7 % higher $C_{\mathrm{f,\,I}}$ than HF biofilms which was attributed to biofilm viscoelasticity.
- Above a Re of approximately 2.5×10^4, G was significantly correlated with C_f^* and could be used to predict $C_{\mathrm{f,\,I}}$.
- Thickness, R_a^* and coverage were significantly correlated with shear modulus under increasing Re but not C_f^*.
- The C_f^* vs. Re trends of LF and HF biofilms were comparable, however from OCT it was evident that different underlying mechanisms were responsible for changes in drag. For LF biofilms a drop in C_f^* was attributed to removal events, and for HF biofilms it was hardening behaviour.

10.2 Limitations and Future Recommendations

A tailored artificial sandpaper system has been proposed for estimating biofilm-associated drag and although biofilm drag trends are successfully captured by the elastomeric system this model can be further developed. The sandpaper model proposed in Chapter 5 might be advanced by coupling OCT with 3D-printing techniques to generate 3D-replicas of natural marine biofilms. It is suggested that the model should incorporate materials with comparable mechanical properties to marine biofilms as informed by results generated here using OCT and a parallel-plate rheometer. A similar approach was adopted recently by Hartenberger *et al.*, (2020) who produced rigid replicas of marine biofilms and compared the drag produced to that of the original biofilms. This current research has demonstrated that biofilm structure and viscoelasticity are interlinked, and that viscoelasticity is significant in influencing drag and therefore should not be neglected when using models. By incorporating a model with controlled variation in mechanical and structural properties different biofilm geometries, such as streamers, could be captured and new information on how biofilms with different physico-mechanical profiles interact with fluid flow and implicate drag could be uncovered. Further, by utilising an artificial system, as opposed to natural biofilms, there could be a higher throughput of drag-related experiments with greater repeatability and greater upscaling opportunities; for more details on benefits of artificial systems see Sections 3.2.4 and 3.3.3.

Researchers interested in marine biofilm viscoelasticity (and the relationship with structure) for the purpose of improving biofilm management and removal techniques could examine marine biofilms cultivated under an array of conditions, for example across different coatings or textures. By using rheometer methods, many coupons can be fouled in-field at one time which offers high through-put experiments for biofilms grown under different conditions. Alternatively, to visualise deformation *in-situ* the set up proposed in Chapter 8 could be adopted where a flow cell and OCT are used in conjunction; due to the sizing of test pieces this would offer a lower throughput but testing conditions would be more akin to that experienced on the side of as ship than a rotating disk.

Whilst research has typically looked at effective G or E (assumed for the entire biofilm) it would be of interest to quantify the spatial variation in these properties and could be achieved by using optical methods such as DIC could be coupled with OCT to measure displacement between consecutive scans (Sutton *et al.*, 1983; Blaber, Adair and Antoniou, 2015). DIC has been previously applied to measure the mechanical properties of biofilms subject to shear (Mathias and Stoodley, 2009) and could offer measurements of a larger surface area than that studied here (where individual features were measured).

Finally, to further investigate the effect of biofilm physico-mechanical properties on ship-related drag a larger flow cell, tow tank or water tunnel should be employed that can access *Re* closer to that experienced by a ship. As previously mentioned, the artificial system proposed in Chapter 5 would lend itself well to upscaling methods.

Future studies on a variety of different biofilms are required to further understand the complex interactions exhibited between biofilm physico-mechanical properties and drag. As whether drag is influenced more by physical structure (such as surface roughness, coverage, or thickness) or mechanical behaviour (viscoelasticity), at a given Re, is likely a function of the biofilm growing conditions, community structure and composition and surface conditions (such as colour).

10.3 Final remarks

To build on rigid conventional models, using sand grains or sandpaper, an elastomeric model system, with a tailored surface roughness and mechanical profile, has been proposed that successfully simulated drag curves like that observed for naturally grown marine biofilms and captured relationships between surface roughness and mechanics that were also observed for naturally grown marine biofilms. Although further work is required to optimise this model, it is has been argued that it is a more appropriate substitute for modelling viscoelastic biofilms and highlights how systems that only capture rigid roughness could be underestimating drag. Further, it offers the ability to execute repeatable and high throughput drag experiments under controlled conditions as complexity and time it takes to grow natural biofilms is removed.

11 References

Aggarwal, S. and Hozalski, R. M. (2010) ‘Determination of biofilm mechanical properties from tensile tests performed using a micro-cantilever method.’, *Biofouling*, 26(4), pp. 479–486. doi: 10.1080/08927011003793080.

Alpkvist, E. *et al.* (2006) ‘Three-dimensional biofilm model with individual cells and continuum EPS matrix’, *Biotechnology and Bioengineering*, 94(5), pp. 961–979. doi: 10.1002/bit.20917.

Andrewartha, J. *et al.* (2010) ‘Drag force and surface roughness measurements on freshwater biofouled surfaces’, *Biofouling*, 26(4), pp. 487–496. doi: 10.1080/08927014.2010.482208.

Andrewartha, J. M. and Sargison, J. E. (2011) ‘Turbulence and Mean-Velocity Structure of Flows over Filamentous Biofilms’, in *Proceedings of the 24th IAHR World Congress*. Available at: http://ecite.utas.edu.au/76555 (Accessed: 23 September 2020).

Araújo, G. R. de S. *et al.* (2019) ‘The mechanical properties of microbial surfaces and biofilms’, *The Cell Surface*, 5, p. 100028. doi: 10.1016/j.tcsw.2019.100028.

Atlar, M. *et al.* (2003) ‘The development of foul-release coatings for seagoing vessels’, *Journal of Marine Design and Operations*, (B4), pp. 11–23. Available at: https://www.researchgate.net/publication/238575879 (Accessed: 4 August 2022).

Azeredo, J. *et al.* (2017) ‘Critical review on biofilm methods’, *Critical Reviews in Microbiology*, 43(3), pp. 313–351. doi: 10.1080/1040841X.2016.1208146.

Baba, E. and Tokunaga, K. (1980) ‘Study of Local Roughness Effect on Ship Resistance for Effective Cleaning and Portection of Hull Surface’, *Publication of: Society of Naval Architects and Marine Engineers*, 48, pp. 721–762.

Baniasadi, M. *et al.* (2015) ‘Nanoindentation of Pseudomonas aeruginosa bacterial biofilm using atomic force microscopy’, *Materials Research Express*, 1(4). doi: 10.1088/2053-1591/1/4/045411.

Barai, P., Kumar, A. and Mukherjee, P. P. (2016) ‘Modeling of mesoscale variability in biofilm shear behavior’, *PLoS ONE*, 11(11), p. e0165593. doi: 10.1371/journal.pone.0165593.

De Beer, D., Stoodley, P. and Lewandowski, Z. (1997) ‘Measurement of local diffusion coefficients in biofilms by microinjection and confocal microscopy’, *Biotechnology and Bioengineering*, pp. 151–158. doi: 10.1002/(SICI)1097-0290(19970120)53:2<151::AID-BIT4>3.0.CO;2-N.

Berlanga, M. and Guerrero, R. (2016) ‘Living together in biofilms: The microbial cell factory and its biotechnological implications’, *Microbial Cell Factories*. BioMed Central Ltd. doi: 10.1186/s12934-016-0569-5.

Blaber, J., Adair, & B. and Antoniou, & A. (2015) ‘Ncorr: Open-Source 2D Digital Image Correlation Matlab Software’, *Experimental Mechanics*, 55, pp. 1105–1122. doi: 10.1007/s11340-015-0009-1.

Blauert, F. (2017) *Investigating biofilm deformation using optical coherence tomography and fluid-structure interaction simulation*. Available at: http://wasserchemie.ebi.kit.edu/ (Accessed: 9 April 2020).

Blauert, F., Horn, H. and Wagner, M. (2015) ‘Time-resolved biofilm deformation measurements using optical coherence tomography’, *Biotechnology and Bioengineering*, 112(9), pp. 1893–1905. doi: 10.1002/bit.25590.

Böl, M. *et al.* (2013) ‘Recent advances in mechanical characterisation of biofilm and their significance for material modelling’, *Critical Reviews in Biotechnology*, 33(2), pp. 145–171. doi: 10.3109/07388551.2012.679250.

Böl, M. and Ehret, A. E. (2012) ‘Modelling mechanical characteristics of microbial biofilms by network theory’, *Journal of The Royal Society Interface*. doi: 10.1098/rsif.2012.0676.

Boudarel, H. *et al.* (2018) ‘Towards standardized mechanical characterization of microbial biofilms: analysis and critical review’, *npj Biofilms and Microbiomes*. doi: 10.1038/s41522-018-0062-5.

Camps, M. *et al.* (2014) ‘Antifouling coatings influence both abundance and community structure of colonizing biofilms: A case study in the Northwestern Mediterranean Sea’, *Applied and Environmental Microbiology*, 80(16), pp. 4821–4831. doi: 10.1128/AEM.00948-14/ASSET/2A4CD35F-C317-4F09-9C56-F82F865CF3C0/ASSETS/GRAPHIC/ZAM01614-5546-T04.JPEG.

Candries, M., Atlar, M. and Anderson, C. D. (2003) ‘Estimating the impact of new-generation antifoulings on ship performance: the presence of slime’, *Journal of Marine Engineering and Technology*, 2(1), pp. 13–22. doi: 10.1080/20464177.2003.11020165.

Cao, H. *et al.* (2016) ‘Revealing region-specific biofilm viscoelastic properties by means of a micro-rheological approach’, *npj Biofilms and Microbiomes*, 2(1), pp. 1–7. doi: 10.1038/s41522-016-0005-y.

de Carvalho, C. C. C. R. (2018) ‘Marine biofilms: A successful microbial strategy with economic implications’, *Frontiers in Marine Science*. Frontiers Media S. A, p. 126. doi: 10.3389/fmars.2018.00126.

Cense, A. W. *et al.* (2006) ‘Mechanical properties and failure of Streptococcus mutans biofilms, studied using a microindentation device’, *Journal of Microbiological Methods*, 67(3), pp. 463–472. doi: 10.1016/J.MIMET.2006.04.023.

Characklis, W. G. (1980) *Biofilm development and destruction*.

Charlton, S. (2019) *Rheological characterisation of biofilms in both linear and nonlinear viscoelastic regimes*. Newcastle.

Charlton, S. G. V. *et al.* (2019) ‘Regulating, Measuring, and Modeling the Viscoelasticity of Bacterial Biofilms’, *Journal of Bacteriology*, 201(18). doi: 10.1128/jb.00101-19.

Christensen, B. E. and Characklis, W. G. (1990) ‘Physical and chemical properties of biofilms’, in *Biofilm*. New York: Wiley, pp. 93–130.

CHT (2019) *MM730FG silicone*. Available at: https://cht-silicones.com/products/moulding_rubbers (Accessed: 13 April 2021).

Chung, D. *et al.* (2021) ‘Predicting the Drag of Rough Surfaces’, *Annual Review of Fluid Mechanics*, 53, pp. 439–471. doi: 10.1146/annurev-fluid-062520-115127.

Cimbala, J. M. (2013) *Experimental Uncertainty Analysis*, *Mathematics for Mechanical Engineers*.

Colebrook, C. F. (1939) ‘Turbulent Flow in Pipes, with particular reference to the Transition Region between the Smooth and Rough Pipe Laws’, *Journal of the Institution of Civil Engineers*, 11(4), pp. 133–156. doi: 10.1680/IJOTI.1939.13150.

Costerton, J. W. (1995) ‘Overview of microbial biofilms’, *Journal of Industrial Microbiology*, 15(3), pp. 137–140. doi: 10.1007/BF01569816.

Crusz, S. A. *et al.* (2012) ‘Bursting the bubble on bacterial biofilms: a flow cell methodology’, *Biofouling*, 28(8), p. 835. doi: 10.1080/08927014.2012.716044.

Das, S. and Kumar, A. (2014) ‘Formation and post-formation dynamics of bacterial biofilm streamers as highly viscous liquid jets’, *Scientific Reports*, 4(1), pp. 1–6. doi: 10.1038/srep07126.

Davidson, I. C. *et al.* (2020) ‘An experimental test of stationary lay-up periods and simulated transit on biofouling accumulation and transfer on ships', *https://doi.org/10.1080/08927014.2020.1769612*, 36(4), pp. 455–466. doi: 10.1080/08927014.2020.1769612.

Demirel, Y. K. *et al.* (2014) 'A CFD model for the frictional resistance prediction of antifouling coatings', *Ocean Engineering*, 89, pp. 21–31. doi: 10.1016/j.oceaneng.2014.07.017.

Demirel, Y. K. *et al.* (2017) 'Effect of barnacle fouling on ship resistance and powering', *Biofouling*, 33(10), pp. 819–834. doi: 10.1080/08927014.2017.1373279.

Demirel, Y. K., Turan, O. and Incecik, A. (2017) 'Predicting the effect of biofouling on ship resistance using CFD', *Applied Ocean Research*, 62, pp. 100–118. doi: 10.1016/j.apor.2016.12.003.

Dennington, S. *et al.* (2015) 'Miniaturized rotating disc rheometer test for rapidscreening of drag reducing marine coatings', *Surface Topography: Metrology and Properties*, 3(3). doi: 10.1088/2051-672X/3/3/034004.

Dennington, S. P. *et al.* (2021) 'A rapid benchtop method to assess biofilm on marine fouling control coatings', *Biofouling*. Available at: https://www.researchgate.net/publication/352119091_A_rapid_benchtop_method_to_assess_biofilm_on_marine_fouling_control_coatings (Accessed: 21 June 2021).

Depetris, A. *et al.* (2019) 'Automated 3d optical coherence tomography to elucidate biofilm morphogenesis over large spatial scales', *Journal of Visualized Experiments*, 2019(150). doi: 10.3791/59356.

Derlon, N. *et al.* (2008) 'Stratification in the cohesion of biofilms grown under various environmental conditions', *Water Research*, 42(8–9), pp. 2102–2110. doi: 10.1016/J.WATRES.2007.11.016.

Desmond, P., Morgenroth, E. and Derlon, N. (2018) 'Physical structure determines compression of membrane biofilms during Gravity Driven Membrane (GDM) ultrafiltration', *Water Research*, 143, pp. 539–549. doi: 10.1016/j.watres.2018.07.008.

Dexter, S. C. *et al.* (1975) 'Influence of Substrate Wettability on the Attachment of Marine Bacteria to Various Surfaces'', *APPLiED MicRoBioLoGY*, 30(2), pp. 298–308.

Dobretsov, S., Abed, R. M. M. and Teplitski, M. (2013) 'Mini-review: Inhibition of biofouling by marine microorganisms', *Biofouling*, 29(4), pp. 423–441. doi: 10.1080/08927014.2013.776042.

Dobretsov, S., Abed, R. M. M. and Voolstra, C. R. (2013) ‘The effect of surface colour on the formation of marine micro and macrofouling communities’, *Biofouling*, 29(6), pp. 617–627. doi: 10.1080/08927014.2013.784279.

Donlan, R. M. (2002) *Biofilms: Microbial Life on Surfaces*, *Emerging Infectious Diseases*. Available at: http://www.microbelibrary.org/.

Donley, G. J. *et al.* (2020) ‘Elucidating the G″ overshoot in soft materials with a yield transition via a time-resolved experimental strain decomposition’, *Proceedings of the National Academy of Sciences of the United States of America*, 117(36), pp. 21945–21952. doi: 10.1073/pnas.2003869117/-/DCSupplemental.

Drescher, K. *et al.* (2013) ‘Biofilm streamers cause catastrophic disruption of flow with consequences for environmental and medical systems’, *Proceedings of the National Academy of Sciences of the United States of America*, 110(11), pp. 4345–4350. doi: 10.1073/pnas.1300321110.

Dunsmore, B. C. *et al.* (2002) ‘The influence of fluid shear on the structure and material properties of sulphate-reducing bacterial biofilms’, *Journal of Industrial Microbiology and Biotechnology*, 29(6), pp. 347–353. doi: 10.1038/sj.jim.7000302.

El-Labbad, A. F. (1987) *Techno Economic Analysis of the Problems of the Bottom Maintenance of Ships*. Newcastle University.

Even, C. *et al.* (2017) ‘Recent advances in studying single bacteria and biofilm mechanics’, *Advances in Colloid and Interface Science*, 247, pp. 573–588. doi: 10.1016/j.cis.2017.07.026.

Eyring, V. *et al.* (2010) ‘Transport impacts on atmosphere and climate: Shipping’, *Atmospheric Environment*, 44(37), pp. 4735–4771. doi: 10.1016/J.ATMOSENV.2009.04.059.

Fabbri, S. *et al.* (2016) ‘Streptococcus mutans biofilm transient viscoelastic fluid behaviour during high-velocity microsprays’, *Journal of the Mechanical Behavior of Biomedical Materials*, 59, pp. 197–206. doi: 10.1016/j.jmbbm.2015.12.012.

Fabbri, S. *et al.* (2017) ‘Fluid-driven interfacial instabilities and turbulence in bacterial biofilms’, *Environmental Microbiology*, 19(11), pp. 4417–4431. doi: 10.1111/1462-2920.13883.

Fabbri, S. *et al.* (2018) ‘A marine biofilm flow cell for in situ screening marine fouling control coatings using optical coherence tomography’, *Ocean Engineering*, 170, pp. 321–328. doi: 10.1016/j.oceaneng.2018.10.030.

Fabbri, S. *et al.* (2019) ‘A marine biofilm flow cell for in situ determination of drag and biofilm structure', *Ocean Engineering*, 178, pp. 59–65. doi: 10.1016/j.oceaneng.2019.02.066.

Fanesi, A. *et al.* (2021) 'Shear stress affects the architecture and cohesion of Chlorella vulgaris biofilms', *Scientific Reports 2021 11:1*, 11(1), pp. 1–11. doi: 10.1038/s41598-021-83523-3.

Fernandes, S. *et al.* (2021) 'Overview on the hydrodynamic conditions found in industrial systems and its impact in (bio)fouling formation', *Chemical Engineering Journal*, 418, p. 129348. doi: 10.1016/J.CEJ.2021.129348.

Finnie, A. A. and Williams, D. N. (2010) 'Paint and Coatings Technology for the Control of Marine Fouling', *Biofouling*, pp. 185–206. doi: 10.1002/9781444315462.CH13.

Flack, K. A. and Schultz, M. P. (2010) 'Review of hydraulic roughness scales in the fully rough regime', *Journal of Fluids Engineering, Transactions of the ASME*, pp. 0412031–04120310. doi: 10.1115/1.4001492.

Flack, K. A., Schultz, M. P. and Connelly, J. S. (2007) 'Examination of a critical roughness height for outer layer similarity', *Physics of Fluids*, 19(9). doi: 10.1063/1.2757708.

Flemming, H. C. and Wingender, J. (2010) 'The Biofilm Matrix', *Nature Reviews Microbiology*, 8(9), pp. 623–633. doi: 10.1038/nrmicro2415.

Fortunato, L. *et al.* (2017) 'In-situ assessment of biofilm formation in submerged membrane system using optical coherence tomography and computational fluid dynamics', *Journal of Membrane Science*, 521, pp. 84–94. doi: 10.1016/j.memsci.2016.09.004.

Fux, C. A. *et al.* (2009) 'The Functional Resistance of Bacterial Biofilms', *Antimicrobial Drug Resistance*, pp. 121–131. doi: 10.1007/978-1-59745-180-2_11.

Galvão De Campos, B. *et al.* (2022) 'Occurrence, effects and environmental risk of antifouling biocides (EU PT21): Are marine ecosystems threatened?', *Critical Reviews in Environmental Science and Technology*, 52(18), pp. 3179–3210. doi: 10.1080/10643389.2021.1910003.

Gambino, M. *et al.* (2018) 'Surface colour: An overlooked aspect in the study of cyanobacterial biofilm formation'. doi: 10.1016/j.scitotenv.2018.12.358.

Geissler, E. and Hecht, A. M. (1981) 'The Poisson Ratio in Polymer Gels. 2', *Macromolecules*, 14(1), pp. 185–188. doi: 10.1021/ma50002a038.

Gent, A. N. (1958) 'On the relation between indentation hardness and Young's modulus', *Rubber Chemistry and Technology*, 31(4), pp. 896–906. doi: 10.5254/1.3542351.

Ghosh, U. U. *et al.* (2021) 'Bacterial streamers as colloidal systems: Five grand challenges', *Journal of Colloid and Interface Science*, 594, pp. 265–278. doi: 10.1016/J.JCIS.2021.02.102.

Gloag, E. S. *et al.* (2018) 'Viscoelastic properties of Pseudomonas aeruginosa variant biofilms', *Scientific Reports*, 8(1), pp. 1–11. doi: 10.1038/s41598-018-28009-5.

Gloag, E. S. *et al.* (2020) 'Biofilm mechanics: Implications in infection and survival', *Biofilm*, 2, p. 100017. doi: 10.1016/j.bioflm.2019.100017.

Gloag, E. S. *et al.* (2021) 'Mycobacterium abscessus biofilms have viscoelastic properties which may contribute to their recalcitrance in chronic pulmonary infections', *Scientific Reports* |, 11, p. 5020. doi: 10.1038/s41598-021-84525-x.

Gordon, V. D. *et al.* (2017) 'Biofilms and mechanics: A review of experimental techniques and findings', *Journal of Physics D: Applied Physics*. doi: 10.1088/1361-6463/aa6b83.

Granville, P. S. (1958) 'The Frictional Resistance and Turbulent Boundary Layer of Rough Surfaces', *Journal of Ship Research*, 2(04), pp. 52–74. doi: 10.5957/JSR.1958.2.4.52.

Greaves, G. N. *et al.* (2011) 'Poisson's ratio and modern materials', *Nature materials*, 10(11), pp. 823–837. doi: 10.1038/NMAT3134.

Grigson, C. (1992) 'Drag Losses of New Ships Caused by Hull Finish', *Journal of Ship Research*, 36(02), pp. 182–196. doi: 10.5957/JSR.1992.36.2.182.

Grillet, A. M., Wyatt, N. B. and Gloe, L. M. (2012) 'Polymer Gel Rheology and Adhesion', *Rheology*. doi: 10.5772/36975.

Guélon, T., Mathias, J.-D. and Stoodley, P. (2011) 'Advances in Biofilm Mechanics', in. Springer, Berlin, Heidelberg, pp. 111–139. doi: 10.1007/978-3-642-19940-0_6.

Haisch, C. and Niessner, R. (2007) 'Visualisation of transient processes in biofilms by optical coherence tomography', *Water Research*, 41(11), pp. 2467–2472. doi: 10.1016/j.watres.2007.03.017.

Hakim, M. L. *et al.* (2021) 'Wind-tunnel experiments and CFD simulations to study the increase in ship resistance components due to roughness', *Journal of sustainability science and management*, 16(3), pp. 144–163. doi: 10.46754/JSSM.2021.04.012.

Hansen, R. J. and Hunston, D. L. (1974) 'An experimental study of turbulent flows over compliant surfaces', *Journal of Sound and Vibration*, 34(3), pp. 297-IN2. doi: 10.1016/S0022-

460X(74)80314-7.

Hartenberger, J. (2019) *Drag Production of Filamentous Biofilm*. University of Michigan.

Hartenberger, J. D. *et al.* (2020) ‘Drag production mechanisms of filamentous biofilms’, *Biofouling*. doi: 10.1080/08927014.2020.1806250.

Haslbeck, E. G. and Bohlander, G. S. (1992) *Microbial Biofilm Effects on Drag*, *Ship Production Symposium,*.

Hassanpourfard, M. *et al.* (2015) ‘Bacterial floc mediated rapid streamer formation in creeping flows’, *Scientific Reports 2015 5:1*, 5(1), pp. 1–12. doi: 10.1038/srep13070.

Hewitt, C. L., Gollasch, S. and Minchin, D. (2009) ‘The Vessel as a Vector – Biofouling, Ballast Water and Sediments’, pp. 117–131. doi: 10.1007/978-3-540-79236-9_6.

Hohne, D. N., Younger, J. G. and Solomon, M. J. (2009) ‘Flexible microfluidic device for mechanical property characterization of soft viscoelastic solids such as bacterial biofilms’, *Langmuir*, 25(13), pp. 7743–7751. doi: 10.1021/la803413x.

Holm, E. R. *et al.* (2004) ‘Evaluation of hydrodynamic drag on experimental fouling-release surfaces, using rotating disks’, *Biofouling*, 20(4–5), pp. 219–226. doi: 10.1080/08927010400011245.

Hong, J., Katz, J. and Schultz, M. P. (2011) ‘Near-wall turbulence statistics and flow structures over three-dimensional roughness in a turbulent channel flow’, *Journal of Fluid Mechanics*, 667, pp. 1–37. doi: 10.1017/S0022112010003988.

Howell, D. and Behrends, B. (2006) ‘A review of surface roughness in antifouling coatings illustrating the importance of cutoff length’, *Biofouling*, 22(6), pp. 401–410. doi: 10.1080/08927010601035738.

Huang, D. *et al.* (1991) ‘Optical coherence tomography’, *Science*, 254(5035), pp. 1178–1181. doi: 10.1126/science.1957169.

Huang, J. *et al.* (2019) ‘Programmable and printable Bacillus subtilis biofilms as engineered living materials’, *Nature Chemical Biology*, 15(1), pp. 34–41. doi: 10.1038/s41589-018-0169-2.

Huggett, M. J., Nedved, B. T. and Hadfield, M. G. (2009) ‘Effects of initial surface wettability on biofilm formation and subsequent settlement of Hydroides elegans’, *Biofoul*, 25(5), pp. 387–399. doi: 10.1080/08927010902823238.

Hunsucker, K. Z. *et al.* (2018) ‘Biofilm community structure and the associated drag penalties of a groomed fouling release ship hull coating’, *https://doi.org/10.1080/08927014.2017.1417395*, 34(2), pp. 162–172. doi: 10.1080/08927014.2017.1417395.

Hyun, K. *et al.* (2011) ‘A review of nonlinear oscillatory shear tests: Analysis and application of large amplitude oscillatory shear (LAOS)’, *Progress in Polymer Science*, 36, pp. 1697–1753. doi: 10.1016/j.progpolymsci.2011.02.002.

Hyun, K. and Kim, W. (2011) ‘A new non-linear parameter Q from FT-Rheology under nonlinear dynamic oscillatory shear for polymer melts system’, *Korea Australia Rheology Journal*, 23(4), pp. 227–235. doi: 10.1007/S13367-011-0028-0.

IMO (2021) *Fourth IMO Greenhouse Gas Study*, *4th International Maritime Organization*.

Jafari, M. *et al.* (2018) ‘Effect of biofilm structural deformation on hydraulic resistance during ultrafiltration: A numerical and experimental study’, *Water Research*. doi: 10.1016/j.watres.2018.08.036.

Jana, S. *et al.* (2020) ‘Nonlinear rheological characteristics of single species bacterial biofilms’, *npj Biofilms and Microbiomes*, 6(1). doi: 10.1038/s41522-020-0126-1.

Jang, H., Rusconi, R. and Stocker, R. (2017) ‘Biofilm disruption by an air bubble reveals heterogeneous age-dependent detachment patterns dictated by initial extracellular matrix distribution’, *npj Biofilms and Microbiomes*, 3, p. 6. doi: 10.1038/s41522-017-0014-5.

Joshi, R. V., Gunawan, C. and Mann, R. (2021) ‘We Are One: Multispecies Metabolism of a Biofilm Consortium and Their Treatment Strategies’, *Frontiers in Microbiology*, 12, p. 80. doi: 10.3389/FMICB.2021.635432/BIBTEX.

Kamemaru, K. *et al.* (2018) ‘Irreversible Swelling Behavior and Reversible Hysteresis in Chemically Crosslinked Poly(vinyl alcohol) Gels’, *Gels*, 4(2), p. 45. doi: 10.3390/gels4020045.

Kandemir, N. *et al.* (2018) ‘Mechanical interactions between bacteria and hydrogels’, *Scientific Reports*, 8(1). doi: 10.1038/s41598-018-29269-x.

Karimi, A. *et al.* (2015) ‘Interplay of Physical Mechansism and Biofilm Processes: Review of Microfluidic Methods’, *Lab on a Chip*, 15(1), pp. 23–42. doi: 110.1016/j.bbi.2017.04.008.

Kavanagh, G. M. and Ross-Murphy, S. B. (1998) ‘Rheological characterisation of polymer gels’, *Progress in Polymer Science*. Elsevier Ltd, pp. 533–562. doi: 10.1016/S0079-6700(97)00047-6.

Kim, Y. M., Kwon, T. H. and Kim, S. (2017) ‘Measuring elastic modulus of bacterial biofilms in a liquid phase using atomic force microscopy’, *Geomechanics and Engineering*, 12(5), pp. 863–870. doi: 10.12989/gae.2017.12.5.863.

Klapper, I. *et al.* (2002) ‘Viscoelastic fluid description of bacterial biofilm material properties’, *Biotechnology and Bioengineering*, 80(3), pp. 289–296. doi: 10.1002/bit.10376.

Körstgens, V. *et al.* (2001a) ‘Influence of calcium ions on the mechanical properties of a model biofilm of mucoid Pseudomonas aeruginosa’, *Water Science and Technology*, 43(6), pp. 49–57. doi: 10.2166/wst.2001.0338.

Körstgens, V. *et al.* (2001b) ‘Uniaxial compression measurement device for investigation of the mechanical stability of biofilms’, *Journal of Microbiological Methods*, 46(1), pp. 9–17. doi: 10.1016/S0167-7012(01)00248-2.

Krsmanovic, M. *et al.* (2021) ‘Hydrodynamics and surface properties influence biofilm proliferation’, *Advances in Colloid and Interface Science*, 288. doi: 10.1016/J.CIS.2020.102336.

Kundukad, B. *et al.* (2016) ‘Mechanical properties of the superficial biofilm layer determine the architecture of biofilms’, *Soft Matter*, 12(26), pp. 5718–5726. doi: 10.1039/c6sm00687f.

Kunz, S. *et al.* (2018) ‘Polymer- vs. colloidal-type viscoelastic mechanics of microgel pastes’, *Colloid and Polymer Science*, 296(8), pp. 1341–1352. doi: 10.1007/S00396-018-4352-5.

Lambert, M. F. *et al.* (2009) ‘The impact of biofilm devlopment on pipe roughness and velocity profile’, *Proceedings of World Environmental and Water Resources Congress 2009 - World Environmental and Water Resources Congress 2009: Great Rivers*, 342, pp. 122–134. doi: 10.1061/41036(342)13.

Larson, K. (2017) *Can you estimate modulus from Durometer hardness for silicones?*, *Dow White Paper*. Available at: https://www.dow.com/content/dam/dcc/documents/en-us/tech-art/11/11-37/11-3716-01-durometer-hardness-for-silicones.pdf?iframe=true#:~:text=condensation cure products%2C-,Can You Estimate Modulus From Durometer Hardness for Silicones%3F,must choose your mod.

Laspidou, C. S. *et al.* (2014) ‘Material modeling of biofilm mechanical properties’, *Mathematical Biosciences*, 251(1), pp. 11–15. doi: 10.1016/j.mbs.2014.02.007.

Laspidou, C. S. and Aravas, N. (2007) ‘Variation in the mechanical properties of a porous multi-phase biofilm under compression due to void closure’, *Water Science and Technology*, 55(8), pp.

447–453. doi: 10.2166/wst.2007.289.

Laspidou, C. S. and Rittmann, B. E. (2004) ‘Evaluating trends in biofilm density using the UMCCA model’, *Water Research*, 38(14–15), pp. 3362–3372. doi: 10.1016/J.WATRES.2004.04.051.

Law, K.-Y. (2014) ‘Definitions for Hydrophilicity, Hydrophobicity, and Superhydrophobicity: Getting the Basics Right’, *Journal of Physical Chemistry Letters*, 5(4), pp. 686–688. doi: 10.1021/jz402762h.

Leer-Andersen, M. and Larsson, L. (2003) ‘An experimental/numerical approach for evaluating skin friction on full-scale ships with surface roughness’, *Journal of Marine Science and Technology*, 8(1), pp. 26–36. doi: 10.1007/s10773-003-0150-y.

Legland, D., Arganda-Carreras, I. and Andrey, P. (2016) ‘MorphoLibJ: integrated library and plugins for mathematical morphology with ImageJ’, *Bioinformatics*, 32(22), pp. 3532–3534. doi: 10.1093/BIOINFORMATICS/BTW413.

Lembre, P., Lorentz, C. and Di, P. (2012) ‘Exopolysaccharides of the Biofilm Matrix: A Complex Biophysical World’, in *The Complex World of Polysaccharides*. InTech. doi: 10.5772/51213.

Lembré, P., Di Martino, P. and Vendrely, C. (2014) ‘Amyloid peptides derived from CsgA and FapC modify the viscoelastic properties of biofilm model matrices’, *Biofouling*, 30(4), pp. 415–426. doi: 10.1080/08927014.2014.880112.

Lemos, M. *et al.* (2015) ‘The effect of shear stress on the formation and removal of Bacillus cereus biofilms’, *Food and Bioproducts Processing*, 93, pp. 242–248. doi: 10.1016/J.FBP.2014.09.005.

Lewandowski, Z. and Stoodley, P. (1995) ‘Flow induced vibrations, drag force, and pressure drop in conduits covered with biofilm’, *Water Science and Technology*, 32(8), pp. 19–26. doi: 10.1016/0273-1223(96)00003-0.

Lewkowicz, A. K. and Das, D. K. (1986) ‘Turbulent boundary layers on rough surfaces with and without a pliable overlayer: a simulation of marine fouling’, *International Shipbuilding Progress*, 33(386), pp. 174–186. doi: 10.3233/ISP-1986-3338601.

Lewthwaite, J. C., Molland, A. F. and Thomas, K. W. (1985) ‘An Investigation into the Variation of Ship Skin Fricitonal Resistance with Fouling’.

Li, C. *et al.* (2019) ‘An investigation into the effects of marine biofilm on the roughness and drag characteristics of surfaces coated with different sized cuprous oxide (Cu $_2$ O) particles’, *Biofouling*, 35(1), pp. 15–33. doi: 10.1080/08927014.2018.1559305.

Li, M., Matouš, K. and Nerenberg, R. (2020) ‘Predicting biofilm deformation with a viscoelastic phase-field model: Modeling and experimental studies’, *Biotechnology and Bioengineering*, 117(11), pp. 3486–3498. doi: 10.1002/bit.27491.

Lieleg, O. *et al.* (2011) ‘Mechanical robustness of Pseudomonas aeruginosa biofilms’, *Soft Matter*, 7(7), pp. 3307–3314. doi: 10.1039/c0sm01467b.

Loeb, G. I. *et al.* (1984) ‘The influence of microbial fouling films on hydrodynamic drag of rotating discs.’, *Materials Science*. doi: 10.1007/978-1-4615-9720-9_13.

Lorenzini, M. *et al.* (2009) ‘Uncertainty assessment in friction factor measurements as a tool to design experimental set-ups’, *International Journal of Thermal Sciences*, 48(2), pp. 282–289. doi: 10.1016/J.IJTHERMALSCI.2008.06.006.

Macedo, R. G. *et al.* (2014) ‘A novel methodology providing insights into removal of biofilm-mimicking hydrogel from lateral morphological features of the root canal during irrigation procedures’, *International Endodontic Journal*, 47(11), pp. 1040–1051. doi: 10.1111/IEJ.12246.

Majumdar, S. *et al.* (2017) ‘A study of the rheological properties of visco-elastic materials using fractional calculus’, *Colloids and Surfaces A: Physicochemical and Engineering Aspects*, 516, pp. 181–189. doi: 10.1016/j.colsurfa.2016.12.019.

Di Martino, P. (2018) ‘Extracellular polymeric substances, a key element in understanding biofilm phenotype’, *AIMS Microbiology*, 4(2), pp. 274–288. doi: 10.3934/microbiol.2018.2.274.

Massey, B. S. and Ward-Smith, J. (1998) *Mechanics of Fluids*. 7th edn. CRC Press. Available at: https://books.google.com/books/about/Mechanics_of_Fluids_Seventh_Edition.html?id=atorfhXblZ4C (Accessed: 17 March 2023).

Masuda, S., Watanabe, Y. and Ishiguro, M. (1991) ‘Biofilm Properties and Simultaneous Nitrification and Denitrification in Aerobic Rotating Biological Contactors’, *Water Science and Technology*, 23(7–9), pp. 1355–1363. doi: 10.2166/WST.1991.0588.

Mathias, J. D. and Stoodley, P. (2009) ‘Applying the digital image correlation method to estimate the mechanical properties of bacterial biofilms subjected to a wall shear stress’, *Biofouling*, 25(8), pp. 695–703. doi: 10.1080/08927010903104984.

MATLAB (2021) ‘9.11.0.1837725 (R2021b)’. Natick, Massachusetts: The Maths Works Inc.

Mazza, M. G. (2016) ‘The physics of biofilms—an introduction’, *Journal of Physics D: Applied Physics*, 49(20), p. 203001. doi: 10.1088/0022-3727/49/20/203001.

McCarthy, A. A. *et al.* (1999) ‘Characterisation of cake compressibility in dead-end microfiltration of microbial suspensions’, *Chemical Engineering Communications*, 173, pp. 79–90. doi: 10.1080/00986449908912777.

McEntee, W. (1916) ‘Variation of Frictional Resistance of Ships with Condition of Wetted Surface’, *Journal of the American Society for Naval Engineers*, pp. 311–314. doi: 10.1111/j.1559-3584.1916.tb00632.x.

Medhurst, J. S. (1990) ‘Outline of a draft international standard for the measurement and characterisation of roughness topography in fluid flow’, in *International Workshop on Marine Roughness and Drag*, pp. 1–9.

Milferstedt, K., Pons, M. N. and Morgenroth, E. (2009) ‘Analyzing characteristic length scales in biofilm structures’, *Biotechnology and Bioengineering*, 102(2), pp. 368–379. doi: 10.1002/bit.22075.

Möhle, R. B. *et al.* (2007) ‘Structure and shear strength of microbial biofilms as determined with confocal laser scanning microscopy and fluid dynamic gauging using a novel rotating disc biofilm reactor’, *Biotechnology and Bioengineering*, 98(4), pp. 747–755. doi: 10.1002/BIT.21448.

Moody, L. F. (1944) ‘Friction factors for pipe flow’, *Transaction of the ASME*, 66, pp. 671–684. Available at: http://www.ipt.ntnu.no/~asheim/TPG4135/Moody.pdf (Accessed: 25 August 2021).

Morgenroth, E. and Milferstedt, K. (2009) ‘Biofilm engineering: Linking biofilm development at different length and time scales’, *Reviews in Environmental Science and Biotechnology*, 8(3), pp. 203–208. doi: 10.1007/s11157-009-9163-1.

Murga, R., Stewart, P. S. and Daly, D. (1995) ‘Quantitative analysis of biofilm thickness variability’, *Biotechnology and Bioengineering*, 45(6), pp. 503–510. doi: 10.1002/BIT.260450607.

Murphy, E. A. K. *et al.* (2018) ‘Roughness effects of diatomaceous slime fouling on turbulent boundary layer hydrodynamics’, *Biofouling*, 34(9), pp. 976–988. doi: 10.1080/08927014.2018.1517867.

Murphy, E. A. K. *et al.* (2022) ‘Boundary layer hydrodynamics of patchy biofilms’, *Biofouling*, 37(7), pp. 696–714. doi: 10.1080/08927014.2022.2117033.

Muthukrishnan, T. *et al.* (2014) ‘Long-term microfouling on commercial biocidal fouling control coatings’, *Biofouling*, 30(10), pp. 1155–1164. doi: 10.1080/08927014.2014.972951.

Narciso, D. A. C. *et al.* (2022) ‘Characterization of biofilm structure and properties via processing of 2D optical coherence tomography images in BISCAP’, *Bioinformatics*, 38(6), pp. 1708–1715. doi: 10.1093/bioinformatics/btac002.

Neu, T. R. and Lawrence, J. R. (2015) ‘Innovative techniques, sensors, and approaches for imaging biofilms at different scales’, *Trends in Microbiology*, 23(4), pp. 233–242. doi: 10.1016/J.TIM.2014.12.010.

Ng, S. K. and Walker, J. M. (2012) *Measuring Turbulence Characteristics of Artificial Biofilms using LDV and High Speed Photography*, *18 th Australasian Fluid Mechanics Conference Launceston*.

Nguyen, H. *et al.* (2021) ‘Biofilm viscoelasticity and nutrient source location control biofilm growth rate, migration rate, and morphology in shear flow’, *Scientific Reports*, 11, p. 16118. doi: 10.1038/s41598-021-95542-1.

Nikuradse, J. (1933) *Laws of flow in rough pipes*, *National Advisory Committee for Aeronautics, Technical Memorandum 1292*.

Norton, T. A. *et al.* (1998) ‘Using confocal laser scanning microscopy, scanning electron microscopy and phase contrast light microscopy to examine marine biofilms’, *Aquatic Microbial Ecology*, 16(2), pp. 199–204. doi: 10.3354/AME016199.

Ochoa, J. C. *et al.* (2007) ‘Influence of non-uniform distribution of shear stress on aerobic biofilms’, *Chemical Engineering Science*, 62(14), pp. 3672–3684. doi: 10.1016/J.CES.2007.03.023.

Ohashi, A. *et al.* (1999) ‘A novel method for evaluation of biofilm tensile strength resisting erosion’, in *Water Science and Technology*. Elsevier Science Ltd, pp. 261–268. doi: 10.1016/S0273-1223(99)00176-6.

Oliveira, D., Larsson, A. I. and Granhag, L. (2018) ‘Biofouling The Journal of Bioadhesion and Biofilm Research Effect of ship hull form on the resistance penalty from biofouling Effect of ship hull form on the resistance penalty from biofouling’, *Biofouling*, 34(3), pp. 262–272. doi: 10.1080/08927014.2018.1434157.

Pabst, B. *et al.* (2016) ‘Gel-entrapped Staphylococcus aureus bacteria as models of biofilm infection exhibit growth in dense aggregates, oxygen limitation, antibiotic tolerance, and heterogeneous gene expression', *Antimicrobial Agents and Chemotherapy*, 60(10), pp. 6294–6301. doi: 10.1128/AAC.01336-16.

Papadatou, M. *et al.* (2021) 'Marine biofilms on different fouling control coating types reveal differences in microbial community composition and abundance', *MicrobiologyOpen*, 10(4). doi: 10.1002/MBO3.1231.

Paramanova, E. (2009) *Compressive strength of fungal and oral biofilms*.

Paramonova, E. *et al.* (2009) 'Impact of hydrodynamics on oral biofilm strength', *Journal of Dental Research*, 88(10), pp. 922–926. doi: 10.1177/0022034509344569.

Park, D. J. and Hrymak, A. N. (2016) *Polymer System and Molding Techniques for Surgical Training Polymer System and Molding Techniques for Surgical Training Models Models*. The University of Western Ontario. Available at: https://ir.lib.uwo.ca/etdhttps://ir.lib.uwo.ca/etd/3747 (Accessed: 29 October 2019).

Parthasarathy, R. N. and Muste, M. (1994) 'Velocity measurements in Asymmetric Turbulent Channel Flows', *Journal of Hydraulic Engineering*, 120(9), pp. 1000–1020.

Paul, E. *et al.* (2012) 'Effect of shear stress and growth conditions on detachment and physical properties of biofilms', *Water Research*, 46(17), pp. 5499–5508. doi: 10.1016/J.WATRES.2012.07.029.

Pavissich, J. P., Li, M. and Nerenberg, R. (2021) 'Spatial distribution of mechanical properties in *Pseudomonas aeruginosa* biofilms, and their potential impacts on biofilm deformation', *Biotechnology and Bioengineering*, 118(4), pp. 1545–1556. doi: 10.1002/bit.27671.

Pavlovsky, L., Younger, J. G. and Solomon, M. J. (2013) 'In situ rheology of Staphylococcus epidermidis bacterial biofilms', *Soft Matter*, 9(1), pp. 122–131. doi: 10.1039/c2sm27005f.

Pereira, M. O. *et al.* (2002) 'Effect of flow regime on the architecture of a Pseudomonas fluorescens biofilm', *Biotechnology and Bioengineering*, 78(2), pp. 164–171. doi: 10.1002/BIT.10189.

Perkins, S. C. T. *et al.* (2012) 'The influence of bacteria based biofouling on the wall friction and velocity distribution of hydropower pipes', *Australasian Journal of Mechanical Engineering*, 12(1), pp. 77–88. doi: 10.7158/M12-087.2014.12.1.

Peterson, B. W. *et al.* (2013) 'A distinguishable role of eDNA in the viscoelastic relaxation of biofilms', *mBio*, 4(5). doi: 10.1128/mBio.00497-13.

Peterson, B. W. *et al.* (2015) ‘Viscoelasticity of biofilms and their recalcitrance to mechanical and chemical challenges’, *FEMS Microbiology Reviews*. Oxford University Press, pp. 234–245. doi: 10.1093/femsre/fuu008.

Picioreanu, C. *et al.* (2018) ‘Determination of mechanical properties of biofilms by modelling the deformation measured using optical coherence tomography’, *Water Research*, 145, pp. 588–598. doi: 10.1016/j.watres.2018.08.070.

Picologlou, B. F., Zelver, N. and Characklis, W. G. (1980) ‘Biofilm growth and hydraulic performance’, *Journal of the Hydraulics Division*, 106(HY5), pp. 733–746.

Pimentel, L. C. G., Cotta, R. M. and Kakaç, S. (1999) ‘Fully developed turbulent flow in ducts with symmetric and asymmetric rough walls’, *Chemical Engineering Journal*, 74(3), pp. 147–153. doi: 10.1016/S1385-8947(99)00036-4.

Prades, L. *et al.* (2020) ‘Computational and experimental investigation of biofilm disruption dynamics induced by high velocity gas jet impingement’, *American Society For Microbiology*, 11(1), pp. e02813-02819. doi: 10.1101/824532.

Qian, P.-Y. *et al.* (2007) ‘Marine Biofilms as Mediators of Colonization by Marine Macroorganisms: Implications for Antifouling and Aquaculture’, *Marine Biotechnology*, 9, pp. 399–410. doi: 10.1007/s10126-007-9001-9.

Quan, K. *et al.* (2022) ‘Water in bacterial biofilms: pores and channels, storage and transport functions’, *Critical Reviews in Microbiology*, 48(3), pp. 283–302. doi: 10.1080/1040841X.2021.1962802.

R Core team (2020) *R: A language and environment for statistical computing. R Foundation for Statistical Computing*, *R Foundation for Statistical Computing*.

Rmaile, A. *et al.* (2013) ‘Microbial tribology and disruption of dental plaque bacterial biofilms’, *Wear*, 306(1–2), pp. 276–284. doi: 10.1016/j.wear.2013.02.010.

Rupp, C. J., Fux, C. A. and Stoodley, P. (2005) ‘Viscoelasticity of Staphylococcus aureus biofilms in response to fluid shear allows resistance to detachment and facilitates rolling migration’, *Applied and Environmental Microbiology*, 71(4), pp. 2175–2178. doi: 10.1128/AEM.71.4.2175-2178.2005.

Rusconi, R. *et al.* (2010) ‘Laminar flow around corners triggers the formation of biofilm streamers’, *Journal of The Royal Society Interface*, 7(50), pp. 1293–1299. doi: 10.1098/RSIF.2010.0096.

Safari, A. *et al.* (2015) ‘Mechanical properties of a mature biofilm from a wastewater system: from microscale to macroscale level’, *Biofouling*, 31(8), pp. 651–664. doi: 10.1080/08927014.2015.1075981.

Salta, M. *et al.* (2013) ‘Marine biofilms on artificial surfaces: Structure and dynamics’, *Environmental Microbiology*, pp. 2879–2893. doi: 10.1111/1462-2920.12186.

Saur, T. *et al.* (2017) ‘Impact of wall shear stress on initial bacterial adhesion in rotating annular reactor’, *PLOS ONE*, 12(2), p. e0172113. doi: 10.1371/JOURNAL.PONE.0172113.

Scheidweiler, D. *et al.* (2019) ‘Unraveling the biophysical underpinnings to the success of multispecies biofilms in porous environments’, *ISME Journal*, 13(7), pp. 1700–1710. doi: 10.1038/s41396-019-0381-4.

Schiebel, J. *et al.* (2020) ‘Analysis of three-dimensional biofilms on different material surfaces’, *Cite this: Biomater. Sci*, 8, p. 3500. doi: 10.1039/d0bm00455c.

Schindelin, J. *et al.* (2012) ‘Fiji: an open-source platform for biological-image analysis’, *Nature Methods*, 9(7), pp. 676–682. doi: 10.1038/nmeth.2019.

Schultz, M. P. (2004) ‘Frictional Resistance of Antifouling Coating Systems’, *Journal of Fluids Engineering*, 126(6), pp. 1039–1047. doi: 10.1115/1.1845552.

Schultz, M. P. (2007) ‘Effects of coating roughness and biofouling on ship resistance and powering’, *Biofouling*, 23(5), pp. 331–341. doi: 10.1080/08927010701461974.

Schultz, M. P. *et al.* (2011) ‘Economic impact of biofouling on a naval surface ship’, *Biofouling*, 27(1), pp. 87–98. doi: 10.1080/08927014.2010.542809.

Schultz, M. P. *et al.* (2015) ‘Impact of diatomaceous biofilms on the frictional drag of fouling-release coatings’, *Biofouling*, 31(9–10), pp. 759–773. doi: 10.1080/08927014.2015.1108407.

Schultz, M. P. and Flack, K. A. (2007) ‘The rough-wall turbulent boundary layer from the hydraulically smooth to the fully rough regime’, *Journal of Fluid Mechanics*, 580, pp. 381–405. doi: 10.1017/S0022112007005502.

Schultz, M. P. and Myers, A. (2003) ‘Comparison of three roughness function determination methods’, *Experiments in Fluids*, 35(4), pp. 372–379. doi: 10.1007/s00348-003-0686-x.

Schultz, M. P. and Swain, G. W. (2000) ‘The influence of biofilms on skin friction drag’, *Biofouling*, 15(3), pp. 129–139. doi: 10.1080/08927010009386304.

Shanbhag, A. G. (1994) ‘Utilization of Information Measure as a Means of Image Thresholding’, *CVGIP: Graphical Models and Image Processing*, 56(5), pp. 414–419. doi: 10.1006/cgip.1994.1037.

Shaw, T. *et al.* (2004) ‘Commonality of elastic relaxation times in biofilms’, *Physical Review Letters*, 93(9), pp. 1–4. doi: 10.1103/PhysRevLett.93.098102.

Shen, Y. *et al.* (2017) ‘Role of Biofilm Roughness and Hydrodynamic Conditions in Legionella pneumophila Adhesion to and Detachment from Simulated Drinking Water Biofilms’, *Physiology & behavior*, 176(3), pp. 139–148. doi: 10.1016/j.physbeh.2017.03.040.

Simões, L. C. *et al.* (2022) ‘Biofilm formation under high shear stress increases resilience to chemical and mechanical challenges’, *Biofouling*, 38(1), pp. 1–12. doi: 10.1080/08927014.2021.2006189.

Snowdon, A. *et al.* (2022) ‘Elastomeric sandpaper replicas as model systems for investigating elasticity, roughness and associated drag in a marine biofilm flow cell’, *Ocean Engineering*, 266. doi: 10.1016/j.oceaneng.2022.112739.

Snowdon, A. *et* al. (2023) 'Surface properties influence marine biofilm rheology, with implications for ship drag', *Soft Matter*, 19. pp. 3675 - 3687. doi: 10.1039/d2sm01647h.

Soares, A. *et al.* (2022) ‘Hydrodynamic Effects on Biofilm Development and Recombinant Protein Expression’, *Microorganisms*, 10(5). doi: 10.3390/MICROORGANISMS10050931/S1.

Song, S. *et al.* (2021) ‘Investigating the Effect of Heterogeneous Hull Roughness on Ship Resistance Using CFD’, *Journal of Marine Science and Engineering 2021, Vol. 9, Page 202*, 9(2), p. 202. doi: 10.3390/JMSE9020202.

Song, S., Demirel, Y. K. and Atlar, M. (2019) ‘An investigation into the effect of biofouling on the ship hydrodynamic characteristics using CFD’, *Ocean Engineering*, 175, pp. 122–137. doi: 10.1016/j.oceaneng.2019.01.056.

Souza-Egipsy, V. *et al.* (2021) ‘Biofilm mechanics in an extremely acidic environment: microbiological significance’, *Soft Matter*, 17(13), p. 3672. doi: 10.1039/d0sm01975e.

Staudt, C. *et al.* (2004) ‘Volumetric measurements of bacterial cells and extracellular polymeric substance glycoconjugates in biofilms’, *Biotechnology and Bioengineering*, 88(5), pp. 585–592. doi: 10.1002/BIT.20241.

Stefano, A. Di *et al.* (2009) ‘Viscoelastic properties of Staphylococcus aureus and Staphylococcus epidermidis mono-microbial biofilms’, *Microbial Biotechnology*, 2(6), pp. 634–641. doi: 10.1111/j.1751-7915.2009.00120.x.

Stewart, E. J. *et al.* (2015) ‘Artificial biofilms establish the role of matrix interactions in staphylococcal biofilm assembly and disassembly’, *Scientific Reports*, 5. doi: 10.1038/srep13081.

Stoodley, P. *et al.* (1998) ‘Oscillation characteristics of biofilm streamers in turbulent flowing water as related to drag and pressure drop’, *Biotechnology and Bioengineering*, 57(5), pp. 536–544. doi: 10.1002/(SICI)1097-0290(19980305)57:5<536::AID-BIT5>3.0.CO;2-H.

Stoodley, P., Boyle, J., Cunningham, A. B., Dodds, I., *et al.* (1999) ‘Biofilm Structure and Influence on Biofouling Under Laminar and Turbulent Flows’, in *Biofilms in Aquatic Systems*. Royal Society of Chemistry, pp. 13–24. Available at: https://eprints.soton.ac.uk/id/eprint/158959.

Stoodley, P., Boyle, J. D., de Beer, D. and Lappin-Scott, H. M. (1999) ‘Evolving Perspectives of Biofilm Structure’, *Biofouling*, 14(1), pp. 75–90.

Stoodley, P *et al.* (1999) ‘Influence of hydrodynamics and nutrients on biofilm structure’, *Journal of Applied Microbiology Symposium Supplement*, 85(28), pp. 19–28. doi: 10.1111/j.1365-2672.1998.tb05279.x.

Stoodley, P., Lewandowski, Z., Boyle, J. D., *et al.* (1999) ‘Structural deformation of bacterial biofilms caused by short-term fluctuations in fluid shear: An in situ investigation of biofilm rheology’, *Biotechnology and Bioengineering*, 65(1), pp. 83–92. doi: 10.1002/(SICI)1097-0290(19991005)65:1<83::AID-BIT10>3.0.CO;2-B.

Stoodley, P., Lewandowski, Z., Boyle, J. D, *et al.* (1999) ‘The formation of migratory ripples in a mixed species bacterial biofilm growing in turbulent flow’, *Environmental microbiology*, 1(5), pp. 447–455. doi: 10.1046/j.1462-2920.1999.00055.x.

Stoodley, P. *et al.* (2002) ‘Biofilm material properties as related to shear-induced deformation and detachment phenomena’, *Journal of Industrial Microbiology and Biotechnology*, 29(6), pp. 361–367. doi: 10.1038/sj.jim.7000282.

Stoodley, P., Boyle, J. D. and Lappin-scott, H. M. (2000) ‘Influence of flow on the structure of bacterial biofilms’, in Bell, C. R., Brylinsky, M., and Johnson-Green, P. C. (eds) *Microbial Biosystems: New Frontiers, Proceedings of the 8th International Symposium on Microbial Ecology*, pp. 263–269. Available at: https://eprints.soton.ac.uk/id/eprint/157631.

Stoodley, P., Boyle, J. D. and Lappin-Scott, H. M. (1999) *Influence of flow on the structure of bacterial biofilms*, *Atlantic Canada Society for Microbial Ecology*.

Stoodley, P., DeBeer, D. and Lewandowski, Z. (1994) ‘Liquid flow in biofilm systems’, *Applied* *and Environmental Microbiology*, 60(8), pp. 2711–2716.

Stoodley, P., Hall-Stoodley, L. and Lappin-Scott, H. M. (2001) ‘Detachment, surface migration, and other dynamic behavior in bacterial biofilms revealed by digital time-lapse imaging’, *Methods in Enzymology*, 337(406), pp. 306–319. doi: 10.1016/S0076-6879(01)37023-4.

Strathmann, M., Griebe, T. and Flemming, H. C. (2000) ‘Artificial biofilm model- A useful tool for biofilm research’, *Applied Microbiology and Biotechnology*, 54(2), pp. 231–237. doi: 10.1007/s002530000370.

Suastika, I. K. *et al.* (2021) ‘Characteristics of drag due to streamwise inhomogeneous roughness’, *Ocean Engineering*, 223. doi: 10.1016/J.OCEANENG.2021.108632.

Sun, T. L. *et al.* (2013) ‘Physical hydrogels composed of polyampholytes demonstrate high toughness and viscoelasticity’, *Nature Materials*, 12(10), pp. 932–937. doi: 10.1038/nmat3713.

Sutton, M. *et al.* (1983) ‘Determination of displacements using an improved digital correlation method’, *Image and Vision Computing*, 1(3), pp. 133–139. doi: 10.1016/0262-8856(83)90064-1.

Swain, G. *et al.* (2006) ‘Short-term testing of antifouling surfaces: the importance of colour’, *Biofouling*, 22(6), pp. 425–429. doi: 10.1080/08927010601037163.

Swimberghe, R. C. D. *et al.* (2019) ‘Efficacy of sonically, ultrasonically and laser-activated irrigation in removing a biofilm-mimicking hydrogel from an isthmus model’, *International Endodontic Journal*, 52(4), pp. 515–523. doi: 10.1111/IEJ.13024.

Sylvester, F. *et al.* (2011) ‘Hull fouling as an invasion vector: can simple models explain a complex problem?’, *Journal of Applied Ecology*, 48(2), pp. 415–423. doi: 10.1111/J.1365-2664.2011.01957.X.

Taherzadeh, D. *et al.* (2010) ‘Computational study of the drag and oscillatory movement of biofilm streamers in fast flows’, *Biotechnology and Bioengineering*, 105(3), pp. 600–610. doi: 10.1002/bit.22551.

Taherzadeh, D., Picioreanu, C. and Horn, H. (2012) ‘Mass transfer enhancement in moving biofilm structures’, *Biophysical Journal*, 102(7), pp. 1483–1492. doi: 10.1016/j.bpj.2012.02.033.

Tallawi, M., Opitz, M. and Lieleg, O. (2017) ‘Modulation of the mechanical properties of bacterial biofilms in response to environmental challenges’, *Biomaterials Science*. Royal Society of Chemistry, pp. 887–900. doi: 10.1039/c6bm00832a.

Team, R. C. (2019) ‘R: A language and environment for statistical computing.’ Vienna: R foundation for Statistical Computing. Available at: https://www.r-project.org/.

Tierra, G. *et al.* (2015) ‘Multicomponent model of deformation and detachment of a biofilm under fluid flow’, *Journal of The Royal Society Interface*, 12(106), p. 20150045. doi: 10.1098/rsif.2015.0045.

Titow, W. V. (1984) *PVC Technology*. 4th edn, *PVC Technology*. 4th edn. Elsevier Applied Science Publishers. doi: 10.1007/978-94-009-5614-8.

Towler, B. W. *et al.* (2003) ‘Viscoelastic Properties of a Mixed Culture Biofilm from Rheometer Creep Analysis’, *Biofouling*, 19(5), pp. 279–285. doi: 10.1080/0892701031000152470.

Townsin, R. L. (2003) ‘The Ship Hull Fouling Penalty’, *Biofouling*, 19, pp. 9–15. doi: 10.1080/0892701031000088535.

Tuck, B. *et al.* (2022) ‘Extracellular DNA: A Critical Aspect of Marine Biofilms’, *Microorganisms*, 10(7). doi: 10.3390/MICROORGANISMS10071285/S1.

Turan, O. *et al.* (2016) ‘Experimental Determination of Added Hydrodynamic Resistance Caused by Marine Biofouling on Ships’, in *Transportation Research Procedia*. Elsevier B.V., pp. 1649–1658. doi: 10.1016/j.trpro.2016.05.130.

Vadillo-Rodriguez, V. and Dutcher, J. R. (2009) ‘Dynamic viscoelastic behavior of individual Gram-negative bacterial cells’, *Soft Matter*, 5, pp. 5012–5019. doi: 10.1039/b912227c.

Valladares Linares, R. *et al.* (2016) ‘Compaction and relaxation of biofilms’, *Desalination and Water Treatment*, 57(28). doi: 10.1080/19443994.2015.1057036.

Vieira, J. M. *et al.* (2020) ‘Rheology and soft tribology of thickened dispersions aiming the development of oropharyngeal dysphagia-oriented products’, *Current Research in Food Science*, 3, p. 19. doi: 10.1016/J.CRFS.2020.02.001.

Vieira, M. J., Melo, L. F. and Pinheiro, M. M. (2009) ‘Biofilm formation: Hydrodynamic effects on internal diffusion and structure’, *http://dx.doi.org/10.1080/08927019309386244*, 7(1), pp. 67–80. doi: 10.1080/08927019309386244.

Vincent, J. F. V. (2012) ‘Basic Elasticity and Viscoelasticity’, in *Structural Biomaterials*. Third. Princeton University Press, pp. 1–27. Available at: https://www.jstor.org/stable/j.ctt7tbgv.4%0AJSTOR.

Vinogradov, A. M. *et al.* (2004) ‘ Rheology of biofilms formed from the dental plaque pathogen Streptococcus mutans ’, *Biofilms*, 1(1), pp. 49–56. doi: 10.1017/s1479050503001078.

Wagner, M. *et al.* (2010) ‘Investigation of the mesoscale structure and volumetric features of biofilms using optical coherence tomography’, *Biotechnology and Bioengineering*, 107(5), pp. 844–853. doi: 10.1002/bit.22864.

Wagner, M. and Horn, H. (2017) ‘Optical coherence tomography in biofilm research: A comprehensive review’, *Biotechnology and Bioengineering*, 114(7), pp. 1386–1402. doi: 10.1002/bit.26283.

Wahl, M. (1989) ‘Marine epibiosis. I. Fouling and antifouling: some basic aspects’, *Marine Ecology Progress Series*, 58, pp. 175–189. doi: 10.3354/MEPS058175.

Walker, J. M., Sargison, J. E. and Henderson, A. D. (2013) ‘Turbulent boundary-layer structure of flows over freshwater biofilms’, *Experiments in Fluids*, 54(12), pp. 1–17. doi: 10.1007/s00348-013-1628-x.

Watanabe, S. (1969) ‘Augmentation in frictional resistance due to slime’, *Journal of the Kansai Society of Naval Architecture*, 131, p. 45. Available at: https://www.worldcat.org/title/augmentation-in-frictional-resistance-due-to-slime/oclc/36668571 (Accessed: 23 August 2021).

Werb, M. *et al.* (2017) ‘Surface topology affects wetting behavior of Bacillus subtilis biofilms’, *npj Biofilms and Microbiomes*, 3(1). doi: 10.1038/s41522-017-0018-1.

White, A. R. *et al.* (2020) ‘Bacteria forming drag-increasing streamers on a drop implicates complementary fates of rising deep-sea oil droplets’, *Scientific Reports 2020 10:1*, 10(1), pp. 1–14. doi: 10.1038/s41598-020-61214-9.

White, A. R., Jalali, M. and Sheng, J. (2019) ‘A new ecology-on-a-chip microfluidic platform to study interactions of microbes with a rising oil droplet’, *Scientific Reports 2019 9:1*, 9(1), pp. 1–11. doi: 10.1038/s41598-019-50153-9.

Wilking, J. N. *et al.* (2011) ‘Biofilms as Complex Fluids’, *Materials Research Society Bulletin*, 36, pp. 385–390. doi: 10.1557/mrs.2011.71.

Winston, M. *et al.* (2003) ‘Rheology of Biofilms’, *Proceedings (electronic) of the ASCE 16th Engineering Mechanics Conference (EM2003)*, pp. 1–5. Available at: www.ce.washington.edu/em03/proceedings/papers/548.pdf.

Wloka, M. *et al.* (2004) ‘Rheological properties of viscoelastic biofilm extracellular polymeric substances and comparison to the behavior of calcium alginate gels’, *Colloid and Polymer Science*, 282(10), pp. 1067–1076. doi: 10.1007/s00396-003-1033-8.

Xi, C. *et al.* (2006) ‘High-resolution three-dimensional imaging of biofilm development using optical coherence tomography’, *Journal of Biomedical Optics*, 11(3), p. 034001. doi: 10.1117/1.2209962.

Yan, J. *et al.* (2018) ‘Bacterial Biofilm Material Properties Enable Removal and Transfer by Capillary Peeling’, *Advanced Materials*, 30(46). doi: 10.1002/ADMA.201804153.

Yeginbayeva, I. A. *et al.* (2020) ‘Effects of “in-service” conditions-mimicked hull roughness ranges and biofilms-on the surface and the hydrodynamic characteristics of foul-release type coatings’, *Biofouling*, 36(9), pp. 1074–1089. doi: 10.1080/08927014.2020.1855330.

Yusim, A. K. and Utama, I. K. A. P. (2017) ‘An Investigation Into The Drag Increase on Roughen Surface due to Marine Fouling Growth’, *IPTEK The Journal for Technology and Science*, 28(3). doi: 10.12962/J20882033.V28I3.3221.

Zargiel, K. A., Coogan, J. S. and Swain, G. W. (2011) ‘Diatom community structure on commercially available ship hull coatings’, *Biofouling*, 27(9), pp. 955–965. doi: 10.1080/08927014.2011.618268.

Zargiel, K. A. and Swain, G. W. (2014) ‘Static *vs* dynamic settlement and adhesion of diatoms to ship hull coatings’, *Biofouling*, 30(1), pp. 115–129. doi: 10.1080/08927014.2013.847927.

Zhang, T. C. and Bishop, P. L. (1994) ‘Density, porosity, and pore structure of biofilms’, *Water Research*, 28(11), pp. 2267–2277. doi: 10.1016/0043-1354(94)90042-6.

Zheng, S. *et al.* (2021) ‘Implication of Surface Properties, Bacterial Motility, and Hydrodynamic Conditions on Bacterial Surface Sensing and Their Initial Adhesion’, *Frontiers in Bioengineering and Biotechnology*, 9. doi: 10.3389/FBIOE.2021.643722.

Zou, G. X., Qu, J. P. and Zou, X. L. (2007) ‘Optimization of water absorption of starch/PVA composites’, *Polymer Composites*, 28(5), pp. 674–679. doi: 10.1002/pc.20333.

Appendix A

This section provides supplemental information relevant to Chapter 5.

c) Elastomer-P40

d) Elastomer-P240

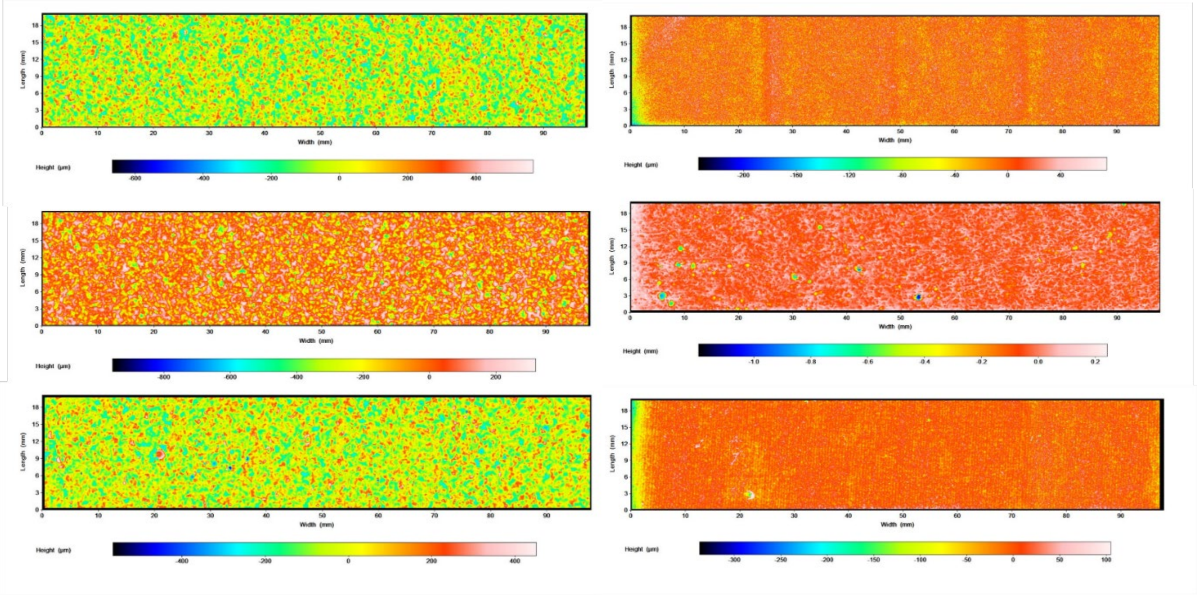

a) Filler-P40

b) Filler-P240

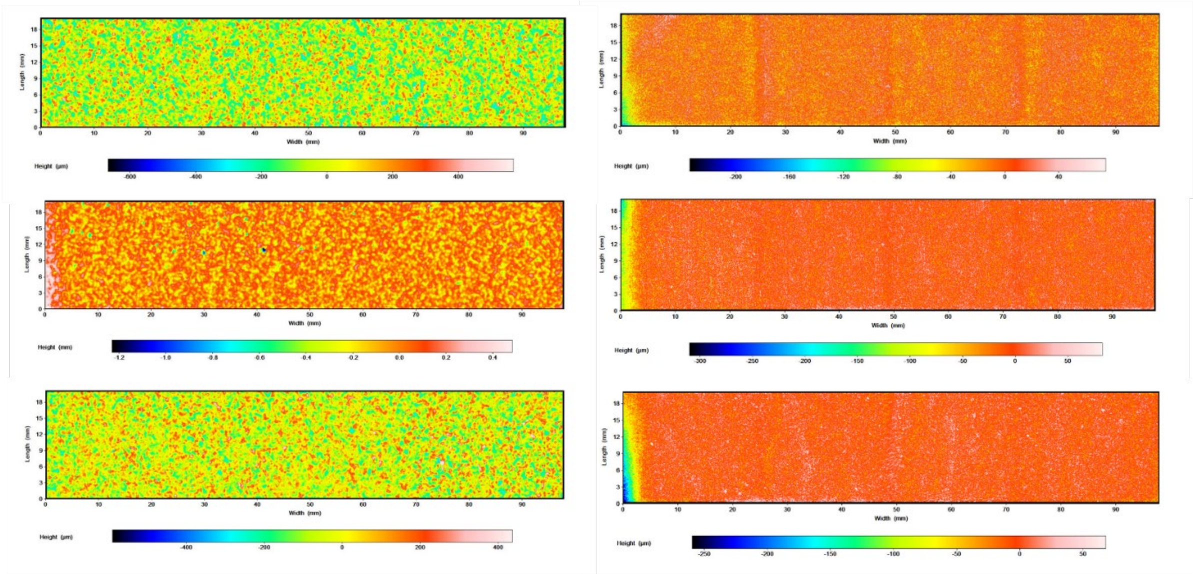

Figure A - 1. *Aerial images taken using a blue light interferometer of the P40 and P240 sandpaper replicas to show surface roughness. Using a) Elastomer-P40 as an example, from top to bottom the three images are of the source: sandpaper-P40, the intermediate: urethane-P40 and replica: elastomer-P40.*

Table A - 1. *Summary of the intermediate materials, including roughness measurements and elastic modulus. The compatible replica material, which is poured into the intermediate material mould to create the final replica of the source is also listed. A '-' indicates that no data was collected.*

***Intermediate* material**	**S_a (FEPA standards)**	**S_a pre-flow (um)**	***E* (MPa)**	**Compatible *replica* material**
Silicone rubber	Smooth	7.0 ± 2.0	0.9 [a]	Epoxy filler + 25% extra curing agent
	P240	16.9 ± 1.9		
	P80	44.7 ± 1.0		
	P40	97.3 ± 4.8		
Urethane putty	Smooth	-	~ 15. 6 [b]	PDMS-based elastomer
	P240	18.3 ± 2.2		
	P80	49.1 ± 1.6		
	P40	97.1 ± 4.1		

[a] Value taken from the technical datasheet for MM730FG silicone rubber provided by CHT-silicones (CHT, Germany) (CHT, 2019)

[b] Range of values converted using an equation proposed by Gent, (1958) to get elastic modulus from shore hardness (A) (Larson, 2017)

Appendix B

This section provides supplemental information relevant to Chapter 6.

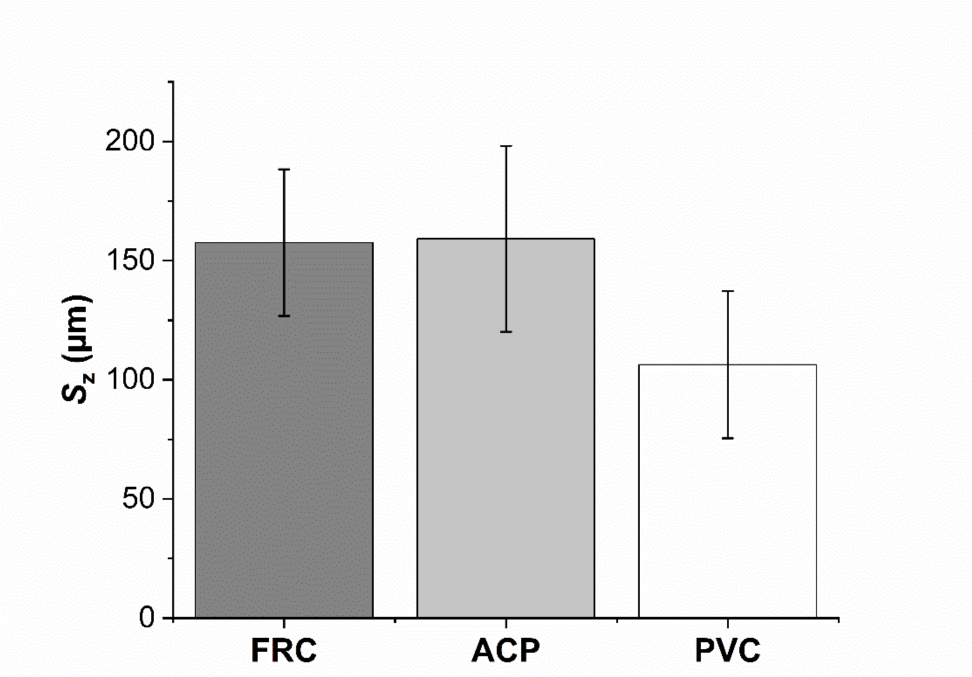

Figure B-1. *A Blue light interferometer (MikroCAD premium, LMI technologies) was used to confirm that coating surface roughness would not influence marine biofilm physico-mechanical properties. Single point scans (20 mm x 27 mm) with a cut-off wavelength of 5 mm were taken of the different surfaces. Mean peak-trough roughness height,* S_z *(µm) is presented as mean ± SD (n = 4). Statistical analysis confirmed that the FRC, ACP and PVC coupons all had a comparable surface roughness (ANOVA,* $P > 0.05$*).*

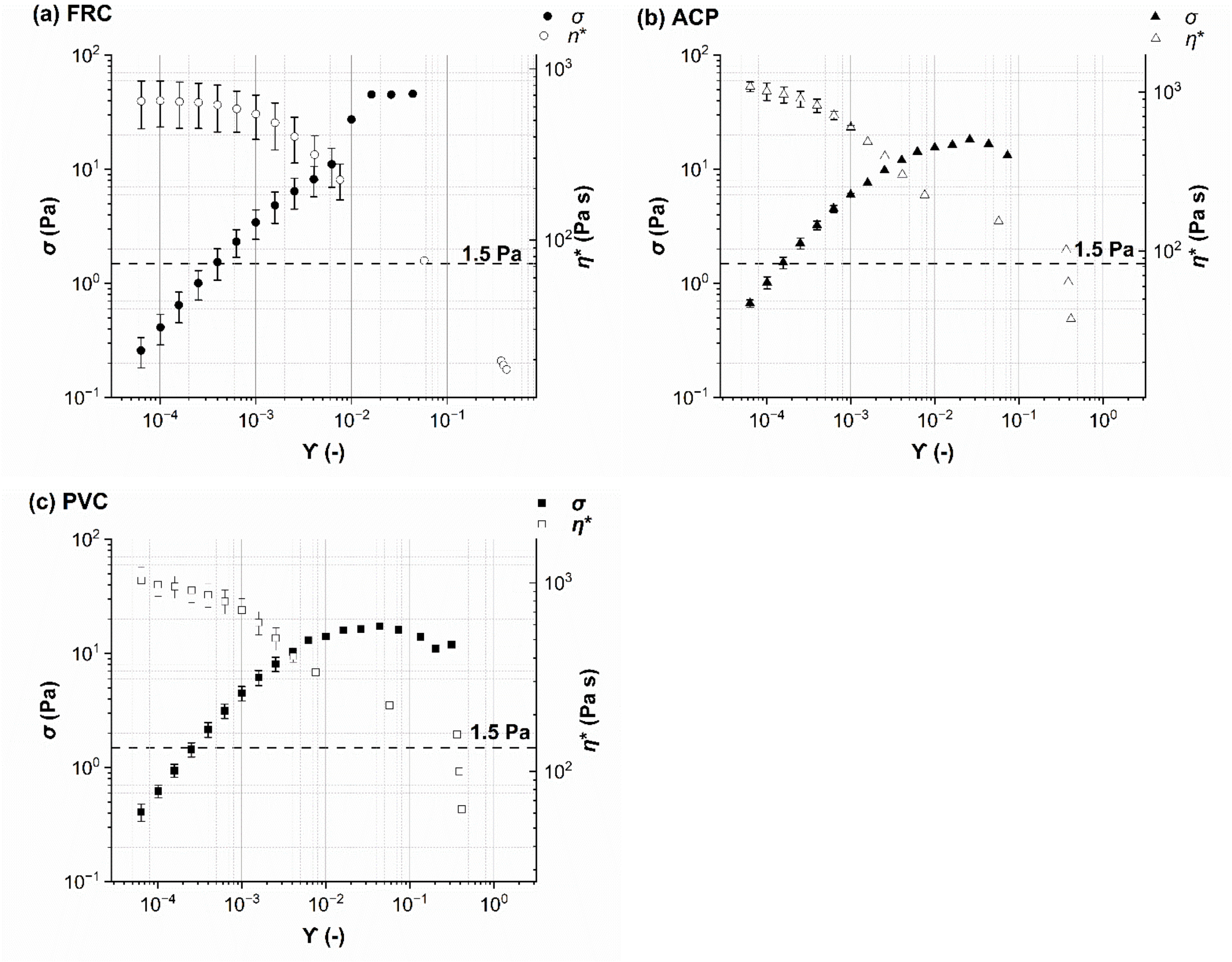

Figure B-2. *Stress, σ (Pa) and complex viscosity, η* (Pa s) vs. against strain, γ (-) for: (a) FRC, (b) ACP and (c) PVC. Data is presented as mean ± SD. A horizontal line has been added at 1.5 Pa to show that this was within the LVR for all coupons and was therefore used for further analysis.*